Cranfield University

Marcello Grassi

Numerical modelling of composite laminates with through-thisess-reinforcements

College of Aeronautics

PhD Thesis

College of Aeronautics

PhD Thesis

Academic Year 2003-2004

M. Grassi

Numerical modelling of composite laminates

with through-thickness-reinforcements

Supervisor: Dr. *X.* Zhang

March 2004

This thesis is submitted in partial fulfilment of the requirements for the Degree of

Doctor of Philosophy.

Abstract

The main objective of the present research study was to develop numerical models to investigate the mechanical properties and effectiveness of z-fibre reinforced laminates. A survey of relevant literature on through-thickness reinforcements (TTR) was undertaken and z-fibre pinning was chosen as the main topic of study. The development of numerical tools was mainly based on the finite element (FE) method and was carried out at different model scale levels.

At a micro-mechanical level of analysis, two models were presented. Firstly a unit cell FE model based on the actual geometric configuration of a z-pinned composite was used. Calculations were performed to understand how the through-thickness reinforcement modified the engineering elastic constants and local stress distributions.

Secondly the study of an analytical micro-mechanical model was undertaken. The model simulated a z-fibre bridging a delamination crack tinder mixed-mode loads. A constitutive law relating the z-pin bridging forces with the crack displacements was defined as the "bridging law". Numerical examples for z-fibre bridging laws under Mode I and Mode II loads were computed along with design evaluations of the effect of several micro-mechanical parameters on the bridging laws. This analytical model was then implemented into a MATLAB code specifically written by the author. The code generated constitutive relationship for interface elements simulating the bridging laws of a single z-pin to be used in a FE analysis.

A detailed numerical study of the mode I interlaminar fracture of composite laminates with z-pins was then carried out. AFL• model of a double cantilever beam (DCB) was developed. The numerical analysis focused on the large scale bridging (LSB) caused by z-pins mechanics, which increased the laminate resistance against delamination growth. The numerical results were validated against experimental data. Computational curves for the energy balance and energy rates were also determined showing that the LSB process consumed a significant amount of irreversible energy. The assumption made by the linear elastic fracture mechanics (LEFM) that all energy dissipations were included in the fracture energy and confined within the damage front, was not valid for z-pinned laminates.

The FE analysis was then extended to study a curved single-lap shear joint, to prove the effectiveness of TTR against debond failure of the joint. The presence of TTR was shown to delay the propagation of the debonding and generally to enhance the load carrying capability of the joint. TTR is proved to be more effective in reducing the Mode I component of debonding driving force than that of the Mode II.

Finally a global-local approach was proposed to implement the TTR elements into large composite stnictural FE models. Possible future studies for TTR numerical modelling were also addressed.

Acknowledgements

I would like to thank all the people which during these years have contributed in many different ways to this work.

I am mostly grateful to my supervisor Dr. Xiang Zhang for her continuous moral and technical support during the course of this research study. Thanks for being always there when 1 needed to sort problems out, for giving me the opportunity to broaden my scientific knowledge, for letting me participate to international conferences and events, for teaching me the methodology to approach this technical challenge.

Thanks to all the members of the MERCURYM project *team* from QinetiQ, Hurel Hispano, Aztex and Hexcel. Thanks for always showing their appreciation for the work being carried out at the College of Aeronautics. Thanks to Dr. Ivana Partridge for introducing me to the international scientific community and to Dr. Denis Carrie and Dr. Manos Troulis for providing me with experimental validation data. Useful technical discussions with Dr. B.N. Cox and Dr. M. Meo are also gratefully acknowledged.

My immense love and gratitude is for Sara. Thanks for following me abroad, accepting all the sacrifices that this choice meant to us. Thanks for being always by my side during this adventure, for coping with me and sustaining me in the difficult moments, for loving me endlessly, and most of all for just giving me the greatest joy of my life, our little Manuel.

My love and gratitude also goes to my parents, my brothers and my little sister Mariagrazia. Thanks for accepting my decision to come to England for a PhD. We all suffered our long separation, we all desperately missed our time together, but our love for each other has overcome this physical barrier. I have always felt your support.

Thanks to Vassilis Gianna, Steffen Malakkone, Mary, Manos, Michelone, Marilena Lelluccia, Derek the Inspector, Paul and Virginie, Axel and Macarena, Maria Jose bamba, Anthony snowboardy and Emine, Malcom and Rachel, all my colleagues and friends at QinetiQ which at different times have helped me in coping with being miles away from home without missing it too much. A special thank to Andrea Gonzalo Labrador for helping me out with the manuscript submission when I was completely snowed under.

At last I would like to thank the good Lord for giving me the immense gift of life, the joy of living it and a chance to make my contribution for a better world ahead.

"Considerate la vostra semenza:	*"Call to mind from whence ye sprang:*
fatti *non foste a vrner come hruh,*	*Ye were not farm'd to live the lift of brutes,*
ma per seguir virtu to e canoscenza"	*But virtue to pursue and knowledge high."*

Dante Alighieri (1265-1321), Divina C'onimedia [Divine Comedy], Inferno]Nall], Canto XJi 11, vr. *115*

List of Contents

Abstract u

Acknowledgements iii

List of Contents iv

List of Figures xi

List of Tables xxi

Nomenclature xxii

Acronyms xxv

Chapter 1

Introduction 1

1,1 A composite challenge for the twenty-first century 1

1.2 Background 2

1.2.1 Towards innovative aerospace design 2

1.2.2 Improving the damage tolerance for composite structures 6

1.3 Problem statement 7

1.4 Research objectives 8

1.5 Methodology 9

1.6 Structure *of* the thesis 12

1.7 Conclusive remarks 12

Chapter 2

Through-thickness reinforcement methods and research **14**

2.1 The enhancement of interlaminar properties 14

2.2 Through thickness reinforcement approach 15

12.1 3-D fabric composites: weaving, braiding, knitting 15

2.12 The Stitching Technique 16

2.2.3 The Z-Fibre insertion technique (z-pinning) 17

2.2.4 Through-the-thickness reinforcement of sandwich constructions: K-Cor, X-Cor 20

2.3 Z-pinning in material design 21

2.4 Review of z-pinning research 23

2.4.1 Mechanical testing of z-pinned laminates 23

2,4.2 Modelling of z-pinned laminates 29

2.5 Conclusions 35

Chapter 3

Analysis of stiffness and stresses in z-fibre reinforced composite laminates **36**

3.1 Introduction 36

3.2 Unit cell models for elastic constants 37

3.2.1 Unit Cell geometry 37

3.2.2 Analytical approach 39

3.13 Finite Element UC approach 39

3.2.4 Derivation of the average stress and strain fields 41

3,2.5 Unit Cell boundary conditions 43

3.3 Model for interlaminar stress analysis 45

3.4 Results and discussion 46

3.4.1 Comparison of elastic constants 46

3.4.2 Stress field around a z-fibre 51

3.4.3 Interlaminar stresses 52

3.5 Conclusions 58

Chapter 4

Micro-mechanical analysis of z-fibre bridging a delamination crack 60

4.1 Introduction *60*

4.2 Problem statement 60

4.2.1 Damage mechanisms for TTR during crack bridging 60

4.2.2 Summary of damage mechanisms during z-pin crack bridging 61

4.2.3 Experimental observations 64

4,3 Modelling procedures 67

4,3.1 Micro-mechanical model formulation for a TTR bridging mixed mode cracks 67

4.3.2 Z-fibre bridging law: Traction-Displacement Relation 67

4.3.3 Constitutive equations 69

4.3.4 Boundary conditions 71

4.4 Numerical examples of z-fibre bridging laws 74

4.4.1 Mode I crack loading conditions 74

4.4.2 Mode II crack loading conditions 81

4.5 Conclusions 87

Chapter 5

Analysis of z-fibre effects on mode-1 interlaminar delamination of composite laminates **89**

5,1 Introduction 89

5.2 Delamination analysis 90

5,2.1 Strain energy release rate and interlaminar fracture toughness G, 90

5.2.2 FE computational techniques for strain energy release rates 92

5.3 Problem Statement 97

5.3.1 Large scale bridging 97

5.3.2 Theoretical beam model for large scale bridging 98

5,4 Modelling procedures 100

5.4.1 Model for z-fibre bridging mechanics 100

5.4.2 DCB finite element model 102

5.4.3 DCB FE model assumptions and boundary conditions 104

5.4.4 Failure criteria implementation 106

5.4.5 The computational algorithm 106

5.4.6 Numerical convergence studies 108

5.5 Results & Discussion 112

5.5.1 Numerical example 112

5.5.2 Z-fibre effects on delamination propagation 112

5,5.3 Large scale bridging effect 116

5.5.4 Effect of z-fibre density 124

5.5.5 Effect of z-fibre diameter 128

5.5.6 Effect of friction energy 130

5.5.7 *Effect of* laminate flexural rigidity and z-fibre insertion depth *132*

5.6 Conclusions 134

Chapter 6

The energy balance and the fracture toughness of z-pinned laminates 136

6.1 Introduction 136

6.2 Fracture Mechanics with large scale bridging 137

6.3 FE computational techniques 140

6.3.1 Computational energy teens and energy rates 140

6.3.2 VCCT for FE models with interface elements 143

6.4 Results and discussion 146

6.5 Conclusions 154

Chapter 7

Structural behaviour of through-thickness reinforced composite joints 155

7,1 Introduction I55

7.2 Mechanically fastened or bonded joints vs. through-thickness reinforced joints 156

7.2.1 Single-lap shear joint 158

159

7.3 Problem Statement 159

7.3.1 Single-lap shear design and experiments 161

7.3.2 Single lap joint analysis with large scale bridging 163

7.4 Modelling procedures 163

7.4.1 Finite element model for curved single-lap joint 166

7.4.2 Model for pin bridging mechanics

7.4.3 Modelling failure modes 166
7.4.4 Computational algorithm 168
7.4,5 Modelling assumptions and limitations 169
7,5 Results & Discussion 171
7.5.1 Numerical examples 171
7.5,2 Bonded joint without pin reinforcement: Joint P 17I
7.5.3 Bonded joint with pin reinforcement: Joint Z 176
7.6 Conclusions 184

Chapter 8

Conclusions and future studies **186**

8.1 Conclusions 186
8.1.i Engineering elastic constants and interlaminar stresses 186
8. I.2 Z-pin bridging mechanics 186
8.1.3 Interface elements for z-pin bridging laws 187
8.1.4 Effect on mode 1 delamination 187
8.1.5 Fracture toughness and energy balance 187
8,1.6 Reinforced structural joints 188
8.2 Future studies 188
8.2.1 3D FE micro-mechanical model of a single z-pin failure 188
8.2.2 Implementation of the z-pin interface elements into a Global-Local FE analysis 190

Refe renc **192**

Appendix A

List of published papers from this research study **202**

Appendix B

Micro-mechanical model equations **203**

Appendix C

Matlab sub-routine for z-pin interface finite element **209**

Appendix ❑

FE model for delamination growth analysis **212**

Appendix E

Energy Plots **233**

Appendix F

Numerical derivation of the bridging law **246**

List of Figures

Chapter 1

Figure 1,1 *The Airbus* A380 *passenger jet scheduled to he in service_ for 2006.* 2

Figure 1.2 *The* A380 *novel materials design.* 3

Figure 1 3 *Innovative design* using *novel composite materials on the FI8 E F (a) by Boeing and Northrop Grumman; (h) The engine inlet ducts of the F18 E F presented de/am/nations.* 4

Figure 1.4 (a) *Lockheed Martin JSF; (1) .suh.ciantial savings in production of a graphite 'epoxy composite upper wing* skin *for* ***the*** *.151'* wing *carry-through assembly. Wing skin was produced at Alliani I echsystem,s, Clearfield, Utah, in their 16-ft. diameter fiber placement machine.* 5

Figure 1.5 *Modelling methodology for through-thickness reinforcements* 11

Chapter 2

Figure 2.1 *(a) 3-D weaving materials architecture; (h) standard 2-dimensional weaving architecture* (l•ort.sch *et al., 2002).* 15

Figure 2.2 *(a) Fibre structure of 5-axes 3-I3 orthogonal interlocked fabric composite (Tanzawa et al., 1999); (h) 3D braiding composite fibre architecture (Poe et al., 1997).*16

Figure 2.3 *Illustrations of* ***the*** *various stitch* ***types used to reinforce*** *laminates* ***(Mouritz*** *and Cox, 2000) and stitching fibre architecture(Poe et al., 1997): (a) lock;* (b) *chain; (c) modified lock stitches; (d) through the thickness stitching architecture; (e) 3-D stitching architecture.* 17

Figure 2.4 *Schematic of the ultrasonic gun insertion method of incorporating Z-pins into the* ***uncured*** *laminate (Cartie, 2000).* 18

Figure 2.5 *(a) Hand-held ultrasonic pin insertion device; (b) Semi-automated ultrasonic gun machine for Z-pinning of composites.* 19

Figure 2.6 *(a) z -pins inclined with respect to their original insertion angle; (h) Optimised cured laminate; (c) C-Scan map corresponding to specimen in (a); (d) ('-Scan map corresponding to specimen in (h) (Troulis et al., 2000).* 20

Figure 2.7 *K-Cor* with *carbon fabric face-sheets.* 20

Figure 2.8 *(a) X Cor 1 schematic; (h) K-Cor*^{7l1} *schematic.* 20

Figure 2.9 Z-pinned specimen geometry for Mode 1 testing (Troulis et al., 2000) 25

Figure 2.10 *Experimental results from (Cartie, 2000) (a)Load - displacement curves for control and pinned specimen.s under Mode I loading; (b) Effects of pin diameter on apparent toughness ('1 roulis, 2003).* 25

Figure 2.11 *T-,Ioint strength evaluation in (Rugg and Cox,* 2002): *(a) Schematic (not to scale) of T-stiffener specimen(P -load applied per unit width: (b) Representative load-displacement curves far T-specimens tested in wide configuration.* 27

Figure 2.12 *Load displacement curves fhr lap shear samples with and without z-fibres* (Rugg *et* al., *1998).* 28

Figure 2.13 *l'E micro-mechanical models presented in (Barret, 1996).* 29

Figure 2,14 *Z-fibre bridging stress versus crack opening displacement described by a pull-out cun'e in (7_hang et al., 19996): ff(d) fully bonded.* 31

Figure 2.15 *Elastic stretching and dehonding phases of z-fibre bridging curves under crack opening loads (Mode I) in (Liu and Mai, 2001).* 31

Figure 2.16 *Single-leg analytical models representing: schematic of through-thickness reinforced IJCB (a) distributed applied 7TR pressure(Mabson and Deohaldl 2000); (h) discrete z-reinforcements reaction loads (Liu and Mai, 2001).* 33

Chapter *3*

Figure 3.1 *Microscopic photograph of a unidirectional laminate with a single z-fibre* (0.28 *mm diameter), showing the curved fibres and resin pocket at either side of the z-pin.* 38

Figure *3.2 Schematic of a 2% z -pinned composite unit cell, where the ratio* l_n•*d defines the angle of misaligned in-plane_fibres.* 38

Figure 3.3 *3D finite element unit cell model (XY view) used in this study.* 40

Figure 3.4 *Three dimensional FE mode!, for a quarter unit cell.* 40

Figure 3.5 *Boundary conditions and applied displacements for the quarter unit cell models for two typical applied* in-plane loads. 44

Figure *3.6 Boundary conditions Pr pure shear load on QM/ unit cell model,* 44

Figure *3.7 Schematic of'a single z-pin reinforced plate with a parametric distance from the free-edge.* 45

Figure 3.8 *Finite element model of '4* /0, *90/ z -pinned laminate. Applied strain e,-=0.1 %.* 45

Figure *3.9 Stiffness variations for the E modulus for different kind of laminates: without z-fibre and with 2% density* 0.28 *diameter z-fibres,* 49

Figure 3.10 Stiffness variations for the E, modulus for different kind of laminates: without z-fibre and with *2% density* 0.28 *diameter z-fibres,* 49

Figure 3.1 1 *In plane shear stress (MPa)* distribution *around a z -pin. Note: deviated fibre region carried loads• providing extra stiffness that offset the added compliance of the pure resin region.* 50

Figure 3.12 *Quarter unit cell model: o stress field with perturbed stress field that disappeared after one z -fibre diameter.* 51

Figure 3.13 *Quarter unit cell model: introduced shear path along the misaligned fibre region.* 52

Figure 3,14 *Contour plot of 1 8 FE model of (0,90]_4 laminate without z-fibre reinforcements: z stress distribution (MPa). The critical inter-lamina area can be seen in the 0-90 interface.* 53

Figure 3.15 *Contour plot of 1.8 FE model of[0,90/, laminate without z-fibre rein jbrcement a stress distribution (MPa). 1 he critical interlaminar area is still the 0-90 interface. 53*

Figure 3.16 F *results* of a stress *distribution fnr* /0. $90j_s$ *cross-ply laminate: (a) Through-thickness* variation *(z-axis); (b) Y-variation from inside plate to the free-edge; (c) Variation along the. free-edge (x-axis).* 55

Figure 3.17 *Contour plot of I'2FL model of [±45], cross ply laminate without z-fibers: stress distribution* ***(MPa).*** *The critical inlerlatninar area can* ***be*** *detected* ***in*** *the* ***145 45*** *interface.* 56

Figure **3.18** *Finite element results of r , stress for /±45J.s angle-ply laminate: (a)Through-thickness variation (z-axis); (h) Y-variation .from inside plate to the free-edge; (c) Yariation along the free-edge (x-axis).* 57

Chapter 4

Figure 4.1 *Schematic representation of a laminate reinforced through the thickness by zfibre,s subjected to delamination. Mode I loads associated with crack opening displacement (u3) and Mode II loads related to crack sliding displacement* (u_1). 61

Figure 4.2 Z-ibre *bridging mechanics under pure Mode I loading conditions: (a) delamination reaching the bridging entity, (b) z-fi.hre debonding with slip zone growth, (c) slip zone growth up to the z-fibre end and consequent pull-out failure opposed by friction.* 62

Figure 4.3 *Bridging mechanics of an angled z-pin under Mixed Mode loading conditions: (a) delamination reaching the bridging entity, (h) z -pm debonding with slip zone growth and further delamination propagation in the laminate, (c) plastic shear deformation, (d)z-fibre splitting with fibres rotation towards load direction, and laminate matrix crumbling, (e) TIR lateral ploughing with the widened locus (x ,υ plane).* 63

Figure *4.4 Z-fibre bridging mechanisms following delamination (Rugg et al., 1998): (a) Angled fibre debonding and pull-out; (h) resisting fibre bending and plastic• d fbrtnations at delamination plane.* 64

Figure 4.5 *Failure of a z-f bre reinforced cubical specimen under shear loads (Cartie, 2000): (a) carbon BMl rod pullout failure; (h) SEM picture showing the rod bent in the fracture plane: (c) SEM of a damaged z-fibre after ultimate pullout; (d) Pullout failure of a titanium pin with an insertion angle complying the applied load; (e) tensile failure of a titanium pin with an insertion angle opposing the applied load.* 65

Figure 4.6 *T-fibre failure modes during delamination bridging: (a) SEM of a D('R_failed specimen surface where the pulled-out z-pins are visible (Cartie, 2000); (h) SEM of the locus left in the D('R upper arm surface after z -pins have been pulled-out (Troulis, 2003); (c) Optical micrograph of a single-lap joint failed surface reinforced with 1.7 diameter z-fibres showing the holes remaining after the pullout of the reinforcement (Rugg et al., 1998).* 66

Fiore 4.7 *Stitching failure during Mode 1 delamination bridging from (Dransfield et al., 1998): (a) Carbon epoxy laminate cross section showing the stitching threads; (h) SEM fractograph displaying the tensile failure of the stitching Kevlar thread and successive pullout; (c) corresponding hole remaining after thread pullout.* 66

Figure 4.8 *Bridging failure mechanics of a 3-1] orthogonal interlocked carbon-epoxy fabric from (Tanzawa et at, 1999): (a) z-fibre yarn bundle bridging a delamination crack under mode 1 loading condition; (b) SE/vf showing the z -yam breakage near the top or bottom surfaces and its pullout.* 67

Fiore 4.9 The schematic representation of the micro-mechanical model parameters in (Cox and Sridhar, 2001): (a) bridging 711? deformed under the traction load T with an initial a-= 0 (complying configuration); (h) bridging TTR with a resisting initial configuration cr O. 68

Fiore 4.10 *Equilibrium of the loads acting at the crack plane on the deformed z-reinforcement, with the farces expressed along the x ' car z' axes. 1', and "1:; are the bridging traction forces touted from the model equations.* 71

Fiore 4.11 *Applied boundary conditions for the pure mode I loading.* 74

Figure 4.12 *Normalised z-fibre axial stress* vs. *embedded length for different friction* stresses. 76

Fiore 4.13 *Normalised z-fibre axial stress vs. embedded length _for different z-fibre radii.* 77

Figure 4.14 *Computed* $Fs\text{-}u_3$ *curves for single z-fibre pullout with influence of different friction stresses: (a) Stable slip zone growth; (h) .stable frictional sliding .rtage.* 78

Fiore 4.15 *Computed* F_3*-u3 curves for single z-fibre* pullout *with influence of different z-fibre axial moduli (Ed: Stable slip zone growth.* 78

Fiore 4.16 *Bridging laws for mode I loading conditions for dmerent z-fibre embedding depths: (a) bridging traction during slip zone growth;* (b) *bridging traction during frictional sliding.* 79

Figure 4.17 *Bridging laws for mode I loading conditions for different z-fibre radii: (a) bridging traction during slip zone growth; (h) bridging traction during frictional* sliding. 80

Figure 4.18 *Computational curves for the z-fibre deflection angle Bo: (a) pre-pullout phase; (h) pullout phase.* 83

Fiore 4.19 *Micro-mechanical model computational curve: (a) z-fibre axial stress* an *trend during pre pullout phase; (b) z-fibre axial stress ao trend during pullout phase.* 84

Figure 4.20 *Micro-mechanical model computational curve:* axial *z-fibre* stress a() *vs. crack plane deformation angle B0* during *pre pullout and pullout* phases. 85

Fiore 4.21 *Micro-mechanical model computational curve: :fibre deflection length (o) vs. crack plane deformation angle (Br,) during pre-pullout and pullout* phases. 85

Fiore 4.22 *Micro-mechanical model computational curves: z-fibre bridging force 1",* vs. *crack plane deformation angle B0 during pre-pullout and pullout phases.* 86

Fiore 4.23 *Micro-mechanical model computational curves: z-fibre bridging force Fl vs. crack sliding displacement vector (u* I) *during pre-pullout and pullout phases for d fferent assumed, riction coefficients.* 86

Fiore 4.24 *Micro-mechanical model computational curves: z-fibre bridging force Ft vs. crack sliding displacement vector (u1) during pre-pullout and pullout phases for different assumed friction stresses r~ and punch loads* 87

Chapter 5

Fiore 5.1 *Typical remote loading conditions for fracture specimens: Mode 1 (opening mode); Mode II (shear mode); Mode 111 (tearing mode).* 91

Fiore *5.2 b'CCT approach for G-calculation (Wang and Raju. 19915): Crack problem in 2D plate; (h) through-crack in 3D body.* 93

Fiore 5.3 *FE mesh near the crack front with upper and lower sub-laminates defined with coincident coupled nodes behind the crack: (a) , four-noded linear shell element; (h) nine-noded shear deformahle quadratic element.* 94

Fiore 5.4 DCB theoretical model. 99

Fiore 5.5 Interface element: active silliness at i-th iteration. 101

Fiore 5.6 (a) Schematic of double cantilever beam OCR) specimen with z-fibres. Notice the distance for the first z -pin row; (h) FE model of DBC specimen, with zoomed interface element area. 103

Fiore 5.7 The implemented ANSYS graphical user interface for the FE model. 104

Fiore 5.8 Finite Element computational mode/ for a z-pinned DCB. 107

Figure 5.9 The *FE computation of delamination growth for a 2% z-pinned laminate z-pin radius* (r = *25()mn): (a)a=Jo mm,N~,$_b$-70; (b) a,- 20 mm,N,,$_b$=105; (c) a-300 mm,* ***- 143.*** 109

Figure 5.10 ***(a) Numerical*** *convergence* of *SERR for the plane strain model.* (b) *Numerical convergence of SERB_ for the 2D-Shell models.* 110

Figure 5.11 *Numerical convergence studies (S).* 1 **l** l

Figure 5.12 *Numerical convergence studies (dt.~l,;stt}.* 111

Figure 5.13 *Load-displacement curve for unpinned I)['8 (control case): Numerical vs. experimental results.* I13

Figure 5.14 *Load-displacement curves J r o z -pinned I)C'B: Numerical vs. experimental results.* 114

Figure 5.15 *P-8 curves, for a 2% z-pinned D(7B: experimental specimen* ***[Ιt*** *row misplaced at I mm from the crack tip; numerical model 1' row placed* ***5*** *mm from the crack tip; 1 r, z-pin row at 5 mm from the crack rip and modified elastic constants.* 115

Figure 5.16 *Load-displacement curve P r z -pinned IX'B: Numerical vs. experimental results.* 1 15

Figure 5.17 *The 4f.* ***.y*** *and the 4$_{ff;v}$ LSB areas characterizing the high bending moment (M_y) and high stresses region oz-pin reinforced laminate: (a) 3D view; (h) xz plane view.* 118

Figure 5.18 *Z-fibre bridging process during delamination growth fir a 0.5% z-pinned IX'B: z-fibre mechanics (bar-chart), M., $_{f\cdot Lt}$- location (o), z fibre ratio in area (-).* 119

Figure 5.19 *Z -fibre bridging process during delamination growth for a I % z-pinned IX 'B: zfihre mechanics (bar-chart), M$_{\cdot 1\cdot f\cdot LV}$ location (o), zfihre ratio in* $_{f\,n_{ei},}$ *area (-).* 119

Fig[r]***ure*** *5.20 Zfrhre bridging process during delamination growth _for a 2% z -pinned DCB: zfihre mechanics (bar-chart), M$_{\&f.a}$ location (o), z -fibre ratio in area (-).* *120*

Figure 5.21 Z_-fibre bridging process during delamination growth for a 4% z-pinned DCB: z-fibre mechanics (bar-chart), MLS location (of z-fibre ratio in area (-). *120*

Figure 5.22 Laminate stresses vs. delamination length, for 0.5% z pinned laminate: the O,,,,

, a at the ^{o}m,,., , 6, at delamination front section for unpinned laminate. *121*

Figure 5.23 Laminate, failure mode introduce by LSB mechanics ofz-fibre reinfarce ▸ nents.121

Figure 5.24 Laminate stresses vs. delamination length pr 1% H pinned laminate: a, at the cAm„r, . 6, at the'^{P}m· , o at delamination front section / or unpinned laminate. *122*

Figure 5.25 Laminate stresses vs. delamination length for 2% z -pinned laminate: o at the O_{ifiin}, ox at the $^{O}_{mar}$, aL at delamination front section for unpinned laminate. 122

Figure 5.26 Laminate stresses vs. delamination length for 4% z -pinned laminate: the4,;,, a, at the $^{O}_{n,ax}$, 6x at delamination front section for unpinned laminate. [s, at 123

Figure 5.27 Large Scale Bridging length against delamination propagation. 123

Figure 5.28 Computational P-Scurves•for different z-fibre densities and comparison with un-pinned case (r = 1411 pn). 125

Figure 5.29 Computational P-Scues fnr different z -fibre densities and comparison with un-pinned case (r -- 250,wn). 126

Figure 5.30 Load vs. delamination length for different z-pin densities (r=140 pm) and comparison with unpinned case. IT results (symbols); polynomial interpolation (smooth lines). 127

Figure 5.31 Load vs. delamination length for different z -pin densities (r-250 pm) and comparison with unpinned case. FE results (symbols); polynomial interpolation (smooth lines). 128

Figure 5.32 Computational P-S curves for different zfbre radii: rr-0.14 mm and r_2=0.25 mm. 129

Figure 5.33 Load vs delamination length curves for different :fibre radii: ri =0.14 mm and r2==0.25 mm. 129

Figure 5.34 Load vs delamination length curves for different friction stresses (r. 130

Figure 5.35 Load vs delamination length curves for d rent friction stresses (r). 131

Figure 5.36 Load vs. delamination length curves: effect of laminate_ flexural rigidity (0.5% z-pin density and 0.14 mm :fibre radius). 132

Figure 5.37 Load vs. delamination length curves: effects of laminate thickness & z -pin insertion depth (0.5% z -pin density and 0.14 mm z-frhre radius). 133

Figure 5.38 Load vs. delamination length curves: effects of laminate thickness α_{Tpin} insertion depth (2% z -pin density and 0.14 mm z-fibre radius). 133

Figure 5.39 Load vs. delamination length curves: effects of laminate thickness c z-pin insertion depth (2% z -pin density and 0.25 mm z-fibre radius). 134

Chapter 6

Figure 6.1 General loading condition for a cracked body undergoing self similar crack growth. 137

Figure 6-2 *Schematic of irreversible energy U1 computation at iteration i-th and i-th+1, .for crack length a, and a +-A respectively, when 3 z-pins are active. The incremental variation between the two PE runs is also outlined* 142

Figure 6.3 *Computational interface element nodal. f6rces* **F3** *for 7 z-fibre rows against crack length a: c = 0.5% and r = 15 Ml'a.* 143

Figure *6.4 Delamination analysis (c = 0.5%, r = 140pm, r -15 MPa): (a) Load P against delamination length; (h) percenta>e of load increment to propagate delamination; (c) G-matrix array interpolation ofG/'~ I computed using L`C:'['T.* 145

Figure 6.5 *Computational energy terms fir z-reinforced 17C'B FE model (c = 0.5%, r = 140 pm): (a) total crack length; (b) end of validity of LEl ill* assumption. 147

Figure 6.6 *Energy* terms *for z-reinforced DCB FE model: c = 1%, r 14(1 pm.* *148*

Figure *6.7 Energy terms tot- z-reinforced DCB FE model: c - 2%, r = 140 pm.* 148

Figure *6.8 Enemy terms. for z-reinforced DC'l3 FE model: c = 4%, r = 140 pm.* 149

Figure *6.9 Normalised FE energy computations (Ener) far different z f bre densities.* 149

Figure 6.10 *Normalised FE energy computations (Energy) for d Brent z-fibre. friction stresses.* *150*

Figure 6.1 i *Computed energy rates* (K± *m2) for z -pinned DCB: c = 0.5%, r = 110 pm.* 151

Figure 6.12 *Computed* energy *rates (K1 'm') for z-pinned DCB: c - 1%, r = 1401rm.* 152

Figure 6.13 *Computed energy rates (KJ m2) for z -pinned DCB (c -= 2%, r = 250 pm) for increasing_ friction stresses at pin-laminate interface.* 152

Figure 6.14 *Computed energy rates (KJ in') /hr zpinnedlXB (r = 250 pm) for increasing pin densities.* 153

Figure 6.15 *Averaged energy rates during stable LSB process for different z-pin densities and radii.* 153

Chapter *7*

Figure 7.1 *Lightweight carbon fibre composite joints: (a) T-joint; (h) nodal join.* 157

Figure *7,2 Tyoints structural design: (a) bolted co-bonded 1' joint; (b) z-pinned co-bonded T joint.* 157

Figure 7.3 *Schematic diagram of stresses in a single-lap adhesive joint where the adhesive shear stress is r and a is the transverse peel stress at the adhesive bond.* *158*

Figure 7.4 *Schematic diagram of failure modes for advanced composite bolted joints after Hart-Smith (1987): (a) tension failure; (6) shear-out failure; (c) cleavage-tension failure; (d) bearing failure.* 159

Figure *7.5 Joints* design: *(a) bolted-bonded single-lap shear joint; (h) pinned-bonded single-lap shear joint.* 159

Figure *7.6 Curved single-lap shear .specimens.* 160

Figure *7.7 Through-thickness reinforced joint: possible pin configurations.* 161

Figure 7.8 *Strain gauge locations on the CSLI.* 161

Figure 7.9 FE *model of the GFRP* ***curved*** *.single-lap joint (CSLI) used in this study (a), and the important model features in the overlap area (b).* 164

Figure 7.10 *Schematic* of *adhesive , failure modes: (a) cohesive failure with crack propagation in the adhesive layer; (b) crack propagation along or near the adhesive-adherends interface; (c) wavy crack growth along the two interfaces.* *167*

Figure 7.I l *Peel stress induced delamination failure in composite joints.* 167

Figure *7.12 Flow chart of the numerical solution algorithm procedures.* 170

Figure 7.13 *Numerical and experimental results ,for Joint P: Load (P)-Displacement (8 curves. FE predicted. failure mechanisms are also outlined in the graph.* 172

Figure 7.14 *Strain gauge* output *(E~ for Joint P: experimental values (thick lines), and FE. computations (dotted lines).* 172

Figure 7.15 *Bending strains £h (load direction x) for Joint P: experimental values (thick* lines), *and* FE *computations (dotted* lines). 173

Figure 7.16 *Membrane strains sm (load direction x) for Joint P: experimental values (thick lines), and FE computations (dotted lines).* 173

Figure 7.17 FE results (n; = 15, *P = 3118 N): contour plot fir 6r top layer of lower adherend, and deformed shape. The most critical area is outlined in the zoomed picture. Me tension failure of the top layers in the GRFC lower adherend is predicted to occur hefire the dehonding_ failure of the_ joint will start.* *174*

Figure 7.18 *Bending effects due to load path eccentricity: (a) CSL] deformation showing gross rotation; (h) gross rotation (in rad) of the joint overlap vs. non-linear analysis steps (n). the onset of the dehonding coincides with the 27th iteration (P=4645 N).* 175

Figure 7.19 SERR *distributions for Joint P across the joint width* (B) *at concave and convex ends: (a) Mode I component: (b) Mode II component.* 176

Figure 7.20 *Numerical and experimental results for Joint Z: Load (P)-Displacement (8) curves. FE predicted failure mechanisms are also outlined the graph.* 177

Figure 7.21 *Strain gauge output () for Joint Z: experimental values (thick lines), and FE computations (dotted lines).* 178

Figure 7.22 Bending *strains Eh (load direction x) for Joint Z: experimental values (thick* lines), *and FE* computations *(dotted lines).* 178

Figure 7.23 *Membrane strains sm (load direction x) for Joint Z: experimental values (thick lines), and FE computations (dotted lines).* 179

Figure 724 *Averaged SERR values (GI and G_{tt}) at the dehond front vs. dehond length* (a..180

Figure *7.25 Averaged SERR ratio Gt Grf at the dehond front vs. dehond length (a).* 180

Figure *7.26 Bridging closure forces F', and F3 opposing sliding and opening displacements, exerted by the pins at the convex end during dehond growth.* 181

Figure *7.27 Bridging closure force Fr and l' opposing sliding and opening displacements, exerted by the pins at the concave end during debond growth.* 182

Figure 7.28 *Left hand v-axis: angle of deflection at the fracture plane Co vs. dehond length a.; right hand y-axis: pin axial stress F.,r vs. debond a2.* 182

Figure 7.29 *The deflected zone length >1o, the slip length Ls and the pullout length Ds of pin number **4** vs. dehond length.* 183

Figure 7.30 *The crack sliding displacement at the pin 4 location vs. dehond length.* 183

Chapter 8

Figure 8.1 Pull-out *failure process of a single z-pin: (a) Load displacement curve-numerical* simulation; *(h) Load Displacement curve- experimental results; (c) z -pin elastic stretching: (d) z -pin dehonding: (e) z-pin frictional sliding.* 189

Figure 8.2 Global ***FE*** *model ofa composite stiffened panel, with a local model to simulate* local *damage* growth. 190

Figure 8.3 *Implementation* of the *z-pin macro-element into a shell FE model.* 191

List of Tables

Chapter 2

Table 2-1 *Typical distances between two adjacent zfhres far typical densities.* 19

Chapter 3

Table 3.1 *Basic material properties used in the finite element models.* *40*

Table 3.2 *Stiffness values for control cases (unpinned).* 47

Table 3.3 *Stiffness values for z pinned (IL] laminate [0]$_4$ with 2% z-fibre density.* 48

Table 3.4 Stiffness *values for z -pinned cross ply [0, 90Js with 2°%r, z-fibre density.* 48

Table 3.5 *Stiffness values for z -pinned angle ply /**45,** -45Js with 2% z-fibre density.* 48

Table 3.6 *S t i f f n e s s values f o r z -pinned laminate [**45,** 0, **-45,** 90J, with 2% z-fibre density.* 48

Chapter *5*

Table 5-1 *Applied boundary conditions for the UCH specimen.* 105

Table 5-2 *Typical parameters in the FE model.* 107

Table *5-3 DC'B specimen geometric typical dimension.* 112

Chapter *7*

Table *7.1 Pape material properties.* 160

Table 7.2 *Pin material properties.* 160

Table 7.3 *Typical parameters of a C'SL I FF model.* 163

Table 7.4 *CSLI model boundary conditions.* 166

Nomenclature

a	Crack length
aU	Initial crack length
of	Debond length (joint concave end)
a 2	Debond length (joint convex end)
$A,$	Z-fibre cross-sectional area Model
B	width
$B,$	Finite element width
p	Angle of misaligned in-plane fibres
c	Z-fibre density
D	Large scale bridging area
d	Z-fibre diameter
da	Differential crack increment
$d_{1\_2\_3}$	Z-fibre distance from the laminate free-edge
dr	Pullout distance
S	Total displacement
	FE crack increment FE incremental displacement at the i-ih iteration
	Crack width
$Al\ El$	Imposed initial displacement
	Beam flexural rigidity
$E.r$	TTR axial Young modulus
eh	Laminate axial Young modulus
one	Bending strain
	Membrane strain

so.	Generic micro-strain component
	Applied macro-strain
F	Bridging force vector exerted by a single z-fibre
	FE nodal force components Mode I fracture
Gig	toughness Mode IT fracture toughness Mode I
Giro	strain energy release rate Mode II strain energy
{;1f	release rate Fracture energy
F	Finite element stiffness matrix Stiffness constants for adhesive spring elernemts
[K1	Length of the resin pocket Half-length of a z-pin
~.4	projected on the z-axis Limit of the z-pin slip
'p	zone Friction coefficient
lr	Step function
l~	Model length Joint overlap length
H	Number of sub-steps Z-fibre bridging load (force or moment)
L	Irreversible energy rate Distributed
L2	traction force Z-fibre angle of insertion
	Z-fibre radius
Wz	Unit cell surface
Pir	Z-fibre circumference
qi	
r S	
s	

err	Axial stress in a z-fibre at the fracture plane (z=O)
	Transverse compressive stress
6	Axial stress in a z-fibre
of az	Generic micro-stress component
	Interlaminar peeling stress
T	Generic micro-stress component
	Bridging stress vector exerted by a single z-fibre
tc(t	Laminate half-thickness
r~.	Adhesive thickness Friction shear stress at z-fibre-laminate interface
	Friction stress within the enhanced friction zone
Tr)	Friction stress within the constant friction zone
rxZ	Z-pin shear-flow at the fracture plane inter!aminar
p	transverse-shear
on	Z-fibre angle of deflection
U	Z-fibre angle of deflection at the fracture plane
U'	Strain Energy for an homogeneous material
tie	Strain Energy for an heterogeneous material
Uk	Stored elastic energy
Uir u	Kinetic energy
o f	Irreversible energy
u3	Displacement vector of a z-fibre
ucx	Crack sliding displacement
ucy	Crack opening displacement
	Unit cell length
	Unit cell width

2r,v,w	Nodal displacement components
V	Unit cell volume
4(z)	Displacement x for a TTR section
(z)	Displacement z for a TTR section
zr,	Limit of the z-pin deflection zone
W	External Work

Acronyms

CAI	Compression after impact
CET	Crack extension technique
CFC	Carbon fibre composites
CFRP	Carbon fibre reinforced polymers
CFS	Closed form solution
COTE	Coefficient of thermal expansion
CSU	Curved single lap joint
DCB	Double cantilever beam
ENF	End notch flexure
GFRP	Glass fibre reinforced polymer
HE I	High explosive incendiary Linear
LEFM	elastic fracture mechanics Large
LSB	scale bridging
MMB	Mixed mode bending
OHT	Open hole tension
RVE	Representative volume element
SEM	Scanning electron microscope

SERR	Strain energy release rate
TTR	Through-thickness reinforcement
LID	Unidirectional laminate
UC	Unit cell
VCCT	Virtual crack closure technique

Chapter 1

Introduction

1.1 A composite challenge for the twenty-first century

Composite materials are the new products of the so-called advanced engineering age. Their unique integration of mechanical properties such as high specific stiffness and strength along with their customized fabrication provide the building blocks of our modern infrastructure. From the aerospace to the automotive industry, composite materials have just started to dominate the future engineering reality of the twenty-first century. Even in the area of decreasing research budgets for frontier materials research, the development of new composite materials with unique characteristics moves rapidly on.

Unfortunately, their high discovery rate does not come without cost. For the first time in our engineering history, it is difficult for structural engineers and designers to assimilate such a huge volume of new materials because of a lack of design methodologies and tools specifically addressed to the use of these materials.

As a consequence the aerospace industry is very conservative and reluctant to adopt new designs involving new materials. Significant safety issues and low profit margins provide little incentive to change. Even when new aircraft are introduced, they tend to build heavily upon past designs, introducing only incremental updates in technology. Large changes can occur, but the process is very slow as very recently the case of Glare (Glass fibre reinforced composite) has shown (Vlot, 2001). In order to avoid structural problems current design procedures have led to rather low allowable strain levels (within 4000 micro-strains in compression) which are strain fields typical for metallic structures (Lagace, 2002, Grassi and Nicastro, 1999). Moreover, the certification process of composite structural components is found to be very costly in terms of time and money, due to the large amount of testing involved in the various verification procedures of the so-called building block approach (Rouchon, 1990; Tropis et al., 1994). In particular, the larger structural tests of this approach are very expensive in terms of specimen production and test set-up and only help to provide qualitative empirical data to aid in understanding the response of the structure (Martin, 1998). Existing certification procedures for metallic materials have been modified to account for the different behaviour of composites, especially their extreme sensitivity to defects. One of the frequently encountered failure modes, for example, is interlaminar delamination due to low velocity accidental impact. The lack of reliable methods to predict the stable and unstable propagation of such defects often requires that a "no growth" condition is considered in the design work (Roudolff and Gadke, 2000).

What a modern composite designer should always bear in mind is that the structural performance offered by composite materials is much more versatile than their metallic counterpart; therefore in order to put such versatility to its advantage a full comprehension of the principles governing their structural behaviour and failure mechanisms is crucial.

The development and rapid improvement in digital computers and computational methods has provided powerful tools to solve increasing complex problems, which were extremely tedious or not usually available in an analytical closed forms. The finite element method nowadays stands as a crucial tool to solve highly non-linear complex phenomena such as those associated with composites structural analysis and design. Its versatility and robustness, together with the open architecture of the software packages, allow the structural engineers to tackle and implement accurate and flexible models. Computational models to simulate composite behaviour and failure modes have been developed extensively within the last decade using either damage mechanics (Allix and Ladeveze, 1992; Johnson and Pickett, 1999, 2000; Borg et al. 2001), or fracture mechanics (Raju and Wang, 1996; Raju et al., 1996; Martin,1996, 1998; Mi et al., 1998; Kruger et al., 1999; Kruger and O'Brein, 2000).

The development of these computational models is crucial in order to have predictive design tools for simulating the structural response of composite components, reducing the amount of mechanical tests required for their characterisation and ultimately promoting a more effective computational structural design,

1.2 Background

1.2.1 Towards innovative aerospace design

The realization of future air vehicles requires the synergistic coupling of a number of revolutionary and leading-edge technologies, as well as novel engineering tools and manufacturing techniques. This should lead to *the* improvement of structural efficiency and the reduction of manufacturing costs.

Figure 1.1 *The Airbus A38O passenger jet scheduled io be in service Ji.r 2006*[1].

Reductions in airframe weight, for example, result in lower fuel consumption and decreased environmental impact, while the use of cheaper or more efficient materials and designs, as well as improved manufacturing processes allows for the lowering of aircraft purchase prices. A paradigm shift in designing with novel materials is therefore

.airbus. cam

required, together with a long term strategy capable of absorbing and applying them in to primary structural design, with all their potential characteristics used in an optimised configuration.

Despite the worldwide crisis that has hit the aerospace sector after the dramatic events of 11th September 2001, encouraging signals of recovery can be found in novel composite material research and structural applications.

The leading edge nose of the Airbus A340-600 new-series has been recently redesigned by Fokker, replacing the metallic D-nose with a composite J-nose made of Cetex E-glass fabric with a polyphenylene sulphide matrix. With a 20% weight save the J-nose combines the metal and honeycomb parts in a single assembly that are manufactured in large sections, reducing the number of joints and sections. The materials where chosen for their resistance to impact and chemicals (Offringa, 2002).

In the ambitious Airbus plan to win the challenge to build the biggest passenger jet ever, the A380 (figure 1.1), the use of novel materials and technologies to reduce weight and manufacturing costs has been an inevitable choice. An unprecedented 40% of the A380's frame and skin is designed to be made of high tech plastics, carbon-fibre composites and the latest light weight metal alloys. The control surfaces, the floors of the decks and the rear bulkhead are to be constructed by carbon fibre reinforced plastics (CFRP) plus, for the first time in commercial aircraft construction, the wing boxes (figure 1.2).

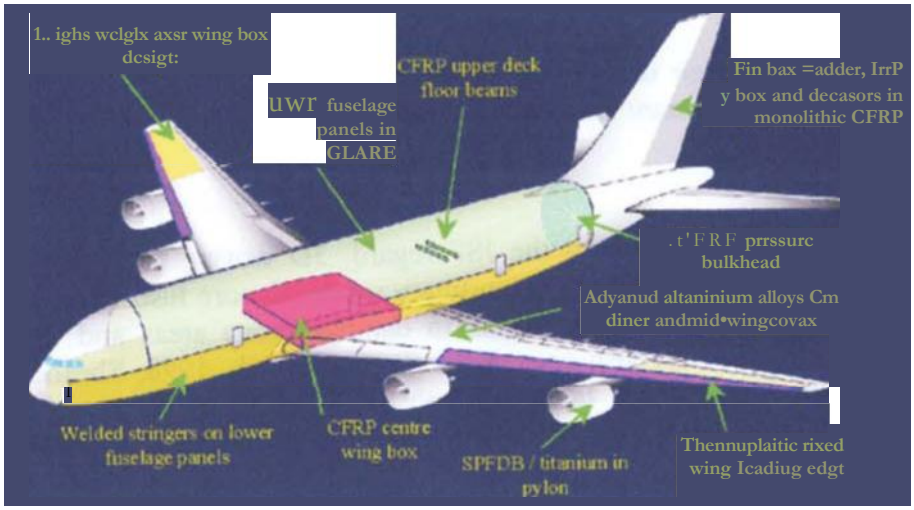

Figure 1.2 *the* A380 *novel materials design*[1].

As already mentioned, about 380 square meters of Glare will be used in the upper fuselage skin. The material is built up from alternating layers of fibreglass and aluminium bonded together, which can take loads up to 25% higher than current aluminium alloys, being also 10% lighter and more damage tolerant. The laser welding technology will allow the joining of the bottom half of the body and fuselage panels together reducing the number of rivets and speeding up the production.

[1] www.flightinternational.com

Innovative design using novel composite materials has also been applied by Boeing and Northrop Grumman in collaboration with the Naval Air System Command (Koo and Schoeppner, 2002). The engine inlet ducts of the F18 EIF presented delaminations and bond failure between the skin and stiffener elements (figure 1.3). To enhance the bond strength and damage tolerance of the structural part, through thickness reinforcements using the Z-Fiber[3] technology developed by the Aztex were used. Implementation of the technology was driven to realize significant cost and weight savings, and z-fibres replaced 4000 titanium fasteners of the previous bolted stiffener design. The design proved to save $83.000 and 35 pounds of weight for each of the 220 aircraft involved in the program. Moreover fewer assembly hours and parts were required.

With the Joint Strike Fighter (JSF) (figure 1.4), Lockheed Martin, in collaboration with NASA, is aiming to apply all the technologies and materials developed within several composite projects: Advanced Composites Technology (ACT), Composite Affordability Initiative (CAI), Robust Composite Sandwich Structures (ROCSS), Low Cost Composite Structures (LCCS)[4].

(a) (b)

***Figure* 1.3** *Innovative design using novel composite materials on the I'I8 ET (a) by Boeing and Northrop Grumman; (b) The engine inlet ducts of the PI8 E[l]k' presented delarninatiom*[5].

Innovative design concept applied in the JSF regard: 3D woven, preforms resisting ballistic impacts for bulkheads and frames, primary sandwich core fuselage, innovative assembly. Through thickness reinforcements in damage prone areas and where 3D preforms meet 2D fabrics were also considered (Bersuch et al., 1998; Sheahen et al,, 2000). By replacing conventional fasteners with z-pins JSF designers predict 70% savings in costs and 10.3 pounds weight per 1000 fasteners.

[a] www.aztex-z-fiber. com

[4] www. nasa.gov

[5] www.boeing.com

(a)

(b)

Figure *1.4 (a) Lockheed Martin .ISF; (h) substantial* savings *in production of a graphite. epoxy composite upper* wing skin *for the .ISP' wing carry-through assembly. Wing skin was produced at Al/lam Techsystems, Clearfield Utah, in their 16-ft. diameter fiber placement machine*[s].

Within the European aerospace research the TANGO (Technology Application to the Near term business Goals and Objectives of the aerospace industry) project represents an integrated approach to the validation of new large-scale structural technologies. More than 30 members of the European aeronautics industry, based in 12 countries, are working together in the construction of major airframe structural components, including composite lateral and centre wing boxes and fuselage sections, metal composite joints and advanced metallic fuselage sections. To achieve the ambitious targets of 20% reductions in both weight and cost, new design and testing methodologies have been adopted, including multi-disciplinary optimisation, advanced simulation techniques and design for assembly. In addition, design-oriented and other new materials are being used. These include aluminium-lithium alloys, aluminium-magnesium-scandium alloys, and new carbon fibre composites such as: textile composites, through-thickness reinforcements, 3D interlocked fabrics, and second generation toughened epoxies. Innovative manufacturing and assembly processes include the use of embedded fibre optic sensors (Kehlenbach and Betz, 2002), resin transfer moulding, resin film infusion, automated lay-up of composites and adhesive bonding.

Other similar research projects exploring alternative and more efficient design methodologies for the certification of composite structures have been: the Efficient Design and Verification of Composite Structures project (EDAVCOS); and the More Effective Research Certification Using Rapidly Young Materials project (MERCURYM). The first featuring DLR, Onera, and ESA-ESTEC as consortium members aimed to validate computational methodologies at different scale levels, i.e. coupon, sub-element, sub-structures; the latter comprised a consortium involving QinetiQ, Snecma, Aztex, Hexcel, Cranfield University aimed to the application of through thickness reinforcements and second generation toughened epoxy resins to enhance the damage tolerance of composite nacelle skin components. The MERCURYM project also constitutes the framework in which this PhD research study has been carried out.

6 www.lmaeronautics.coml

In Europe as well as in the USA government agencies, industry, and academia are embarking on major technological and cultural changes for the 2I'1 century. The synergistic coupling of a number of revolutionary and leading-edge technologies offers the potential of developing robust air vehicles with unprecedented levels of performance and capability.

In concurrence *with the* centenary of Wright's brothers first flight, air vehicles of today bear little resemblance to the one that flew for few seconds over the sands of Kitty Hawk, North Carolina, a hundred years ago. Similarly, future air vehicles will bear little resemblance to those of today. The realization of this vision requires new levels of multidisciplinary collaboration towards the research and development of more effective and innovative methodologies, design tools and material technologies.

1.2.2 Improving the damage tolerance for composite structures

Damage tolerance is the measure of the structure's ability to sustain a level of damage due to the presence of flaws, cracks or other defects, and be able to perform its operating functions for a specified period of time. The concern, explained in the JAR 25.571, is the damaged composite structure having adequate residual strengrth and stiffness to continue in service safely until the damage can be detected by scheduled maintenance inspection and repaired, or if the damage is undetected, for the remainder of the aircraft's life (MIL-Handbook 17), The damage growth must be slow and predictable, the aircraft component may then continue to be operated safely in the presence of a known level of damage, and decommissioned or overhauled with a satisfactory safety margin. Another concept exploited in the JAR 25 is the fail safe design, which consists of providing alternative load paths to a structure withstanding ultimate load without experiencing catastrophic failure.

Service experience and component testing have shown that current composite aircraft structures have excellent resistance to environmental deterioration and fatigue damage, leaving in service damages as a primary consideration for composite damage tolerance design and maintenance. Types of service damage include edge and surface gouges and cuts or foreign object collision and blunt object impact damage caused by dropped tools or contact with service equipment. These cuts and gouges are usually more severe for tension loading while impact damage is generally the more severe damage type for compression loading. Impacts on the laminate surface, especially those made by a blunt object, may cause considerable internal damage and delamination without producing visible evidence on the surface.

In metal structure, a major concern about damage tolerance is not only initial damage but also growth of damage prior to the time of detection. Consequently, much development testing for metals has been focused on evaluating crack growth rates associated with defects and damage, and the time for the defectldamage size to reach residual strength criticality. In general, damage growth rates for metals are relatively consistent and after test data has been obtained, can be predicted satisfactorily. Thus, knowing the expected stress history for the aircraft. intervals for inspection have been defined that confidently ensure crack detection before failure.

In the wake of what has been done for metal structures, the resistance against delamination propagation can be studied accurately by means of fracture mechanics. Resistance to delamination damage is related to the material's interlaminar fracture toughness *Gc*, as indicated by strain energy release rate properties which wi11 be discussed soon. This parameter represents the ability of the resin to resist inter-laminar delamination, and hence damage, in the three modes of fracture. The beneficial influence of resin toughness on both damage resistance and tolerance, has been demonstrated by tests on new toughened thermoset laminates and with the tougher thermoplastic material systems, even though among the international scientific community, the unification of test protocols for the material fracture toughness seems far from the end (0' Brien, 1998).

Several methods are available for improving the fracture toughness and thus the damage tolerance of composites, but they can essentially be divided in two main approaches. One approach aims to increase the inherent toughness of the composite by using tougher resin matrix, hybrid fibre composites (Kevlar or Glass with Carbon Fibres) embedded together in a matrix, fibre coating and intermittent bonding concepts (Kim and Mai, 1991), The second considers a certain amount of fibres directed through the thickness of the laminate acting as delamination resisters, which can absorb extra energy required during delamination crack propagation due to mechanisms like fibre bridging.

Within this research study the enhancements of the composite fracture toughness and therefore structural damage tolerance by means of through thickness reinforcements (TTR) were studied and analysed.

1.3 Problem statement

When designing conventional laminated composites, the poor through-the-thickness strength due to interlaminar weakness is probably the most difficult aspect to overcome. This low interlaminar strength between the laminate plies results in a low damage resistance to out-of-plane loads, damage tolerance, compression-after-impact (CAI) strength, and fracture toughness. As already mentioned in the previous section, out-ofplane loads, such as impact loads, will lead to delaminations, catastrophic crack propagation, skin-stiffener separation, and failed joints.

The through-thickness reinforcement technique of Z-fibre pinning (z-pinning) has been developed to overcome the notorious delamination problem by increasing the interlaminar strength and damage tolerance of laminated composites used in the aircraft structures (Altergott, 1994; Childress and Freitas, 1992; Freitas et al., 1994, 1996).

As often happens with the introduction of a new material there is the need to develop reliable and robust analysis tools to investigate and therefore be able to predict the material elastic and fracture mechanical behaviour under different loading conditions.

Firstly, a common problem to be considered is the knock-down in the in-plane stiffness and strength properties of the laminate when z-pins are inserted. Z-fibre insertion causes a considerable misalignment of the laminate in-plane fibres, which is thought to affect

the laminate elastic moduli; furthermore the laminate fibre misalignment could promote micro-buckling failure of the laminate under compressive loads.

Secondly, another aspect is the effect of z-pinning on Iaminate resistance to delamination initiation and growth. The mechanics of z-pinning bridging a delamination crack is an important aspect to be investigated; the so-called large scale bridging process introduced by z-fibres during delamination growth is thought to invalidate the use of linear elastic fracture mechanics for such materials. In Carrie (2000), the so-called enhanced fracture toughness of a z-pinned laminate has been derived using standard experimental protocols developed for typically unidirectional (UD) laminates. There is often a debate among material scientists and structural engineers as to whether fracture toughness values derived from the data reduction of the experimental results are an intrinsic material property or a structural property of the specimen due to the TTR energy absorbing mechanisms.

Thirdly, the characteristic dimension of the stress concentrations introduced by z-fibre in the laminate, are less than the thickness of an individual ply. Aircraft analysts rarely develop models finer than a ply. Therefore the local effects due to z-fibre usage cannot be predicted by routine FE analysis. The implementation of a micro-mechanical analytical model into the FE simulation could provide a robust numerical tool to study z-fibre effect on composite structural models without the need to have refined and computationally expensive meshes to capture the micro-mechanics of the TTR.

1.4 Research objectives

The work comprises a numerical study of composites laminates reinforced through the thickness by z-fibres. The objectives are summarized as follows:

- To study the Z-fibre effect on the elastic mechanical response of different kinds of composite laminates.

- To investigate stress distributions and concentrations introduced by z-fibres into a laminate.

- To analyse interlaminar stresses reduction due to the presence of a z-fibre near stress risers such as free-edges,

- To investigate the micro-mechanical behaviour of' z-fibres bridging a delamination crack under different loading conditions, in order to derive and implement z-fibre bridging laws into computational models.

- To develop computational models combining micro-mechanical analytical formulations with the finite element method to predict z-fibre effect on delamination growth. Results are to be validated against experimental data. The mechanisms occurring within the laminate, associated with fibre bridging during delamination growth are to be outlined in detail, and the additional failure modes due to z-fibre presence are to be verified.

- To study the relative importance of different z-fibre physical and geometrical parameters in enhancing the delamination resistance of composites.

- To seek an energy balance formulation for z-pinned laminates in order to derive the contribution of the reinforcements to the total fracture toughness. And, thereby, to establish the relevance of application of the linear elastic fracture mechanics to z-reinforced composites.

- To assess the effect of z-fibres on structural joint strength and debond growth. The importance of certain z-fibre micro-mechanical parameters on the joint strength will be studied in detail. Results are to be validated against experimental data.

- To explore the possible applications of the developed computational tools in a real structural component design using the global-local approach.

1.5 Methodology

The research methodology pursued in this work is intended to prove a design concept in the study and characterization of a novel composite material involved in a certification process of an aerospace structural component. The development of computational models at different levels can furnish considerable insight into the material behaviour, outlining the material key properties, and finally reducing the amount of mechanical testing required for material characterization.

A schematic graph of the research methodology adopted in this thesis, is presented in figure 1.5. On the abscissa the different model scales are reported and on the ordinate the model outputs sought.

Prior to their application to real aircraft structures, numerical models must first be developed and validated at a coupon level. Their general applicability and validity must

then be demonstrated at ditTerent structural levels of the pyramid approach (Rouchon 1990). This concept of building block approach involves a step-by- step validation of the numerical models from coupon to structural levels.

Firstly micro-level modelling, with a characteristic geometrical length equal to one z-fibre radius, has been considered within this work. It is intended to analyse the stiffness and stresses of z-fibre reinforced laminate, and to explain the associated micro-mechanics during delamination resistance. Within this level of the analysis a detailed micro-mechanical model is studied. The derived z-fibre bridging laws are therefore implemented into the computational models of the following level of the analysis.

The definition micro-mechanical model is often related to the distinct representation of the fibre and the matrix. The micromechanical representative volume element (RVE) is defined to be small enough to distinguish microscopic heterogeneities, but sufficiently large to represent the overall behavior of the heterogeneous medium. As within this study a single carbon z-fibre is represented as a homogeneous continuum without the distinct representation of its constituents this level of modelling should be referred as meso level. Nevertheless the diction micro-mechanical was used within this thesis to describe this level of analysis, purely considering the scale of models (gm). Moreover in the published literature the analytical models furnishing the bridging laws for through-the-thickness reinforcements were named micro-mechanical analytical models (Cox, 1999a; Cox, 1999b; Cox and Sridhar, 2002).

Then coupon level modelling is pursued to analyze the enhancement of delamination resistance, the effect of material and geometrical parameters on the structural fracture toughness. The coupon level model is validated using test data generated by our research partners at the Advanced Materials Department, Cranfield University (Cartie, 2000). The large scale bridging mechanisms of z-pins during delamination growth are studied in detail. The delamination model also tackles the energy absorption capability of z-pinned laminates.

Thirdly in the schematic graph a composite single-lap-joint is depicted, where z-pinning can improve joint strength and reduce the tendency to fail in shear-debond. In this model carbon fibrous rods were simulated at the adherends interface, and the mixed-mode debonding failure of the joint was studied in detail.

The structural element computational model is then considered to identity possible delamination prone areas and to implement the validated computational models into the large structural element analysis via a global-local numerical analysis.

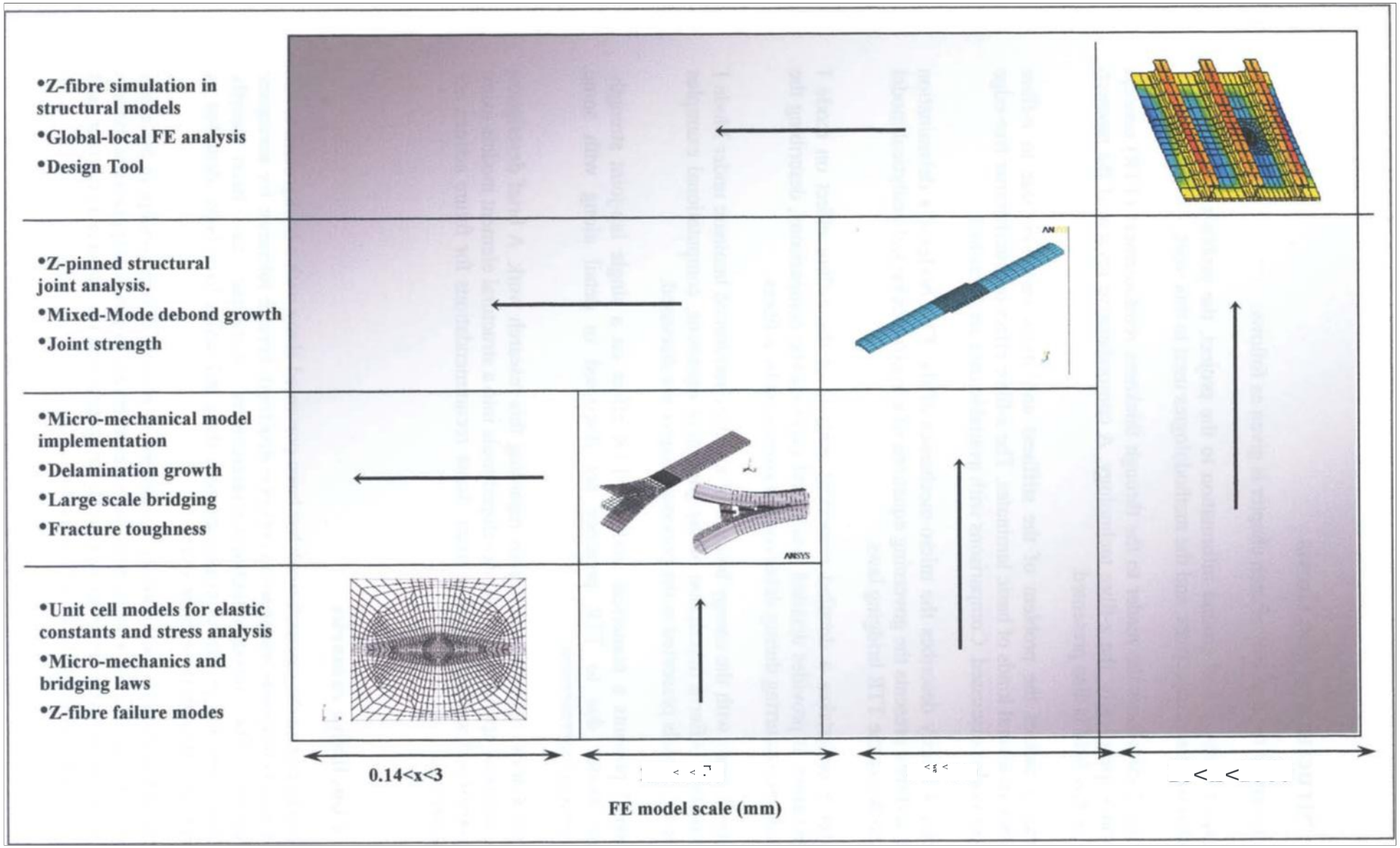

Figure 1.5 *Modelling methodology for through-thickness reinforcements.*

1.6 Structure of the thesis

A summary of the contents of each chapter is given as follows:

Chapter 1 outlines background information to the project, *the* problem statement, the research work and objectives, and the methodologies used in this work.

Chapter 2 introduces the reader to the through thickness reinforcement (TTR) concept and more specifically, the z-fibre technology_ A comprehensive review of the research done in this field is also presented.

Chapter 3 tackles the problem of the stiffness and stress variations due to z-fibre presence in several kinds of basic laminates. The z-fibre effect on interlaminar free-edge stresses is also discussed. Comparisons with available data are furnished.

Chapter 4 briefly describes the micro-mechanics of the TTR bridging a delamination crack and then presents the governing equations of a micro-mechanical analytical model used to derive the TTR bridging laws.

Chapter 5 undertakes a detailed numerical analysis of the z-fibre effect on mode I delamination. It provides detailed results and experimental comparisons, describing the mechanisms occurring during delamination arrestment by z-fibres.

Chapter 6 deals with the energy balance of a z-fibre reinforced laminate under Mode I delamination. After a description of the governing equations, computational examples for the FE models presented in the previous chapter are discussed.

Chapter 7 presents a numerical study of TTR effect on a single lap joint strength. Failure modes due to TTR presence are discussed in detail along with some experimental comparisons.

Chapter 8 draws specific conclusions regarding this research work. A brief description of the potential application of the developed tools into a structural element models using the global-local approach is also given, Some recommendations for future actions are also addressed.

1.7 Conclusive remarks

An introduction to the research work has been presented along with a background to the use of novel composite materials to enhance structural damage tolerance for aerospace components. The through-thickness-reinforcement technique has been briefly introduced, and the problems associated with their utilisation have been identified as research objectives of the current study.

The presented research methodology is intended to prove a design concept in the study and characterisation of a novel composite material by developing computational models at different scale levels, in order to provide an insight into the material behaviour, and therefore outlining the material key-properties.

The development of computational models as design tools for simulating the structural response of composites is considered as the way forward in order to reduce the amount of mechanical tests required for their analysis. Consequently the costs associated with the certification of composite aerospace components are seen to he reduced whenever such kind of computational models are fully integrated into the design phase.

A summary of the contents of each thesis chapter has also been given in the end.

Chapter 2

Through-thickness reinforcement methods and research

2.1 The enhancement of interlaminar properties

The interlaminar weakness may be seen as the Achilles' heel of composite laminates, resulting in a low damage resistance to out-of-plane loads, damage tolerance, compression-after-impact (CAI) strength, and fracture toughness. In response to the poor through-thickness strength characteristics, diverse techniques have been developed to strengthen the interlaminar region. These techniques can be divided in two main groups.

The first group is based on toughening the material by altering the matrix, the fibres, the matrix-fibre interface, the laminate structure or stacking sequence. The matrix may be toughened by using thermoplastic (e.g. Peek) rather than thermoset matrices (Turton, 2000), or by including micro-particles of thermoplastics or rubber in to the resin (Baillie et al., 1992; Troulis, 2002a; 2003). However, stronger and tougher resin systems are generally difficult to process and often extremely expensive. The Fibre-matrix interface can be processed by fibre coating and intermittent bonding concepts, whilst the laminate structure may be altered into a hybrid configuration by replacing part of the brittle carbon fibres with either glass or Kevlar fibres, using their ductile behaviour to enhance composite fracture toughness (Kim and Mai, 1991). The interleaving fibres of another material between the carbon layers can have the form of unidirectional tows (Woods et al., 1994) or chopped fibres (Sohn and Hu, 1994). They both can present problems such as reduction of carbon fibres volume fraction by as much as 7%, extra and unevenly distributed resin between continuous carbon fibre layers, and consequent waviness and misalignment of the in-plane carbon fibres which may lead to further reduction in compressive strength. Instead of an additional composite layer, a matrix layer typically 50-200 gm thick of the same composite thermoset system, can be interleaved between the plies to increase the fracture toughness, using the relief of plastic constraint at the crack-tip (Singh and Partridge, 1995). However a severe weight penalty is incurred along with reduced modulus and increased moisture absorption (Turton, 2000), The impact damage tolerance may also be improved by tailoring the stacking sequence. It has been shown that putting angle plies on the surface improves impact resistance, the relative angle between the plies should never exceed 45°, and plies of similar orientation should be dispersed to avoid matrix cracking, and therefore promoting delamination initiation (Jegley, 1991).

The second group of techniques is based on incorporating some form of fibrous reinforcement across the lamina interface through the thickness direction of the laminate, creating different kinds of 3D fibre architecture. Because these techniques are based on the same principle, we can refer to them generically as the "Through Thickness Reinforcement (TTR)" approach. Small amounts of TTR, up to 5% volume fraction, have shown greatly enhanced interlaminar properties, arresting delamination effectively, and providing alternative solution in the assembling of co-cured composite components. The TTR may be composed of carbon, Kevlar or glass in the form of short fibre rods or continuous threads. In some applications metallic TTR have also been used.

Depending on the fibres' architecture, properties and manufacturing techniques they can grant different level of enhancement in impact resistance, delamination resistance and compression after impact; as a trade off they can also present some disadvantages in terms of reduction of in-plane properties, or introduction of alternative failure modes.

2.2 Through thickness reinforcement approach

2.2.1 3-D fabric composites: weaving, braiding, knitting

Three dimensional fibre architectures have been considered for the enhancement of interlaminar properties, often based on different manufacturing techniques. The achievement of 3-D properties does not add any additional step to the conventional manufacturing process.

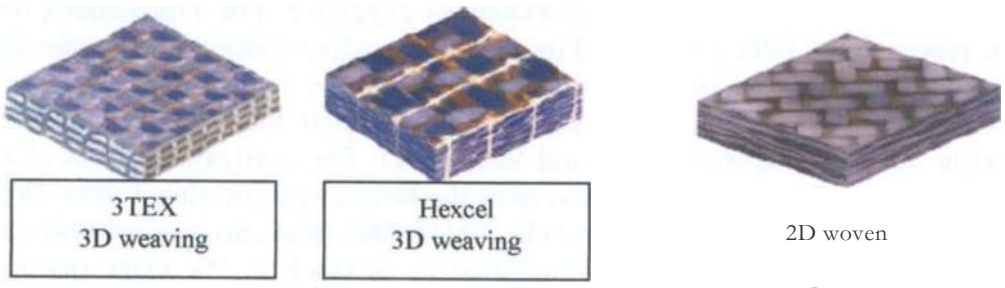

Figure 2.1 *(a) 3-D weaving materials architecture; (h) ,standard 2-dimensional weaving architecture* (F[rtsch et al., 2002).

In the 3D weaving a substantial amount of crimp is avoided as the bi-axial in-plane fibres are held together by a fill yarn oriented through the thickness of the ply_ The percentage of fibre yarns that may pass through the thickness direction is normally limited by the in-plane yarns architecture. Figure 2.1 shows schematic graphs of 3D weaving materials manufactured by 3Tex Weaving G1100-1000, and from Hexcel (a); a standard 2D fabric is also presented as comparison (b).

Despite the improvements in impact resistance compared to the simple 2D fabric, 3D fabrics can promote matrix cracks in the resin pockets created by the fibre architecture,

during either impact loads or with compression-compression loads (FOrtsch W. et al., 2002). The fibre architecture of an orthogonal interlocked fabric composite used in the work by Tanzawa et al., (1999) is presented in Figure 1 2 (a). It is composed of five fibre-yarn axes, four of them being in the in-plane (x-y) and the other in the z direction. Even though the percentage of z-yarns was in a range between 0.27 and 0.78% of the total fibre volume fraction, the fracture toughness of the material was reported to be improved by a factor of up to seven.

(a) (b)

Figure 2.2 *(a)Fibre structure (0-ayes 3-1) orthogonal interlocked_ fabric composite (T a n a et al., 1999) ;* (b) *3D braiding composite fibre architecture (Poe et al., 1997).*

Figure 2.2(b) shows the interlocked fibre architecture obtained by the braiding process. The high fibre volume percentage and the inter-locking weave furnish excellent structural properties and through thickness strenf~th. For a comprehensive review on the 3-D textile technologies the reader may read the work of Chou (Chou and Ko, 1989). In general it can be said that the production of 3-D textile composites requires special and expensive techniques. Their complexity and limited shapeability and processability confine their use to special applications where high tri-axial stress states are predominant.

2,2.2 **The Stitching Technique**

Transverse stitching threads across the laminate to hold the plies together normally requires one additional production step to the typical manufacturing of laminates, bonded or co-cured components.

The process involves dry fabrics rather than pre-preg fabrics and the stitching threads need to be abrasion resistant and flexible to survive the sewing process, the textile is then embedded in to a matrix system and cured. To provide improvement in toughness the thread must also possess high tensile strength and stiffness, and should not be affected by the successive curing process. In figure 2.3 various stitch types and typical stitch architectures are shown.

Typical threads consist of several plies of fibres twisted to form a single entity with a circular cross-section, and made of Kevlar (K40, K60 and K80), Glass or T900 carbon (Dransfield et al., 1994). Fibre breakage and misalignment of the in plane load-bearing yarns occur during the stitch needle penetration, causing the formation of resin rich packets around the thread and thereby reducing the tensile strength; crimping and kinking of the surface fibres has also been reported (Mouritz et al., 1997). Elastic in-

plane stiffness constants have also been reported to be reduced by up to 20%. Fibre waviness may also *be* introduced which promotes fibre micro-buckling and compression failure (Mouritz and Cox, 2000). Stitching may also encourage moisture penetration.

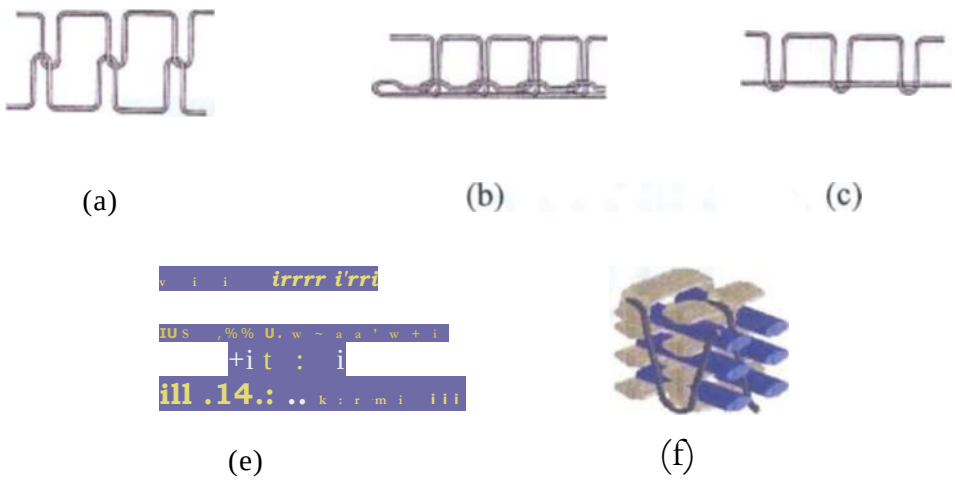

Figure ***2.3*** *Illustrations of the various stitch types used to reinforce laminates (Mount: and C')x, 2000) and stitching fibre architecture(Poe et of., 1997). (a) lock; (b) chain; (c) modified lock stitches; (d) through the thickness stitching architecture; (e) 3-1J stitching architecture.*

Nevertheless great performances in impact damage tolerance, Mode I and II fracture toughness and lap joint strength have been reported (Dow and Smith 1989; Larsson, 1990; Liu, 1990 ; Dransfield et al,, I994; 1998; Jain et al., 1998; Tong et al., 1998). Moreover, stitching application to airframe structures has been evaluated within the Advanced Composite Technology program at NASA Langley since 1989 (Poe et al., 1997).

2.2.3 The !-Fibre insertion technique (z-pinning)

The Z-Fiber technology (Freitas et al., 1994; 1996; Childress and Freitas, 1992; Altergott, 1994) has been under development for over ten years. This novel through-thickness reinforcement was originally developed by Foster-Miller Inc., and then during the past six years at a very accelerated rate under Aztex Inc. Within the last three years, research programmes involving this novel technology have attracted organizations such as: U.S. Navy, Lockheed Martin, Boeing, Sikorsky Helicopters, NASA in the USA and QinetiQ, NLR, FADS, Hurel-Hispano, BAE Systems, Airbus, Hexcel in Europe.

The tern *Z-fiber is* derived from the orientation of the fibres along the `z-axis' of analytical laminate models which is the through-the-thickness direction, and it involves the direct insertion of reinforcing fibres in the thickness direction of laminates and structural interfaces during the manufacturing process, before the resin matrix is cured, effectively pinning the layers together (Childress and Freitas, 1992; Altergott, 1994). These z-fibres are often referred to as "z-pins", and the technology is often named "z-pinning".

The pins are driven through the uncured laminate in a two stage process, which involves the use of a specialized ultrasonic insertion gun and a sequential removal of the collapsible foam in which the Z-fibres are held (figure 2.4). The use of ultrasonic vibration reduces the pressure required to drive the pins into the laminate, and the high frequency vibration generates heat which assists the process. The foam supports the fibres during insertion, preventing them from buckling and can be thermoformed to conform to curved surfaces.

The Z-fibres are small, solid, cylindrical pins and can be made of steel, titanium, glass-epoxy or carbon-epoxy, and have a diameter range between 0.15 mm and 1 mm. The small diameter of the pins and the possibility to insert them at the point of minimum viscosity of the matrix system prevents significant fibre damage which can lead to in-plane property degradation. Small diameter pins also maximize the laminate thickness to pin diameter (11d) ratio which is important in thin laminates where the primary failure mode is pin pull-out.

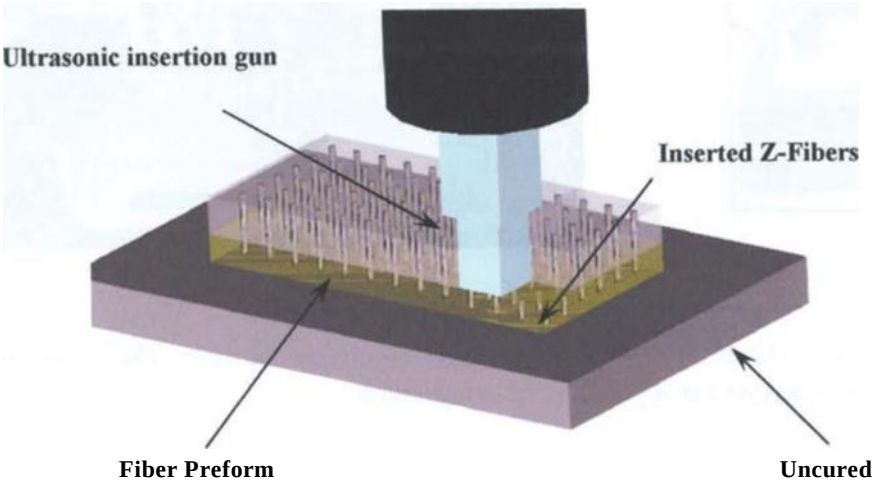

Figure 2.4 *Schematic of the ultrasonic gun insertion method of incorporating z_pins into the uncured laminate (Cartie, 2000).*

Pre-forms are available in thickness that ranges from I-51 mm, whilst the Z-fiber areal density ranges from *0.5%* up to 5% (Altergott, 1994) and is always arranged in a square array manner. Typical pin square arrays of carbon pins considered were 0.5% "low density" and 4% "high density" with two typical diameters, 0.28 mm and 0.5 mm. Characteristic geometrical distances for available square arrays of carbon pins are reported in table 2.1.

Typical Z-pins actually used are made of carbon-fibre pultruted rods, embedded in an epoxy matrix (T300BMI). The advantage of carbon pins is primarily easy of manufacture as the pins are driven in to the required depth of the laminate and any excess length is removed easily by shear cutting. These pins are chamfered at one end to aid insertion and push the laminate fibres aside. Carbon pins also offer excellent adhesion to thermoset matrix resins.

Table *2-i* *Typical distances between two adjacent :-fibres for typical densities,*

r **in density** ***spin*** **diameter**	*0.5%*	- 1 %	*2%*	4%
0.280 *mm*	*3.51 mm*	2.48 *mm*	1.75 *mm*	*1.24 mm*
0.500 *mm*	*6.39 mm*	*4.52 mm*	*3,2 mm*	*2.26 mm*

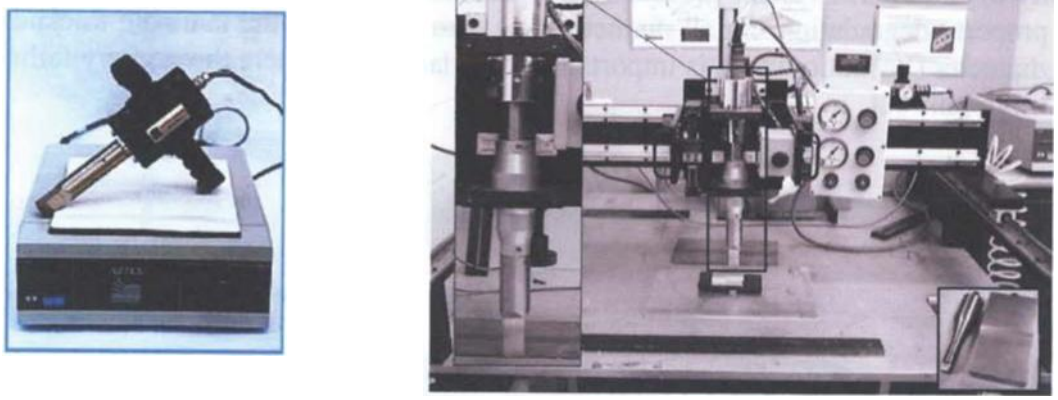

(a) (b)

Figure 2.5 *(a) Hund-held ultrasonic pin insertion device: (b) Semi-automated ultrasonic gun machine for Z -pinning of composites .*

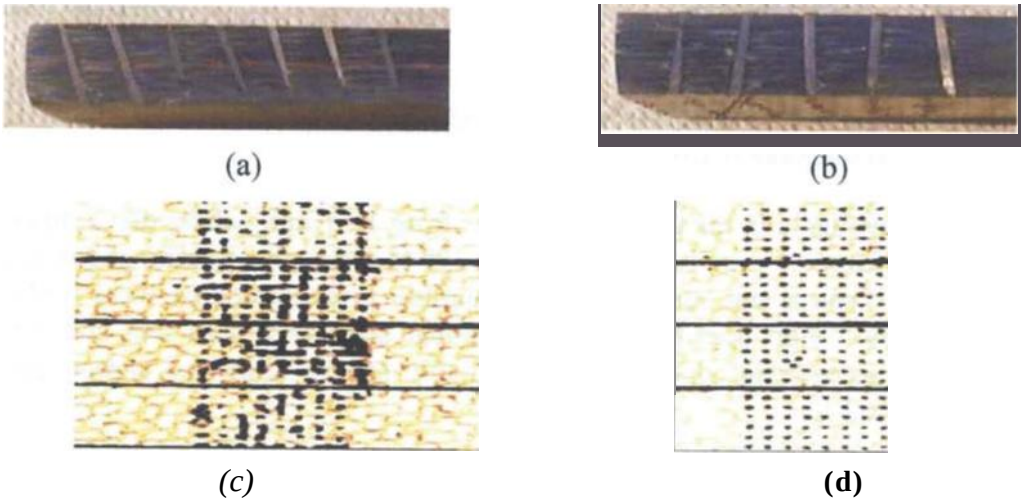

Figure *2.6* *(a) :-pins inclined with respect to their original insertion angle; (b) Optimised cured laminate; (c) t'-Scan map corresponding to specimen in (a);* (d) *C'-Scan map corresponding to specimen in (b).* (Troulis *et* al., *2000).*

' Courtesy of Advanced Materials Department, Cranfield University.

The hand-held and semi-automated ultrasonic gun devices have been developed at Aztex Inc. to carry out local manual pinning reinforcement or global z-pinning of structural components (figure 2.5). High-resolution C-scanning techniques as well as visual inspection have been used at Cranfield University Advanced Material Department to assess the quality of the z-pinning process (figure 2.6).

2.2.4 Through-the-thickness reinforcement of sandwich constructions: K-Cor, XCor

Through-the-thickness reinforcement in sandwich constructions has been proposed to increase the interlaminar strength and the damage tolerance. K-Cor and X-Cor are reinforced sandwich structures through the use of pins placed in the foam-core at a certain angle to form a three-dimensional truss configuration, figure 2.7. Testing to date has shown that for the same mechanical properties of Nomex or Korex honeycomb-core sandwich, they offer 10% - 20% weight saving, (Marasco, 2003).

Figure *2.7 K-('or with carbon fabric face-sheets.*

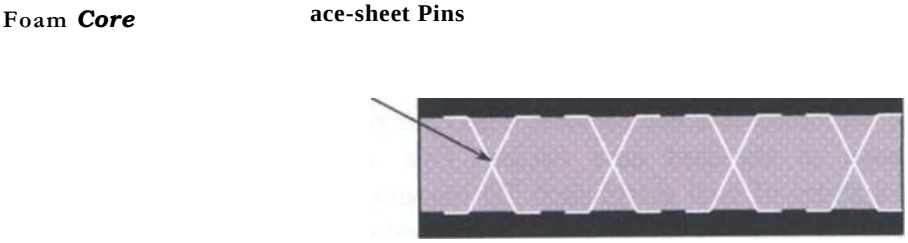

Figure 2.8 *(a) X-Cor[mr] schematic; (b) K-Cor i schematic*[9].

The pins used as reinforcement are similar to those typical for z-pinning, and can be made from a variety of materials (carbon, titanium, steel). For both sandwich materials, the inserted pin length exceeds the foam thickness. In the case of X-Cor the pins penetrate, during lamination, both the laminate face-sheets of the sandwich (figure 2.8a), providing a superior skin/core bond without the need of adhesives and acting as through-thickness reinforcement in the laminate, mechanically interlocking the face-sheet to the core. In the case of the K-Cor the part of the pins that extends beyond the foam is folded back, splayed between the core and the skins, figure 2.8b. The use of an

[8] **Courtesy of Aztex inc.**

[9] **Courtesy of Marasco A., Cranfield University, Advanced Material department.**

adhesive film is in this case always necessary (Marasco, 2003). The core material is a low density Rohacell[1M] foam (usually Rohacell M 31 IG) and its function is to hold the pins in place acting as pin buckling stabiliser.

A vertical position of the pins enhances the compression behaviour of the sandwich structures. For shear resistance the angle of the pins should be increased. Reinforcing the foam with pins is an attempt to improve the damage resistance and the impact performance for sandwich structures. Conventional cores suffer mainly from in-plane shear, core compression failure, buckling instability and face-sheet-to-core debonding. Pin-reinforced sandwich composites proved to exhibit superior damage containment and tolerance, the prominent failure mode was pin buckling, while the secondary failure modes were z-pin push through failure and crushing failure of face-sheets.

2.3 Z-pinning in material design

When used at the stage of aircraft conceptual design when the overall structural arrangement is being formulated, z-fibre reinforced materials can change the current design approach for damage tolerant structures. Designers have become accustomed to the characteristics of metals and the standard metal approaches; they tend to approach the composite in much the same way, as if it were just another alloy. Z-fibre pinning process is one of the first structural approaches to be developed solely and uniquely applicable to composite structures (Freitas et al., 1996).

The kind of global design decisions made during the preliminary design phase tend to dominate the final cost and weight results. Once the overall structural configuration is chosen 80% of the outcome is fixed, leaving only the 20% that can be optimised throughout the remainder of the program. Therefore, if z-fibre is introduced early in the process, an entirely different product is likely to result (Freitas et al., 1994).

The z-pinning process converts a 2-D pre-preg lay-up to a 3D laminate, with little or no change to standard cure cycles. This allows composite designers to utilize the advantages of well established 2D manufacturing approaches yet obtain 3D properties where needed. Therefore z-fibres will reduce the designer's need to design around the lack of through-the-thickness strength inherent to composite structure.

Design of composite structural joints usually causes some other problems. Using the stringer approach to stiffen the skin raises great concern about how to safely and securely attach the two components (e.g. stiffener to a panel)_ The options are:

1. Co-cured, co-bonded or secondarily bonded attachment.
2. Stitching.
3. Mechanical fastening,
4. Z-pinning.

Option one may be very fragile and has resulted in major redesigns in many programs. Total reliance on any form of bonding alone is risky, particularly when damage tolerance and impact requirements are considered.

Option two, stitching, may be limited due to several manufacturing problems:

a) Difficulty in accessing the critical regions: stiffener radii, intersections of stiffening elements and areas close to the perpendicular structure; typical areas where through-thickness reinforcement might be needed.

b) Necessity of having access to both sides of the component to be stitched.

c) Stitching can not be effectively applied to pre-pregs because the in-plane fibre damage may be too substantial and a debulked laminate might not be easily penetrated.

Option 3, fastening, which is the most widely used, might be expensive for composite components. It also increases the weight, decreases in-plane properties (stress concentrations) and introduces the threat *of* fuel leaks *and* lightening strikes. Nevertheless fasteners are low efficiency since they carry no load until the adhesive fails, whilst numerous small pins provide a much larger bearing area than a single fastener. The volume of z-fibres needed to replace a fastener represents only a portion of the shank section of the fastener.

Currently, most joints used in industries are bonded and then mechanically fastened to provide fail-safe structural redundancy. Eliminating fasteners at a preliminary design stage might offer a good potential for cost reduction. Therefore structural attachments using z-fibres could eliminate the fastener installation process; consequently reducing costs and weight, as the Joint Strike Fighter case has proved.

Nevertheless the z-pinning process using carbon pins could match the properties of the carbon-epoxy laminates so that the galvanic reaction problem between these laminates and aluminium fasteners could be removed. Secondly, structural attachment using z-fibres may allow the formation of complex shapes not presently possible, by connecting simple, *easy* to *form* components with small pins. Moreover the on-tool reinforcement process, unlike stitching, could be done with only one side access (Altergott, 1994).

Summarising, the potential areas of interest for z-pins, for the designers and stress engineers might be:

1) A global or local new reinforcement for increasing through-the-thickness strength, stopping delamination growth and improving the global structural damage tolerance.

2) A secondary structure attachment method for greatly improved joint performance, pull-off increasing load values for stiffened panels at a reduced cost and weight.

2.4 Review of z-pinning research

2.4.1 Mechanical testing of z-pinned laminates

• *In plane compressive strength*

Intuitively because of the in-plane fibre misalignment caused by the z-pin insertion process compressive strength associated with fibre micro-buckling failure is predicted to decrease. The in-plane compressive properties appear to have been overlooked in the early studies as interest was focused on the through-thickness properties. In the work by Childress and Freitas (1992) a compressive test was carried out on a 6.5 mm thick AS413501-6 woven rectangular plate showing inconclusive results with the compressive strength enhanced by the z-pins, but a rather vague "minimal loss in in-plane strength" was stated. In the work by Steeves and Fleck (1999a; 1999b) a significant investigation, combining mechanical tests and numerical analysis, was conducted. The study performed on a unidirectional T300/914C z-pinned laminate (2% areal density) measured a reduction in the compression strength of approximately 30%, and it was explained by the increase in-plane fibre waviness introduced during z-pinning.

The extent of the degradation was found dependent upon the distance between consecutive z-pins and the angle (8} that the z-pin array makes with the axis of the specimen. It was stated that an optimised z-pin insertion process and z-pin pattern distribution would cause less fibre waviness and therefore have less impact on the compressive strength.

• *In-plane tensile and open hole tensile strength*

A 2% reduction in tensile strength was reported in the experiment conducted by Childress and Freitas (1992) on an AS413501-5A woven laminate reinforced with 0.5% z-pin density (0.28 mm diameter). In the work by Altergott (1994) a reduction between 2- 9% was reported, and successively in the work by Freitas et al. (I996) a relation between z-pin areal density and tensile strength was determined. AS4/3501 woven laminates reinforced with 2%, 5% and 10% pins were tested, and the tensile strength reduction were higher than those of the previous study.

The effects of 0.28 mm and 0.51 mm diameter z-pins on the tensile strength of cross-ply and fabric specimens were tested in (Troulis, 2002b; 2003) by the standard open hole tension (OHT) test in order to ensure failure in the gauge section of the specimen. The z-pinned area was across the entire width of the specimen and the reported knock-down in the ultimate tensile strength of the sample were between 11-14%. The explanation for such kind of reductions is associated with the promotion of intralaminar splitting in the z-fibre insertion areas.

• *Impact Damage and Compression After Impact (CAI) strength*

The concept of reinforcing composites using z-pinning appears to have been initially driven by attempts to improve damage tolerance, impact resistance and laminate-stiffener bond strength. Impact damage properties were therefore key characteristics to be analysed.

In the work by Childress and Freitas (1992) the compression after impact (CAI) test was used to evaluate the damage resistance and residual compression strength of a damaged panel made of AS4-3501 carbon-epoxy. The CAI specimen was 12.7 cm wide by 25.4 cm long and an aluminium ball was shot at the centre, with approximately 42 J impact energy value. The specimen was then mounted on to a side-supported compression test fixture and a static load was applied until failure. The typical failure mechanism of the CAI panels is controlled by the interlaminar normal and shear strength of the material therefore transverse shearing and normal strength of the laminate were improved by z-fibres presence. Basically, an improvement up to 46% was achieved on z-pinned (0.5% z-pin density) quasi-isotropic panels, while impact damage areas showed a reduction of 30-50% over a wide range of impact conditions.

More recently, similar results were obtained in (Bitsianis, 1999) and (Houslow, 2000) at Cranfield University. A standard Boeing size quasi-isotropic lay-up $[+45_2, -45_2, 0_2, 90_2]_{2s}$ was used to test the impact resistance and CAI of a T3001914 z-pinned laminates. The coupons were locally reinforced by z-pins, over a 25 mm square area in the centre, where the impactor struck. For low velocity impacts, a reduction in the damage area of between 16% and 30% was recorded, and CAI strength was enhanced by 30% to 50% for small diameter pins, and between 18% and 37% with larger diameter pins. In (Houslow, 2000) in particular CAI strength improvement of around 45% was reported, for different laminate thickness and impact energies. The work was formally published in 2003 (Zhang et al., 2003),

The effects of low velocity impact on sandwich panels reinforced with z-pins at 10° and 20° insertion angle was analysed in (Palazotto et al., 1999). *The main* failure process by pin push-through was outlined, with the 10° pinned sandwich showing higher threshold impact energy.

• *Delamination resistance*

During the last four years, delamination fracture tests such as double cantilever beam (DBC), end notch flexure (ENF), and mixed mode bending (MMB), have been performed extensively at the Advanced Material Department, Cranfield University (Cartie, 2000; TroWis, 2002a). The research effort studied the fracture toughness enhancement in composite laminates due to the z-fibre presence. A considerable amount of data was produced, and some z-fibre parameters like density and diameter were evaluated.

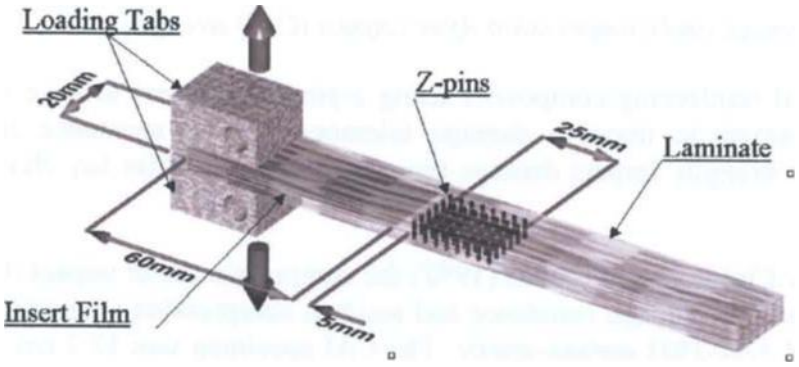

Figure 2.9 *7_ pinned specimen geometrylor Iviode I testing (Troulis et al..* 2000)

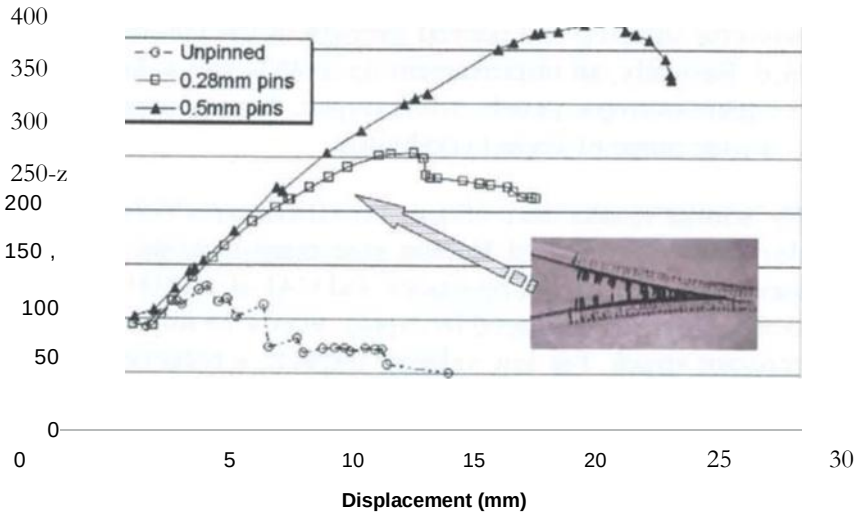

(a)

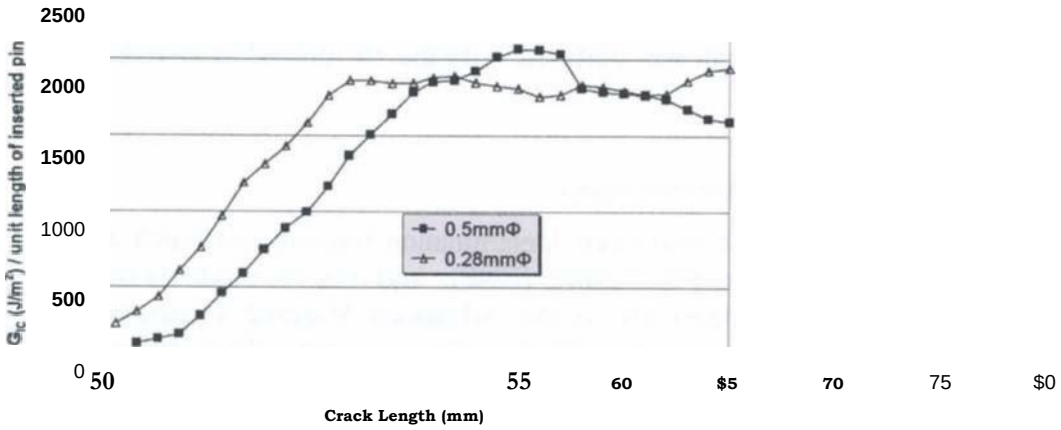

(b)

Figure 2.10 *Experimental results from (Carrie, 2000) (a)Load - displacement curves for control and pinned specimens under Mode I loading;* (b) *Effects of pin diameter on apparent toughness (I rauli.c, 2003).*

A typical z-pinned DCB specimen configuration is shown in figure 2.9, with the z-fibre array starting 5 mm behind the standard crack starter film. Z-fibre density tested were between *0.5%* and 4%, specimens' thickness was between 3 and 7 mm, and the material systems chosen for the analysis were either carbon-epoxy unidirectional tape 1MS/924 (Cartie, 2000) or woven fabrics G986/M21 (Troulis, 2002a; 2003).

In the delamination fracture tests conducted on z-pinned IMS/924 unidirectional laminate beams with carbon fibre/BMI z-pins, it showed up to twenty-fold increase in the critical strain energy release rate value of the composite to crack propagation under Mode I loading conditions (DBC test), depending on the areal density of the reinforcing pins (figure 2.10). The crack initiation load was unaffected by the presence of the pins (5 mm ahead of pre-cracked area) as shown in figure 2.10a. Another noticeable effect of z-pinning was the change of the R-curve for crack propagation: from a flat shape in the unpinned control samples (indicative of minimal fibre bridging) to a steeply rising R-curve in the `high-density' pinned samples. In practice, as a crack propagates the number of reinforcing fibre rows increases resulting in increased fracture toughness (figure 2.10b).

The ENF tests indicated less critical effect by z-pinning on Mode II fracture toughness with a 7-fold increase, moreover under mode II loading in the z-pinned specimens no catastrophic shear failure was reported (Cartie and Partridge, 1999).

• *Structural joints*

Some "Proof of Principle" tests were conducted on z-pinned joints (Childress and Freitas, 1992) to demonstrate the applicability of z-pins to mitigate two problems: delamination effect of high velocity impact, and de[p]ending of substructures due to high explosive incendiary (HEI) blast and fragment damage. The HEI tests performed on a stiffened panel in which one stiffener was co-cured and pinned on the foot-print flanges and the other was co-cured and unpinned showed that the pinned stiffener remained attached after the shot whilst the unpinned stiffener was found lying on the ground completely separated from the test panel. The debond occurred in the unpinned stiffened panel either in the first ply of the panel or in the first ply of the stiffener flange with a random pattern, whilst the pinned flange of the other stiffener shown large section still solidly bonded with a delaminated area of several millimetres in the buckled stiffener area.

The static pull-off test conducted on a stiffened panel (Freitas et al., 1996) showed that after initial failure, z-pinned panels carried to 70% more load than the fastened structures. At this point instead of a catastrophic failure, i.e. pull-off of the stiffening element, the z-pinned specimens showed a delamination in the skin. It was concluded that the initial failure loads could be increased when combining innovative design practices (tailoring the stiffener radius, inserting an interlayer of soft-material) with z-fibre (density, diameters)_

A more accurate experimental analysis was conducted by Rugg and Cox (2002), for a T -joint (figure 2.11). The specimen was designed to simulate the types of application that z-pinned laminates may find in service. The laminates material was IM71977

fiberite (harness satin weave), with different lay-up for the J section flange and web of the stiffener and for the skin. The z-fibre density considered in the stiffener flange was 2% or 4%, z-pin radius was 0.25 mm and they were fully pinned through the thickness of the laminate.

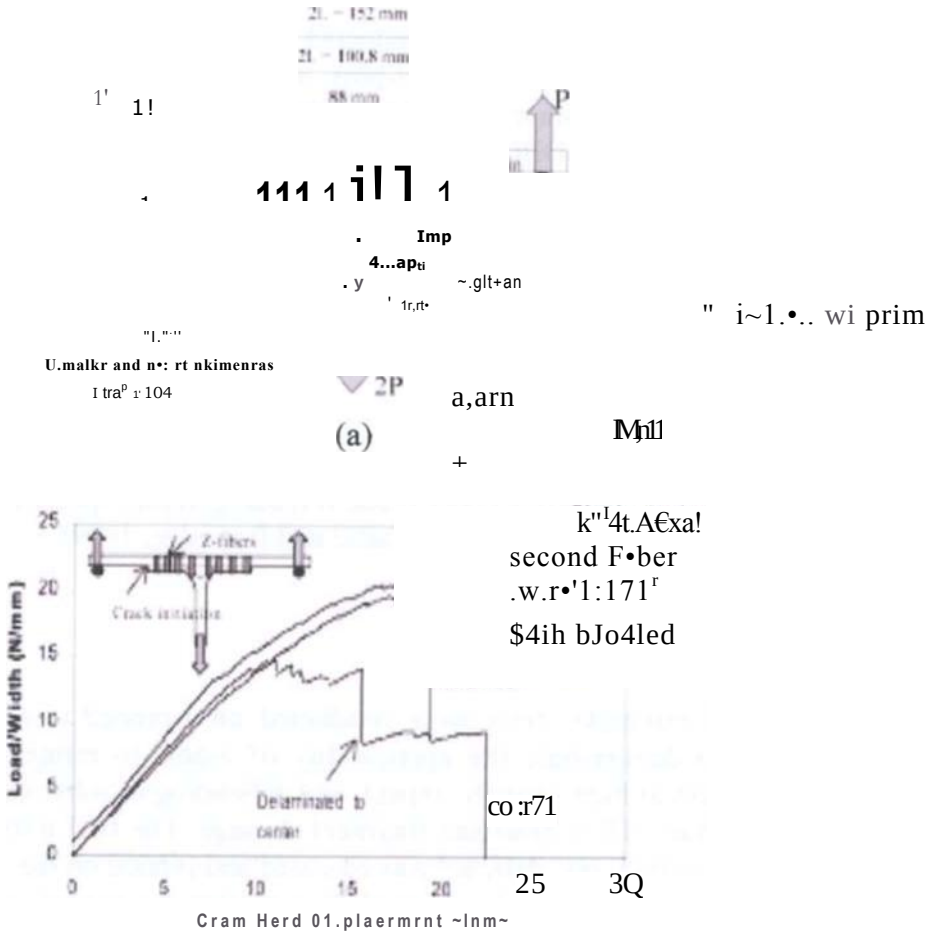

Figure 2.11 *T-Joint strength evaluation in (Rugg and Cox, 2002): (a) Schematic (not to scale) of T-stiffner specimen(P - load applied per unit width; (b) Representative load-displacement curves fnr 7-specimens tested in wide configuration.*

The specimens were tested in two configurations that differed only in the separation distance between the top supports (figure 2.11a). However, this modest shift in the supports completely changed the failure process determining whether delamination crack initiated at the radius of the T or at the end of the ski flange interface away from the web.

Useful conclusions were drawn about z-fibre arrestment of delamination growth. It was stated that z-fibre were more effective in suppressing the mode I delamination component in a mixed-mode crack configuration after a certain crack length the crack was concluded to advance in pure mode II conditions. In some cases the presence of z-

fibres results in a change of the failure mechanisms from skin-stiffener delamination to micro-buckling of the laminate skin under bending loads. Nevertheless in the specimens tested in the wide configuration a substantial increment of the pull-off failure load was found, from 14 Nlmm for the control specimen to 22 Nlmm for the 2% z-pinned specimen,

A single lap shear specimen reinforced with angled z-fibres was the subject of the analysis in (Rugg et al., 1998). Lap-shear specimens were cut from a carbon-epoxy (M4J/7714A tape) 50-ply quasi isotropic flat panel, being reinforced through the thickness with 5% z-fibre at insertion angle of 45° to the plane of the laminate. The load-displacement curves for the above described analysis are reported in figure 2.12 with a control specimen curve for companson.

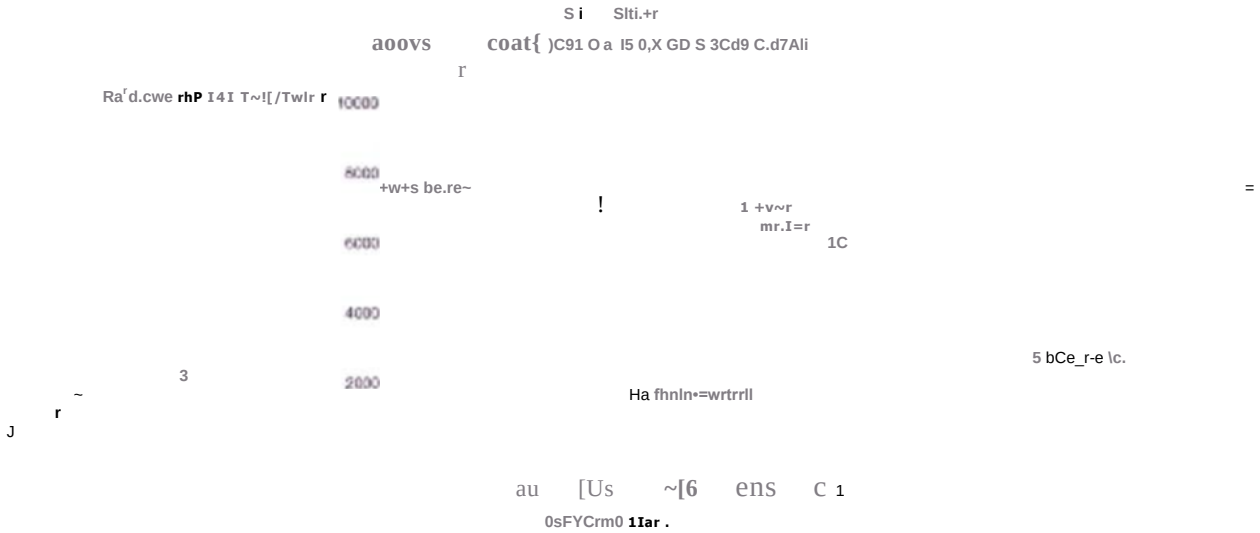

Figure 2.12 *Load displacement curves fir lap shear samples with and without fihres (Rugg et al., 1998).*

A modest increase in the initial delamination failure load and a large increase in the ultimate load were found. However the study assessed all the mechanisms of deformation and damage in the z-fibres, relevant to their role as bridging entities during delamination crack propagation and pullout. The explanation of z-fibre bridging mechanics will constitute the basis for the analytical micro-mechanical model to be discussed in detail within chapter four.

■ *Fatigue*

In the work of (Graftieaux, 1999; Graftieaux et al., 2000) the effect of z-fibres on mode I and Mode II fatigue crack growth were investigated. The specimens used in the mechanical test were: double cantilever beam (DC13) and end loaded split (ELS). Some difficulties were addressed because of the z-fibre presence: crack closure during the fatigue cycles could not be achieved due to the hysteresis caused by the debonded z-fibres. In the ELS tests difficulties were registered in obtaining the external compliance calibration required by the standard data analysis. Nevertheless the results did indicate a slow down of the crack growth rates under cyclic loads due to z-fibres.

2.4.2 Modelling of z-pinned laminates

Elastic stillness and stress analysis

The first numerical model on the mechanics of z-fibre reinforcement was developed by Barret (1995; 1996). Using the FE approach two models were implemented: a two dimensional axi-symmetric model to examine the thermal stresses in the region around a z-fibre and the crack-tip stresses under uniform crack opening load; a three-dimensional model using eight noded isoparametric solid elements and consisting of a rectangular block of laminate that contained two z-fibres (figure 2.13).

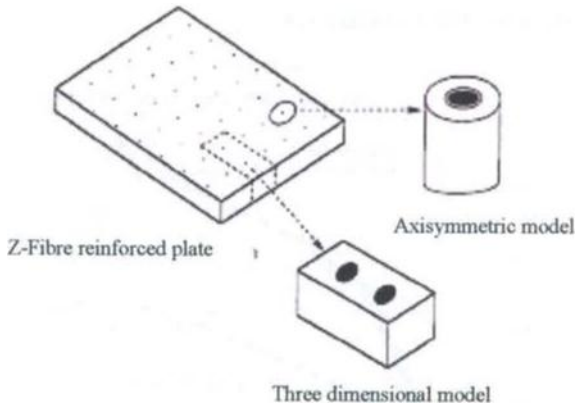

Figure 2.13 *FE micro-mechanical models presented in (Barret, 1996)*

The latter dealt with the z-fibre effect on crack tip stresses for a uniformly applied crack opening load, without any crack-growth analysis. The axi-symmetrical two-dimensional analysis underlined the importance of choosing materials for the laminate and the z-fibre with similar coefficient of thermal expansion (COTE) to control the thermally induced shear stresses within the interfacial resin between a z-fibre and laminate. More importantly, it was shown that a z-fibre within a region of intact laminate resisted through-the-thickness loads only when those loads were applied in the immediate vicinity (two z-fibre diameters) of the reinforcement. Therefore it was concluded that the effect of z-Fibre on crack initiation would be minimal. However from the three-dimensional analysis a significant effect on crack-tip stresses was predicted when an intact z-fibre was behind the location of an assumed in-plane crack; the z-fibre effectively picked-up part of the opening loads.

For the analysis of the in-plane elastic response, an analytical closed-form solution of the stiffness for the z-fiber reinforced sandwich panel was derived by (Lin and Chan, 1999). The closed-form solution was based upon transferring z-fiber stiffness onto the laminate plane and superimposing with the face skin laminate stiffness. The analysis was limited to the in-plane properties and it did not take into account the important micro-mechanical details of the z-pinned laminate structure such as the resin pocket surrounding an inserted z-fibre and in-plane fibre misalignment due to z-fibre insertion into the laminate.

Those details were incorporated into a detailed FE micro-mechanical model elaborated by (Dickinson, 1999) to study the influence of different z-pin parameters on the three-dimensional elastic constants of z-pinned laminates. Parameters investigated where the z-pin material, density, diameter, insertion angle, and different kinds of laminate stacking sequences. The conclusion, in summary, was that z-pinning had little effect on in-plane extensional and shear stiffness, E_{a}, $E_{,}$ and $G_{,n,,}$ and the out-of-plane stiffness E, could be greatly enhanced by z-fibre insertion. However a detailed stress analysis appears to have been omitted; furthermore the method for the elastic constants' computation was not presented in detail. A more recent study by Ker (2001) presented a more detailed 2D and 3D stress analyses of representative z-fibre volume elements.

+ Micro-mechanical models

Extensive studies have been devoted to the micro-mechanisms associated with a z-fibre bridging a delamination crack, under different loading conditions. The principal aim of this kind of studies was the derivation of a closed form solution for the z-fibre bridging law. The bridging law is the relation:

$$_{I,}= f[\sim^{i}] \qquad (2\text{-}1)$$

Vdltere F is the traction or crack closure force vector, exerted by a single z-fibre in the delaminating crack wake, and a is the displacement vector to which the z-fibre is subjected during delamination propagation, The bridging force can be in terms of either a stress (forcelcross-section-area of the TTR) indicating the axial stress in the bridging tow, or a force indicating the total force provided by the TTR in the crack wake. The integration of the bridging force over the entire displacement vector can furnish an estimation of the energy absorbed by the z-fibre bridging mechanics. Generally in the micro-mechanical model's formulation several through-thickness-reinforcement geometrical and physical parameters can come into play. Most of these models were firstly developed for stitching reinforcement and then adapted to z-fibre mechanics.

Under mode I loading conditions z-fibre bridging exhibited similar mechanisms to the one observed for a single fibre embedded into a resin. Those mechanisms were: elastic stretching of the fully bonded fibre, debonding at the z-fibre-matrix interface and pullout of the matrix opposed by frictional sliding. Bearing this in mind, the first micro-mechanical model adaptable to simulate z-fibre bridging laws under the mode I loading conditions was formulated by Li (1992). By ignoring the elastic bond, a simple force equilibrium based on the shear-lag theory was derived between the traction force acting *on the* fibre and the constant frictional stress insisting on the fibre-matrix interface. This model was implemented in the work by (Jain and Mai, 1994) to study the effect of stitching on Mode I delamination.

The case of a steady state fibre pull-out was extensively covered in (Zhang et al., 1999a; I 999b). In this analysis, the whole pullout process was simulated in a three-stage analysis, in which the relationship between the pull-out displacement (representative of the crack face opening) and the fibre axial stress (related to the fibre bridging force) was

given by three different functions (figure 2.14). In the first stage, the interface between the z-fibre and the laminates is perfectly bonded.

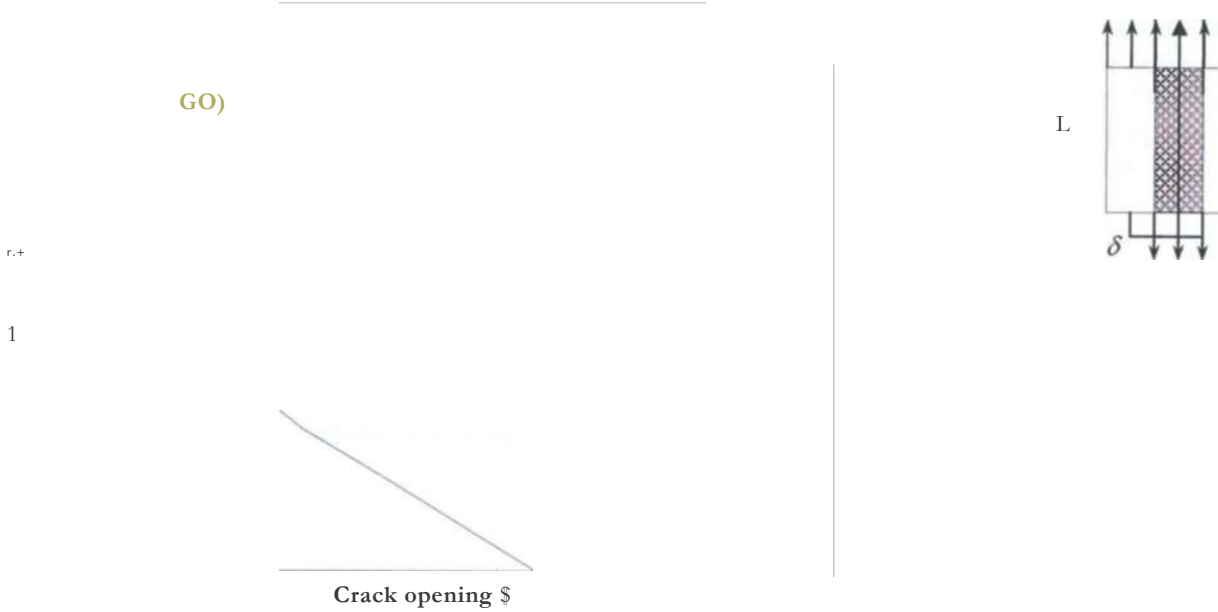

Figure 2.14 *Z -fibre bridging stress versus crack opening displacement described by a pull-out curve in (Zhang et a1., 1999b): f~(S) fully bonded, $f_z(8)$ partially' dehonded,* f 3 *(S) frictional sliding.*

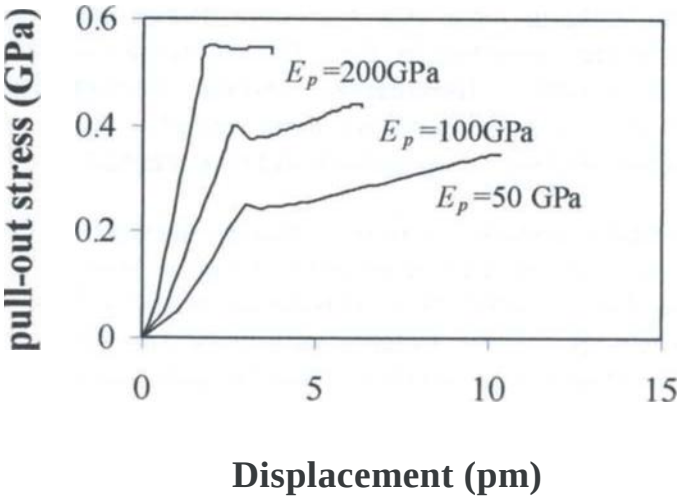

***Figure* 2.15** *Elastic stretching and dehonding phases of fibre bridging curves under crack opening loads (Mode 1) in (Lni and Mai, 2001).*

The bridging stress is caused by the elastic deformation of the z-pin. At a certain value of the crack opening displacement, the interfacial shear stress between the z-pin and the laminate would exceed the interfacial shear strength, debonding would start and propagate. In this stage the bridging stress of a z-fibre is caused by both the elastic deformation (in the bonded region) and interfacial friction (in debonded region). After the interface has been fully debonded, the z-pin is pulled out from the laminate, and the bridging stress is completely opposed by friction.

The parameters to be specified in the model equations were: fibre axial modulus, radius and embedded length, interfacial shear strength (r), and friction coefficient (p), fibre radial shrinkage during curing.

Therefore from the equations the bridging force for a given crack opening displacement could be calculated, studying the influence on the bridging law of different micro-mechanical parameters

Figure 2.15 presents the bridging curves for a 0.14 mm radius, 2 mm long z-fibre, computed from the above described model. The *curves refer* to the fully bonded z-fibre, and propagation of debonding phase, and were derived for three different z-fibre axial moduli in (Liu and Mai, 2001).

It was concluded that the effect of the elastic axial modulus of a z-fibre on the total bridging curve was minimal, and more importantly it was shown that the elastic stretching and debonding phases lasted only for a few pm in the computed bridging curves, whilst the frictional sliding of the fully debonded z-fibre was the most significant energy absorbing mechanism associated with z-fibre bridging under mode I opening loads.

The formulation of a micro-mechanical model for a z-reinforcement bridging a delamination crack under Modell loading conditions (crack sliding displacements) was discussed in (Cox, 1999a; 1999b). The model that was based on the experimentally observed bridging mechanisms of through thickness reinforcement described in (Rugg et al., 1998) was subsequently improved to cope with mixed-mode loading conditions and different insertion angles of z-fibres. Different boundary conditions allowed the simulation of z-fibre reinforcement or stitching, and some experimental comparisons with the work of (Turrettini, 1996) for stitching and of (Cartie', 2003) for z-pinning were made. The assumptions and equations will be discussed in detail in Chapter 4, where computational examples will also be presented.

Delamination Models

Some work has already been devoted to quantify the effect of z-fibre on interlaminar delamination growth and fracture toughness under mode 1, II and mixed-mode loading conditions by employing analytical (Mabson and Deobald, 2000; Liu and Mai, 2001; Massabo and Cox, 2001) or finite element approaches (Cartie', 2000). Analytical models solved the constitutive and equilibrium equations of DCB, ENF, MMB specimens by using simple or shear deformation beam theories combined with discrete or continuous linear distributed bridging loads for the z-fibre simulation.

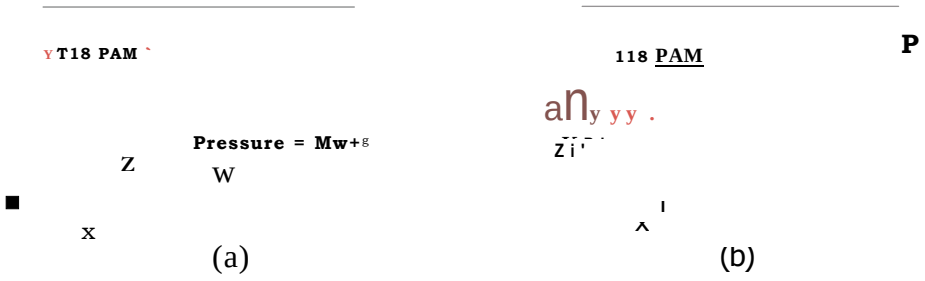

Figure 2.16 *Single-leg analytical models representing: schematic of through-thickness rein forced DCB (a) distributed applied T7R pressure(Mah.son and Deohaldf 2000);* (b) *discrete _-reinforcements reaction loads (Liu and Mai, 2001).*

In (Mabson and Deobald, 2000) a single leg of a DCB specimen was analyzed as a rigidly fixed cantilever beam in pure bending, using linear elastic fracture mechanics at the crack-tip, and linear traction models to represent the through-thickness reinforcements (figure 2.16a).

The Eulero-Bernulli governing differential equation for the beam deflection was then written as:

$$\frac{d^a}{d'x\ 1:I} + 1\ (mw+n)=0 \qquad (2\text{-}2)$$

The absence of shear deformations, led to the solution of the differential equation and its unknown constants in a closed form.

From a known displacement relationship the J-integral method was then used to calculate the strain energy release rate (SERA) GI:

$$GI = \frac{z}{F.IW\ W} - wd\ (rnw_d + 2n) \qquad (2\text{-}3)$$

Despite the simple assumptions, it was shown that the unloading moment was due to the pressure field applied by the z-fibres on the DCB leg within the trough thickness reinforced path (figure 2.16(a)); moreover useful design curves were produced through this analysis.

In (Liu and Mai, 200]) the z-fibres were simulated by discrete bridging entities (figure 2.16b), and the study was essentially built on the wake of the body work developed by the same group of authors on the analysis of stitched laminates (Jain and Mai, 1994; Jain and Mai, 1995; Dransfield et al., 1998; Jain et al,, 1998; Zhang et al., 1999a).

The Eulero-Bernoulli equation was expressed as:

$$
\begin{cases}
EI\dfrac{d^2w}{dx^2} = P \cdot x & (0 \le x \le x_1) \\
EI\dfrac{d^2w}{dx^2} = P\,x - P_1(w)(x-x_1) & (x_1 \le x \le x_2) \\
EI\dfrac{d^2w}{dx^2} = P\,x - \sum_{i=1}^{i} P_i(w)(x-x_i) & (x_i \le x \le x_{i+1}) \\
EI\dfrac{d^2w}{dx^2} = P \cdot x - \sum_{i=1}^{N} P_i(w)(x-x_i) & (x_N \le x \le \Delta_{TTR})
\end{cases}
\tag{2-4}
$$

Where P was the external load applied to the DCB leg, x_i and P_i indicated respectively the location and bridging force for the i-th z-pin, and N was the total number of bridging z-reinforcements. Because a non-linear traction model for the reaction forces was employed (Zhang et al., 1999b), analytical closed-form solutions could not be derived. An approximate method for the solution was utilized. Therefore the strain energy release rate was calculated by:

$$
G_T = \frac{1}{B}\left[\frac{N^2}{EIW}\left(\sum_{i=1}^{N} P_i(\Delta_{TTR} - x_i)\right)^2\right] \tag{2-5}
$$

Once again the first term at the right hand side of the equation is the typical expression valid for a composite DCB; the second represents the unloading contribution of the through-thickness-reinforcements.

It has to be underlined that the boundary conditions applied to the beam model to simulate the crack-tip usually underestimate the GI values at the crack front. Besides, when the bridging tractions are expressed as functions of the crack displacement, even using linear functions the resulting crack behavior is generally nonlinear (Massabo and Cox, 2001).

A numerical model using 2D plane-strain finite element analysis was developed to study a DCB by inserting an experimentally derived bridging law to simulate the effect of various z-fibre properties (Cartie', 2000). A strong dependence on the availability of experimental data was noticed; hence different tests would be required for different material and z-pin quality.

Closed-form solutions have been developed to quantify the TTR effect on Model delamination growth, but all of these analytical solutions suffered from some limiting assumptions. The beam theory and simple but realistic bridging laws for the through-thickness reinforcements were implemented in (Massabo and Cox, 2001) for the

analysis of a MMB specimen. The mixed-mode solution was sought superimposing the derived solutions for a DCB and ENF specimens. The implemented bridging laws were continuous over the through-thickness-reinforced path length and either constant, or proportionally linear, or more generically using both constant and proportional terms. It was shown that crack propagation was rendered stable by the bridging mechanisms. The mode ratio was shown to decrease progressively from the nominal *Gr G* 114 to a pure Modell condition due to the bridging mechanics of through-thickness reinforcements more effective in suppressing the opening rather than sliding displacements. Summarizing it is worthy to mention the significant research work elaborated within the last five years by Cox and Massaba on modelling the stitching effect on ModeII delamination loads; specifically the reader may wish to read (Cox et al., 1997; He and Cox 1998; Massabo et al., 1998; Cox et al., 2001) for completeness.

2.5 Conclusions

Several techniques to enhance the interlaminar properties of composite laminates were presented. The group of techniques based on incorporating some form of fibrous reinforcement across the lamina interface through the thickness direction of the laminate was defined as the TTR approach.

After a succinct description of the 3D fabric composites and the stitching technique, the z-fibre insertion technique was presented. An exhaustive review of the z-pinning research effort was then tackled; the research studies were divided in two main groups, mechanical testing and modelling of z-pinned laminates. Published works mainly dealt with z-fibre effects on delamination growth and structural joints' performance, which are considered to he potential key areas for z-pin utilisation.

The studies in the mechanical testing field showed encouraging results for the mechanical performance of z-pinned laminates. Both delamination resistance and joints' strength were found to be increased due to z-pin insertion, some issues related to the reduction in compressive strength were also found in the published research.

Within the research modelling effort, analytical models simulating z-pin micro-mechanics were shown to provide the so called "bridging laws" of a single z-fibre bridging a delamination crack. A micro-mechanical model capable of simulating z-pin bridging laws under mixed-mode loading conditions was introduced. Within chapter 4, such a model will be treated in more detail. The analytical delamination models suffered from a series of over simplistic assumptions in order to derive closed-form solutions for the strain energy release rate calculation. These assumptions regarded the use of the beam theory, the imposed boundary conditions at the crack-tip and the use of constant or linear continuous bridging laws for the z-pin simulation. A more detailed numerical study is therefore thought to be necessary to investigate z-pin mechanics during delamination growth,

Chapter 3

Analysis of stiffness and stresses in z-fibre reinforced composite laminates

3.1 Introduction

The z-pinning process will affect the laminate stiffness properties and hence the global elastic response to the applied load. Therefore, crucial to the development of the technology is to obtain a better understanding of the mechanism and mechanics of z-pinned composites. Evaluating the engineering stiffness constants and examining the stress distribution around a z-fibre could be the first step toward the development of a design tool for predicting damage initiation and damage propagation in z-pinned composites.

For conventional laminated composites, there are two approaches to obtain the stiffness properties, i.e. macro-mechanical and micro-mechanical methods. The former uses experimental data from standard coupon specimens to build a set of material constitutive equations that result in engineering elastic constants. This approach treats a composite as homogenous orthotropic continuum, which may yield a useful design tool. However, to obtain an in-depth understanding of the material behaviour and accurate mechanical properties an alternative method is necessary.

The micro-mechanical approach does not assume homogeneity, but defines the micro-structural details and uses the known material properties specific to both fibre and matrix to determine the overall behaviour of the composite material (Sun and Li, 1988; Sun and Vaidya, 1996; Weinecke et al., 1995; Dasgupta et al., 1996; Sun W. et al., 2000; Whitcomb et al., 2000; Lin and Chan, 1999; Dickinson, 1999). Assuming that both the material structures and the mechanical response are periodical, composites can be modelled by a representative volume element (RVE) or a unit-cell (UC). A unit cell is the smallest region in a periodic material structure. This technique can also mode] more complex textile composites (Weinecke et al., 1995: Dasgupta et al,, 1996; Sun W, et al., 2000; Whitcomb et al., 2000). The unit cell approach has also been employed for modelling z-pinned laminates (Lin and Chan, 1999; Dickinson, 1999)

It is also important to examine the stress changes due to the insertion of z-fibres, so that stress-based failure criteria may be applied for predicting damage initiation at stress raisers, e.g. laminate free edges and open-hole edges. The stress state in a laminate is basically two-dimensional, but in the presence of transverse loads (such as impact load) or geometrical discontinuities (such as free edges, open holes, and ply-drops) it

becomes essentially three-dimensional with very high interlaminar stress components (Hu et al., 1997; Kant and Swaminathan, 2000; Lessard et al., 1996; Yang and He, 1994; Wei and Zhao, 1991).

The objective of this chapter was to evaluate the effect of z-pinning on the engineering elastic constants and local stress distributions near a z-fibre. The laminates used in the study had 2% volume fraction of z-fibres, which is the typical density used in many structural tests (Cartie, 2000), The work was carried out using a finite element unit cell model for stiffness analysis and a more detailed micro-scale 3D FE model for interlaminar stress analysis. The results presented in this chapter were calculated in the linear elastic field and curing stresses were not taken into account. It should be noted that work reported in this chapter has been formally published (Appendix A).

3.2 Unit cell models for elastic constants

The periodic structure of a composite laminate can be described by a representative UC in isolation. It is therefore assumed that a uniform external load applied to a periodic structure will produce stress and strains distributions that are also periodic. The material response to external loads is therefore derived from the UC analysis with suitable applied boundary conditions.

When the UC approach is implemented, it is assumed that the UC is located in a uniform stress field far away from geometrical features such as sharp corners, changes of section and free edges where stress gradients may be significant. Moreover no imperfections in the micro-structure are considered, even though fibre composites inherently contain geometrical and material discontinuities and are therefore not entirely periodic. Examples of such deviation from the idealised UC structure include fibre waviness and alignment, fibre-matrix bond strength, presence of broken fibres, particle inclusions and voids.

3.2.1 Unit Cell geometry

A typical microscopic photograph of a unidirectional (UD) laminate with a single inserted z-fibre showing the distinct microstructures of the pure resin pocket and the misaligned in-plane fibres surrounding the z-fibre is shown in figure 3.1. Scanning electron microscope images indicated that the fibres deflected were also out of the plane; however, the magnitude of these deflections was small compared to the in-plane deflections. The micrograph refers to the x-y plane of the unidirectional fibres, where the circular cross-section of a carbon z-fibre is visible. The pure resin packet is due to the matrix which flows into the void opened up by z-fibre insertion between the longitudinal fibres, under the heat and pressure of the laminate curing. The deviated fibre region is due to the fibres that are pushed aside during z-fibre insertion process; at the same time some damage of the in-plane fibres is likely to happen with some fibre breakage, but the z-pinning process discussed in chapter two has been designed to

minimize this side effect. Therefore in this analysis the percentage of broken fibres is considered negligible and consequently will not be considered in the modelling.

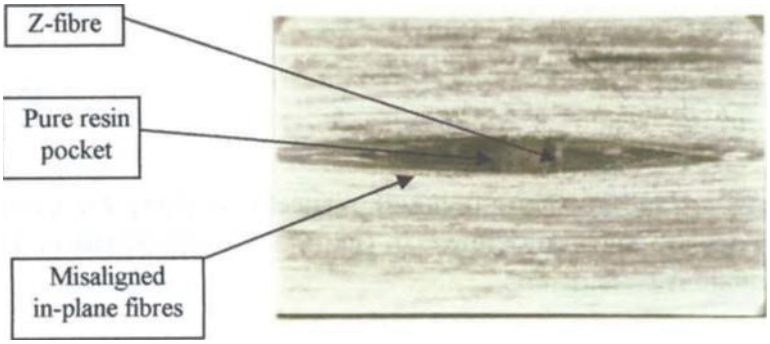

Figure 3,1 *Microscopic photograph of a unidirectional laminate with a single -fibre (0.28 mm diameter), showing the curved fibres and resin pocket at either side of the prn*
!rr

In figure 3.2 a schematic of the microstructure shown in figure 1 1 is presented. The unit cell should capture important features *such as* the misaligned fibre zone and the resin pocket. The misaligned fibre region is assumed to be confined in a zone with a constant inclination, tangential to the circular z-fibre, with the angle of inclination that is defined by the ratio l_p'd.

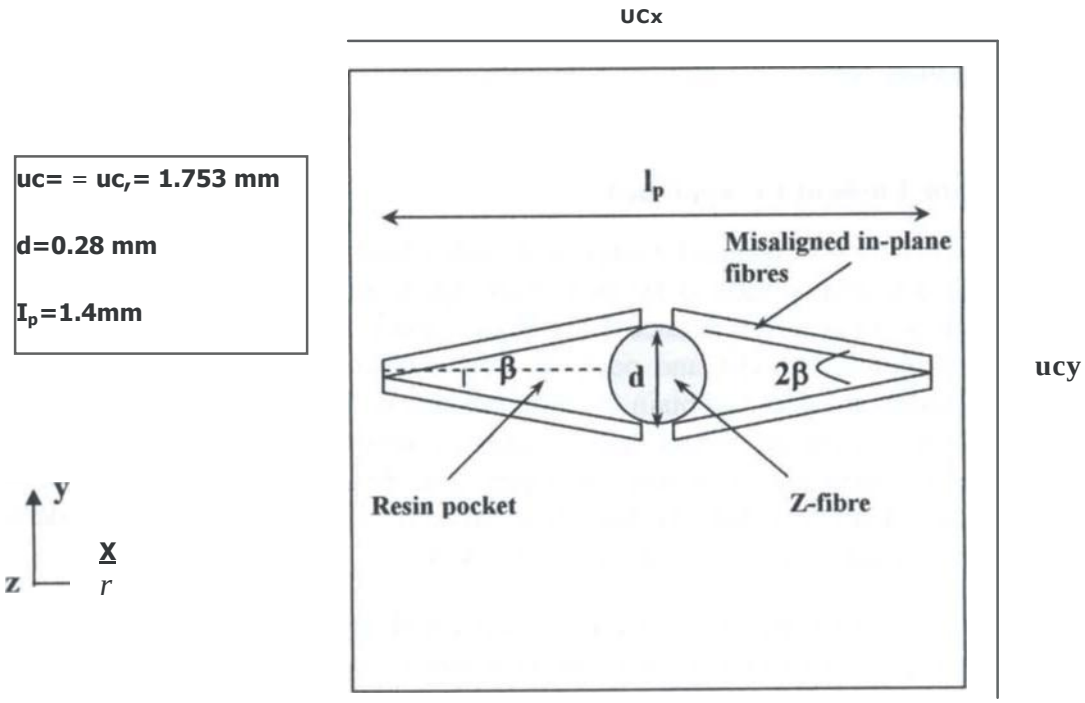

Figure *3.2 Schematic of a 2% pinned composite unit cell, where the ratio lp d defines the angle of misaligned in plane_fibres.*

in Courtesy of Dr. Denis Cartie, Crantield University, Advanced **material** department.

The relation between the misalignment angle (/1), the resin pocket total length 1p and the z-fibre radius r can be worked out easily, taking into account the assumed tangential condition of the misaligned fibres:

$$d_2 \cdot \sin(/.) = r \quad Q\text{-}a\,r\,e\,s\,i\,n \text{ F} \tag{3-1}$$

In order to determine the size ucr
and uc,, of the unit cell, respectively along the x and y directions, the z-fibre areal density must be defined. In figure 3,2 a representative unit cell of a 2% reinforced laminate is considered.

3.2.2 **Analytical approach**

Preliminarily, a simple Matlab code was implemented based on the analytical closed form solution developed by Lin & Chan (1999) for the computation of ET, E,, G.,, and v . in z-pinned laminates. The analytical unit cell model was based on the classical laminate theory, i.e. the rule of mixture, by transferring the z-fibre stiffness onto the laminate plane and superimposing z-fibre stiffness to the in-plane stiffness.

While this approach is applicable to simple laminates, it is over-simplistic for z-pinned composites since it does not consider the interactions between the z-fibre and the surrounding resin zone (figure 3.1). Moreover, no effect of the fibre misalignment is considered, and the computation does not include any information about the properties in the third direction.

3.2.3 Finite Element UC approach

The finite element (FE) unit cell model on the other hand takes account of the important micro-structural details, such as the pure resin region and the misaligned in-plane fibre region, both of which can influence the stiffness values. Dickinson et al (1999) made a detailed FE unit cell model and performed an extensive parametric study of the z-pinned laminates in order to obtain the engineering elastic constants. Ile examined the effects of z-fibre material, volume fraction and insertion angle, and also the influence of the misaligned fibre region around the z-pins and the resin-rich pocket. However, a detailed stress analysis appears to have been omitted, which would help to understand the stiffness variations due to the presence of z-pins.

In this study a 3D finite element micro-mechanical model, figure 3.3, was used to model the microstructure of the unit cell as shown in figures 3.1 and 3,2. This micro-mechanical model consisted of 20-noded hexahedral elements. Each element had eight nodes on the top and bottom faces. The nodes had three degree of freedom u, v, w corresponding to the displacements in the x, y and : directions.

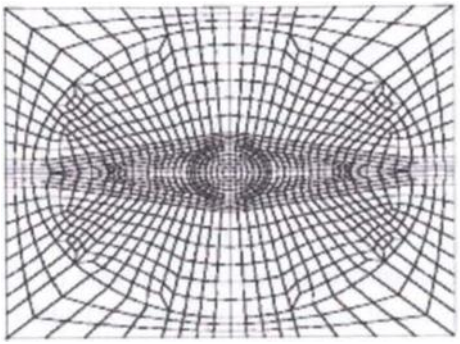

Figure 3.3 *3D finite element unit cell model (XY view) used in this study*

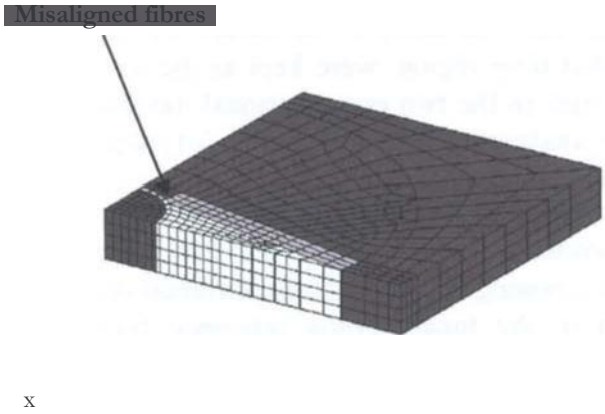

Figure 3.4 *three dimensional FE model for a quarter unit cell.*

A quarter UC model is also shown in figure 3.4, where the finite block of misaligned fibres is in light grey, and the fibre orientation has been defined in a local coordinate system. Most of the load cases could be applied to the quarter model, using the symmetry along the x and y axes.

Table 3.1 *Basic material properties used in the finite element models.*

Materia Is	**E1 (GPa)**	**E2 (GPa)**	E3 **(GPa)**	**G12 (GPa)**	**G23 (GPa)**	G13 **(GPa)**	**V12**	**V23**	**V13**	**Vf**
Lamina (AS4I3501-6)	136.40	8.90	8.90	5.95	3.21	5.94	0.25	0.38	0.25	0.6
Z-fibre (T300/9310)	144.00	7.31	7.31	4.45	2.65	4.45	0.25	0.39	0.25	0.6
Epox ▸ • Resin (3501-6)	4.44	4.44	4.44	1.65	1.65	1.65	0.34	0.34	0.34	

Different geometric shapes were used to mesh different regions within the unit cell following the star-pattern approach (Dickinson et al, 1999) to maintain mesh compatibility across the interface between the plies of different orientations. The NASTRAN software package was employed to perform the FE analysis. Four basic laminate stacking sequences were studied, i.e. unidirectional $[0]_4$, cross-ply [0, 90],, angle-ply [±45],, and quasi-isotropic [+45, 90, -45, 0],. The composite laminate used in this computational example was made of the AS413501-6 carbon epoxy pre-preg, and the z-fibre pins were made of impregnated carbon tows (T300/9310) with axial Young's modulus of 144 GPa. The basic material properties used in the FE model were taken from references (Dickinson et al., 1999; Lin and Chan, 1999) as given in table 3.1 in order to validate the results against published data.

It should be noted that the z-fibre diameter used in the present work was 0.28 mm, but in reference (Dickinson et al., 1999) two z-fibre diameters, 0.254 and 0.635 mm, were used. However, since the main variables of the model, i.e. the size of the resin pocket inclusion (Id and deviated fibre region, were kept as the function of z-fibre diameter, the relative z-fibre densities in the two computational models, as well as the ratio *Ind* which defined the fibre angle of misalignment (eq. 3-1) were the same. Therefore, a direct comparison with (Dickinson, 1999) could be made.

The region of intact lamina was not an issue for this model; therefore each single lamina was modelled as a homogeneous three-dimensional orthotropic continuum with principal axes oriented in the local lamina reference frames without the distinct representation of the fibres and matrix as shown in figure 3.4. Moreover, the distinct representation of the lamina fibres and matrix would imply a smaller scale of the micro-structural model.

The carbon pin was also treated as homogenous and orthotropic, as it attains significant higher values of elastic modulus and strength in the axial direction, which is the z direction of the lamina reference system.

3.2.4 Derivation of the average stress and strain fields

According to references (Sun and Li, 1988; Sun and Vaidya, I996), the engineering elastic constants of a heterogeneous composite can be described by equivalent engineering constants of a macroscopically homogeneous material. This could be done by averaging the actual non-homogeneous micro-stress and micro-strain tensor (au and e',) over the volume of the unit cell (V) to yield the average macroscopic stresses and strains ($a_{,1}$ and), therefore it is possible to write:

$$\int_V f6,\sim(x,y,I)dV \qquad (3\text{-}2)$$

$$s:. = \frac{1}{V_{1.}} f_{E/}(x.v.=)dV \qquad (3\text{-}3)$$

The equivalence between the actual heterogeneous composite medium and the homogeneous medium described by the average stresses and strains and the equivalent elastic constants has been demonstrated in (Sun and Vaidya, 1996) by showing the equivalence in strain energies between the equivalent homogeneous material (U) and the original heterogeneous material (U'):

(3-4)

$$(I = \quad . f O_{ij} 6_{ij} dV \qquad (3\text{-}5)$$

$$U = U. \qquad (3\text{-}6)$$

The direct use of equations (3-2, 3-3) would be computationally expensive especially for models with a large numbers of degree of freedom. In order to avoid such problem the average strains could be related to the boundary displacements of the unit cell by applying the Gauss theorem, so that equation 3-3 can be rewritten:

$$JS_4 dV \quad \underline{2V}\ J(u,n, + u.n;) dS \quad ti \qquad s \qquad (3\text{-}7)$$

Where, V and S are, respectively, the volume and the boundary surface of the unit cell, $u;$ is the i'' component of nodal displacements on the surface S, and nj is the jib component of the unit vector normal to S. The above derived equation makes it possible to evaluate the volume averaged strains using the boundary displacements thus avoiding volume integration (eq. 3.3).

For the equation (3-7) to be valid it is assumed that at the z-fibre and composite-matrix interface the displacements are continuous, therefore perfect bonding exists between the z-fibre and the matrix, which is a reasonable assumption within the elastic field, where no debonding failure is assumed.

The total strain energy U stored in the UC is given in equation 3.4 and in the case of an external load P1 applied on the UC face i the strain energy equivalence states:

$$2^{I};^{S},=2^{a}\text{« V} \qquad \textbf{(3-8)}$$

Where Pi is the external load applied on the unit cell, and S; is resultant displacement found by finite element analysis. From equations (3-7) and (3-8) the average stress component acting on the unit cell is obtained as:

$$\bar{\sigma}_{ij} = \frac{P_i \delta_i}{} \tag{3-9}$$

The effective elastic constants can then be found from the average stress and strain components:

$$\text{a} \quad \text{Vs"-} = \qquad G_{ij} = \frac{\bar{\tau}_{ij}}{\bar{\gamma}_{ij}} \tag{3-10}$$

$6ii$

Where Et is the Young modulus along the $i\text{-}th$ direction, vo is the Poisson ratio between the $i\text{-}th$ and $j\text{-}th$ surfaces, and $G+1$ is the shear modulus.

3.2.5 Unit Cell boundary conditions

Different boundary conditions were applied to the unit cell model in order to calculate the engineering equivalent elastic constants of the representative z-pinned laminate, and also to determine the stress redistribution in the unit cell due to z-fibre inclusion. For the E. E, and A", moduli and Poisson ratios, the quarter unit cell model was analysed using the symmetry of the unit cell for the applied loads. For the shear loads and shear moduli G9, G, $and\ G_{\mathbf{b}}$.. the full unit cell model was considered.

The use of a unit cell requires boundary conditions that cause the cell to behave as if it were part of an infinite continuum. The load introduction on the unit cell has been approached in order to simplify the surface integration of the average strains and stresses described before. Therefore a known constant displacement was applied to the cell boundaries with multi-point constraints defined among the nodes of the unit cell boundary in order to have a straight deformed boundary where the load was applied. From the applied displacement it was possible to work out the unit cell macro-strains (eq. 3-7). The total applied load was then computed from the nodal reaction forces of the unit cell boundary, and knowing all the other geometric quantities equation 3-9 could then be applied. The use of multi-point constraints to hold the edges straight was considered a reasonable assumption as the neighbouring material would impose similar conditions.

Examples of the applied boundary conditions are given in the following figures. In figure 3.5 the symmetry of the model along the x and y axes was considered, and the applied unidirectional micro-strain was derived from the imposed constant displacements of and $u2$, along the x and y directions, respectively.

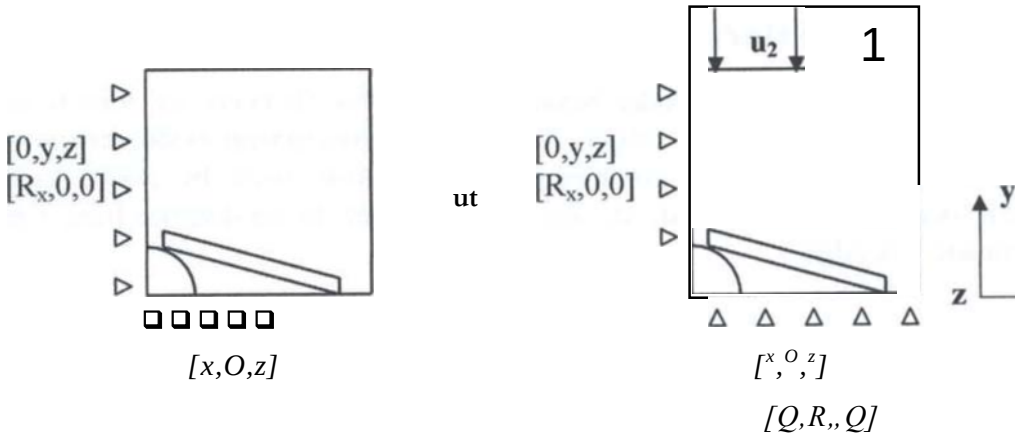

Figure 3.5 *Boundary conditions and applied displacements for the quarter unit cell models for two typical applied in plane loads.*

The applied displacement was the only constrained degree of freedom on the loaded *unit* cell *face.* The *x -y* plane *was* also considered a third plane of symmetry, because all the considered laminate had a symmetric stacking sequence, therefore the under surface of the unit cell was constrained in thew direction. The upper surface of the model is considered free in all the degrees of freedom. The boundary conditions for pure shear load were accomplished by imposing constant displacements along the four lateral faces of the unit cell, as shown in figure 3.6, The nodal reaction forces produced shear stresses in the unit cell. Due to the unsymmetrical loading conditions, the full unit cell had to be analysed.

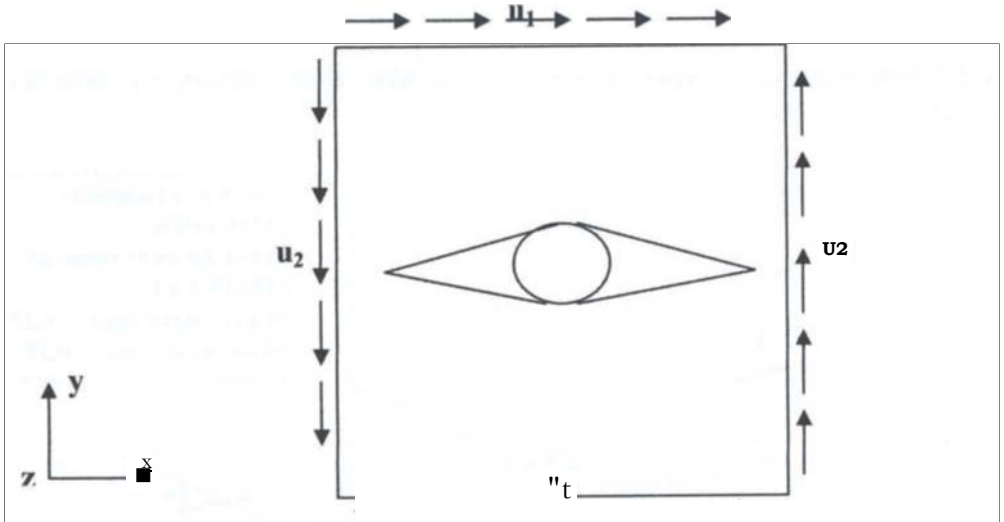

Figure *3.6* *Boundary conditions, for pure shear loud on a, full unit cell model.*

The *use of a* quarter cell model was still possible, but it would imply two runs. The application of a positive shear on the full unit cell resulted in quarter models with equal but opposite shear loading conditions; therefore to obtain the full shear stress both symmetric and anti-symmetric load cases should be run on the same quarter model.

3.3 Model for interlaminar stress analysis

A 3-D model consisting of 20-noded hexahedral quadratic elements was used to model a z-pinned laminate. As shown in figure 3.7, the micro-mechanical model represented a rectangular block of laminate containing one z-pin that might be placed in three different locations indicated as *d1, d2,* and *d3* with respect to the distance from z-pin to the laminate free edge.

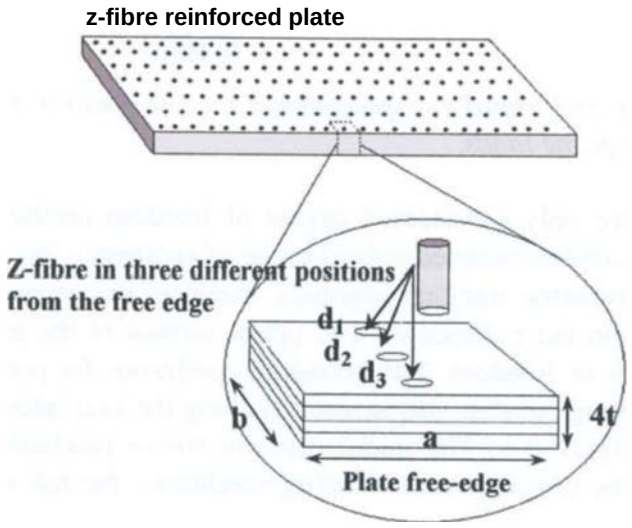

z-fiber density - 2%
z-fiber diameter = 0.28 mm
a - **2.11 mm**
b=1.45mm t= 0.132 **mm**

z-pin distance from the free-edge:

d, = 1.25 mm
d2- 0.69 mm
d3= 0.25 mm

Figure *3.7 Schematic ref a single :-pin reinforced plate with a parametric distance from the* ***free-edge.***

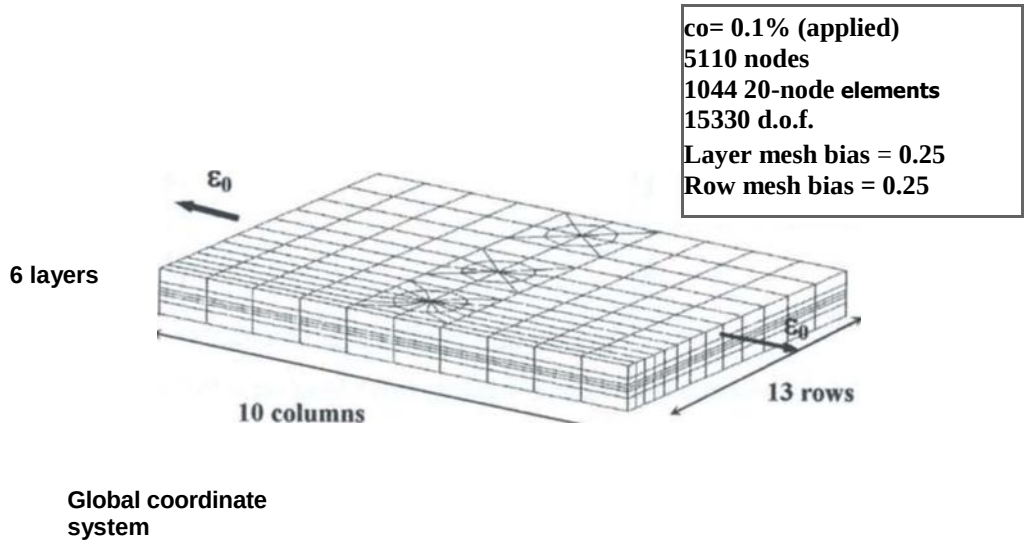

Figure ***3.8*** *Finite* ***element model*** *of ': f0. 90/ pinned laminate. Applied strain* $^{4}o\text{-}^{0.1\%}$

For meshing compatibility three z-fibre locations were allocated in the FE model but only one location was effectively assigned with the z-fibre material property whilst the other two had the properties of baseline laminate. The detailed FE model is shown in figure 3.8.

The z-fibre reinforced laminates analysed in this section were cross-ply [0, 901, and angle-ply [±45], sequences. The z-fibres were arranged in a square array with a space of 2,11 mm representing a volume density of 2%. The length for both models was 2.11 mm; the width was 1.45 mm for the $[0, 90]_5$ laminate (522 20-noded hexahedronal solid elements, 3039 nodes) and 2,9 mm for the [±45], laminate where symmetric boundary conditions cannot he applied (2088 20-noded hexahedronal solid elements, 9489 nodes). This 3D FE model was used to examine the stress distribution near a z-fibre and the interlaminar stress variation at the free edge. The distance between a z-pin and the free edge had a parametric variation of five times a z-pin diameter (pin was placed far from the free-edge, at di position) to one z-pin diameter (z-pin closest to the free edge, at d position). The applied strain was 0.1% along the x-axis.

3.4 Results and discussion

3.4.1 Comparison of elastic constants

As a baseline solution, Table 3.2 provides the elastic constants for the unpinned laminates. Tables 3.3, 3.4, 3.5 & 3.6 contain calculated elastic properties and comparisons with some published results for the four different laminates. All studied laminates had 2% volume density of z-fibres. In this numerical study it was assumed that z-fibres were inserted at right angles (90°) to the principal in-plane axes, i.e. z-*fibres are* parallel to the z-axis of the classical laminate theory.

It should be noted that the closed form solution (CFS) (Lin and Chan, 1999) was originally formulated for a z-pinned sandwich panel with two laminate faceplates and a centre core. The elastic constants quoted in these tables for the CFS were obtained by assuming a zero-thickness centre core. Therefore, two faceplates together with the correct laminate stacking sequence can be treated as a single laminate. The analytical CFS only provided in-plane elastic properties.

The comparisons show that the FE results obtained in this work agreed very well with both the closed form solution (CFS) (Lin and Chan, 1999) and the numerical unit cell solution (Dickinson, 1999). Detailed comparisons for pinned and unpinned laminates based on this study are discussed below.

Firstly, for all four z-pinned laminates considered in this work, the through-thickness longitudinal modulus E2 increased significantly, by 22-35%, as shown in figure 3.9. The magnitude of increment depended on laminate stacking sequence. The Poisson's contraction ratio in the thickness direction was reduced because of the added z-fibre stiffness.

For the in-plane elastic properties, all stacking sequences showed a small reduction in the Young's moduli that were contained within 10%. Examples for the longitudinal modulus EC are shown in figure 3.10.

Table *3.2 StiffneM values for control cases (unpinned).*

Lay-up	E, (GPa)	E,. (CPa)	E, (CPa)	G=~. (CPa)	C „ , (GPa)	G (CPa)	v,y	v1z	V u
Analytical Closed Form Sol Solution (Lin andChan, 1999)									
(0, 01,	136.40	8.90	8.90	5.95	3.21	.94 5.94	0.25	0.38	0.25
10, 90],	72.88	72.88	11	5.95	11	11	0.03	11	11
145, -45],	20.57	20.57	Jl	35.36	11	11	0.73	11	11
145, 0, -45, 90b	53.34	53.29	11	20.65	11	11	0.29	11	11
Unit Cell Model (Dickinsonet al., 1 999)									
01,	136.40	8.85	**8.85**	5.95	3.21	5 .94	0.25	0 .38	0.25
10, **901.**	72.80	72.80	10.05	5.90	4.16	4.16	.03 0.03	0.36	0.36
145, -45],	20.52	20.52	10.05	35.30	4.25	4.25	0.73	0.10	0.10
145, 0, -45, 90],	53.28	53.28	10.05	20.64	4.23	4.2E	0.29	0.26	0.26
Unit Cell Model(thisstudy)									
10, 0],	136.40	8.86	**8.81**	5.95	3.20	5.94	0.25	0.37	0.25
10, 90],	72.80	72.80	10.05	5.94	4.15	4.15	0.03	0.34	0.34
145, -45],	20.60	20.60	10.03	3 5.32	4.29	4.29	0.75	0.12	0.12
145, 0, -45, 90],	53,28	53.28	10.05	20.64	4.21	4.23	0.29	0.26	0.26

The worst casewas Er ofthe UD]aminate$[0]_4$. Thiscan be att attributed the influence of the misaligned in-plane fibres *and* pure resin region caused by insertion of z-fibres; the deviated in-plane fibres along the longitudinal direction and the pure resin zone would make the longitudinal stiffness and strength weaker.

For the [0, 90], laminate the reductions in moduli E, or E. were about 7%. The reduction in the shear modulus G,, for the $[0]_4$ and $[0, 90]_5$ laminates was less significant compared to the reduction in the Young's modulus because the angled fibre region around a z-pin can *carry more* shear load and thus provides extra stiffness that offsets the added compliance due to the pure resin region. The local shear stresses carried by the deviated fibres can be seen in figure 3.11. For the [±45], laminate G 1. was reduced by 9%, whilst for the quasi-isotropic laminate a smooth and almost uniform reduction in E,, and G,, was observed (6-7%).

Table 3.3 *Stiffness values for ;pinned (TD laminate /Oh with 2% z_fibre density.*

	Er (GPa)	**Ey (GPa)**	**E. (GPs)**	Gxy (GPa)	GyT **(GPa)**	G **u (GPa)**	**v:y**	~..	**vu**
CFS "	133.81	8.86	1 1.60	5.79	3.22	5.79	0.26	0.37	0.26
UC [12]	123.€0	**885**	**11.17**	5.80	3.17	5.70	0.31	**0.31**	0.20
UC (this study)	**12180**	8.60	1 L.92	**5.81**	3.13	5.67	0.33	0.27	0.24

Table *3.4Stffness valuer for* pinned cross *ply* TO, *90]s with 2% :Tare density.*

	Ex (GPO	**E, (GPa)**	**Ez (GPa)**	Gxy **(GPa)**	Gv~ **(GPa)**	**C (GPa)**	~~.	**vyx**	**vu**
CFS"	71.50	71.50	11	5.80	11	11	0.032	11	11
UC[12]	67.48	6748	12.30	5.87	4.00	4.00	0.04	0.29	0.29
UC **(this study)**	67.30	67.30	12.3 €	5.82	3.98	3.98	0.05	0.30	030

Table 3.5 *Stiffness values J r .- pinned angle-ply /45, -45]s with 2% fibre density.*

	Ex (GPa)	**E, (GPa)**	**E~ (GPa)**	Gxy **(GPa)**	Gr. **(GPa)**	*G v* **(GPa}**	***Vxy***	**vyx**	**vxa**
CFS"	20.09	20.09	11	34.69	11	11	0.72	11	11
UC'[2]	20.10	20.10	12.37	32.00	4.13	4.13	0.71	0.09	0.09
UC **(this study)**	19.45	19.45	12.27	31.90	4.10	4. €0	0.70	0.10	0.10

Table *3.6 Stiffness values Pr 2-pinned laminate / :- 45, 0, -45, 90J with 2% :-fibre density.*

	Ex (GPa)	**(GPa)**	**E, (Gpa)**	Gxy **(GPa)**	**(GPa)**	G;z **(GPa)**	**vsy**	**v)x**	**vu**
CFS' l	52.35	52.35	11	20.25	11	11	0.28	J1	/1
UC'[2]	49.70	49.70	12.30	19.00	4.09	4.09	0.30	0.21	0.21
LTC **(this study)**	49.51	49.51	12.00	18.87	3.98	3.98	0 .29	0.19	0.19

" (Lin and Chan, 1999)

[12] (Dickinson et al., 1999)

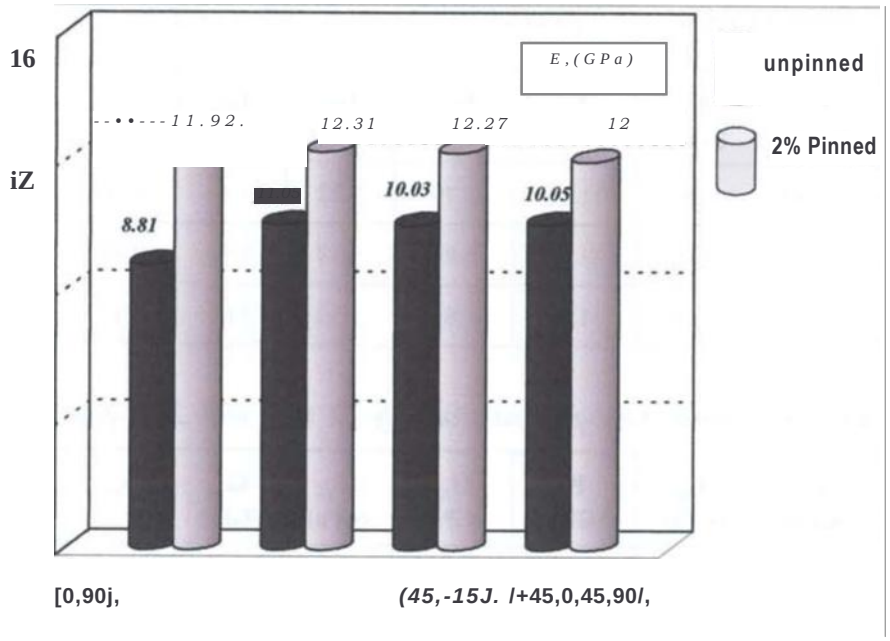

Figure *3.9 Stiffness variations for the Ex modulus for different kind of laminates: without fibre and with 2% density 0.28 diameter :-fibres.*

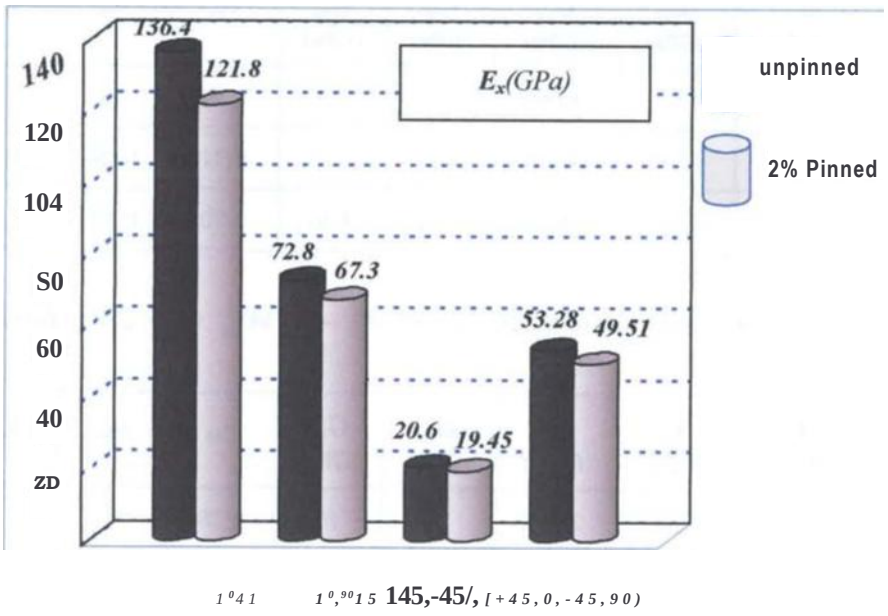

Figure 3.10 *Stiffness variations fir the E modulus for different kind of laminates: without : O r e and with 2% density 0.28 diameter fibres.*

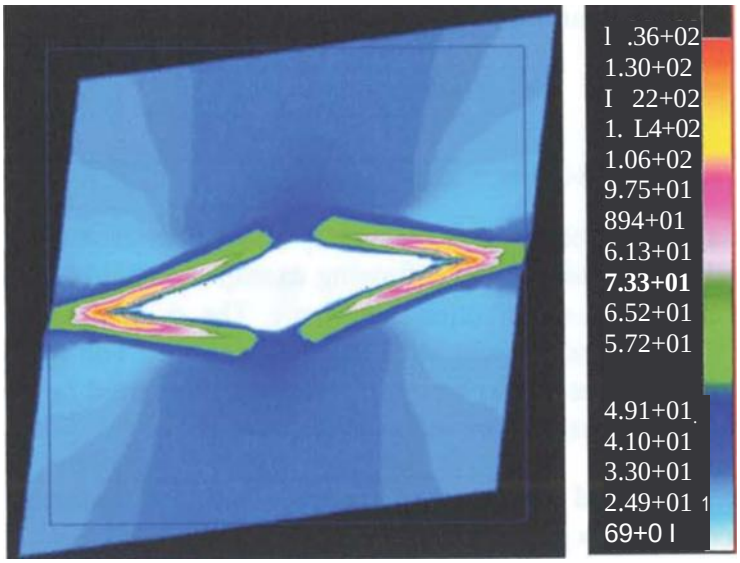

Figure 3.11 *In plane shear stress'MPq) distribution around a .:pin. Note: deviated fibre region carried loads providing extra .st fjYress that rrffcet the added compliance of the pure resin region.*

The computational results demonstrated that the in-plane fibre alignment is a critical factor for the in-plane stiffness values of z-pinned composites. From this point of view, z-pin diameters should be minimised in order to minimise the angle of misaligned in-plane fibres so as to avoid micro-buckling during compressive loads, as addressed by the work of (Steeves and Fleck, 1999b).

The CFS (Lin and Chan, 1999) appeared to have predicted some of the elastic constants quite well. The model was based on the volume fraction of z-fibres using the simple rule of mixture for the laminate properties and the classic laminate theory. Since the z-fibre volume fraction plays a crucial role in some elastic properties, such as the transverse and shear moduli, the CFS was accurate enough for these constants. However, larger differences resulted between the CFS and FE solutions in the in-plane longitudinal modulus, Ex, as shown in tables 3.3, 3.4, and 3.6. In these cases, the CFS overestimated the values of E for the UD and cross-ply laminates, and (a,. for the angle-ply laminate. This is because the closed-form analysis did not consider the effect of the misaligned in-plane fibres and resin pocket around a z-pin, which do low the stiffness and strength in the longitudinal direction. However, the overall results obtained from the CFS were accurate enough. The disagreement with the two FE results was contained within 5-7% as shown in tables 3.3-3.6. The CFS model is easy to use for quick estimation of the in-plane stiffness properties for this new composite material. It is worth mentioning that the FE results of this study were also validated against the experimental data provided by the z-pin material manufacturer[13]. The tests were conducted with a different carbon fibre material using also 2% volume fraction of z-

Preliminary lamina. laminate and sub-element test results for Z-fiber' M reinforced 1N7/977-3 uni-directional tape and fabric. *AZTEX,* 1-'ersion *1.3* - 1998.

fibres. The same range of variations in the elastic constants as in aforementioned examples was found.

3.4.2 Stress field around a z-fibre

The stress field in a z-fibre inclusion is essentially three-dimensional under uni-axial loads. This can be demonstrated by the following example. A uniform strain of 0.1% was applied in the x-axis of a unidirectional laminate. The o axial stress is plotted in figure 3.12 showing high stress concentration around the z-pin. The figure also shows that the stress perturbation due to the z-pin's presence disappeared beyond a distance comparable to the z-fibre diameter from the axis line of the z-pin.

It also resulted in an increased shear path along the misaligned fibre region as well as interlaminar stress components (figure 3.13). This was due to the excessive mismatch of the elastic properties between the z-fibre and the surrounding laminate region. Therefore, z-fibre spacing and its interaction with the resin-rich zone should be further studied.

The FE results also showed that when carrying the through-thickness stress components z-fibres absorbed up to 25% of the total elastic strain deformation energy stored in the unit cell; a non-uniform shear lag at the interface of the z-fibre and matrix was observed from the numerical example. Therefore material compatibility and the interfacial adhesive bond between the z-fibres and their surrounding matrix are important because a large part of the through-thickness loads is transferred to the z-fibres. From this point of view, for carbonlepoxy laminates a carbon z-pin would be a better choice, which offers excellent adhesion to the surrounding thermoset resin and good compatibility characteristics.

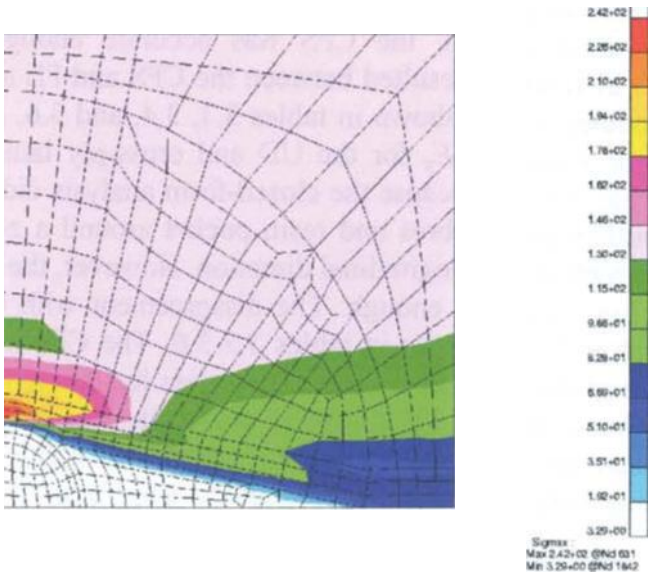

Figure 3.12 *Quarter unit cell model: 6r stress field with perturbed stress field that disappeared after one =-fibre diameter.*

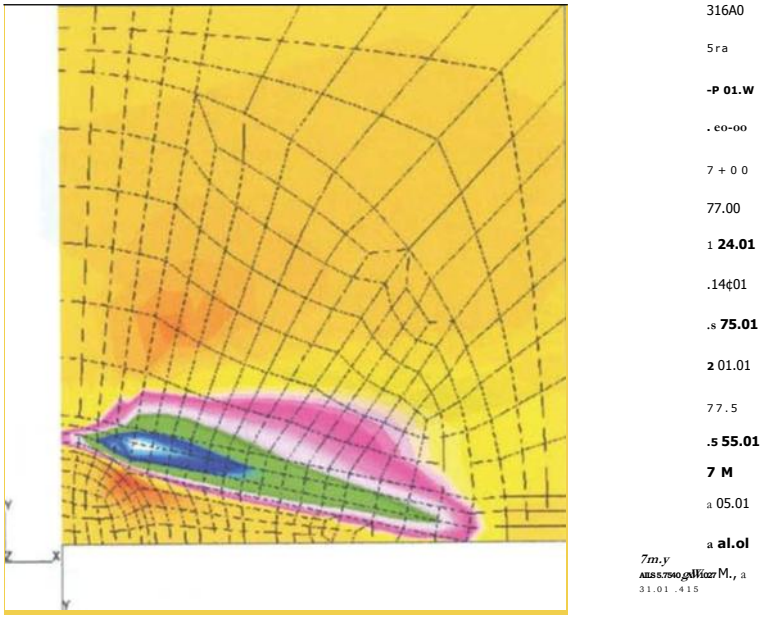

Figure 3.13 *Quarter unit cell model: introduced shear path along the misaligned fibre region. Applied strain e = 0.1% along x direction.*

3.4.3 Interlaminar stresses

At the laminate free edge, the interlaminar stresses are extremely high. According to the classic lamination theory, the interlaminar normal stress (or peeling stress) for the [0/90] cross-ply laminate goes to infinity at the free edge. This is a stress singularity problem. The distance over which the free-edge interlaminar stresses rise shapely is very small. According to the study by Hu & Soutis (1997) this characteristic distance had a maximum length that equals to 2-ply thickness. Therefore, for carbonlepoxy composite this distance is about 0.25 mm- In order to study the effect of z-pinning on interlaminar stresses, z-pins were placed at three parametric distances, i.e. *di, d2* and *d3,* being 1.25, 0.69 and 0.25 mm from the free edge respectively as shown in figure 3.7. It was expected that only the z-fibre position at *d -d;* could give relevant results with regard to stress singularity. Two laminate stacking sequences were studied in the present work. They were [0/90], and $[\pm 45]_5$ laminates.

Since the [0, 901, laminate exhibits only a Poisson mismatch between the layers (no shear coupling), stress components o and rk, are the non-zero interlaminar stresses (figure 3A4, 3.15).

Figure 3.16 shows the distributions of the interlaminar normal stress, cr, along the three principal axes and for both pinned and unpinned laminates. Figure 3.16(a) & (b) shows that the maximum interlaminar peeling stress was reduced significantly at the free edge when a z-pin is placed at the immediate vicinity of the free edge, i.e. d--d_3.

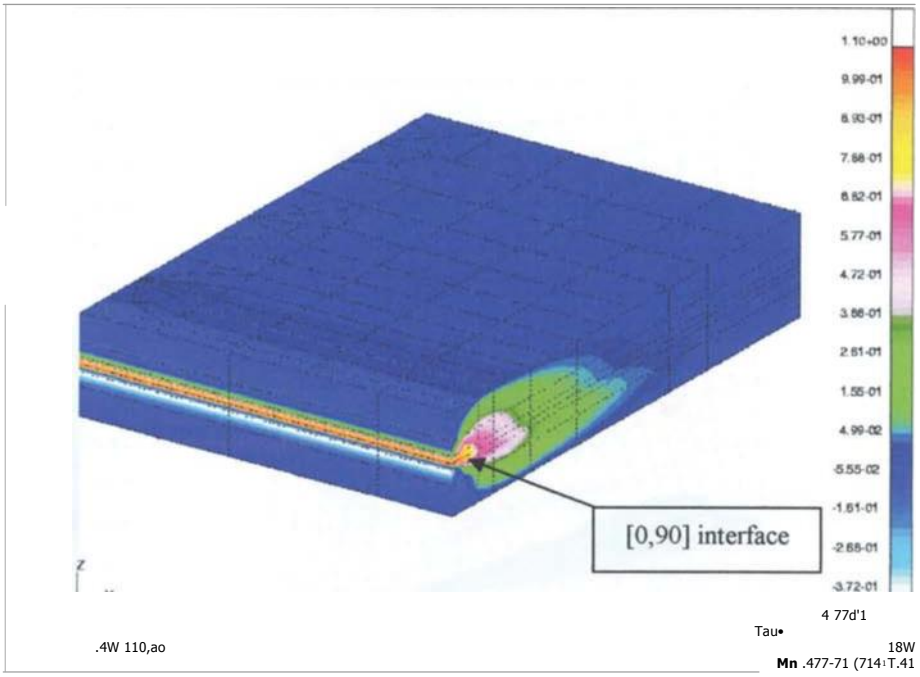

Figure 3.14 *Contour plot of 1.8 FE model of /0,90/s laminate without . -frhre reinforcements:* **C** *stress distribution (MPa). The critical inter-lamina area can be seen in*

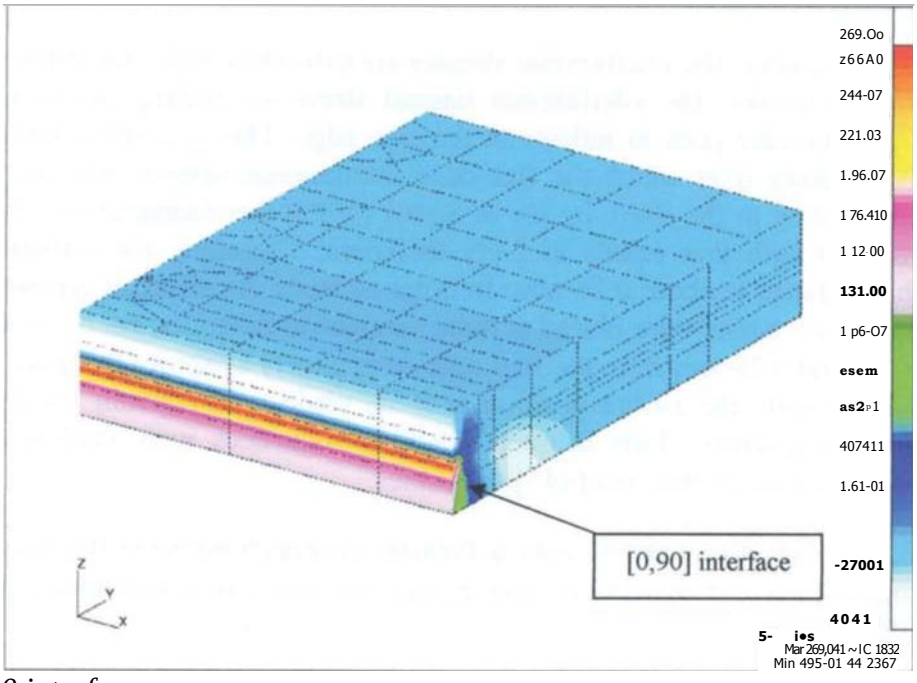

the 0-90 interface.

***Figure* 3.15** *Contour plot of 18 FE model of* [0,90]-,. *laminate without z-fibre reinPrcement o stress distribution (MPa). The critical interlaminar area is still the 0-90*

interface.

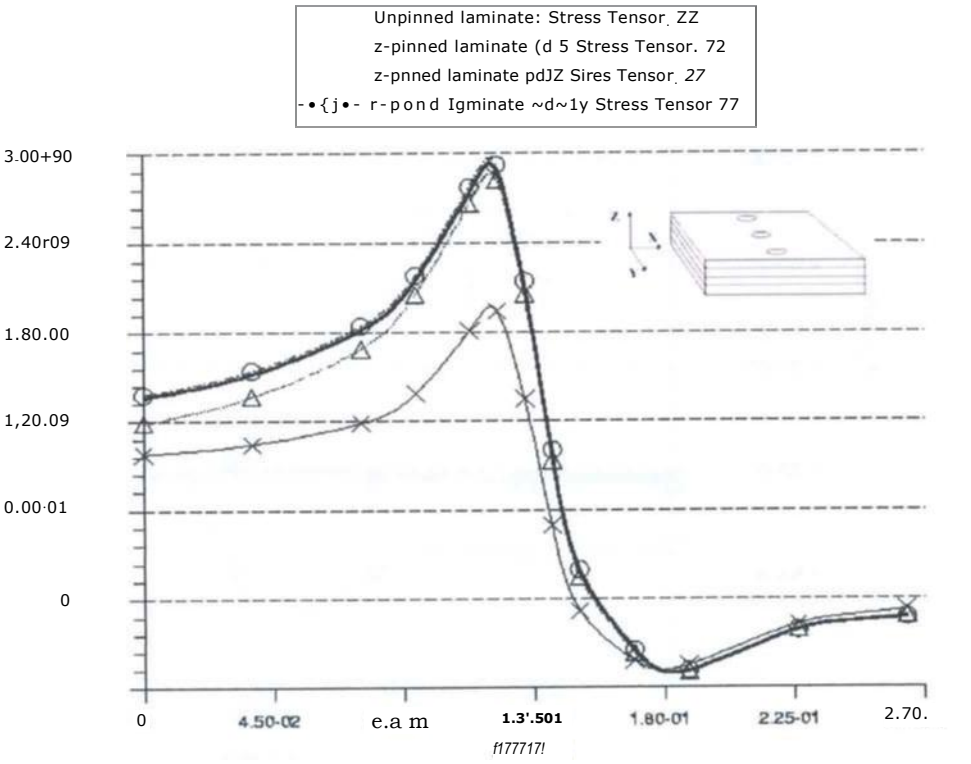
Unpinned laminate: Stress Tensor. ZZ
z-pinned laminate (d 5 Stress Tensor. 72
z-pnned laminate pdJZ Sires Tensor. 27
-•{j•- r-pond Igminate ~d~1y Stress Tensor 77
3.00+90
2.40r09
1.80.00
1,20.09
0.00·01
0
0
4.50-02
e.a m
1.3'.501
1.80-01
2.25-01
2.70.
f177717!

(a)

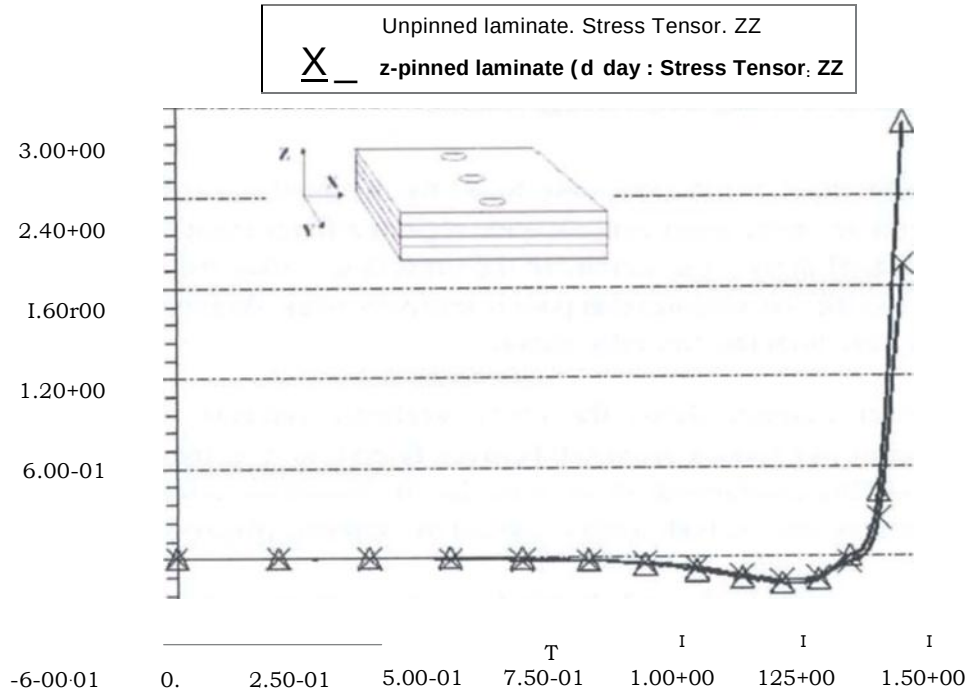
Unpinned laminate. Stress Tensor. ZZ
X_ z-pinned laminate (d day : Stress Tensor: ZZ
3.00+00
2.40+00
I.60r00
1.20+00
6.00-01
-6-00·01
0.
2.50-01
5.00-01
7.50-01
1.00+00
125+00
1.50+00

Onm.

(b)

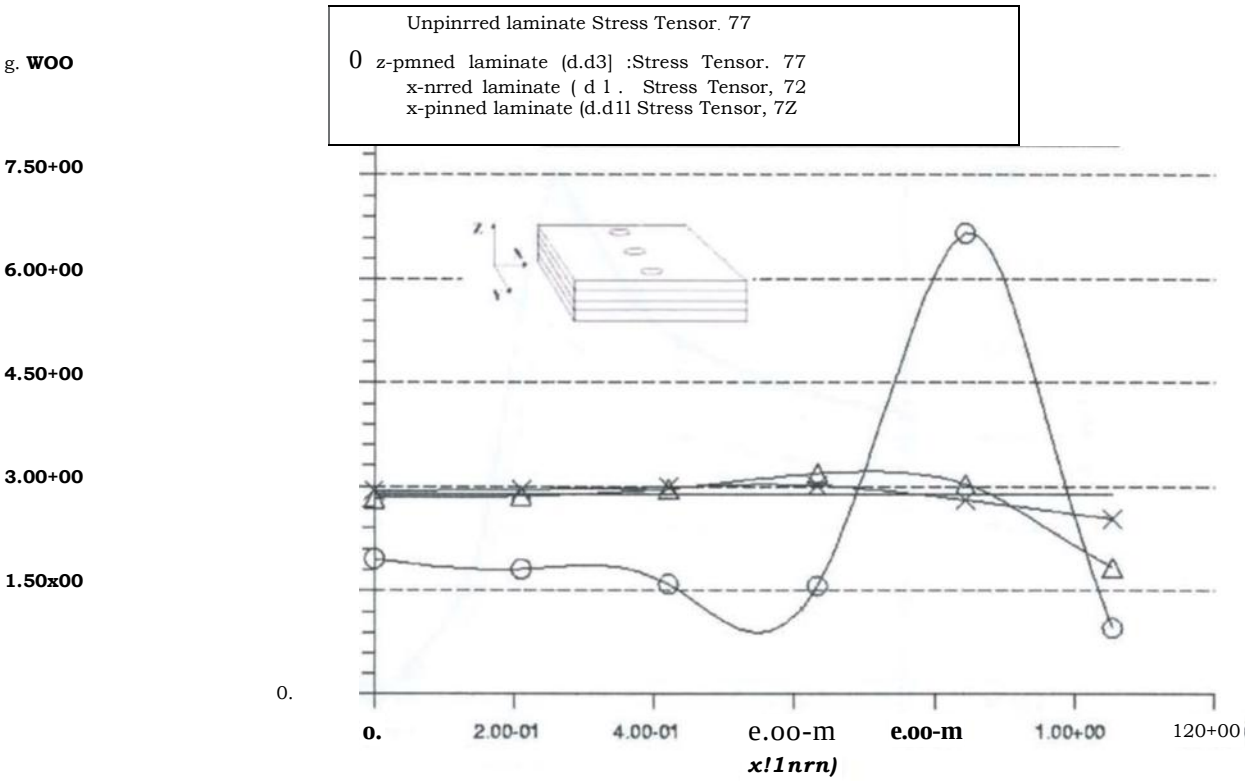

(c)

Figure 3.16 *FF. results of a stress distribution for 10, 90J₃ cross ply laminate: (a) T hrough-thickness variation (s-axis); (h) Y-variation from inside plate to the free-edge; (c) Variation along the free-edge (x-axis).*

Similar stress distributions were found for the interlaminar shear stress component ;,, Therefore, in the stress concentration regions z-fibres resist interlaminar stresses if they are placed in the close vicinity of the stress raiser. Since the interface between a z-fibre pin and the surrounding resin pool is relatively weak, delamination damage is still likely to initiate from this free edge region.

Another example shows the [±45], angle-ply laminate which exhibits only shear coupling (no Poisson mismatch between layers), so ru is the only non-zero interlaminar stress. The interlaminar shear stress has its maximum value at the mid-thickness and reduces to zero on both surface sides of the laminate (figure 3.17).

Figs. 3.18 (a) & (b) plot distributions of r showing that z-pinning can reduce the maximum shear in the mid-thickness by about 15% if a pin was placed at d=d.;. The stress values for pin distances di and *d2* were virtually the same as those of unpinned laminate.

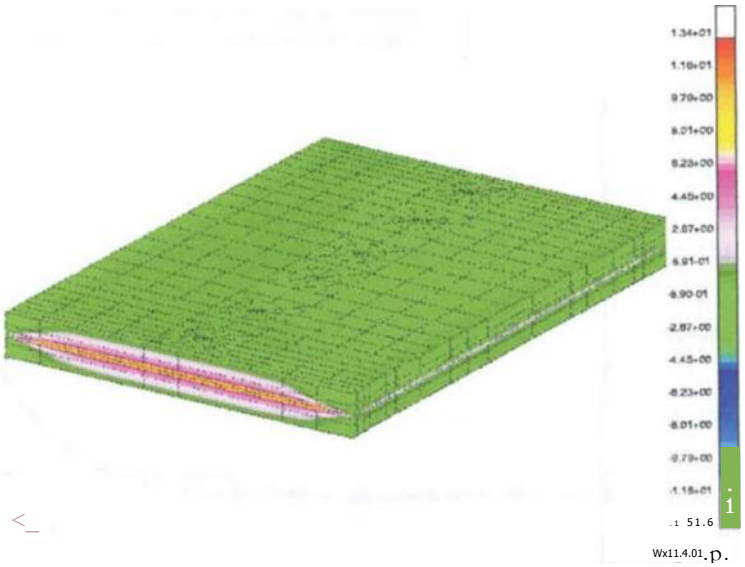

Figure 3.17 *Contour plot of Ii2I L model (?f[57 ., cross ply laminate without -fibers:* r_{12}*stres.s distribution ('MPa). The critical interlaminar area can he detected in the -45'-45 interface.*

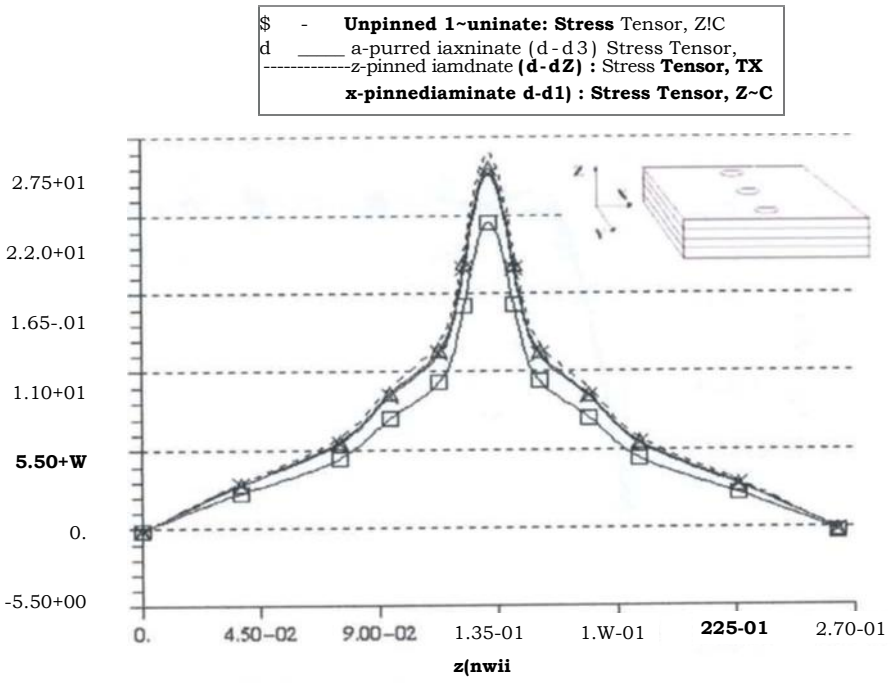

(a)

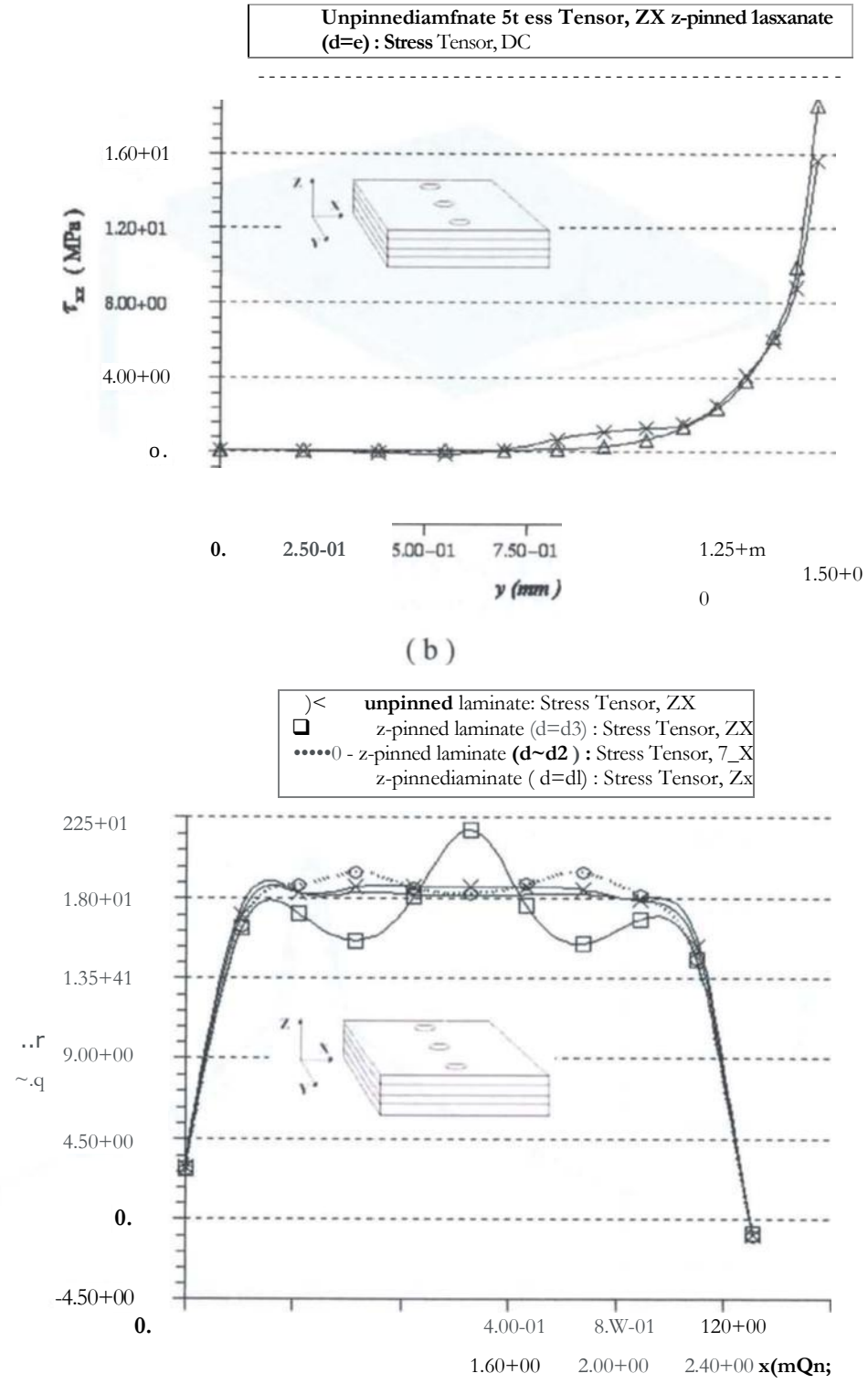

Figure 3.18 Finite *element results of* r . *stress for /±45]r angle Ply laminate: (a)Through-thickness variation (=-axis); (h)Y-variation from inside plate to the free-edge; (c) Variation along the free-edge (x-axis).*

Part of the through-thickness stress was carried by the z-fibre placed at d = d3, as shown in Fig. 3,18 (c).

The above stress analysis showed that interlaminar stress components could be reduced only when z-fibres were placed in the immediate vicinity to the free edge (within 0.25 mm). Even though the stress distributions in the laminate were significantly affected, there were no overall reductions in these peak stresses in the region since the z-pins picked up some high stresses. Barrett (1996) obtained similar results for a different stress singularity problem, i.e. an interlaminar crack in z-pinned laminate under Mode I loading.

It should be noted that over such a small distance (e.g. 0.25 mm) the assumption of material homogeneity for the laminates might break down and the bi-material nature of the composite should be taken into account. Further work is necessary for more detailed stress analysis using micro-mechanical models for the surrounding matrices.

3.5 **Conclusions**

Three-dimensional micro-mechanical finite element models were employed to examine the mechanical behaviour of z-pinned laminates. Tasks performed were: (a) calculation of the engineering elastic constants, and (b) study of stress distribution around a z-fibre and at z-pinned laminate free edges. The following main conclusions may be drawn.

By adding two percent volume fraction of z-fibres the through-thickness Young's modulus (E_r) was increased significantly, i.e. by 22-35%, for the four different laminates studied in this work. The reductions in the in-plane moduli were contained within 7-10%. Therefore, the z-fibre technique is very effective for design against damages caused by out-of-plane loads, e.g. impact and stiffener pull-off.

Material compatibility and the interfacial adhesive bond between the z-fibres and their surrounding matrix were important because a large part of the through-thickness loads were transferred to the z-fibres. From this point of view, for carbonlepoxy laminates carbon z-pins were considered to be a better choice, offering excellent adhesion to the surrounding thermo-set resin and good compatibility characteristics.

The interlaminar stress distributions near the free edge of a z-pinned laminate were significantly affected only when z-fibres were placed within a characteristic distance of one z-fibre diameter from the free-edge. Detailed numerical analysis showed that local z-fibres carried significant amount of the interlaminar normal and shear stresses.

The characteristic dimension of the stress concentrations examined in this chapter were less than the thickness of an individual ply. Design stress models of composite components are rarely developed to such level of detail. In order to avoid increased computational time and costs, the use of an analytical micro-mechanical model to simulate z-fibre mechanics might bridge the gap between standard stress analyses for z-pinned composite components and the refined FE models presented in this chapter.

Furthermore when global FE models of z-pinned components are to be considered for linear stress analyses without any kind of failure, z-fibre presence into the model might be simulated by changing the elastic constants and therefore the stiffness matrix of the those elements within z-pinned areas. On the other hand, for global FE models simulating damage growth, z-pin key properties such as delamination arrestment will have to be simulated.

Chapter 4

(a) (b)

Micro-mechanical analysis of z-fibre bridging a delamination crack

4.1 Introduction

This Chapter tackles the analysis of z-fibre failure phenomena when a delamination crack extends into their field. The micro-mechanical analysis conducted in the previous Chapter is hence broadened to the z-fibre mechanical behaviour occurring during crack bridging. The finite element simulation of z-fibre mechanics, bridging forces, and stresses, would require an extreme level of detail in terms of mesh refinements, type of elements used (solids, contact) and kind of simulation required (non-linear with damage mechanics), resulting in a very comprehensive but computationally expensive model.

It is thought that the essential material property of the z-reinforcements as bridging entities is the constitutive law relating the bridging traction with the crack displacement, the so-called bridging law. For in-plane conditions, both the opening and sliding displacements will occur in the crack plane, and the z-fibre will impose both normal and shear traction on the delamination fracture surfaces.

This chapter describes the analytical micro-mechanical model developed by Cox and co-workers (Cox, 1999a, 1999b; Cox and Sridhar 2001) and the consequent computation of the bridging curves. A description of the most important energy absorbing mechanisms involved in the bridging process is also tackled. The model is formulated in order to be valid for different kinds of through thickness reinforcements (TTR): z-fibre or stitches; the difference in the model is in the applied boundary conditions.

The implementation of the analytically derived bridging laws into the FE simulation could provide a robust numerical tool to assess z-fibre effect on composite structural components without the need to have refined and computationally expensive FE models to capture the micro-mechanics of z-fibres.

4.2 Problem statement

4.2.1 Damage mechanisms for TTR during crack bridging

The different damage mechanisms to which different kind of TTR bridging a delamination

crack are subjected *have* been reported in several works (Dransfield et al.,

(a) (b)

1998; Tanzawa et al, 1999; Rugg et al., 1998) using either the post-mortem analysis of different ENF, DC B, lap joint specimens or small cubical specimens containing a single reinforcement under controlled opening or sliding displacement (Cartie, 2000). Different mechanisms operate at different values of' the total crack displacement vector and the amount of energy absorbed during each mechanism often depends on the type of TTR considered, mode ratio and z-reinforcement inclination angle in respect to the fracture plane.

(a) (b)

In order to introduce some of *the* symbols and terminology used within this Chapter, figure 4.1 shows a schematic representation of a z-pinned laminate subject to mixed-mode delamination loads. Mode I loads are associated with the crack opening displacement (u_3), and mode II loads are associated with the crack sliding displacements *(u_1),* both defined in a local coordinate system.

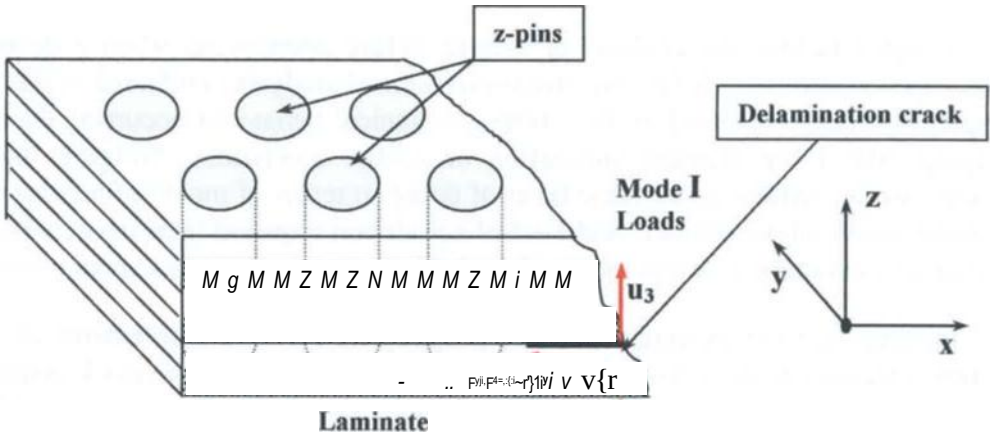

Figure 4.1 *Schematic representation of a laminate reinforced through the thickness by fibres subjected to delamination. Mode I loads associated with crack opening displacement (u_3) and Mode II loads related to crack sliding displacement (u_j).*

The fracture plane is the plane x-z in figure 4.1 and the bridging forces opposing the aforementioned crack displacements will be evaluated in this plane. The delamination crack is assumed to grow at a constant ply interface, no jumps to other ply interfaces are considered for the derivation of the bridging laws.

4.2.2 Summary of damage mechanisms during z-pin crack bridging

A schematic explanation of the different mechanisms involved in the z-fibre bridging of a crack are depicted in figures 4.2 and 4.3 which refer respectively to mode 1 and mixed mode loading conditions.

When a delamination reaches the z-pin field, the crack propagates at the laminate-z-pin interface totally separating the z-reinforcement from the laminate (figure 4.2(a)). The crack opening displacement vector has a value of few μm (3-10 μm) during the elastic

stretching and propagation of debonding phase as the work of Liu and Mai (2001) has

(a) (b)

shown (also see chapter two). The z-fibre then starts developing axial stress opposed by friction at the interface to create a slip zone. During this phase a certain amount of fibre abrasion and matrix crumbling combined with fibre splitting due to the Poisson's contractions of the z-reinforcement cross-section is possible (figure 4.2 (b)). When the slip zone reaches the end of the z-fibre the frictional sliding phase is activated, where the z-pin is progressively pulled out from the laminate almost as a rigid body, and the entity of the bridging force decreases progressively (figure 4.2(c)).

(a) (b)

If the z-reinforcement is anchored to the laminate *as in* the case of stitching or interlocked fabrics then a phase of elastic stretch up to the point of tensile failure of the TTR precedes the ultimate TTR pullout failure.

Under mixed mode loading conditions an angled z-fibre (figure 4.3(a)) bridging a delamination crack tends to debond from the surrounding laminate as soon as the delamination crack reaches it (figure 4.3(b)). Generally debonding involves no fiber/matrix separation within the fibrous z-reinforcement, separating the z-pin as a whole from the surrounding laminate (figure 4.3(b)).

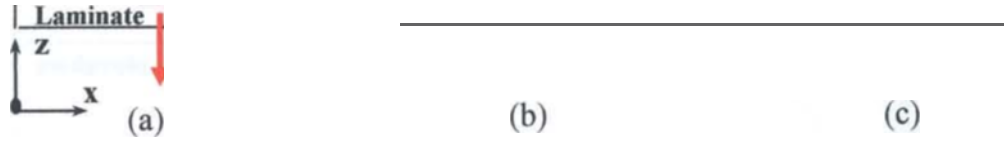

Figure 4.2 *Z -fibre bridging mechanics under pure Mode I loading conditions. (a) delamination reaching the bridging entity, (h) fibre debonding with slip zone growth, (c) slip =one growth up to the :-fibre end and consequent pull-out _failure opposed by friction.*

During the debond growth, a slip zone is created where sliding is opposed by friction, whilst tensile axial stress is developed in the z-fibre as reported for the pure mode I loading condition. The work done against friction during the slip zone growth is often much greater than the fracture energy required for the debonding phase. When the z-reinforcement has been inserted with a certain angle in respect to the fracture plain, or when a certain amount of mode II sliding displacement is present, the z-pin deflects almost immediately through axial shear (fig 4.3 (c)). This is followed by "plasticity" in the laminate, where splitting cracks can be found (fig. 4.3 (d)).

During its deflection in the fracture plane, the z-fibre itself is split by numerous axial matrix cracks, parallel to the fibre direction and strands formed by splitting slide along one another to accommodate large axial shear strains. This allows on one hand the rotation of the fibres along the load direction and limits, on the other hand, the flexural rigidity of the z-pin (fig. 4.2 (d)). Due to these plastic deformations a shear flow r_U will exist in that area. The rotation of the fibres in the damaged z-fibre towards alignment with the delamination fracture surface allows bridging shear tractions much larger than r,} due to the contribution of the axial stiffness of the rotated fibres carrying now part of the load in

(a) (b)

tension. Large rotations exist only near the fracture plane where the pin has ploughed laterally through the laminate, which acts as a plastic medium with matrix mediated deformation and crumbling and resisting the z-fibre's sliding displacement (figure 4.2 (e)). The zone of non-zero rotation is always much shorter that the slip zone, as it will be shown

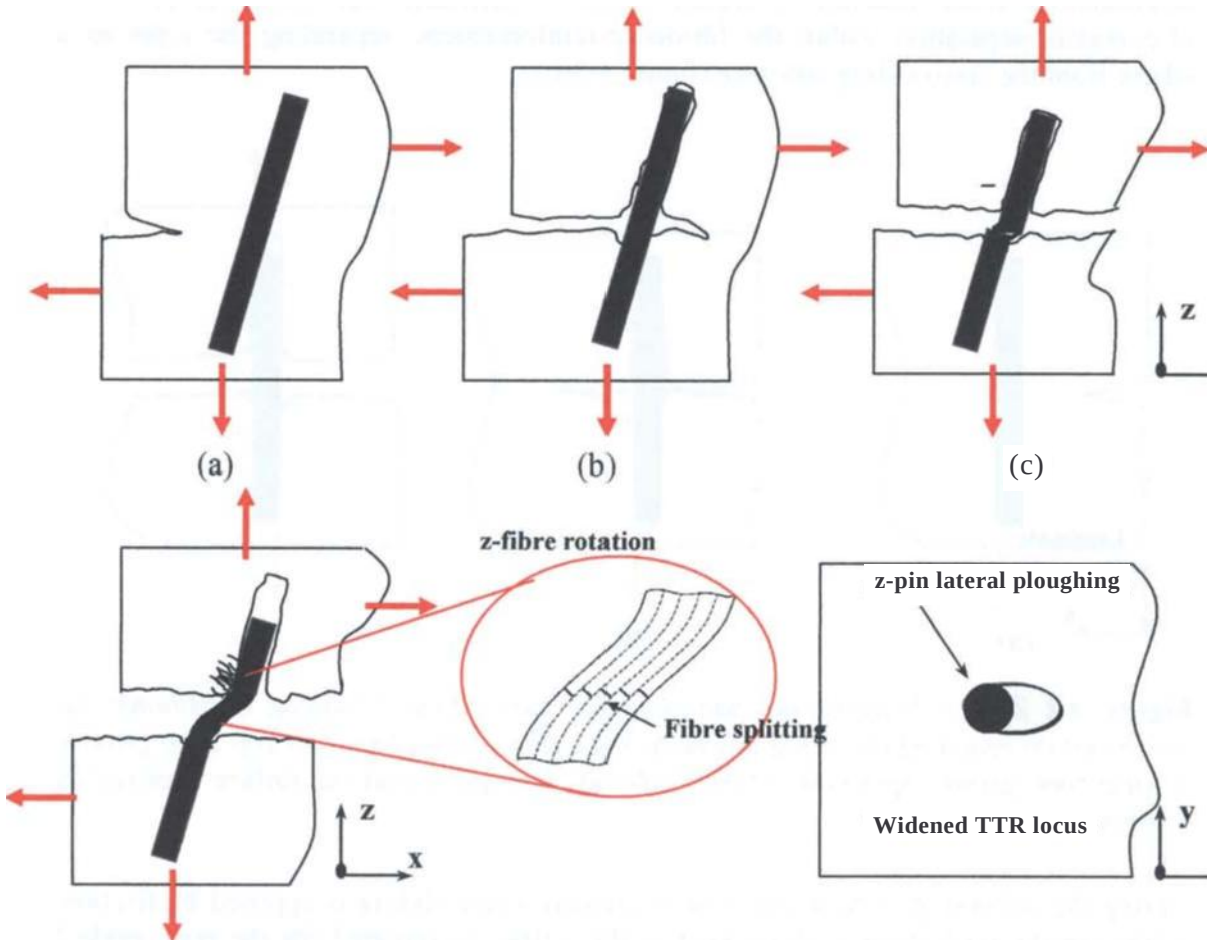

soon.

(d) (e)

Figure *4.3* *Bridging mechanics of an angled pin under Mixed Mode loading conditions: (a) delamination reaching the bridging entity, (b) pin debonding with slip zone growth and further delamination propagation in the laminate, (c) plastic shear deformation, (d):-fibre splitting*

with fibres rotation towards load direction, and laminate matrix crumbling, (e) TTR lateral ploughing with the widened locus (x -y plane).

(a) (b)

At sufficiently high loads, ultimate failure of the bridging z-reinforcement can occur by three main failure mechanisms: tensile failure of the fibres (mostly for stitching and interlocked fabrics), pullout from the laminate (Z-Fibre and broken stitching threads), or z-reinforcement shear failure in the deformed zone near the crack plane (stitching and Z-Fibre of small radii).

Nevertheless because the z-pin debonding and plastic deformation within the reinforcement occurs very close to the delamination crack front, there is no appreciable (a) (b)
interval of crack sliding displacement where deformation is purely elastic.

4.2.3 **Experimental observations**

For clarity, some published evidence of TTR bridging mechanisms and failure modes as described above, are reported in the following.

In figure 4.4 an optical micro-graph of a polished section of a single lap shear specimen made of carbon-epoxy (M46J/7714A tape) plies are reported (Rugg et al., 1998). The reinforcements are carbon z-fibres with a diameter of 1.7 mm. Depending on the orientation of the z-fibre some of them pulled out more easily from the laminate (figure 4.4 (a)), some others deformed near the crack plane in the direction of the applied shear displacement (figure 4.4 (b)).

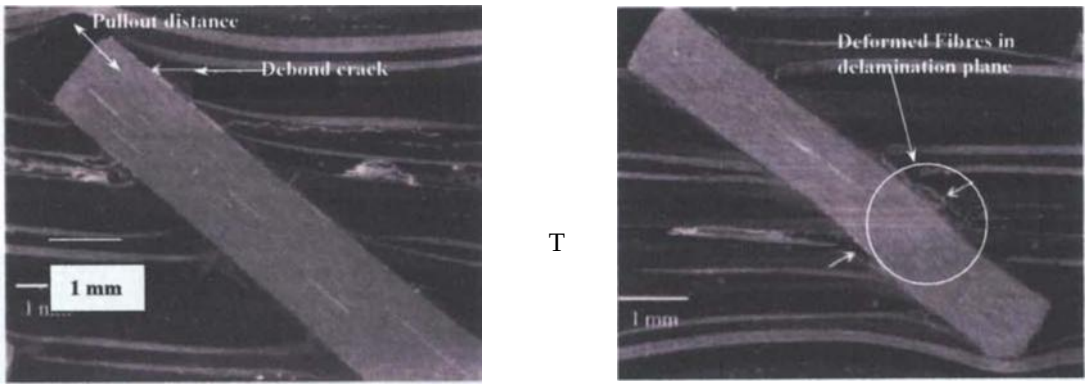

T

(a) *(b)*

Figure 4.4 *Zfibre bridging mechanisms¸ following delamination (Rugg et al., 1998): (a) Angled fibre debonding and pull-out, (h) resisting ¸fibre bending and plastic deformations at delamination plane.*

The same kind of failure mechanisms can be seen in figure 4.5 where small cubical specimens of 32 ply carbon-epoxy IMS/924C laminate or polycarbonate *were* tested in pure Mode I I conditions (Cartie, 2000).

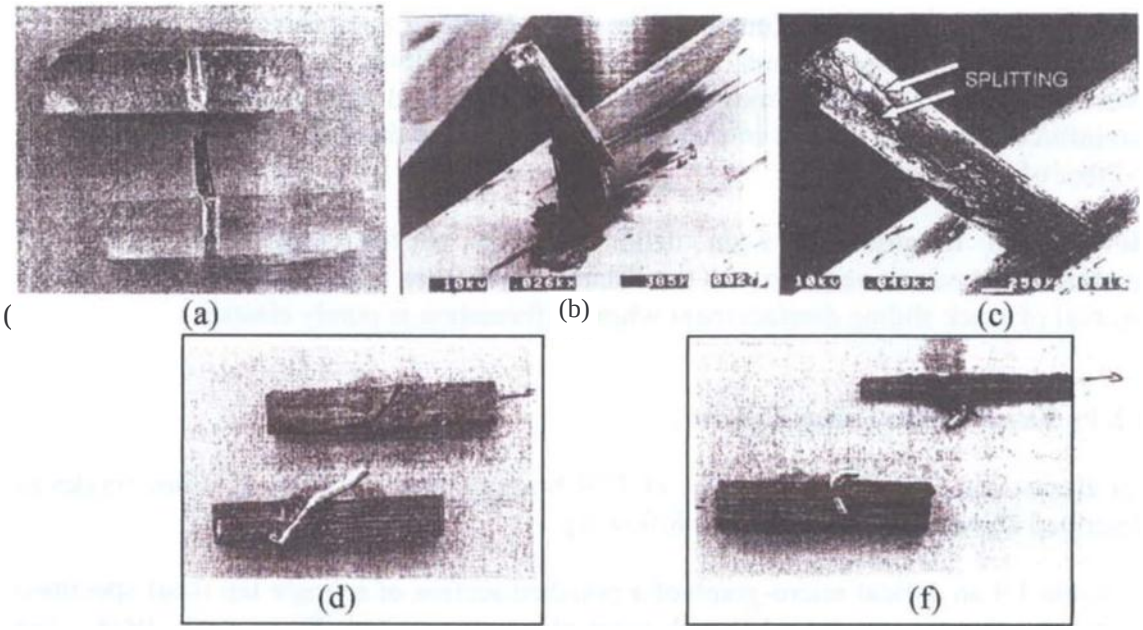

Figure 4.5 *Failure of a :fibre reinforced cubical specimen under shear loads (Cartie,* 2000): *(a) carbonBMJ rod pullout failure; (h) SEM picture showing the rod bent in the fracture plane; (c) SEM of a damaged =fibre after ultimate pullout; (d) Pullout failure of a titanium pin with an insertion angle complying with the applied load; (e) tensile failure of a titanium pin with an insertion angle opposing the applied load.*

A single reinforcement was inserted and it was made either of fibrous carbon/BMl zfbre or of titanium metallic pins. Post-mortem analysis of DCB and single-lap joint specimens reinforced with z-fibres also confirmed the aforementioned mechanisms. The pulled-out z-fibres were visible on the fracture surface of one of the DCB arms, whilst empty loci were found on the other arm,

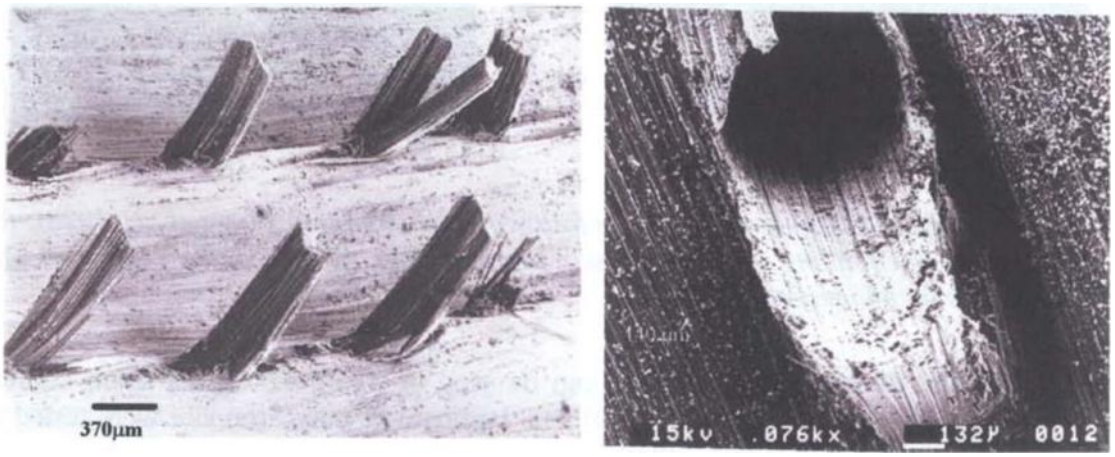

(a) (b)

(a) (b)

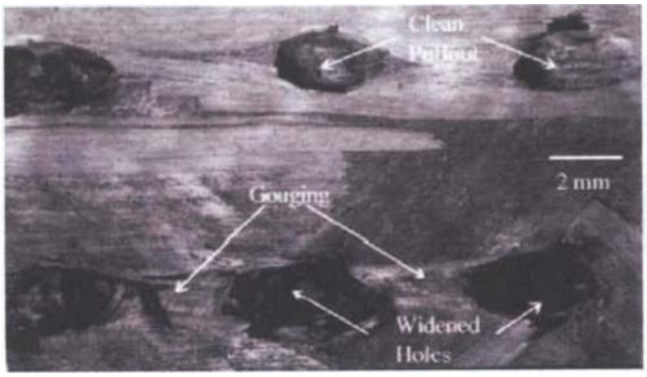

Figure *4.6* *Z-fibre failure modes during delamination bridging: (a) SEM of a DCB failed .specimen surface where the pulled-out :pins are visible (t'artie, 2000) (h) SEP of the locus left in the DCB upper arm surface after :pins have been pulled-out (`Iroulis, 2003); (c) Optical micrograph of a single-lap joint failed surface reinforced with 1.7 diameter . fibres showing the holes remaining after the pullout of the reinforcement (Rugg et al., 1998).*

As for the case of other TTR, the elastic stretch and consequent tensile failure of the Kevlar stitch threads was the most common failure process reported in (Dransfield et al., 1998). The Kevlar stitching threads were used to bridge a delamination crack under mode I loading conditions in a carbon-epoxy fabric laminate (figure 4.7 (a)). It was also reported that most of the stitches did not break in the crack plane but at the thread intersection at the outer surface of the composite (figure 4.7 (b)). Subsequently the broken stitches pulled out (figure 4.7 (c)).

The bridging mechanics of z-yam bundles in a 3-D interlocked fabric presented in Tanzawa et al. (1999) showed once again similarities with the other TTRs, some of the analysis results are reported in figures 4.8. The material system used for the DCI3 tests was a carbon-epoxy laminate with fibre architecture having five fibre-yarn axes, four of them in the x-y direction and one in the z direction.

(a) (b) (c)

Figure 4.7 *Stitching failure during Mode 1 delamination bridging from (Dransfield et al., 1998): (a) Carbon epoxy laminate cross section showing the stitching threads;* (b) *SEM fractograph displaying the tensile failure of the stitching Kevlar thread and successive pullout; (c) corresponding hole remaining after thread pullout.*

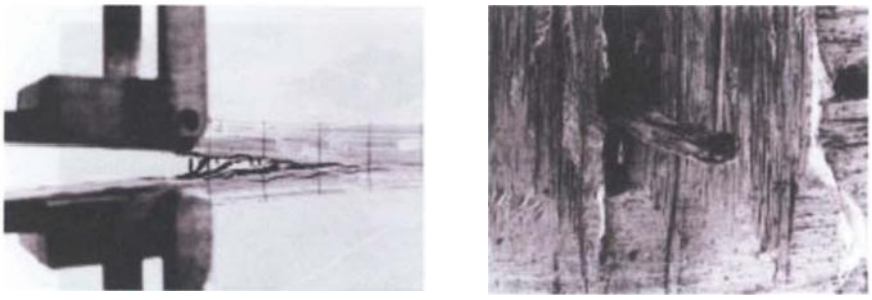

(a) (b)

Figure 4.8 *Bridging failure mechanics of a 3-f) orthogonal interlocked carbon-epoxy fabric from (Ianawa et of., 1999): (a) :fibre yarn bundle bridging a delamination crack under mode I loading condition: (h) SEM showing the yarn breakage near the top or bottom surfaces and its pullout.*

Because of all the similarities reported in the damage mechanisms of different TTR systems bridging a delamination crack, it could be possible to use a single universal model with the boundary conditions modified to represent either the end of a Z-Fibre or the anchoring of a continuous stitch at the outer surface of the laminate and hence to serve for both stitches and Z-Fibre.

4.3 Modelling procedures

4.3.1 Micro-mechanical model formulation for a TTR bridging mixed mode cracks

The micro-mechanical model developed by Cox and Sridhar (2001) is summarised in this section. The analytical model is capable of treating mixed mode loading cases with bridging reinforcements that are inclined relative to the delamination fracture plane (figure 4.9).

4.3.2 Z-fibre bridging law: Traction-Displacement Relation

A z-fibre of general but uniform cross-sectional shape (A,) lies in the x-z plane and bridges a delamination crack on the plane z--O. The unit vector n defines the fibre direction at =O and points out of the TTR half. The area A, refers to the normal section of the TTR, having a *circumference* s, and width D in the y direction. The model also takes into account an initial insertion angle of inclination **0** for the TTR, measured relative to the z-axis. The model output is a non-linear relationship between the bridging tractions applied to the fracture surfaces by the TTR and the opening and sliding displacements of the bridged crack_

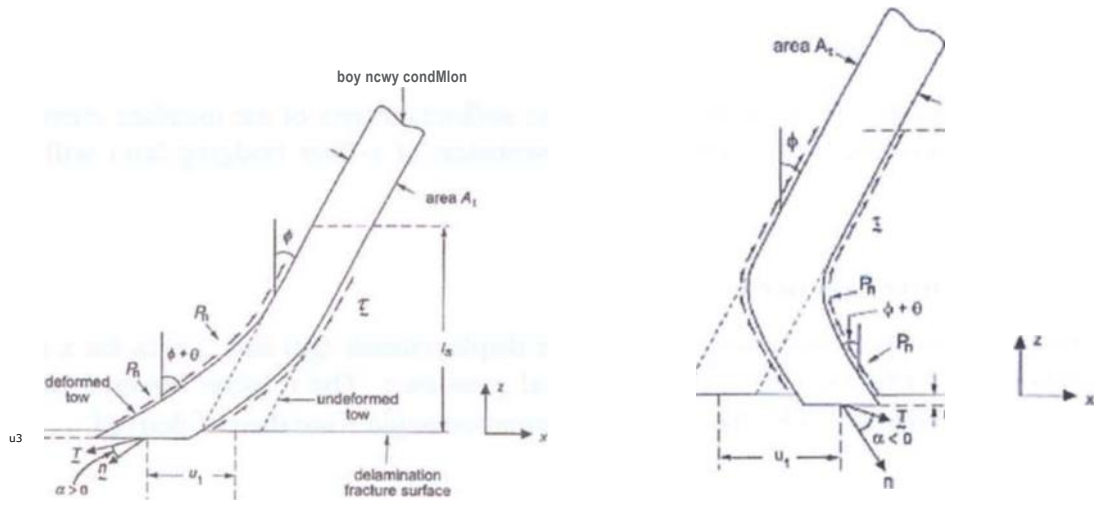

Figure ***4.9*** *The schematic representation of the micro-mechanical model parameters in (Cox and Sridhar, 2001): (a) bridging TTR deformed under the traction load T with an initial a -0 (complying configuration): (b) bridging 1'TR with a resisting initial configuration a:-0.*

For a single TTR a traction vector *T'=(T't,T3)* is introduced along with the total crack displacement vector *u - (ut, u),* with the components defined in the x and z direction of the local crack reference frame (figure 4,9). This bridging traction law *1(u/* can incorporate all the complex bridging phenomena previously described, and the relative importance of the different mechanisms simulated by T[u/ depends on the initial orientation of the rods (0) and on the applied mode ratio.

The angle of deflection of the TTR, 0, is a function of and is assumed positive when the initial TTR angle is complying with the applied load (figure 4.9 (a)), and negative when it is opposite generating a hackling effect (figure 4.9 (b)). For monotonic loading , *B-•0* when *a* -.0 and O-0 when a *0,* where *a* is the angle between *7'* and *n*.

Since *T* depends on the state of deformation, it is defined as a traction vector *1'* , that is acting on the original, un-deformed cross-sectional area of the tow. The relationship between the two traction vectors is:

$$T = \frac{\cos O}{\cos(q5 + 0)} T \qquad (4\text{-}1)$$

The traction vector will be derived from the equilibrium equation of a TTR slice, having therefore the dimensional units of a stress. If the total force vector (F) components have to be derived then substantially we can write:

$$F = \frac{Ar\ T}{\cos 0} \qquad (4\text{-}2)$$

Where $\frac{A'}{\cos 0}$ is the original un-deformed cross-section of the TTR on the fracture plane, This equation will be useful to derive the stiffness matrix of the interface element in chapter 5 where the finite element implementation of z-fibre bridging laws will be discussed.

4.3.3 Constitutive equations

The model formulation starts with defining the displacements (z) and (z) in the x and z directions of a generic TTR section at initial position The relation between these displacements and axial "1TR strain sand defamation angle Bare thereof derived:

$$2(e=\cos O \sim a + \tan O l + 1 + - - 1$$
$$\frac{\partial}{\partial z}$$
$$,. = \tan^{-1} a \qquad (4\text{-}3)$$
$$+ \tan O \; 1\,1 + - - 0 \; aJ$$

The mechanical equilibrium of the slice of material initially lying in the interval (:, d_) is then derived in a local coordinate system (x', =') aligned with the local fibre direction within the slice. The stress components assumed to take part in the equilibrium equation are the axial stress $\alpha^{c'}, z\,z$, the shear stress o $_{ZY}$ and the transverse compression stress q,=6,.

The axial stress is assumed to be uncoupled from the transverse and shear deformations and to follow a simple linear elastic law a- - $\&L,,$ where E, is the Young modulus of the TTR in the fibre direction. Because most of the fibres do not break during the bridging process until eventually the ultimate tensile failure and the E is mostly a fibre-dominated parameter, it is postulated not to change during the TTR defamation. Moreover the axial stress $o^{a'}, (r,y,-)$ is considered a one-dimensional function of: only, and is assumed to be computed along the axis of the TTR, that means uniform in the TTR cross-section (A,).

The shear stress always satisfies the condition:

$$rJ \quad _{r0} \qquad (4\text{-}4)$$

Where $_{r0}$ is the shear flow stress for an assumed elasticlperfectly plastic material, including all the mechanisms of shear deformation described in section 4.2. The transverse compression is non-zero only when the TTR starts deforming.

The friction stress is postulated to be uniform over the whole surface of the slice and to have two distinct constant values along the z direction: z within the un-detlected part of

the TTR, re the enhanced friction due to high contact pressure between the pin and the laminate where deflection has occurred (Cox, 2003).

The resistance of the laminate to lateral ploughing of the TTR as described in section 4.2, is modelled as the resistance of a perfectly plastic medium to the impactation of a punch. A zone of hydrostatic compression is assumed to arise adjacent to the TTR exerting a force P,,, per unit length of the TTR and acting normal to the deflecting pin. P,, is assumed to be uniform along the length da of the slice.

With these assumptions, the equilibrium of the TTR slice in the x and z directions is derived by summing up the forces per unit area acting along x and z:

$$F = 0 \quad (\text{- }) . \quad \underline{A`}\_ + a\ (:+d:)\bullet \frac{\underline{A,}}{\cos(O+B)} + \frac{\underline{d:}}{\cos(O+O)+sr\ \underline{d}} \bullet sin(0+0) = 0$$

$$+l]\sim P \quad \frac{\underline{d:}}{\cos(O+O)+sr\ \underline{d}} \bullet sin(0+0) = 0 \qquad (4\text{-}5)$$

$$\frac{\underline{A,}}{\cos q} + \frac{\underline{A,}}{\cos t} + \frac{\underline{A,}}{\cos(0+B+dB)^{+}} = 0 \text{--} Q`(=) \text{-} \cos(A'$$

$$\text{-} \quad \frac{}{c} \bullet \sin(r+G)+sr\bullet_c \frac{S}{\$} \bullet \cos(\not{c}+0)=0$$

Where - $\underline{A,}$ and $\underline{A,}$ are the surfaces of the deformed slice at: and -d: respectively; $\_\ \underline{d\text{-}}$ is the length of the deformed slice and $ri_1=\pm 1$ in order to have always a positive The model develops solutions only for a tensile load of the TTR at the fracture plane $7' \bullet n > 0$, no solutions for the compression state of the TTR are considered ($7' \bullet n < 0$).
In differentiating the equation 4.4 in = it is assumed a perfect plasticity for the shear term aa_Y, and a small value of the stress ratio a a,

It is possible then to write:

$$au, \quad sr. \qquad (0 \le z \le z_0) \qquad (4\text{-}6)$$

$$a= \quad \frac{= sk - -}{At \cos 0}$$

$$\underline{aa,} \quad \underline{s}\, r, \qquad (z_0 \le z \le l_s) \qquad (4\text{-}7)$$

$$a= \quad \frac{}{A, \cos t}$$

$$a\ B\_ \quad P\ n \qquad (4\text{-}8)$$

$$6+\ a= - -qi$$

These equations can be integrated numerically once defined the boundary conditions; in eq. 4.5 and 4.6, -6 defines the limit of the TTR deflection zone starting from the crack plane (z=0), whilst defines the limit of the slip zone (figure 4.9).

4.3.4 **Boundary conditions** •

Crack Plane

Figure 4.10 reports the TTR stress components at the fracture plane in the coordinate system (x'') aligned with the TTR. *The* bridging tractions *Ti* and Ti have the dimensions of a stress and are averaged on the TTR cross-section as the stress components a-o, a',, an. In reality *6„* that is associated to the contact pressure load P,,, will be concentrated only on the side were the contact force is active, being zero on the other side of the deflecting z-reinforcement. Therefore o„ is interpreted as a spatial average of the

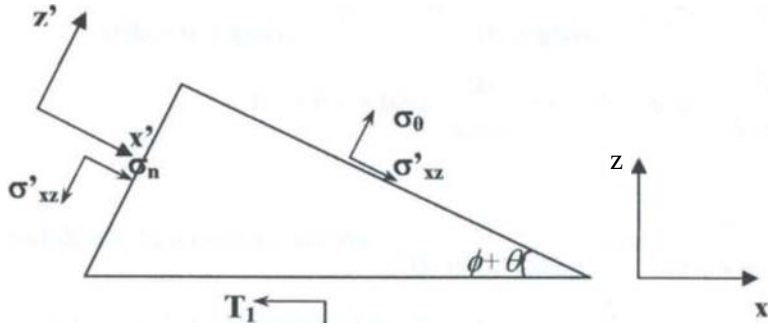

compressive load originated by the contact forces.

Figure 4.10 *Equilibrium of the loads acting at the crack plane on the deformed reinforcement, with the fi)rces expressed along the* x' & *axes, Tj and* 7'3 *are the bridging traction forces touted from the model equations.*

The equilibrium at the crack plane can therefore be expressed in terms of the bridging tractions:

(4-9)

$$T1 - c \sim \left(\underline{+\sim a} \; C \; 2 \; (\; {}^{a}o^{-a}n \;) \; {}^{sin}[\quad +O \; l\sim^{+r}o^{cos}[^{2}(0^{+0}o \right.$$

(4-10)

$$\underline{cos\sim} \; cos \quad e0) \; {}_{0}cos^{2}(\; + \;) \; + \; Q_{,,}sin2(0+0o) - ro \; sin[2(O+o \;)]$$

Where a-', has been substituted with the plastic shear r_0 because the TTR is assumed to begun yielding at very small displacements as discussed in section 4.3, and *ao,* 9 are evaluated at the crack plane:

9o=0(0) **(4-11)**
a,, = c,(0)

• *11R deflection limit*

The zone of TTR deflection mediated by plastic shear is limited by the condition (0 ~ zo). Where zo, defines the upper boundary limit to the TTR deformation zone. The upper bound can therefore be defined:

$\theta(z) = 0$ `dz ~ zo **(4-12)**

- *Slip Zone*

The upper boundary condition of the slip zone depends on its length l,. If the slip zone reaches the end of the TTR then the condition for eq. 4.6 is:

a,Q.z)=0 a, Or)=0 o,O}=0 **(4-13)**

Where the first condition refers to a generic TTR, the second is normally applied to Z-Fibre and it is the half-length of the rod projected on the z-axis. As it will be shown later this condition will limit the amount of axial stress that can be developed in a Z-fibre. The third condition refers to a stitch or a fully pinned z-fibre with being the half-laminate thickness. During the pullout regime the length where the axial stress has to vanish is defined by:

1, = l_r **d** **(4-14)**

Once again ll is the half-length of the rod, ds is the distance that the end of the z-fibre has been pulled out from the original location and is its projection on the z-axis.

The TTR displacements presented in eq. 4,3 can also be expressed in terms of o) and B() as follow:

$$r(z) = \frac{\sin(0+B)}{\cos 0}\,E, \quad \frac{+\sin(0+0)\tan 0}{\cos O}\,dd' \qquad \frac{\cos t+0)}{\cos O}\,6r + \frac{\cos(0+0)}{E.\ \cos O}\,d:_f \qquad \textbf{(4-15)}$$

In the first of the above derived equations the integration is restricted to the zone of non-zero deflection of the TTR so that 0 when :'-:o. In the second equation the integration is restricted to the slip zone, which can coincide with the end of the TTR or with laminate half-thickness. It is also important to outline that in the second equation when --co than I = 0. The crack displacement vector *last* at the fracture plane can than be derived as:

$$ul = -(0) - C^{(0)} \tan(O + B_0)H[-'(0)]\,u; \quad -'(0) \qquad \textbf{(4-16)}$$

Where the second term in the first equation takes in to account the additional mode II displacement generated by the portion of' the bridging TTR that has already been pulled out of the laminate. The step function, H, is nonzero only if the TTR protrudes from the laminate.

The solution of equations 4.6 to 4.10 along with the defined boundary conditions allows the derivation of many important TTR parameters as function *of(a„0)*, or at the fracture plane *(a„ B„)*. The parameters touted in the pre-pullout and pullout regime are: the slip length *lS* (pre-pullout), the pullout distance *cis* (pullout), the deflection zone-end :o, the crack opening and sliding displacement u1, *u3:*

$$\frac{r\,a_0 7\cos 0}{2r.n}\,{}^{r}_{1} \qquad \textbf{(4-17)}$$

$$a_s \text{ is } = =_O + \text{ ycos } r$$

$$z; \qquad \textbf{(4-18)}$$

$$u3 = U3dcf + U3el \quad p$$

$$u1 = ul_{def} + \tan(+9)u1 \qquad \textbf{(4-19)}$$

$$u3 = u_{3def} + u_{3el} + u3\,pull$$

$$ul = u1f + \tan(O + 0,)u3 \qquad \textbf{(4-20)}$$

The length of the deflection zone $=rl$ as well as the slip length is are expressed as function of (co, $9r_j$) and other physical parameters in eq. 4-17 and 4-18, whilst general expressions for the crack displacement are presented outlining the different contributions of different mechanisms to the total crack displacement vector, equation 4-19 refers to the pre-pullout phase and equation 4-20 to the pullout. The expression for elastic stretch contribution um is different for the pre-pullout and pullout phase. For the analytical derivation of the different parameters the reader may refer to Appendix B.

4.4 Numerical examples of z-fibre bridging laws

4.4.1 Mode l crack loading conditions

The bridging laws are derived for a z-fibre orthogonal to the fracture plane under mode I opening displacement conditions. The boundary conditions for such kind of configuration are outlined in the following picture. From equations 4.9, 4.10 and 4.15 the bridging traction forces and the crack displacements, compatible with the applied boundary conditions, can be derived.

Figure 4.11 shows the assumed values of the different micro-mechanical parameters under mode 1 loading conditions. Equations 4.9 and 4.10 give the expression for Tat the fracture plane.

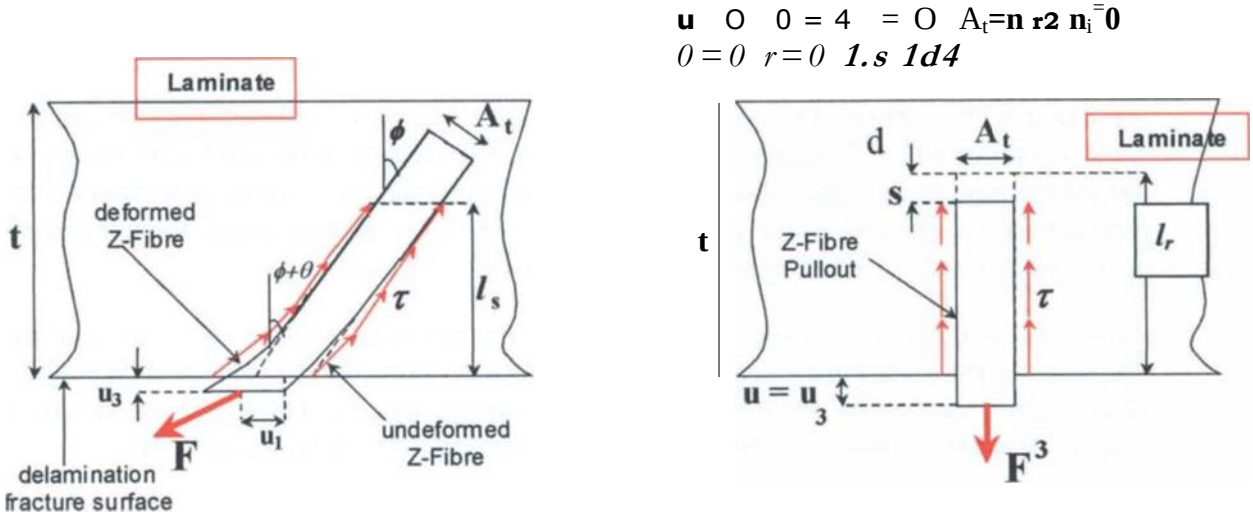

(a) (b)

Figure 4.11 *Applied boundary conditions for the pure mode I loading.*

$$T_1 = 0$$
$$\overline{T}_3 = \sigma_0 \qquad \textbf{(4-21)}$$

Equations 4.15 evaluated at the fracture plane will give

$$(0) = -u, - 0 \qquad (4\text{-}22)$$

If we assume the z-pin with a circular cross-section, and *1'3* as:

$$F;^{=}f;\bullet A, \qquad (423)$$

An explicit relation $F:_3=F;\ (u_i)$ is derived, which makes possible the study of different physical parameters of the bridging law,

$$F;\ =\text{V4ff}E,r\bullet r\bullet A,-u_3 \qquad \textbf{(4-24)}$$

$$\frac{2\text{mr}\ (1_5\text{-}d)=2mT\,xr}{\text{A,}\qquad\qquad\text{A,}\quad_3} \qquad \textbf{(4-25)}$$

Equation 4.24 is obtained by combining equations 4-22 and 4-23. Equation 4-25 derives from equation 4-6, 4-7, assuming *(!r-d5)-u_3* which is thought to be valid with the given boundary conditions (fiTure 4-11). The pre-pullout regime refers to the extension of the slip zone up to the end of the z-reinforcement; during the pullout phase the magnitude of the bridging stress decreases as the pullout length *(Ir ci_s)* increases.

From the condition of the slip length reaching the end of the z-fibre an upper limit on the value of the axial tensile stress developed in the reinforcement is obtained. When the slip length *is* reaches the end of the z-fibre *Ir* then integrating eq. 4.6 in:, and assuming a single value for the friction acting at the z-fibre laminate interface, we can write:

$$\frac{A,a_{,,}\ \text{coS0}\qquad\qquad sti_r}{sr\qquad\qquad\qquad A,} \qquad \textbf{(4-26)}$$

And for an assumed circular z-fibre we can write:

$$aQ\ _{=2r}{}^{l}r \qquad \textbf{(4-27)}$$

Where $I,\ =1$ cosq$, because *Ir* is measured along the z-fibre axis and Is is projected on the z-axis of the global crack coordinate system. Equations 4-26 and 4-27 state that the maximum bridging stress is a function of the friction stress acting on the z-fibre surface, the z-fibre insertion depth, and the aspect ratio *s Ar* (eq. 4-26) or the z-fibre embedded length-radius ratio (eq. 4-27),

A design of a laminate against mode I delamination loads, in order to maximise the bridging traction forces in the crack wake before pins pullout, will imply that smaller

pin diameter utilisation, maximum insertion depth (laminate fully pinned through its thickness), and compatible material systems will enhance the friction stress.

For carbon fibrous rods a typical strength value for tensile axial failure of the z-fibre can be assumed to be I GPa, because of the pullout failure such kind of stress values are barely attained by z-fibre reinforcements. In figure 4.12 and 4.13 the above conclusion are emphasised. On the y-axis the maximum axial z-fibre stress is normalised over the axial strength (1 GPa), and is plotted against increasing z-fibre embedded depth (l_f) for different friction stresses or z-fibre radii.

For a typical z-pinning application considered in this study, a thin laminate of 4 mm thick, fully pinned through its thickness *(1r = 2* mm) with a 0.25 mm z-fibre, this would imply a developed bridging stress (c-o) 50% under the z-fibre axial strength (a„), The frictional stress enhancement could bring towards the condition of z-fibre axial tensile failure, with higher value of the bridging forces (figure 4.12).

The implementation of smaller z-fibre radius in fig. 4.13 also outlines the benefits in terms of bridging stresses. As it has been presented in chapter *2 (section* 2.2.3) the typical z-fibre currently being used are 0.14 mm and 0.25 mm radii. In both graphs the limit to the embedded z-fibre depth Ur) is defined by the half thickness 1 of the laminate.

Computational *F, = I3 (u*)curves are presented from figure 4.14 to 4.17, outlining the effect of the different micro-mechanical parameters on the derived bridging laws. Figure 4.14 shows the bridging force (F_3) versus the crack displacement (u_3) for different friction stresses.

The variation of the z-fibre axial Young's modulus is reported in figure 4.15. Only the pre-pullout phase has been considered for the E, variation. In figure 4.16 the half-laminate thickness was assumed to bet = 4mm and different z-fibre embedding depth were considered. In figure 4.17 three possible z-fibre radii were considered for the computed bridging laws.

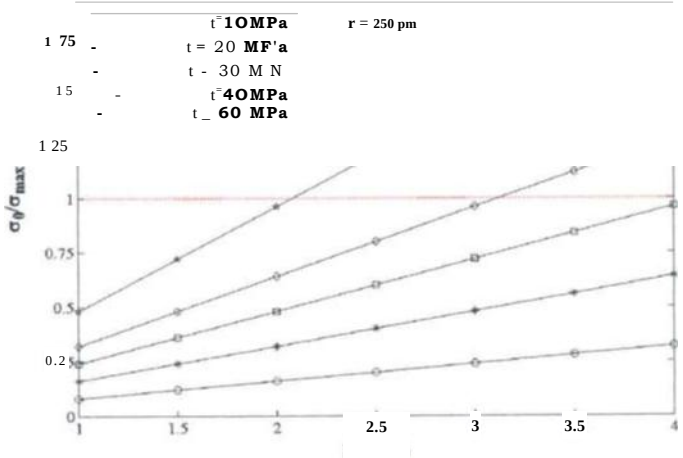

Figure 4.12 *Normalised fibre axial stress vs. embedded length fbr d Brent friction stresses.*

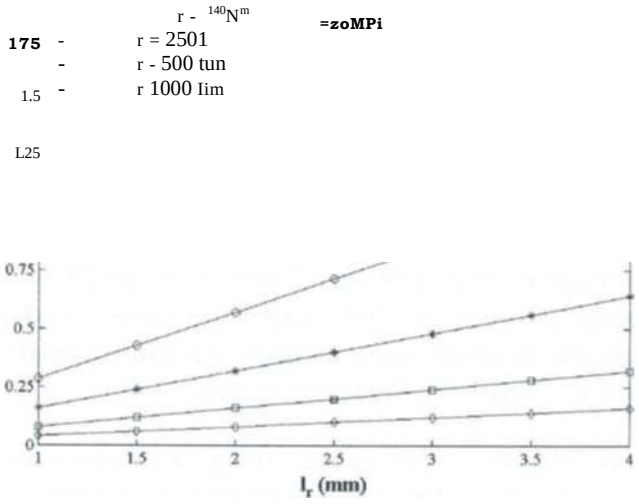

Figure 4.13 *Normalised :-fibre* axial *stress* vs. *embedded length for different :.fibre radii.*

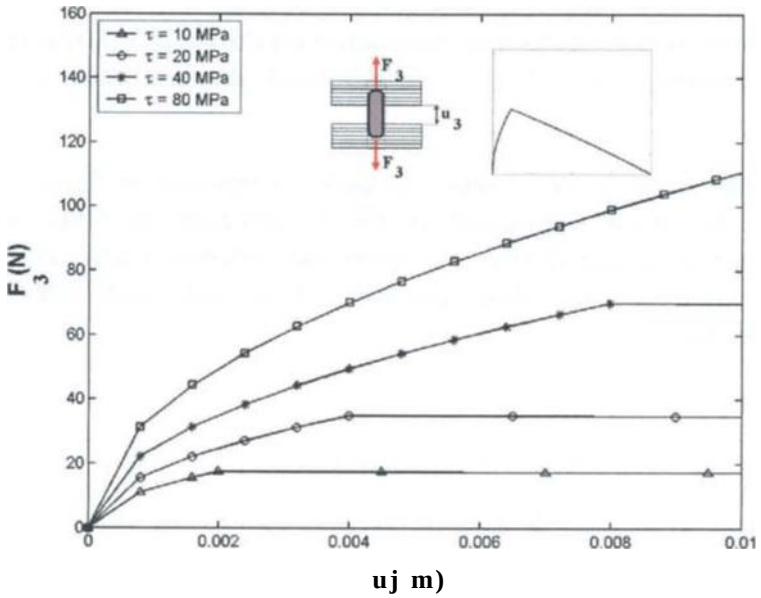

(a)

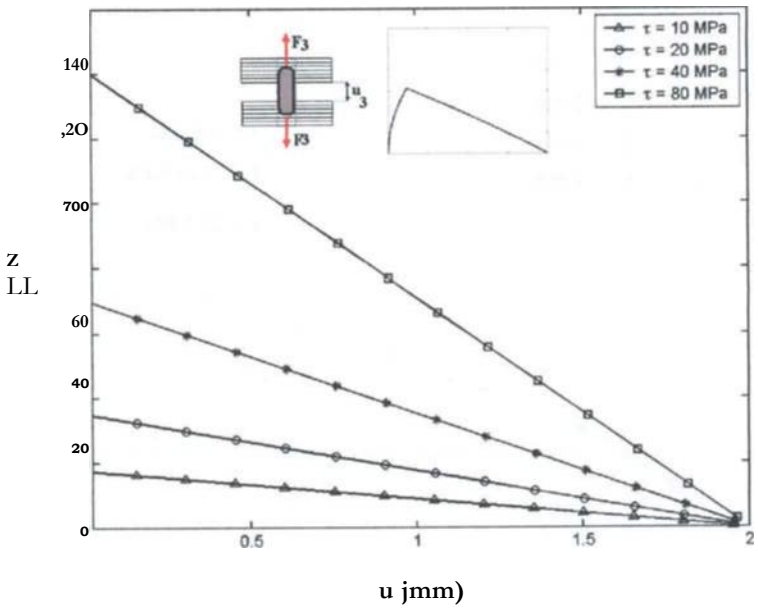

(b)

***Figure* 4.14** *Computed F_3-u_3 curves for single : fihrepullout with influence of different friction stresses: (a) Stable slip :one growth,- (b) .stalale frictional sliding stage.*

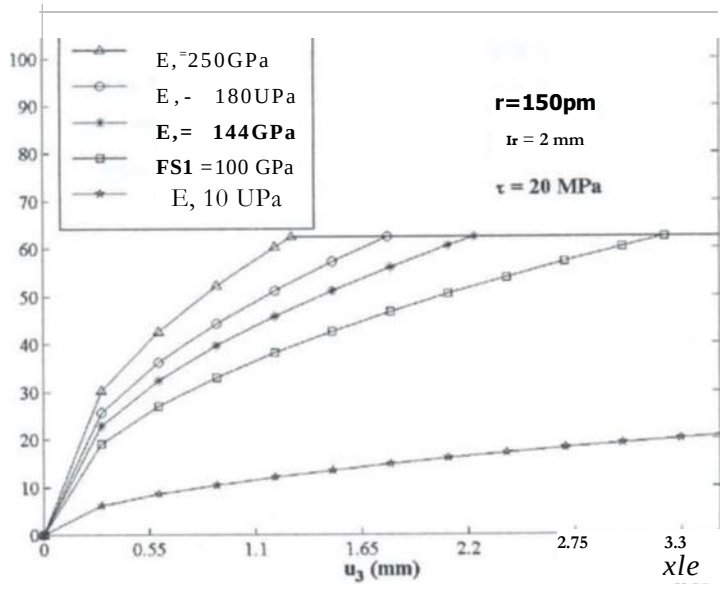

Figure 4.15 *Computed F3 u_3 curves for single -fibre pullout with influence of different -fibre axial moduli (Er): Stable slip lone growth.*

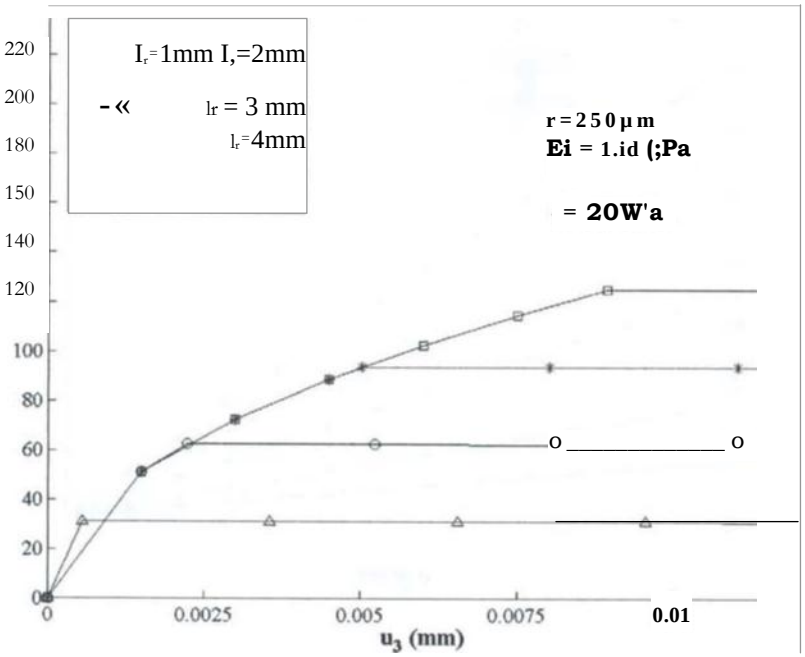

(a)

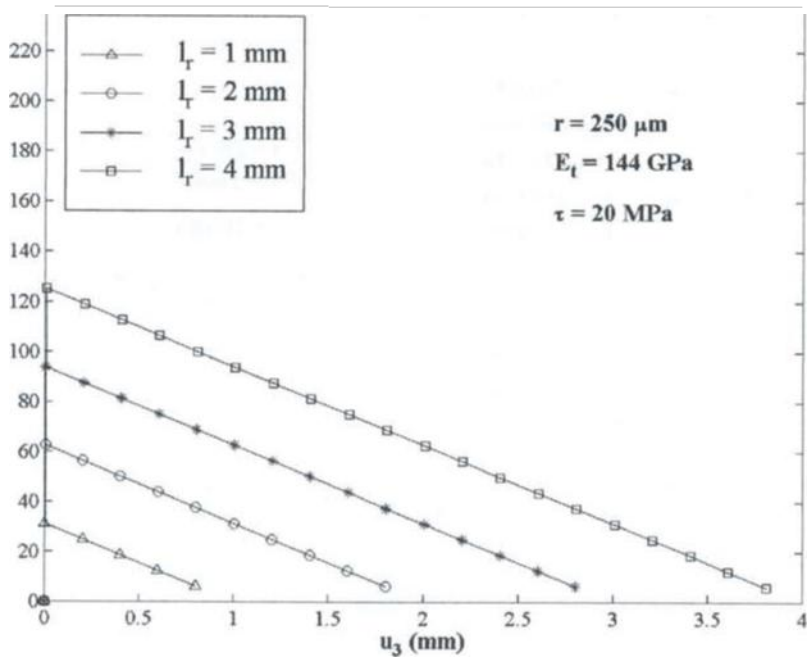

(b)

Figure *4.16* *Bridging laws for mode 1 loading conditions for d ferent =fibre embedding depths: (a) bridging traction during ,clip :one growth:* (b) *bridging traction during frictional sliding.*

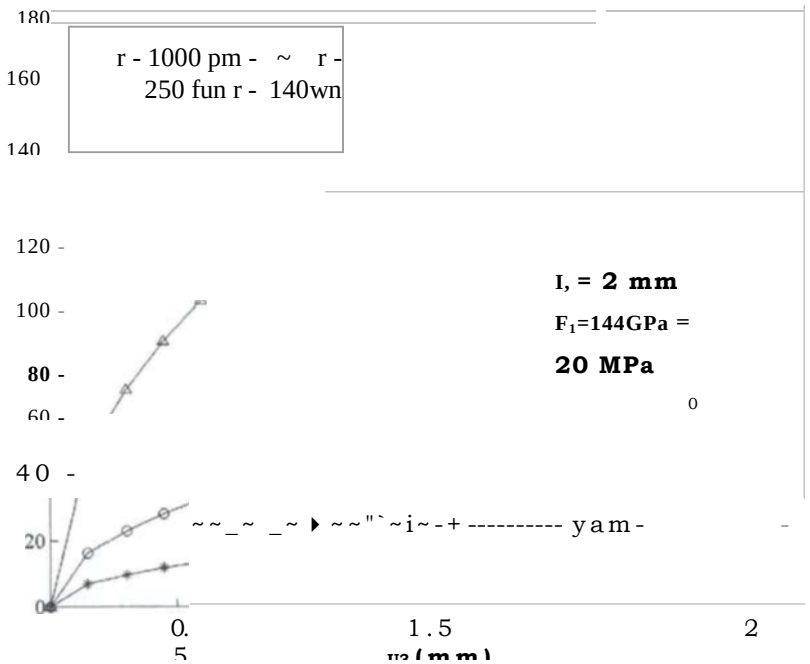

(a)

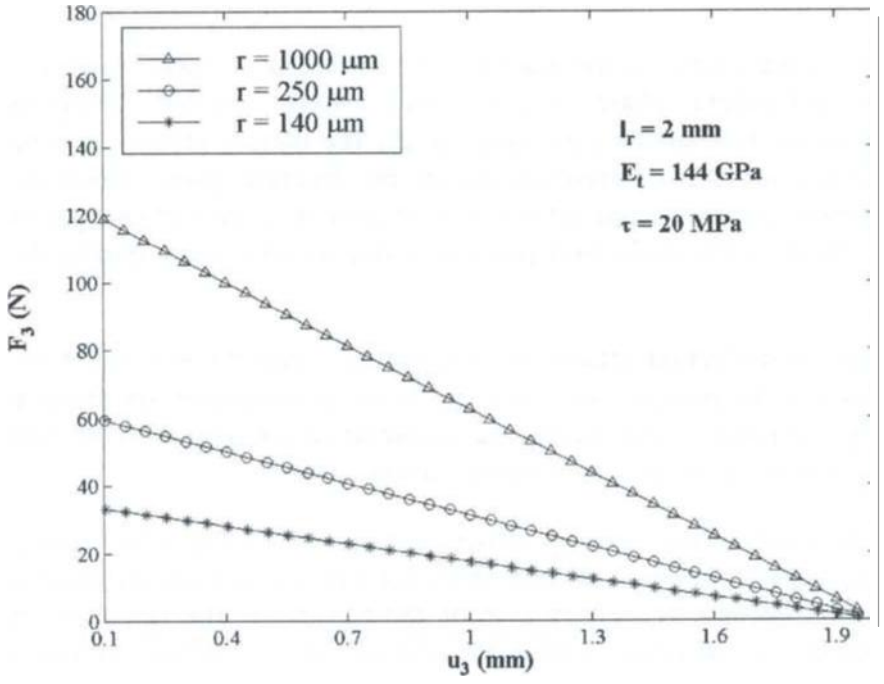

(b)

Figure 4.17 *Bridging laws far mode 1 loading conditions for different :-fibre radii: (a) bridging traction during slip lone growth;* (b) *bridging traction during frictional sliding.*

4.4.2 Mode II crack loading conditions

For the case of pure mode II loading conditions as well as for the mixed-mode configuration, it is not possible to work out a direct explicit relation $Fr\text{-}F_l\ Ju/$ analytically. In (Cox and Sridhar, 2002) assuming small $9o$ an explicit relation was touted for the pre-pullout regime. More conveniently the micro-mechanical parameters can be plotted with the aforementioned equations (4.9, 4.10 and 4.15, 4.18-4.20) as function of the assumed independent variables 8,, and o

The solution domain of the two variables is defined as:

$$0\ o \qquad {}^{5a}{}_{max} \tag{4-28}$$

$$0 < e_{\,0} s\text{--}0 \tag{4-29}$$
$$2$$

Equation 4-28 states that the axial stress developing in the z-pin must not exceed its axial strength, Equation 4-29 defines the z-pin maximum angle of deflection in the fracture plane (limit of model validity). From the condition $us\text{--}O$ that is valid for the special case of pure mode II condition, oo can be expressed as function of leaving only a) as the independent variable. As for the mode I analysis the pre-pullout phase ends when 1, l,., the equation of the pullout regime are then used for the parameters computation.

The deflection of the z-fibre at the fracture (Go) is shown in figure 4.18 for the pre-pullout phase, and pullout phase of a 0.25 mm z-fibre, inserted orthogonal to the fracture plane (0 -0). During the early stage of the pre-pullout phase it can be noticed that the deflection of the z-reinforcement in the fracture plane proceeds rapidly, reaching an almost constant slope after 1 mm of growth and attaining a maximum value of 18°. Most of the deflection process is due to take place during the pullout growth (cl_4).

When the angle of deflection attains 90° the model equations 4-9 and 4-10 become unstable, because of the presence of $cos(0\text{-}$ ***G)*** in the denominator; on physical ground this condition corresponds to the mechanical instability associated with the final pullout of the z-reinforcement (Cox, private communications, 2003).

The trend of the axial z-fibre stress is shown in figures 4.19 and 4.20. During the slip zone growth the axial stress in the z-fibre does not attain its maximum value as for the mode I condition, but due to deformation of the rod in the fracture plane described above it continues to increase within the pullout phase. When pullout phase is sufficiently developed, the slope of the curve becomes negative and ao decreases. The transition from the pre-pullout regime to the pullout regime is evident in figure 4,20, where co has been plotted against the deflection angle R.

The extension of the deflection zone (:o) is presented in figure 4.21 against the angle of deflection at the fracture plane (Go). It is interesting to notice that the percentage of the

z-fibre length interested by the deflection phenomenon is only W% for the pre-pullout phase and 25% circa for the pullout phase; in general it can be seen as a phenomenon occurring at the crack plane.

The graph also shows that a limit exists to the applicability of the model, since :n is predicted to decrease at some relatively high value of O_{11}. Since the plasticity and damage mechanisms associated with the z-fibre rotation are irreversible phenomena a negative slope of the $_{=0\text{-}00}$ curve can not be considered.

The limit of meaningful solutions generated by the model equations is then considered to be associated with the condition:

$$\frac{\partial \sigma_{11}}{\partial \varepsilon_{11}} \geq 0 \qquad \textbf{(4-30)}$$

Generally by the time the above condition is satisfied, the z-fibre pullout is in an advanced staged 1mm), with the axial stress $_{6n}$ that has already attained its peak value starting to decrease. Moreover as it will be also shown in chapter seven the above derived condition is never verified in most of the crack problems analysed within this work, and in general until the crack has reached its maximum specimen length, generating mechanical instability of the problem.

From figure 4,22 to 4.24 computational curves for the bridging traction force *F1 are* furnished. In figure 4.22 the bridging traction force F, increases its magnitude due to the z-fibre deflection in the fracture plane which tends to align the axial z-reinforcement fibres with the applied mode II load, using part of the axial stress o to bridge the crack.

When the deflection is around 60° the pullout is advanced substantially and the limit of validity of the model (eq. 4-27) has also been reached.

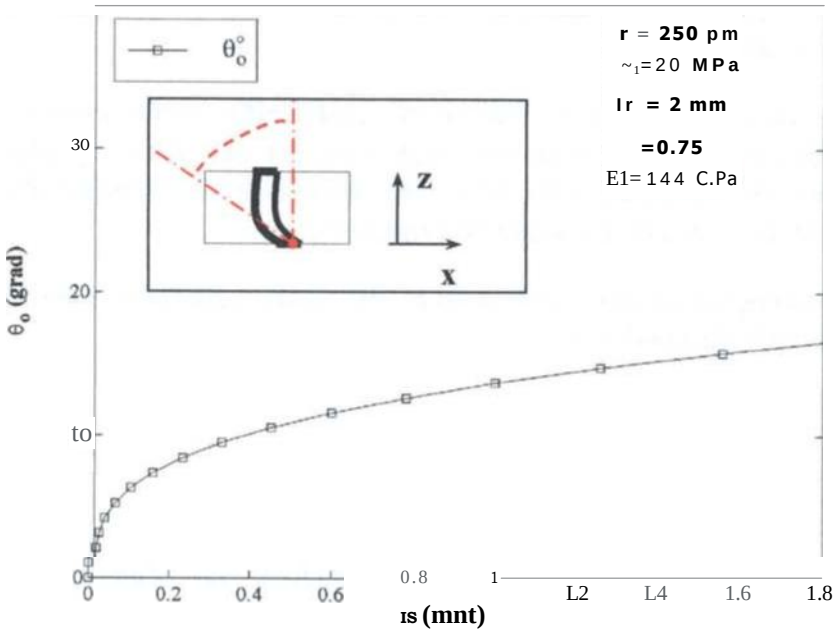

(a)

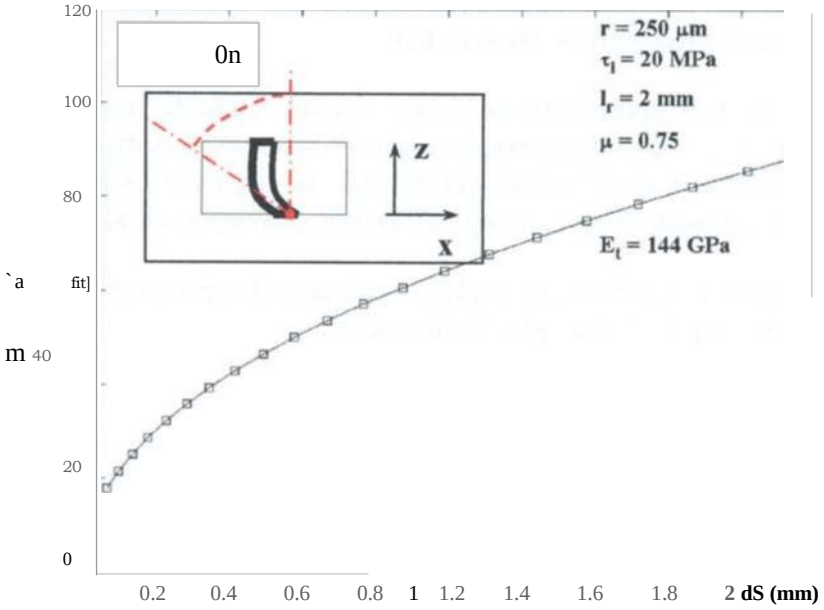

(b)

Figure 4.18 *Computational curves fhr the -fibre deflection angle 0o: (a) pre pullout phase;* (b) *pullout phase.*

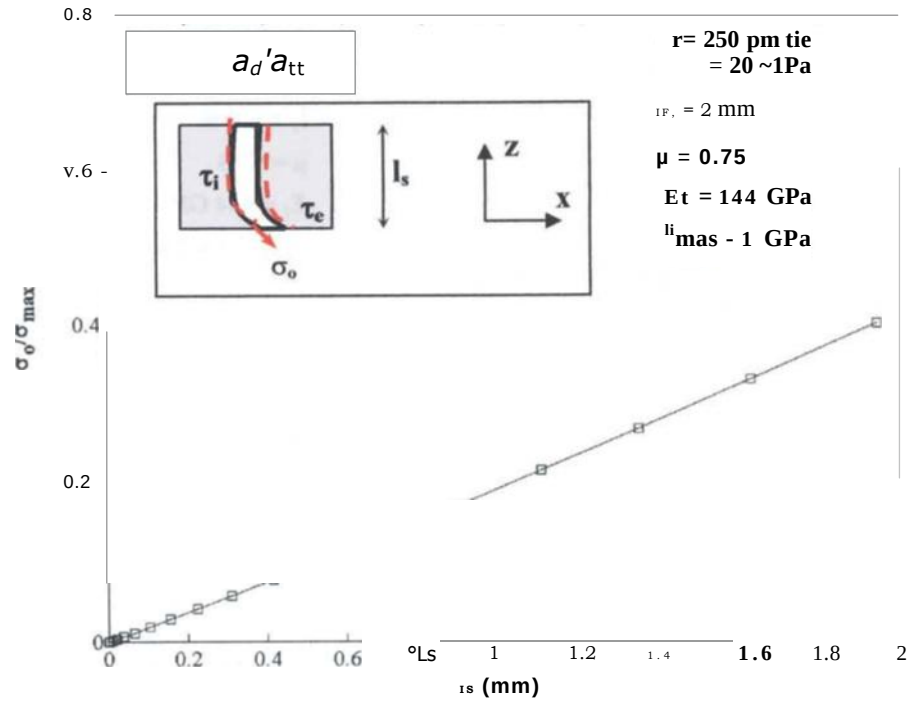

(a)

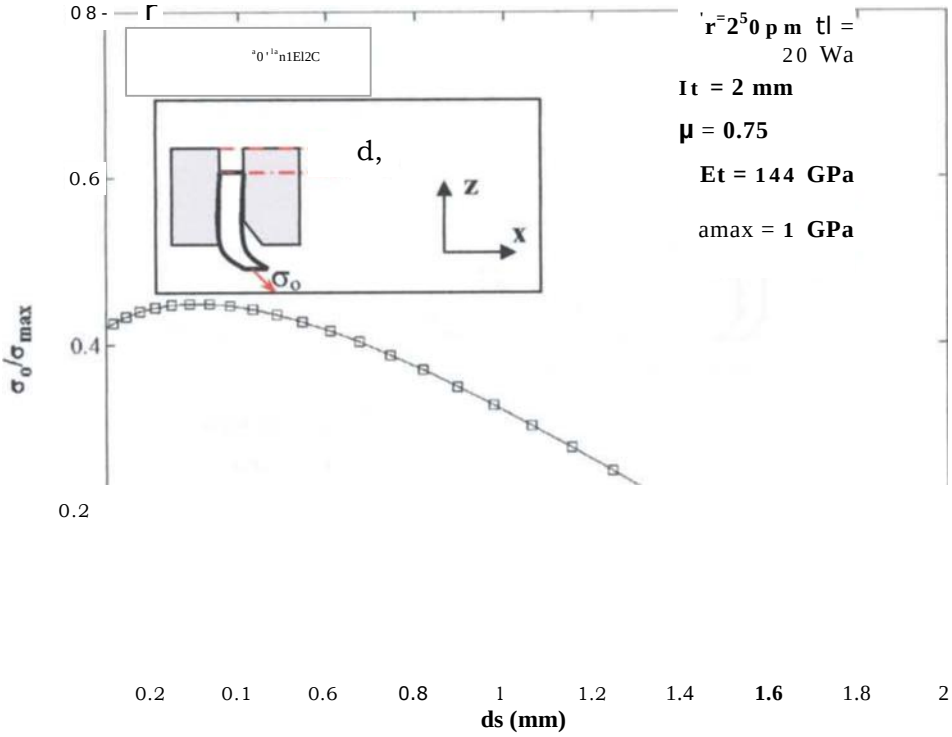

(b)

Figure 4.19 *Micro-mechanical model computational curve: (a) :-fibre axial stress aQ trend during pre pullout phase; (h) =fibre axial stress* co *trend during pullout phase.*

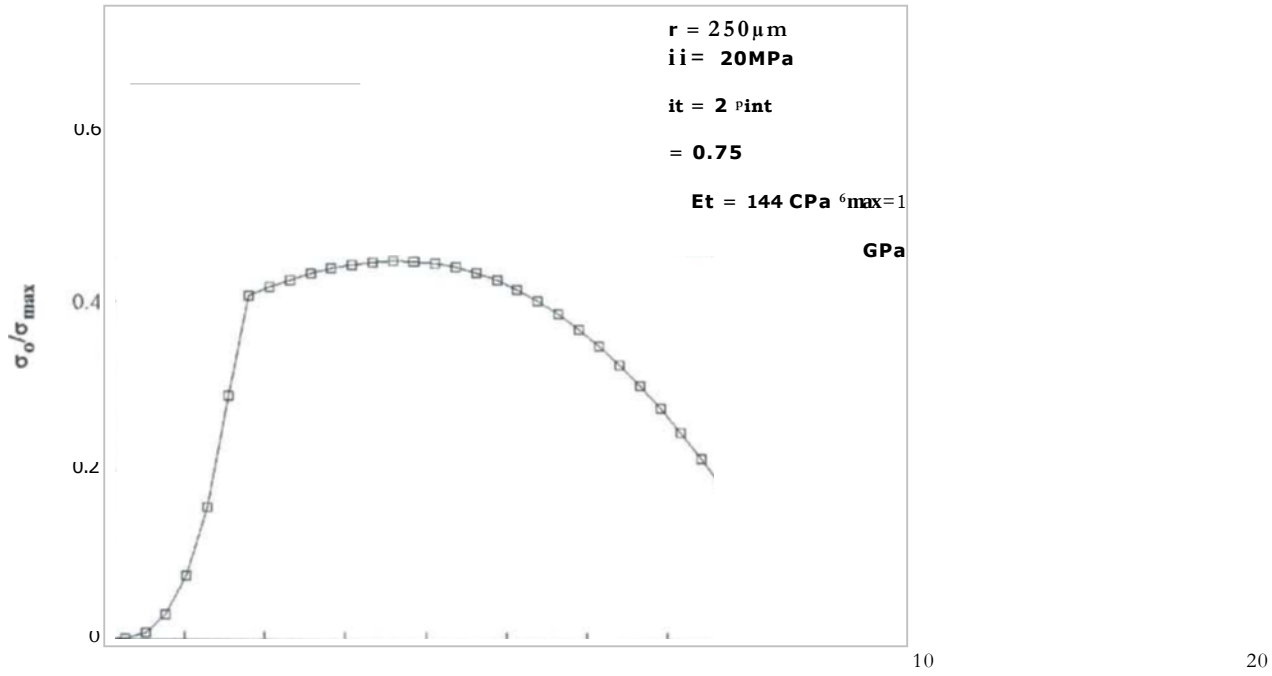

***Figure* 4.20** *Micro-mechanical model computational curve: axial =fibre stress Err vs. crack plane deformation angle 00 during pre-pullout and pullout phases.*

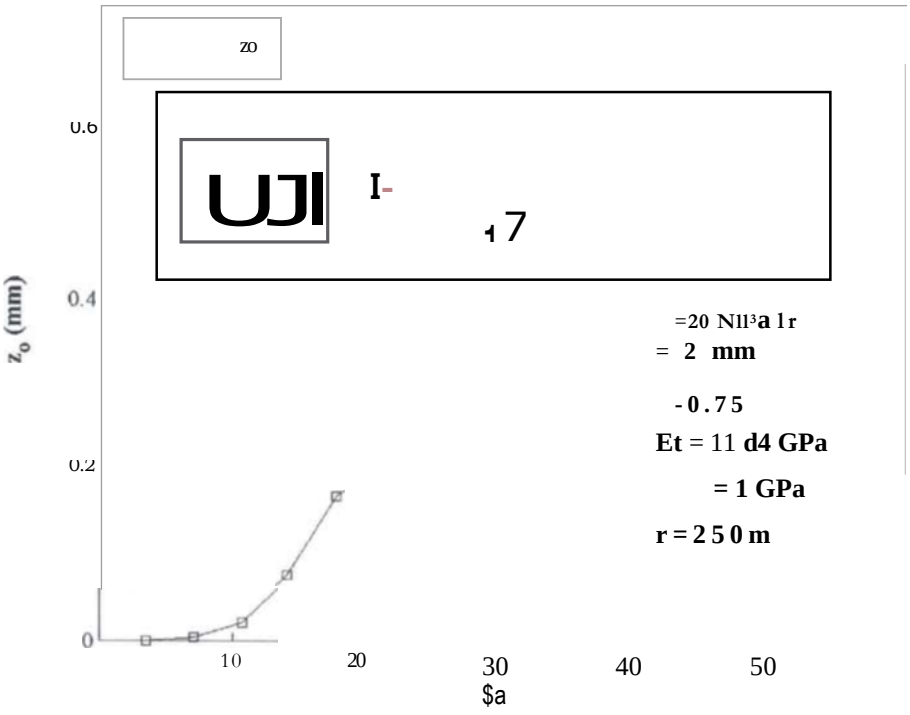

Figure 4.21 *Micro-mechanical model computational curve: fibre deflection length (o) vs. crack plane deformation angle (00) during pre pullout and pullotrl phases.*

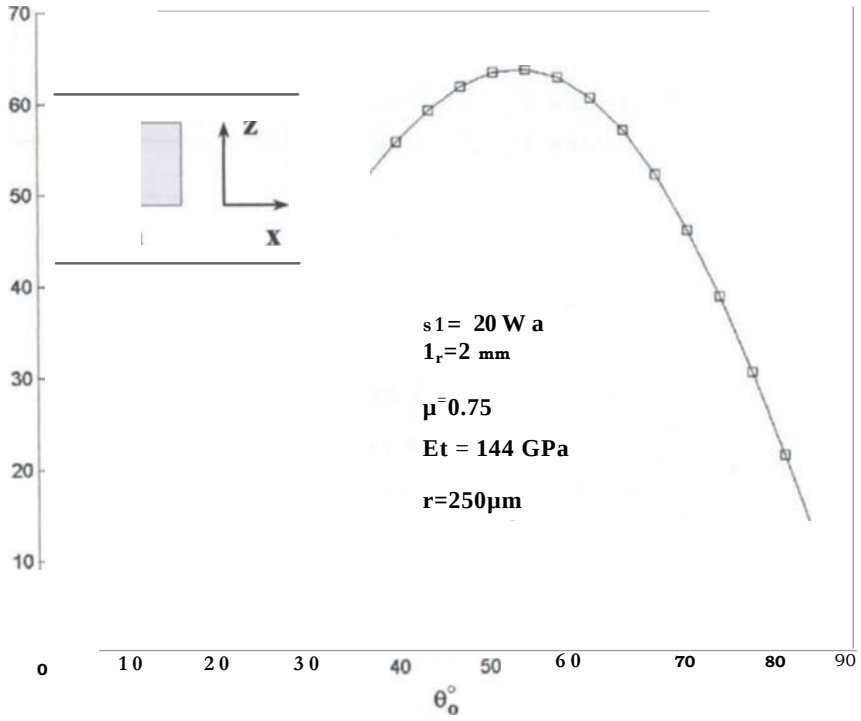

Figure *4.22*
Micro-mechanical model computational curves: fibre bridging force F1 vs. crack plane deformation angle 00 during pre pullout and pullout phases.

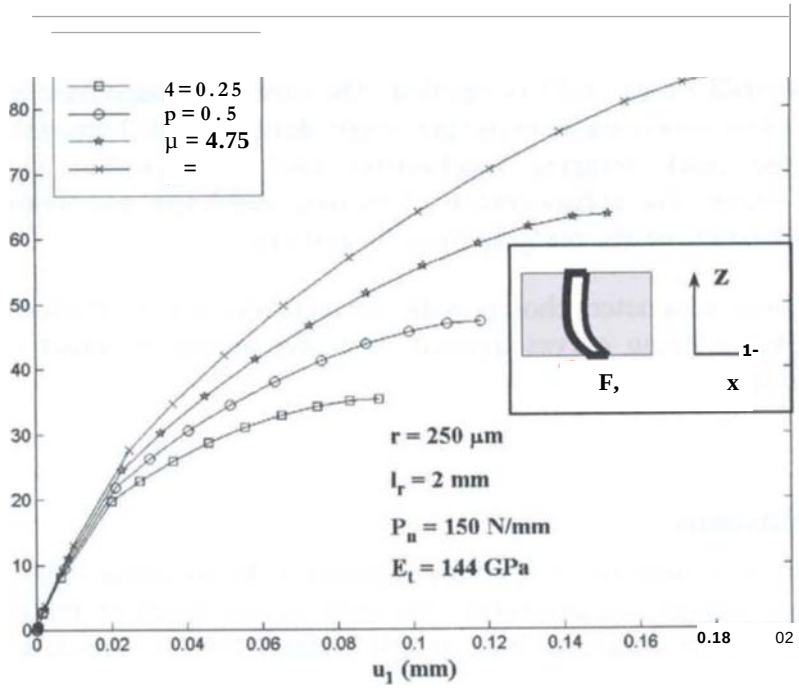

***Figure* 4.23** *Micro-mechanical model computational curves: ;-fibre bridging force FI vs. crack sliding displacement vector (u_1) during pre pullout and pullout phases for dJerent ass•umed friction coefficients.*

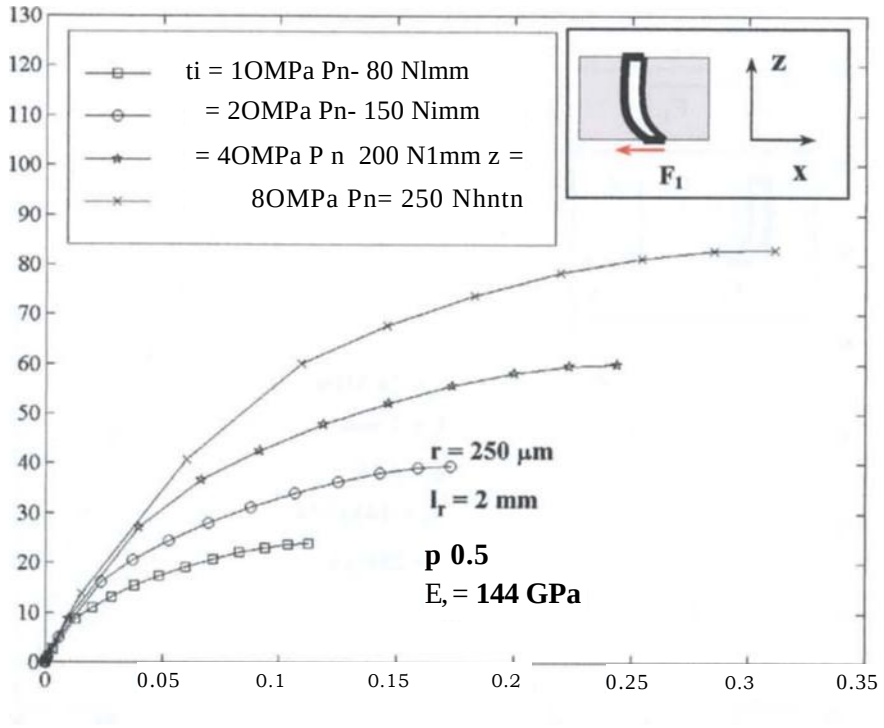

Figure *4.24* *Micro-mechanical model computational curves: . -fibre bridging force Fl vs. crack sliding displacement vector (ud during pre pullout and pullout phases for different assumed friction stresses z and punch loads P,,.*

The numerically derived bridging laws $_{1f(u_d)}$ for different z-fibre parameters are reported in figures 4.23 and 4.24. The computational curves have been plotted until the condition described by eq. 4-27 is verified. The orders of magnitude of the bridging traction forces seem comparable to the previously derived mode I traction *forces; on* the other hand the crack bridging mechanisms take place within a smaller crack displacement vector. The enhancements of friction coefficient and friction stress have both beneficial effects on the bridging force magnitudes.

The other physical parameters chosen in the computation $(l_r, r, Er, P_{,,})$ have been used to fit experimental bridging curves derived from the testing of small cubical z-fibre reinforced specimens.

4.5 Conclusions

A micro-mechanical analysis of a z-fibre bridging a delamination crack under mixed-mode loading condition was presented. The analysis was based on the implementation of an analytical model developed by Cox and Sridhar (2002) to simulate TTR bridging mechanics.

Energy absorbing mechanisms provided by z-pins during delamination crack bridging were outlined and, where possible, comparisons with published experimental observations were made.

A traction vector $T=i/u]$ was defined as the essential material property to simulate z-pin presence in the crack wake. This constitutive law relating the bridging traction vector (7), with the crack displacement vector (u) was defined as the "bridging law". Afterwards, constitutive equations and boundary conditions from the implemented analytical model were presented.

Numerical examples for z-fibre bridging laws under Mode I and Mode II loading conditions were given along with plots regarding relevant micro-mechanical parameters. Z-pin bridging traction forces against Mode 1 loads were shown to increase by employing smaller pin diameters, maximum pin insertion depth and by enhancing the friction stress at the pin-laminate interface. Due to the pullout failure mode, currently used carbon pins were shown to develop axial stresses well under the pin material axial strength. The condition of z-pin tensile axial failure during bridging rather than pullout could be obtained by introducing pin surface roughness and employing 280 pm diameter pins.

In the case of Mode 11 loading condition, bridging laws were derived numerically. The axial stress in the z-pin was shown to increase during the pullout phase due to the z-fibre deflection in the fracture plane; furthermore this deflection occurred only for a portion of the total pin length. Bridging forces were shown to increase due to the z-fibre alignment with the shear loads, with the axial stiffness of the rotated pins supporting those loads. It is therefore concluded that inclined z-pins would provide a better bridging force against shear loads having part of the axial stiffness already oriented towards the shear loads.

The implementation of the above derived bridging laws into the FE simulation could provide a robust numerical tool to assess z-fibre effect on composite structural components without the need to have refined and computationally expensive FE models to capture the micro-mechanics described in this chapter. The micro-mechanical level of analysis is therefore left behind, redirecting the analysis on the study of z-fibre effect on delamination growth.

Chapter 5

Analysis of z-fibre effects on mode-I interlaminar delamination of composite laminates

5.1 Introduction

Parameters that control damage development and failure of a composite component are, among others, the strength of the constituent materials of the composite lamina, the fibre-matrix interfacial strength and the ability of the composite to absorb energy under critical loads. The ability of the composite to absorb energy reduces the developed damage and the related material toughness secures its resistance to crack propagation. Thus, in a number of loading cases, toughness rather than strength is the key property of the composite material to withstand delamination growth (Gdoutos et al., 2000; Friedrick, 1989).

Consequently, one of the key problems in the design and analysis of this novel material is to characterize and quantify its effect on interlaminar delamination growth and fracture toughness of composite laminates. With reference to structural integrity, the analysis should assess the damage tolerance enhancement in a z-pinned composite structure.

The applicability of linear elastic fracture mechanics (LEFM) for studying delamination cracks involving large scale bridging (LSB) processes has been questioned since: the Fibre cross-over of the delaminated surfaces was noticed. This phenomenon was found in unidirectional fracture specimens under mode I loading conditions (Russel, 1987; Bao and Suo, 1992; Sorensen and Jacobsen, 1998b; Lindhagen and Berglund, 2000). Similarly it is thought that the rising crack growth resistance in z-pinned fracture specimens can only be explained through the analysis of the large scale bridging process generated in the crack wake, by z-reinforcements.

Mode I interlaminar fracture has been a topic for many researchers using the double cantilever beam (DCB) configuration and employing analytical approaches (Liu and Mai, 2001; Mabson and Deobald, 2000; Massaba and Cox, 2001; Dow and Smith, 1989). Analytical models solve the constitutive and equilibrium equations of the DCB by using the simple or shear deformation beam theories combined with discrete (Liu and Mai, 2001) or linear continuous bridging loads (Mabson and Deobald, 2000; Massaro and Cox, 2001) for the z-fibre simulation. As discussed in Chapter 2, under certain assumptions closed-form solutions were derived outlining the large scale bridging mechanisms and their effects on the strain energy release rate (G,) of the laminate. In these beam models boundary conditions applied at the crack tip usually underestimate the GI values at the crack front. Besides, when the bridging tractions are

expressed as functions of the crack opening displacement, even using linear functions the resulting crack behaviour is generally non-linear (MassabO and Cox, 2001). Moreover, the DCB arms of a z-pinned specimen are usually subjected to very large opening displacements due to large increments of the applied load required to propagate the delamination; this will introduce additional non-linear behaviour (Zhang et al., 1999a; Dransfield et al., 1994; Larsson, 1990). This chapter presents a detailed numerical analysis for studying the characteristics of delamination fracture with z-fibre effect. A finite element DCB model was developed using thick-layered shell elements to model the composite laminates and non-linear interface elements to simulate the through thickness reinforcements. The micro-mechanical bridging functions relating the delamination crack displacements and bridging forces, derived in Chapter 4 were used for the non-linear interface element behaviour. The analysis is aimed at the mode 1 model, that can be easily adapted to other single or mixed failure modes providing that the correct boundary conditions and micro-mechanical solutions are implemented

The objective is to develop and validate a design approach that combines the finite element method with the implemented micro-mechanical model so that the effect of z-fibre on delamination propagation may be predicted. The following problems have been investigated: numerical convergence of the computational model, effect of z-fibres on delamination growth and crack arrestment, the LSB mechanics, the stress field in z-pinned laminate during delamination growth, influence of z-fibre properties and insertion densities. The numerical solutions were validated against available experimental data (Cartie, 2000; Cartie and Partridge, 2001). It should be noticed that part of the work reported in this chapter has been formally published (Appendix A).

5.2 Delamination analysis

To characterise the onset and growth of delamination the use of fracture mechanics has become common practice over the past two decades (01 Brien, 1982; O'Brien, 1998; Martin, 1998). For composites, idealised as orthotropic or anisotropic materials, the strain energy release rate rather than stress intensity factors has been found convenient for delamination onset and growth analyses.

5.2.1 Strain energy release rate and interlaminar fracture toughness Ge

The linear elastic fracture mechanics (LEFM) assumes that the propagation of the delamination is self-similar with a uniform width (B) and calculates the strain energy release rate (SERR) **G** by solving the equilibrium of the loads acting on the delamination front.

The SERR value is considered a quantitative measure of the crack growth driving force and for a self-similar crack growth under constant load condition is defined as:

$$\frac{1}{B}\frac{dU}{da} \qquad (5\text{-}1)$$

Where (Ie is the total strain energy of the structure, B is the model width, and da is the incremental crack growth length, therefore $B\,da$, is the change of the crack area. The

negative sip is used since reduction in system energy results in an increase in energy available for external work (Friedrich, 1989).

The threshold condition for crack propagation is characterized by the critical value of G, termed Ge, which can be determined experimentally. The experimental methods used for the characterization of the interlaminar fracture toughness are typically based on three remote loading conditions: Mode I (opening mode), Mode II (shear mode) and Mode Ill (tearing mode). The critical SERR values Ge are consequently associated with the three crack loading conditions: Gk, G_{flc} and Gff_k. Figure 5.1 shows the three different loading conditions.

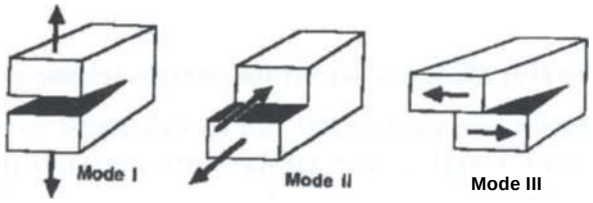

***Figure* 5.1** *Typical remote loading conditions .f r fracture specimens: Mode 1 (opening mode); Mode II (shear mode); Mode III (tearing mode).*

The following are the commonly used test configurations to evaluate the composite interlaminar fracture toughness: double cantilever beam (DCB) for Mode I (Wilkins et al.; O'Brien and Martin, 1993), end notch flexure test (ENF) (Carlsson et al., 1986) and its four point bend version (4ENF) (Martin, 1997), end-loaded split (EIS) laminate test for mode II, mixed mode bending (MMB) (Crews and Reeder, 1988) and single-leg bending (SI.B) specimens for mixed modes configurations.

The techniques applied to interpret the data recorded during aforementioned delamination tests may be grouped in two categories, compliance methods and direct methods and are generally classified as data reduction methods. The former can be based on either an analytical or empirical formulation for the compliance calibration; the latter uses the area enclosed within the loading-unloading curve to compute the critical SERR value.

Analytical compliance calibration methods can themselves be based on different assumptions: simple beam, transverse shear deformable beam on elastic foundations (Friedrich, 1989). Once the compliance expression has been obtained, the strain energy release rate G is evaluated by differentiation of the compliance expression with respect to the crack length:

$$G = -\frac{P'}{2B}\frac{dC}{da} \qquad (5\text{-}2)$$

Where *P* is the external applied load and *C* is the specimen compliance and *B du is the* incremental crack surface area. Equation 5-2 may have different expressions according to the mode component considered and data reduction method implemented (Gdoutos et al., 2000),

Among the international scientific community there is still an on-going effort to achieve internationally accepted test standards for interlaminar fracture toughness and perhaps more than the choice of test configuration and data reduction methods used is the interpretation of the property being measured that still remain an open question (0' Brien, 1997; 1998).

For through-thickness reinforced composite structures, the question of the properties being measured, the validity of data reduction methods and more generically the applicability of the LEFM are even more disputable because of the 3D architecture of the novel composites and because of the energy absorbing mechanisms associated with their bridging process. This challenging issue will be covered in Chapter 6 of this thesis.

5.2.2 FE computational techniques for strain energy release rates

In a finite element analysis, the total SERR can be calculated from two finite element solutions, one with a crack length a, and another with a slightly different crack length $a + A$ The SERB for a self-similar crack growth under constant load condition defined in equation 5-1 can be rearranged in a difference form:

$$G = \frac{1}{B}\frac{du}{da} \approx \frac{(1e^{*'} - LTA`}{BA} \qquad (5\text{-}3)$$

Where U r ' is the incremental strain energy of the FE model between the two runs, B is the model width, and d is the crack increment in the FE model, generally coincident with the mesh size at the crack front. This gives a value for the total SERR, $G_{,or,}$ and is generally known as the Crack Extension Technique (CET). Because a delamination may grow under a combination of different failure modes, the value of $G_{,1}$ should he broken into its components $G1,$ G1, and $G1l1$ (Martin, 1998).

Different forms of G-formulae were proposed in the literature to improve the computational efficiency. One of them is based on the virtual crack closure technique (VCCT) proposed in the work of Rybicki and Kanninen (1977), it is an approximate method that dispenses with the need for two analysis steps. The nodal forces at the crack front and the displacement behind were used to calculate the SERB for a cracked, isotropic domain modelled with four-noded quadrilateral, non-singular elements. Similar formulae were subsequently derived for higher order and singularity elements (Raju, 1987; De Roeck and Wahab, 1995). Referring to figure 5.2 the mode-I, mode-II and mode-III strain energy release rates are obtained by calculating the work required to close the crack from a d to a. Then the SERB formulae are:

$$G_I = \lim_{\Delta \to 0} \frac{1}{2A\delta_y} \int_0^{\Delta} \sigma_z(x, y, 0)\, w(x - A, y, 0)\, dx\, dy$$

$$G_{II} = \lim_{\Delta \to 0} \frac{1}{2A\delta_y} \int_y^{y+\delta y} \left| \int_0^{\Delta} \tau_{xz}(x, y, 0)\, u(x - A, y, 0)\, dx \right| dy \qquad (5\text{-}4)$$

$$G_{III} = \lim_{\Delta \to 0} \frac{1}{2A\delta_y} \int_y^{y+} \tau_{yz}(x - A, y, 0)\, v(x - A, y, 0)\, dx$$

$$G_{TOT} = G_I + G_{II} + G_{III}$$

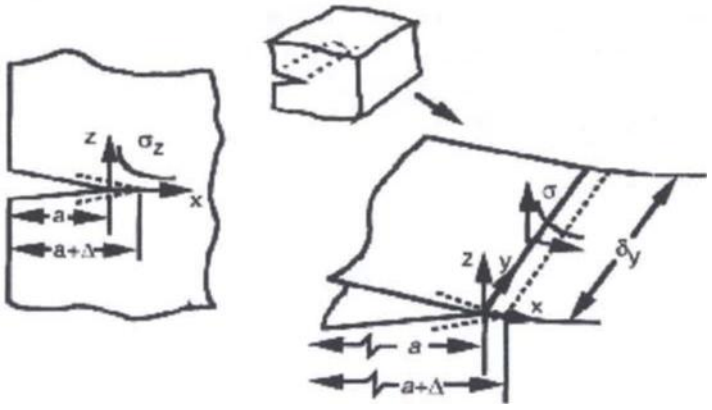

tal LYeck In 2D plate (D) 1 hrough-er.ck Erl 3D b y

frigun

Figure 5.2 VC.'CI' approach for G-calculation (Wang and Raju, 1996): Crack problem in *2D plate;* (b) *through-crack in 31) body.*

Where in equation (5-4) w, u, and v are the crack opening, sliding and tearing displacements, respectively, A, is the width of the crack front over which crack closure occurs, and σ_{zz} and τ_{xz} are the normal and shear stresses on the crack plane and ahead of the crack front. The physical interpretation of VCCT is that the energy released during the virtual crack extension by a length of 4 is equal to the work required to close the crack to its original length while the external loading remains unchanged.

From the general equations (5-4), different finite element formulae have been presented to compute the SERR from the FE model results for plane-strain analyses (Rybicki and Kanninen, 1977; Raju, 1987), 2D-Shell analyses (Wang and Raju, 1996; Raju et al., 1998a; 1998b; Glassgen and Raju, 1999), and 3D-solid analyses (De Roeck and Wahab, 1995; Davidson et al., 1995; Raju et al., 1996; Falzon et al., 1999; Krueger and O'Brien, 2000; Shen et al., 2001).

In the shell FE models for the VCCT computation, upper and lower sub-laminates where interlaminar delamination is predicted to grow are modelled as two separate plates. The intact part of the laminate is then modelled by enforcing displacements compatibility between the nodes of the upper and lower shells (figure 5.3).

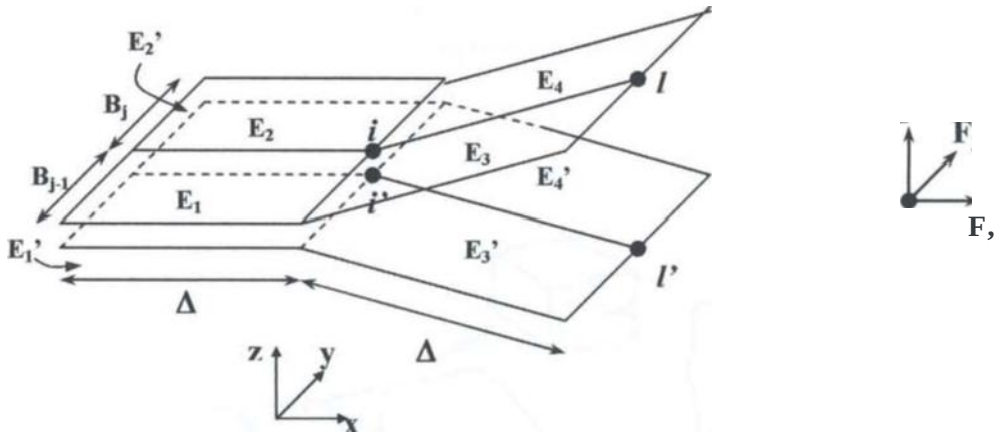

(a)

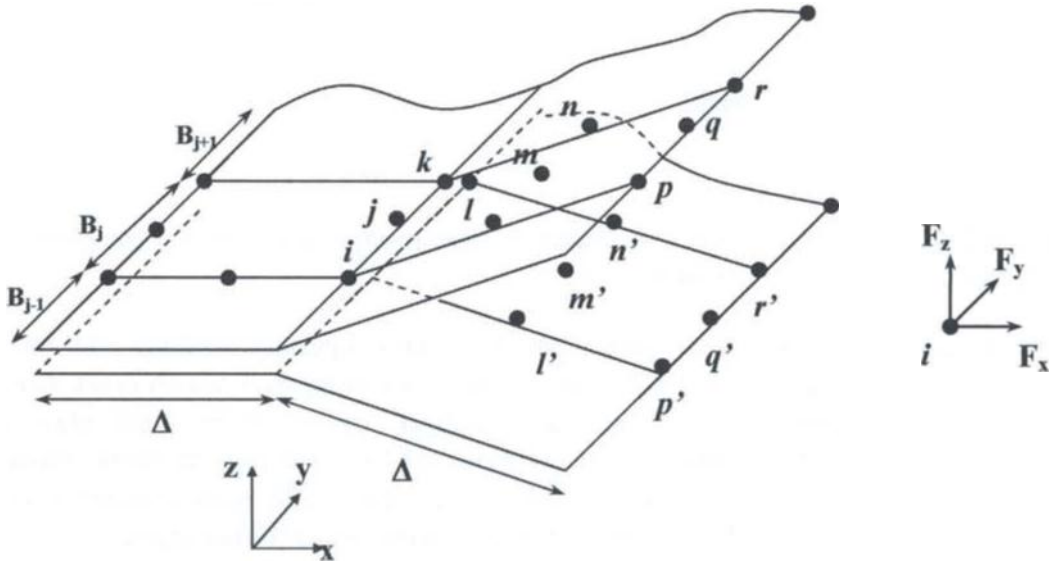

(b)

Figure 5.3 *FE mesh near the crack-front with upper and lower sub-laminates defined with coincident coupled nodes behind the crack: (a) fbur-noded linear shell element: (b) nine-noded shear defrormahle quadratic element.*

In conventional shell element models, the element nodes are placed at element mid-plane. In order to avoid complex constraints to tie the upper and lower sub-laminate

nodes, an offset distance of the nodes from the mid-plane of both upper and lower sub-laminates has to be defined. The implemented formulae assumed the nodes placed along the sub-laminates interface (Wang and Raju, 1996).

The SERR values can be calculated from the nodal forces at the crack front and the nodal displacements behind it from a single finite element analysis (figure 5.3). Typical SERR formulae for 2D-Shell elements are reported below. Depending on the element formulation and on the sub-laminates nodal constraints, different expressions for G may be found (Wang and Raju, 1996).

The node i on the delamination front belongs to the upper sub-laminate group of elements and the node i' is the corresponding node that belongs to the lower group of elements (figure 5.3a), Three forces (F_r, F_{ti}., 1;0 exist at each of these nodes. These forces at nodes i and i' can be computed from the element forces contributions from the upper *gaup of* elements *El,* E_2. E3, E_1 and lower group of elements E_2', E_3', E_4' respectively. The forces at node i and those at node i' are equal in magnitude and of opposite signs because of equilibrium considerations and are computed in a local crack reference system (figure 5.3a).

If the sub-laminates are modelled with four-noded shell elements then the VCCT equations are:

$$G_I = -\frac{1}{2B_i\Delta}\left[F_{z_i}\left(w_l - w_{l'}\right)\right]$$

$$G_{II} = -\frac{1}{2B_i\Delta}\left[F_{x_i}\left(u_l - u_{l'}\right)\right] \qquad (5\text{-}5)$$

$$G_{III} = -\frac{1}{2B_i\Delta}\left[F_{y_i}\left(v_l - v_{l'}\right)\right]$$

$$B_i = \frac{1}{6}\left[b_{j-1} + b_j\right]$$

For shell elements with quadratic formulations, the VCCT formulas take into account the contribution of the mid-nodes to the different G components. In contrast with the four-nodes element modelling the G-values can be calculated at all corner and mid-**nodes, like** i, .j and *k in figure 5.3b.*

The formulas for nine-nodes quadratic shell elements for the corner and mid-nodes can be written:

$$Gr_{\_} - \qquad (w - w. \qquad) + F, (wr - w_{l.} + \qquad 2B, A$$

$$2B.4$$

$$1\,\text{Ci} << (wq - wq) + F\ (w,,, - war_{IJ} \qquad (5\text{-}6)$$

$$= - \sim \underline{UI} \sim F(w,, - w -) + Fz(^{w},_{r} - w,, . \ 28/1_{k} \qquad r$$

$$Gr_{k}$$

$$G_{II}|_i = -\frac{1}{2B_i\Delta}\Big[F \quad (up - up) + 1;\ (u! - t!1$$

$$G_{II}|_j = -\frac{1}{2B_j\Delta}\Big[I \quad (wq - wy) + F,\ (u - um.1] \qquad (5\text{-}7)$$

$$G_{II}|_k = -\frac{1}{2B_k\Delta}\Big[I \quad (ur - ur) + {}_{Y} \quad {}_{-u,,} \text{IJ}$$

$$7111 \quad 2\blacksquare 7\ \text{p1}[\text{FS}\ (p - v\ p.) + F \quad y.(V! - V1)]$$

$$G\ i\ l\ l\ \Big[\ 7111\sim 1\ (v\ q -) + I\ (\ - \ )\text{J} \qquad (5\text{-}\$)$$

$$2\ B\ \ A \qquad\qquad {}_{j}7$$

$$\frac{1}{k}\text{-} \qquad (v - v\ r) + Fy(v - \text{vll}$$

$$G_{,1,}\ 2\ \ B\ z\ \ f\ r\ ;\ ,\ , \qquad\qquad \text{I}$$

Where B;, B_k and B_I are the equivalent widths apportioned to corner and mid-side crack front nodes, respectively, and are obtained by assuming that the computed SERR are constant *within each* layer:

$$B_i = \frac{1}{6}\Big[b_{j-1}$$

$$B_j = \frac{2}{3}b_j \qquad \{5\text{-}9)$$

$$Bk = 6\{bj. + b$$

$$\text{J+l}$$

In the formulation of the above presented G-formulae it is assumed that the upper and lower sub-laminate shell elements have independent rotations, and therefore the interface nodes can not carry any moment, which means that the magnitude of the individual moments at the upper group of nodes *i, j, k, e, f* and g and at the corresponding lower group i', j', k', e', f and g' are both identically equal to zero.

The above presented formulae were successfully implemented in skin-stiffener debond analyses, showing good agreement with 2D plane-strain analyses and fully 3D analyses, and outlining the constraints to be implemented among the interface nodes at delamination front (Wang and Raju, 1996; Raju et at., 1996; 1998a; 1998b; Glassgen and Raju, 1999).

In the work by Wang and Raju (1996) good correlation with plane-strain values was found for delamination length a 2t>l, whilst for values of a'21<1 some convergence problems for the G-values were encountered. This was due to the fact that plate model assumption is not valid for small delamination length. Good correlation with SERR values computed with 2D plane strain FE analyses was also proved in the work by (Raju et al., 1998b) using shear-deformable shell elements for the FE plate delamination model.

$E/^{dsu3}$

cix $x=D$

Where, $u3$ & where the bri(

In the case o problem are discontinuous also discontin

Concluding this section about the application of the VCCT technique to FE using shell elements, several points must be underlined:

- These formulae allow the calculation of the individual mode SERB tampon' G, , G,, f) from nodal forces ahead and crack opening displacements behind t front in a local crack coordinate system.
- Providing the FE mesh is sufficiently refined at the delamination front o element run is sufficient to accurately compute the SERR components.
- The FE mesh must be symmetric on the crack plane and about crack front, small values of A which is the element size at the crack front and usually coinci the crack length advancement.
- Nodes of the upper and lower sub-laminates are placed along delamination (offset).
- Kinematic constraints have to be defined between the upper and lower group [allowing independent rotational degree of freedoms and coupling translational c freedoms.
- Higher order transverse shear element formulation should be implemented to crack tip transverse-shear deformation (Raju et al., 1998b).

The use of VCCT also avoids the need to employ special crack tip element entail the shifting of mid-nodes to the quarter point position relative to the c These elements assume a square-root stress singularity, but this does not repro true nature of the stress singularity for a delamination front in composite s (Shen et al., 2001).

5.3 Problem Statement

5.3.1 Large scale bridging

When a delamination crack develops, z-fibres form a bridging area at the cra that shields the delamination crack front from the interlaminar stresses. Thy bridging effect and its mechanisms will modify the crack-tip stress field and re crack propagation rate.

It is already well established that in-plane fibre cross-over bridging can enh crack growth resistance with increasing crack extension. The rising crack resistance is usually described by the concept of R-curves, i.e. the crack resistance Gi as function of the crack extension u (Russel, 1987; Bao and Suo, 1

There have bt described in (Mai, 2001).

In this study, methods. In f bridging zone generically as

When the bridging is restricted to a zone that is much smaller in length 1 specimen dimensions (small scale bridging), the rising crack growth resist curves) can be regarded as a material property. However, for many crack problems the fibre bridging length (the length of the crack where bridging oc[be comparable with or exceed the specimen dimension. This is called lai bridging (LSB) (Sorensen and Jacobsen, 1998a; 1998b).

In linear i
required tc
consequen
damage zo
the crack-t

Thus in si
LEFM the,
total crack
controlled
(Sorensen
2001). The
geometry.
toughness

As far as t
should be

$$^{o}z(^{x})^{=}\ 0\ ,(\ x,c,I),P,u,El)$$

where, c is the z-fibre density, I) the length of bridging zone involving many i pins, *P* the applied load, *u* the displacement vector within the LSB area, *El* th rigidity of the laminate, and P_ the bridging load (force or moment) of a sink that itself is a function of many parameters depending on the micro-mechani used:

$$= \sim'.\ (^{u`},^{0},0, r, r_{o}, \mathrm{c}_{o}\ , E\ ,\ ,r\ ,\ _{AA,}, Ir\ )$$

where, u' is the displacement vector of the *i-th* z-fibre cross section at del wake, 9 z-pin rotation in the x-z plane, q z-fibre insertion angle, r frictit stress at the z-fibre and laminate interface during frictional sliding, $_{r0}$ shear f due to sliding displacement (u_i), cr the axial stress of the z-pin rod, *E*, the modulus of z-fibre, r z-fibre radius, A, cross sectional area of z-pin, and insertion depth into the laminate (see figure 4.11).

5.3.2 T **h**

The doubt
study the t
arm can b
simulating

For the be
are assum
beyond are

$$_{r}d^{4}u$$

$$p\ i\ +$$

$$[\mathrm{LC}^{4}$$

$$El\ '1\ _{u3}$$

$$dxa$$

The bound

w(0) th

$$EI\frac{d^{2}u_{3}}{dx^{2}}$$

$$EI\frac{d^{2}u_{3}}{dx^{2}}$$

5.4 Modelling procedures

5.4.1 Model for z-fibre bridging mechanics

With z-pinned laminates, a challenging problem facing the modeller representation of the z-fibre behaviour during delamination growth. Within the mechanisms of z-fibres bridging a delamination crack and the computation of the bridging laws, have been described in detail. It was prof from the modelling point of view, those complex bridging mechanisms incorporated into a bridging function *Flu]*, that was the relation between the traction force vector (I) acting on the fracture surfaces and the crack displacement vector [u].

Under the mode I loading condition and with the z-fibre having an insertion ar and a circular cross sectional area as reported in the manufacturing data (Carl z-fibre debonding and pullout resisted by *friction was* presented *as* the mechanics and a set of computed force vs. deflection $(F_3\text{--}u_3)$ curves was discu

Therefore the micro-mechanical model function presented in equation become:

$$+1\sim\_ = {}^{F};(^{u}:;)$$

This is a mono-dimensional function that relates the opening displacement (i force exerted along the z direction in the crack reference system.

To implement the previously derived micro-mechanical solution into an FE pins presence in the delamination wake was modelled by an interface *(('C)MRIN39)* available from the ANSYS element library. This is an I D ele the capability of taking generalized non-linear force-deflection relati longitudinal option provides a uni-axial tension-compression element with u

degrees of freedom at each node, i.e. translations in the x, y, and = directions; no bending or torsion is considered. The torsional option is a purely rotational element with three degrees of freedom at each node: rotations about the nodal x, y, and z-axes, no bending or axial loads are considered. The assumption that the z-reinforcement bending stiffness is negligible is believed to be valid within the range of laminate thickness considered in this study (2mm 5 2t 5 7 mm).

The element is defined by two initially coincident nodal points and a generalized force-deflection curve *1(u)* which is defined in a local reference frame following delamination crack growth. The F(u) relationship is obtained by assigning a discrete number of vector points */F, u],* representing the computed bridging laws presented in Chapter 4 (figure 5.5).

To avoid numerical convergence problems during the non-linear analysis a limit was imposed to the minimum change of deflection for the interface element between two iterations i and i ' 1:

$$u_{;}{}_{1} - u_{;} > \mathrm{du}_{.,,,}$$

$$\mathrm{d} = \frac{u_{\mathbf{max}} - u_{\mathrm{nlin}}}{\quad} \qquad \textbf{(5-19)}$$

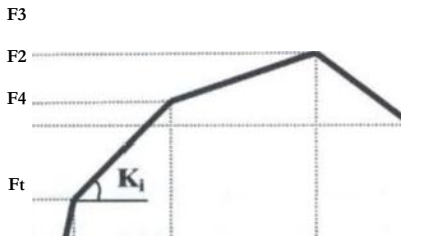

Figure 53 *Interface element: active stiffness at i-th iteration.*

Where u,,,,, and u,,,;,, are the maximum and minimum displacement vector respectively. No stiffness was considered for negative deflection which on physical ground would mean interpenetration of the delaminating DCB arms.

The interface element nodal forces exerted on the crack wake on the generic P /' node at the iteration can be written as:

$$\begin{aligned} &(1)\mathrm{F}'(\mathrm{uj})'\mathrm{i} = 0 \qquad u'l_i = 0 \\ &(2)F'(u')_{I,} = \mathrm{F}\,3(\mathrm{u}\,3) \quad 0 < u' \qquad {}^{\mathrm{tf}}{}_{\mathbf{max}} \\ &(3)\mathrm{Fj}(\mathrm{u}')\mathrm{I}, = 0 \qquad u' \end{aligned} \qquad \textbf{(5-20)}$$

In the above equations the force P' acting on *the j-th* node is oriented along the local direction (z) and assumes different expressions: (I) when the damage is not yet propagated into the z-pinned field, the interface element nodes are coincident, then the relative displacement is zero, and the bridging force is zero too; (2) when the damage propagates, the coincident upper and lower sub-laminates nodes are un-coupled and the relative displacement vector is greater than zero, causing the activation of bridging force **F3;** (3) when the total nodal displacement reaches a critical value, the bridging reaction force drops to zero simulating total pull-out of pins from the laminate. The force-displacement relation is given in the local nodal coordinate system.

During the stiffness pass of a given *r-th* iteration, the interface element uses the results of the previous iteration to determine which segment of the input force-deflection curve is active, to work out the active stiffness value. During the stress pass, the deflections of the current equilibrium iteration are examined to see whether a different segment of the force-deflection curve should be used in the next equilibrium iteration. At the i-th iteration for a displacement between ut and v_2 the active stiffness value K_i is implemented (figure 5.5), whilst if the displacement vector exceeds a maximum value defined by the bridging law the interface element stiffness is set to zero again.

A specific MATLAB subroutine was developed by the author. It allows the calculation of the micro-mechanical parameters presented in Chapter 4, and the generation of an input command list for the finite element analysis, automatically defining the interface elements. Another subroutine operating directly in the ANSYS environment specifies z-fibre density, diameter, dimensions of the 3-D reinforced area and then applies the non-linear bridging laws to the nodes of an already meshed laminate model (Appendix C).

5.4.2 DCB finite element model

Figure 5.6(a) shows a DCB specimen reinforced by z-fibres. The total externally applied load is P; it is applied on the DCB either using piano hinges or through special aluminium end blocks bonded on to the surface of the laminate, in order to secure load application across the same line. The total displacement is S, and the initial crack-front position is placed at a_0 and is introduced in the composite test specimen by placing a starter thin film (Teflon, Kapton) at the mid-plane of the composite laminate during the lay-up stage of the composite manufacturing (film thickness = 125 pm). The specimen dimensions are: laminate width B, length L and total thickness 21. The crack growth increment is identified by Au, and the coordinate system is oriented with the x direction along the length of the laminate beam, the y along its width and the L through its thickness.

An FE model was created as shown in figure 5.6(b). The numerical model consists of two main mesh sizes: a coarse mesh for the undamaged part and a fine mesh in the delamination growth zone. The area where interlaminar delamination was expected to grow was modelled with two sub-laminates having the nodes coupled with an offset position at the delamination interface. The positioning of the z-fibre elements at the interface of the DCB sub-laminates is also indicated in figure 5.6(b).

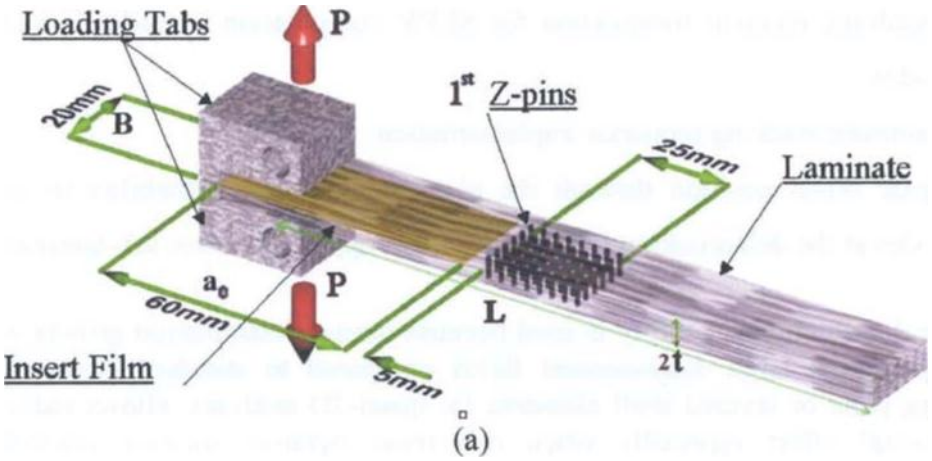

109

(a)

(b)

Figure 5.6 ***(a)*** *Schematic of double cantilever beam* (DC:R) *specimen with :-frhres*[13]*. Notice the distance for the first :pin row; fib) FE model of DBC specimen, with :domed interface element area.*

The distance between two consecutive interface elements depends on the assumed z-fibre density and diameter. Table 2.1 in Chapter 2 showed typical z-pin diameters and standard z-pin densities that were used for the simulation. The non-linear layered shell element (Shell-91) from the ANSYS element library was found suitable to model the composite laminate. It has several useful properties compatible with the VCCT computations presented in section 5.2,2, such as:

Shape functions with transverse-shear deformations included.

Large deformation capabilities. Suitable for highly non-linear analysis.

13 Courtesy of M.Troulis, Advanced Materials Department, Cranfield University.

Quadratic element formulation for SERR computation at mid-side and corner nodes.

Laminate stacking sequence implementation.

Node offset position through the element thickness. Possibility to place the nodes at the delamination interface between upper and lower sub-laminates.

The large deformation capability is used because during delamination growth z-pinned DCB experiences large displacement fields compared to standard unpinned B. Employing plate or layered shell elements for quasi-3D analyses, allows reducing the computational effort especially when non-linear iterative solution algorithm are adopted.

5.4.3 DCB FE model assumptions and boundary conditions

Using the advanced programmable ANSYS language a user friendly interface was developed in order to easily handle several geometric and physical FE model parameters (figure 5.7). The length (L), width (13) and half-thickness *(t)* of the model, external starting load (P) which is given as imposed constant displacement in *mm,* the initial crack length (a_f,), the mesh dimensions close to the crack front (size is a fine mesh) and within the undamaged part of the model *(size2* is a coarse mesh). The parameters *LI* and *1.2* define the length of the refined mesh region ahead and behind the crack front respectively. The material model of the laminate can be implemented from a defined material library.

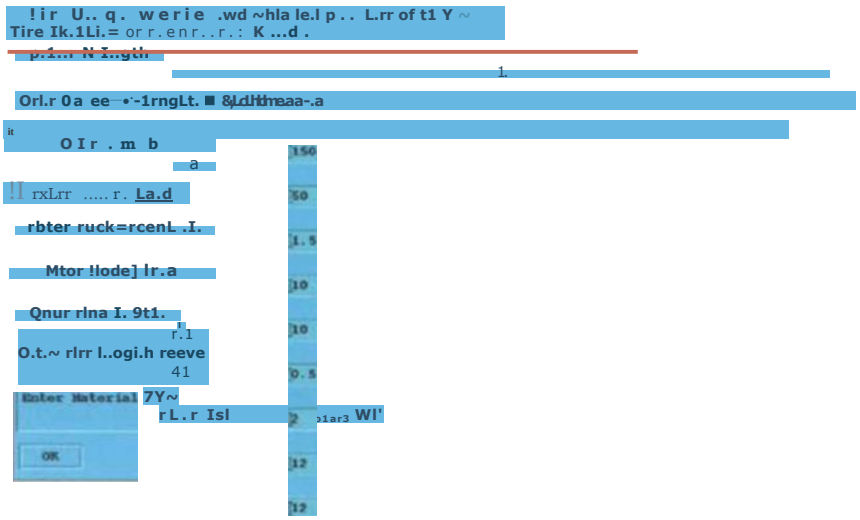

Figure 5.7 *The implemented ANSYS graphical user interface for the 1'L- model.*

The Shell-91 element has the layered option available to define different lay-up configuration, nevertheless the homogenization approach was used for the element

material properties because of the constant d° orientation of the DCB plies in the experimental analysis.

In case of multiple delaminations among different ply interfaces or crack splitting, this assumption would not be appropriate, nevertheless in a DCB experiment the delamination is assumed to grow along a defined constant interface with no aberration or splitting of the crack. Therefore the assumption of two homogenized orthotropic sub-laminates having only one common delamination interface, with kinematic constraints relating the interfacial nodal displacements, is thought to be appropriate for the current simulation.

The upper and lower sub-laminates have the displacement matrix [(1) simplified by the coupled field assumption. The number of independent degrees of freedom is limited imposing constraint equations among the nodes of the upper and lower sub-laminate:

$$= \quad \mathrm{k} \qquad \textbf{(5-21)}$$

At the i-th non-linear iteration, during the displacement matrix computation only the degree of freedom of the upper sub-laminate generic node j, u'' are effectively calculated whilst these calculated values are then assigned to the dependent degree of freedom of the lower corresponding sub-laminate nodes k included in the coupled field, kI *to*

The model boundary conditions are summarized in the following table.

Table S-1 *Applied boundary conditions for the DCB specimen.*

$x=0$	$-\frac{B}{2}\le y\le+\frac{B}{2}$	0 5 x 5 L $y=\pm B$	$x=L$
$ux=uy=u,\ =0$		$u\ y,\ =0$	u, = coast
	$=0$	$Bs=0$	

Cylindrical bending boundary conditions were imposed, whilst the DCB end is cimped to avoid numerical errors for an insufficiently constrained model. Multipoint constraint equations were applied to the nodes placed al the DCB free ends to impose equally applied displacement. Using the ANSYS programmable language, several subroutines were developed and implemented into the main code to model the following features: z-fibre material model, auto-meshing, computation of GI with the technique described in section 5.2, non-linear iterative solution, and delamination growth simulation (Appendix D).

5.4.4 **Failure criteria implementation**

The SERR values computed at the crack front with the VCCT described in section 5.2 are then implemented into a fracture mechanics failure criterion which in a generic polynomial expression can be written:

$$\frac{G_I}{G_{,}} + \frac{G_{11}}{G_{m,}} = 1 \qquad (5\text{-}22)$$

Equation 5-22 incorporates the different mode ratios and the relative importance of one of the two terms on the left hand side of the equation can be defined via the exponential coefficients m and n .

The critical material fracture toughness values $(G_{k.} , (h)$ of the un-reinforced composite material *are* used also for the z-pinned models and the reasons for this assumption are examined within Chapter 6.

In the simple mode I DCB configuration a simple expression for the failure criteria can be made $(n - 1) :$

$$G:^{'E"r} \sim G1c \text{ ---> } Failure(damage\_growth) \qquad \textbf{(5-23)}$$

The term is computed by the FE analysis using the VCCT. Experimental analysis has to be carried out in order to establish the fracture toughness values of the unreinforced composite material.

5.4.5 The computational algorithm

A displacement-controlled non-linear FE analysis was performed with the full Newton-Raphson option adopted in order to reduce the numerical error. A standard force and moment convergence criterion was used for the Newton-Raphson method and several other parameters can be controlled and defined properly in order to optimise the iterative numerical solution, computational time and accuracy[1'].

The solution algorithm starts with an applied initial displacement on the DCB arms that brings the model up to a SERB value at the crack front close to the critical delaminating value but still under it (figure 5.8).

This assumption on the solution algorithm was due to the experimental curves observations: the composite specimens showed a linear behaviour up to the point where delamination started propagating and then a detailed non-linear analysis in this first part of the process was computationally expensive in terms of iterations and redundant in terms of results.

The solution-algorithm then mainly performs two separate tasks: (I) if the condition described by equation 5-23 is not met then the applied displacement is increased by a value and the GI value at the crack-front are re-computed, (2) if the failure criteria is

1' **ANSYS Structural Analysis Guide, Chapter 8**

satisfied then the nodes at the delamination front are uncoupled, while keeping the applied displacement unchanged, and a new iteration is performed starting from the previous configuration. Of course the delamination increment (z) is a function of the element mesh size near the crack-front (figure 5.8).

The restart algorithm executes several commands: reloading the computed force-displacement and the derived stress-strain matrices from the previous converged sub-step analysis, updating the global model stiffness matrix [KJ because of the new boundary conditions introduced and the increased load, solving the new sub-step. During the solution process the model also checks for sub-laminate failure and for maximum delamination length propagation.

The output data stored automatically during the *i-th* non-linear iteration are: nodal SERR values at the delamination front for each crack length and for every single sub-step, average SERB values for every sub-step, applied displacement value for every sub-step, and computed reaction load at the DCB end. A typical numerical model specification is given in table 5.2, and the computational model is shown in figure 5.8.

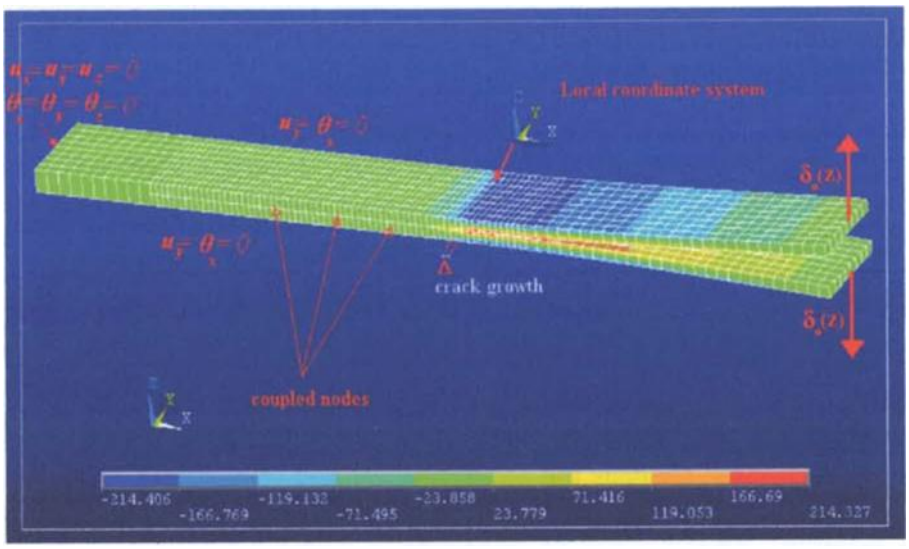

Figure *5.8* *Finite Element computational model for a pinned DC'B.*

The local coordinate system is placed at the delamination front; the imposed displacements of the laminate arms are iteratively increased and the coupled nodes at the sub-laminate interface are decoupled at the delamination front (figure 5.8). The contour plot i n figure 5.8 refers to the o, stress component in the laminate during delamination growth.

Table 5-2 *Typical parameters in the I E model*

DOF	**Nodes**	**Shell-91**	**Interface**	r	Si	**Nsun**	Ni	a
10318	4432	554	10	4 mm	0.2 mm	128	445	30 mm

Table 5-2 provides typical values: the total number of degree of freedom (DOF) and nodes, total number of shell-91 layered elements and interface z-fibre elements (e.g., c = 0.5%), applied initial displacement (~) to the DCB arms, and the incremental added

displacement (A), the total number of sub-steps required ($N_{s,r}n$) to propagate the damage for *a,* with a total number of Newton-Raphson iterations Ni.

Figures 5.9 shows FE delamination growth results for a 2% z-pinned laminate at different delamination lengths and non-linear iteration numbers.

5.4.6 Numerical convergence studies

Studies were undertaken to evaluate the sensitivity of the SERR to the mesh size at the crack front region and to optimise some of the FE parameters to achieve numerical convergence with a sufficient degree of accuracy for the model. The FE results *(G-f.f_.%f)* are correlated by the theoretical beam value $G_{f\_REM}f$.

In figure 5.10a normalised computed SERR values are plotted against different crack-tip element sizes for a 2D plane-strain analysis. Plane 42 is a four-noded linear plate element, whilst Plane 82 is an eight-noded quadratic plate element. From a crack-tip mesh size of 0.5 mm both elements and both techniques proved to converge to a stable Gf value, even though the plane 82 showed a faster convergence especially with the VCCT.

In figure 5.lOb normalised computed SERR values are plotted against different crack-tip element sizes for a 3D DCB modelled by plate elements. Shell 63 is a four-noded linear shell element, whilst Shell 91 is an eight-noded quadratic shear deformable shell element, and Shell 99 has the same formulation of shell 91 but can accept a higher number of composite layers. From a crack-tip mesh size of 0.5 mm both quadratic shell 91 and 99 elements proved to converge to a stable GI value comparable with plate82 plane-strain solution. The shell 63 element always resulted to underestimate SERR values at crack front, and therefore is not suitable for accurate SERB computations.

A displacement-controlled non-linear FE analysis was performed with the full Newton-Raphson option adopted. In order to reduce the numerical error during the convergence process of the non-linear analysis the arc-length method was used. It was found that in order to achieve numerical convergence a suitable incremental displacement b, had to be chosen carefully. After a series of delamination analyses undertaken using tentative incremental displacements for the DCB arms (figure 5.11) a *S, - 0. Imm was used. An* excessively small incremental displacement resulted in an excessive number of non-linear iterations, (i.e. A =0.02 mm and N = 523) and consequently produced a computationally expensive analysis (25 hours for a full run). A relatively large incremental displacement either did not achieve numerical convergence or did not simulate the experimental curves accurately.

In terms of computational time the complete run of the non-linear model took on average 8 hours on a 2.1 Ghz machine with 1 GB of ram memory for a total of 130 Newton-Raphson iterations. The FE models having higher non-linear bridging functions (higher z-pin density) were found to he computationally more expensive with a complete run taking about 12 hours. All the ANSYS runs were executed in batch mode. The mesh size at the crack front also affected the number of iterations required to propagate the delamination and the accuracy of the SERR computations. Satisfactory **results in terms** of computational time and accuracy were achieved for a mesh size of 0.5 mm (figure 5.12 and 5.10b).

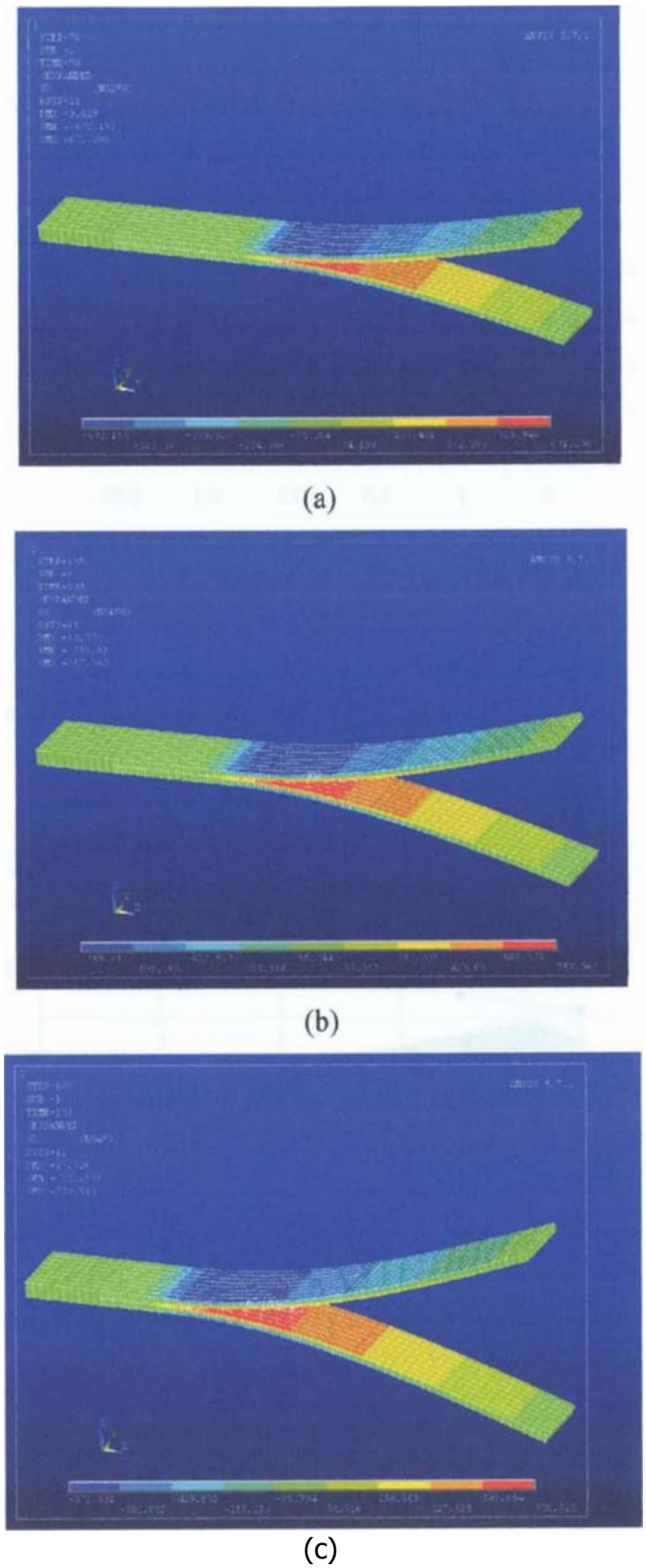

Figure *5.9* *The FE computation cfdelumination growth for a 2% :Tinned laminate pin radius (r = 250 (a) a - 10 mm, Nsu**h** = 70; (b) a - 20 mm, N,**ub** - 105; (c) a - 30 mm, IV$_{st,t,}$* ***= 143.***

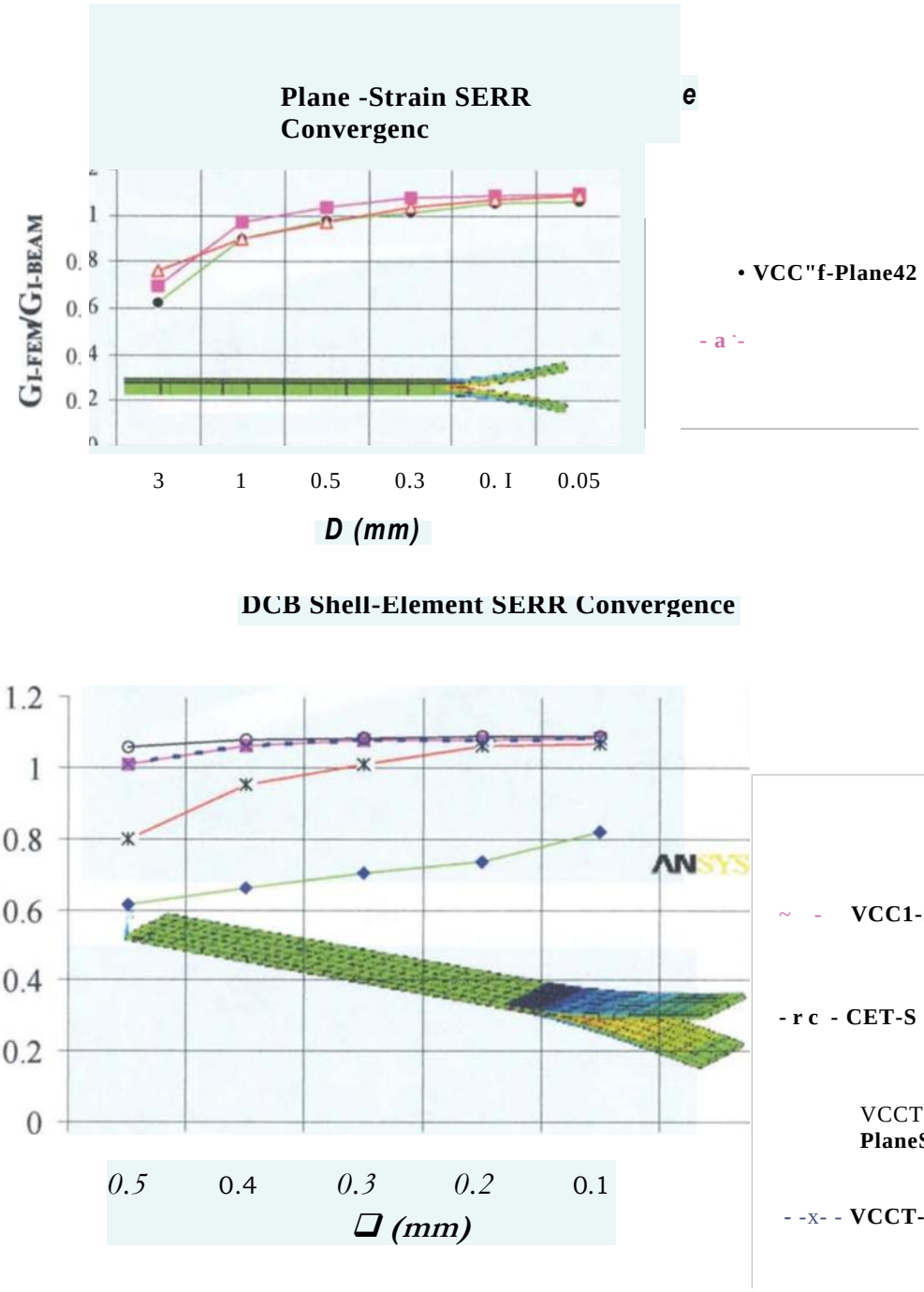

Figure 5.10 (a) *Numerical convergence of SEI for the plane strain model.*
(b) *Numerical convergence of SEW? for the 2D-Shell models.*

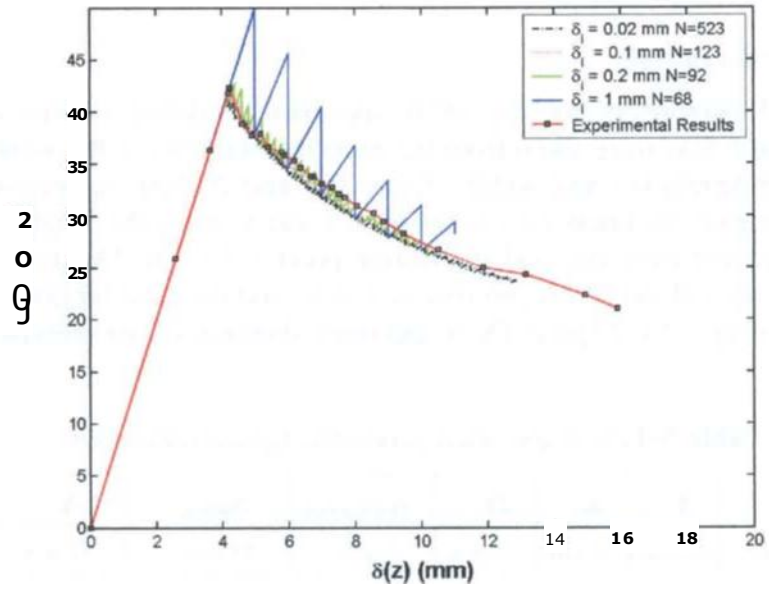

Figure 5.11 *Numerical convergence studies'* W.

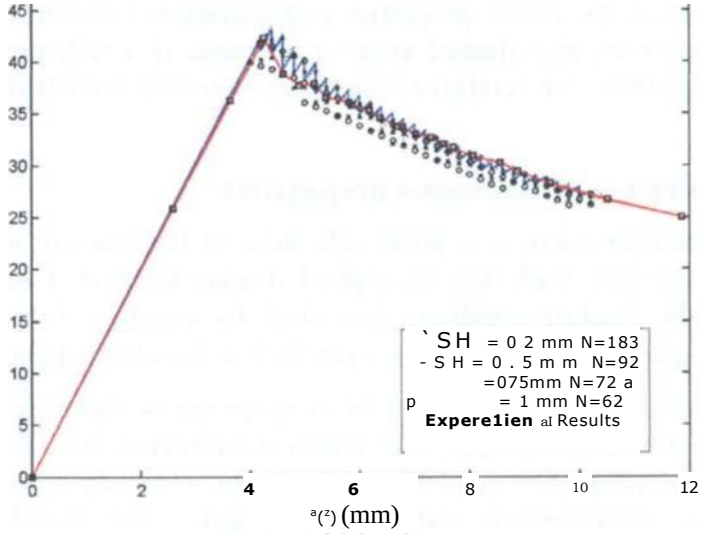

Figure 5.12 *Numerical convergence studies*

5.5 Results & Discussion

5.5.1 Numerical example

The geometrical parameters for the DCB specimen modelled in this chapter and outlined in figure 5.6(a) were taken from the experimental tests in the work by (Cartie, 2001). The DCB length *(L)* and width *(B)* are 160 and 20 mm, respectively, and the range of the laminate thickness (2t) is between 3 and 6 mm. The length of the crack starter (a_n) considered from the load application point is 50 mm. The distance between the initial crack tip and the first z-pin row is 5 mm, and the total length of the pinned block is 25mm (Fig. 5.6). Typical DCB specimen dimensions are summarized in the following table.

Table *5-3 DCB specimen geometric typical dimension.*

B	L	**as**	**2t**	**ONO PINS**	**PINS**	A
20 **mm**	160 mm	50 **mm**	3.2 mm	5 **mm**	25 **mm**	30 **mm**

The DCB is made of carbon-epoxy IMS1924 unidirectional plies with a single ply thickness of 0,125 mm and the following typical elastic properties: L_{tf}*=138 GPa,* L_{22}*=1IGPa,* $G_{,2}$*=4.4GPa, vta* =-0.34. Four different z-fibre volume densities (0.5%, 1 %, *2%,* & *4%)* and two typical z-fibre diameters (0.28 and 0.51 mm) were simulated. In this z-pinned area the elastic bending stiffness was reduced in order to take account of the z-pinning effect on the elastic properties as discussed in Chapter 3. Different z-fibre insertion depths (Tr) were also studied to cover the range of a fully pinned laminate and partially pinned laminate. Un-reinforced laminates were also modelled as control cases.

53.2 Z-Iibre effects on delamination propagation

The force-displacement curve is a good indication of the fracture process of a DCB specimen. With the first load step an applied displacement of 4 mm will bring the model close to the fracture condition described by equation 5-23. An incremental applied displacement of 0.1 mm (8,2) for each DCB arm is then applied.

Firstly, the control case of an unpinned DCB specimen is shown in figure 5.13. The linear rising part of the curve refers to the elastic deformation of the DCB arms without any damage propagation (first load step). When the crack tip GI value reached the critical value G, c, delamination started to propagate. This initial crack extension occurred at the load level of 40 N. This load level is a turning point from which the external load decreased with the increasing applied displacement. The experimentally measured data are also shown in the same figure, and the agreement is excellent.

The control specimen analysis was also useful to calibrate the critical G_{tr} value that was implemented into the fracture criterion of equation 5-23, For this case the value of 250]!m² was used for G_tr, which was also used as the critical value for the z-pinned laminates at the crack-tip zone.

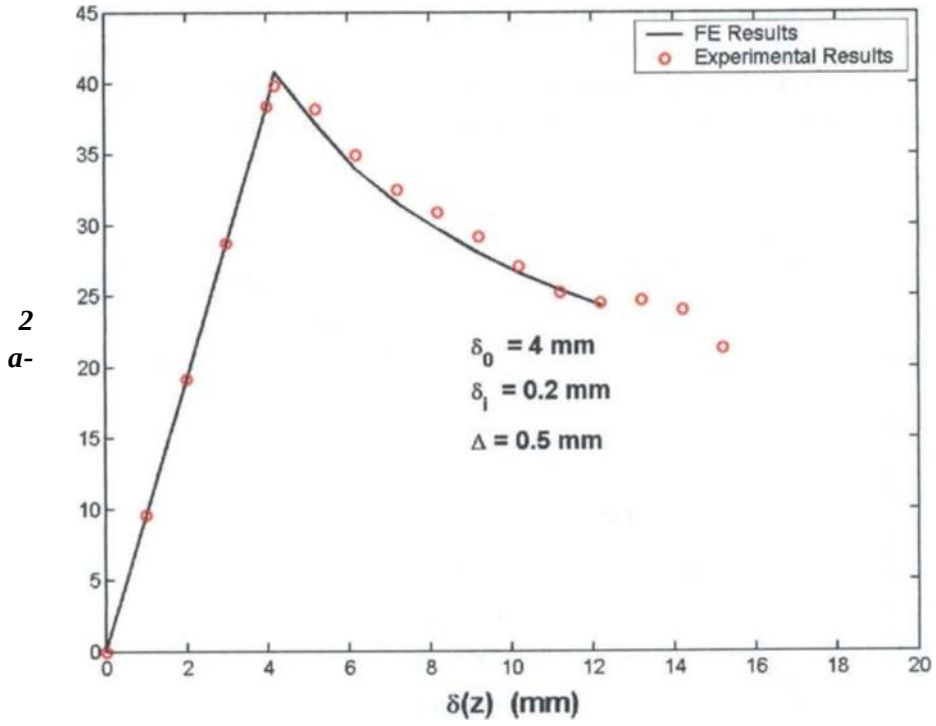

Figure 5.13 *Load displacement curve for unpinned DCB (control case): Numerical vs. experimental results.*

Figure 5.14 shows the load-displacement curves of a z-pinned DCB configuration with a pinning density of 0.5%. The carbon z-fibres had a radius of 0,14 mm.

The critical load for initial delamination propagation was about the same as the un-reinforced laminate, around 40 N as indicated by the first load drop. However, the force quickly picked up after the initial delamination growth, and the curve shape altered completely, i.e. from a declining *P-S* curve of unpinned case (figure 5.13) to a rising curve (figure 5.14).

This is because delamination has propagated into the z-fibre field where the resistance to damage growth is significantly higher than that of the unpinned case. The sudden drop of the load at about 40N was due to the initial delamination propagation within the first 5 mm zone where no z-fibres were placed (figure 5.6a). After passing the first z-fibre row, the bridging mechanics worked by rising the external load (P) necessary to propagate the damage further. Then at the load of 48 N there was another drop in the external load. This corresponds to another damage growth just before the damage front meeting the second row of z-fibres_ This phenomenon repeated regularly exhibiting stable crack propagation behaviour.

This distinct shape of the *P-S* curves in a through-thickness reinforced laminate was referred as the "stick-slip" behaviour in the literature (Dransfield et al., 1998; Dransfield et al., 1994; Tanzawa et al., 1999; *Singh and* Partridge, 1995); *it was* assumed to be caused by the presence of z-fibre or stitching rows at regular intervals.

For a lower z-fibre density, a direct relationship between the number of working z-fibre rows and the observed local load drops of the P-8 curve could be established. In this case (figure 5.14), five z-fibre rows were actively involved in the bridging field. According to the experimental observations (Cox, 2002), a constant value of 15 MPa was assumed for the frictional stress in the bridging law (see Chapter 4).

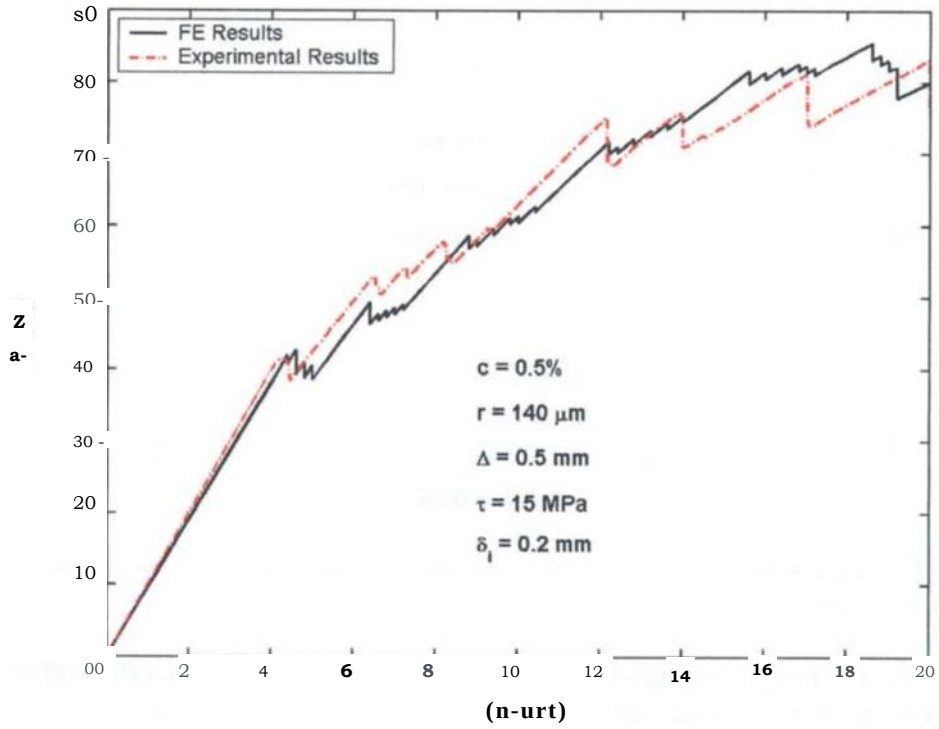

Figure 5.14 *Load-displacement curves for :Tinned DCB: Numerical vs. experimental results.*

Figure 5.15 shows a higher density (2%) pinning case, in which two ❑CB specimens reinforced with 0.28 mm diameter z-fibres were simulated. Both numerical simulation and experimental data are shown in the same graph for comparison.

Firstly, the "stick-slip" characteristic in the previous P-S curves of figure 5.14 (lower pin density of 0.5%) seemed to have disappeared in figure 5.15. This is because that more pins were bridging the crack in the high-density case. The P-6 curves also show a maximum load value of about 180 N, after which an increment of the applied displacement (0.2 mm) corresponds to a small decrement of the external load, and this corresponds to *the* full development of the bridging area. This will be discussed in section 5.5.3.

Secondly, a discrepancy between the experimental and numerical results was found in the first FE run (dashed line). A close examination of the failed fracture surface revealed that the position of the first row of z-pins was misplaced at about 1 mm ahead of the initial crack position *(a_0)* instead of the usual distance of 5 mm (figure 5.6a), for which the FE model mimicked initially.

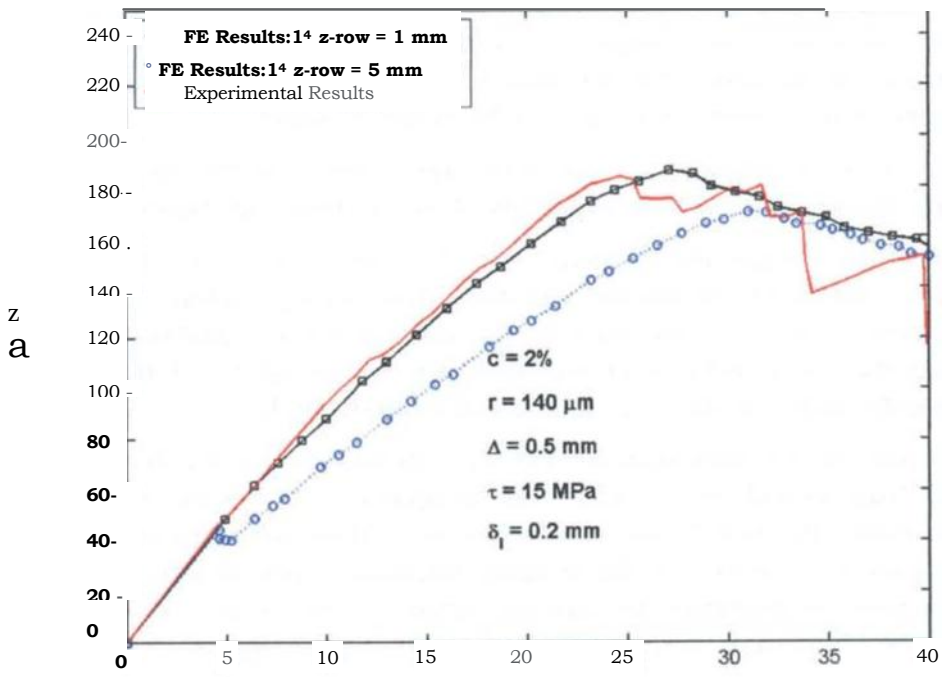

Figure 5.15 *P-S curves . for a 2% 1-pinned DCB: experimental .specimen 1" row misplaced at 1 mm from the crack tip; numerical model 1 s·row placed 5 mm from the crack tip,- 1'" zz-pin row at 5 mm from the crack tip and modified elastic constants•.*

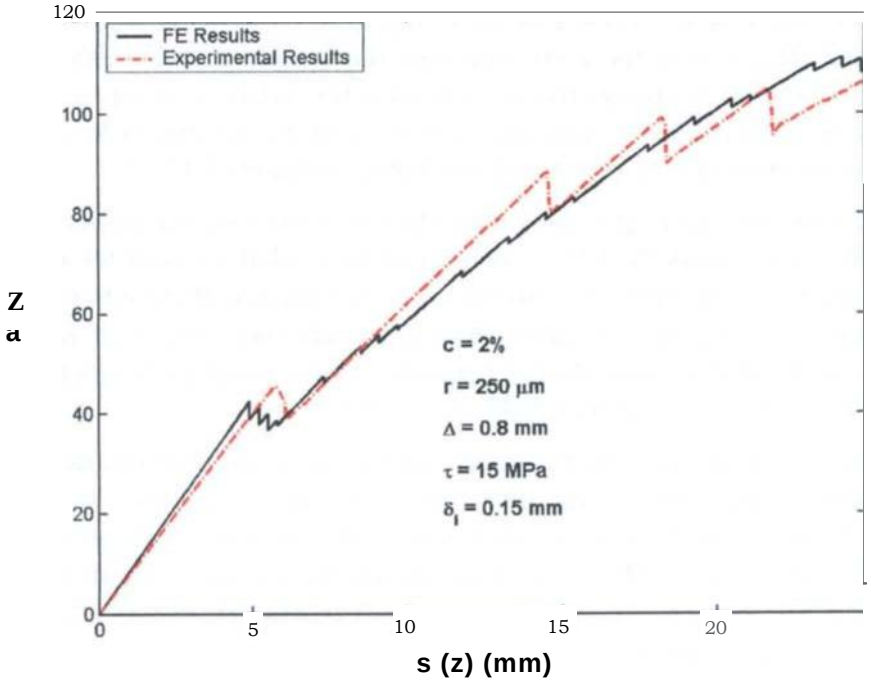

***Figure* 5.16** *Load-displacement curve for -pinned D['B: Numerical vs. experimental results.*

The FE model for this case was adjusted by placing the interface z-fibre element row at the actually measured position. The effect of z-pining on the elastic constants of the laminate was also taken into account by considering a more compliant laminate in the z-pinned area of the laminate. This was done by changing *the* stiffness matrix constants of the elements in the z-reinforced region of the model (Chapter 3).

The revised FE model showed a much better agreement with the experimental data. This example demonstrates also the capability of the FE model developed in this study.

Figure 5.16 shows another load-displacement FE results compared with experimental data for a 2% z-pinned DCB laminate, with the z-fibre having a radius of 0.25 mm. The difference in the mesh size at the crack front is due to mesh compatibility problems. In order to place the z-fibre with the correct array pattern (see table 2.1), the element size and consequently nodes position has to be tailored appropriately.

Once again both the FE computations and the experimental results showed a sudden drop of the load around 40N, which was associated with the initial delamination propagation within the first 5 mm zone where no z-fibres were placed (figure 5.6a). After passing the first z-fibre row, the bridging mechanics worked by rising the external load (P) necessary- to propagate the damage further. A maximum load of 110 N was predicted by the FE analysis, corresponding to a total displacement of 25 **mm.**

5.5.3 Large scale bridging effect

The LEFM theory assumes that all energy dissipations are confined within the crack tip zone. However, for reinforced laminates *the z-fibres* within the bridging zone will actively bridge the crack wake by producing traction forces and consuming large amount of applied energy, which is irreversible and will modify the delamination process. The FE analysis has found that the bridging force function djx) will reach its maximum value *ct* within *the* LSB zone that has length *D* and width B. It is also found that the maximum bridging effect is related to the numbers of active z-fibre rows, the maximum bending moment, laminate stresses, and the maximum bridging length. These findings are summarised below and illustrated in figures 5.17-27.

A steady LSB zone was developed soon after the first z-pin row was pulled out. During the subsequent crack growth the LSB zone moved forward along with the delamination front. Behind the LSB zone there was no traction force because those z-pins had already been pulled out (yrx 0, figure 5.17 a&b). Similar steady-state processes were reported for DCB specimens of the conventional laminates and in stitched laminates when the bridging entities started failing (Dransfield et al., 1998).

In figure 5.17a the contour plot for the upper sub-laminate has been omitted in order to show the z-fibre behaviour within the LSB zone. It is possible to identity the delamination front position and the area where the bridging function reaches its maximum value O,,,,., two z-fibre rows have already been pulled out whilst the region where the ply axial stress 6, is maximum coincides with the region where the LSB function attains its maximum *cp,,,*

This idea is further explained in figure 5.17b where a schematic bending moment distribution along the x axis of a DCB arm is reported. The maximum bending moment due to delamination loads is not positioned at the crack front but in the area where the

LSB mechanics is acting, effectively shielding the delamination crack front from the full delaminating loads.

In the specific case reported in picture 5.17b the maximum bending moment due to applied external load was acting on the laminate section corresponding to the fifth z-fibre position, 10 mm ahead of the delamination front position.

When the LSB process is fully developed, the bridging function OA) reached a constant value. In terms of the discrete bridging forces, $+'_{7,}$ when a new row of z-pins is involved in the bridging process another row will fail (z-pins pullout) leaving the total amount of bridging forces acting in the bridging area almost constant. Then essentially we can write:

cl~;. cons' & E $cons/$ **(5-24)**

Phenomenon expressed by equation 5-24 can he further explored. Figures 5.18 to 5.21 show the number of z-pin rows (left axis) versus delamination growth length for 0.5, 1, 2, 4% z-fibre density, respectively. The white columns refer to the total number of z-fibre rows involved in the bridging process, the grey bars represent number of z-fibre rows in the maximum bridging area, and the black bars represent the z-pin rows that have already been pulled out $(I$ 0). The open-circle points correspond to the number of z-fibre row where the maximum bending moment occurred. The smooth curve plots the ratio of number of z-fibre rows in the $o_{„u,r}$ area to the total number of working z-pin rows; the value refers to the y-axis on the right hand side.

It is important to highlight that the analysis of the maximum bending moment and the consequently derived laminate stresses does not include the crack-tip stress analysis which is conducted via energy principles and will be discussed in Chapter 6. The stress analysis that follows deals with laminate macro stresses due to the external applied delaminating loads and based on equilibrium considerations.

The external plies of the two DCB arms are considered, and axial stress (a_r) due to the applied loads is investigated. Even though the ply stress is a generic function $cr_r(ry)$ and is assumed constant within *the i-th* ply thickness at a defined height from the laminate plane :', because of the assumed cylindrical bending conditions the ply stress can be assumed a mono-dimensional function of the crack length $a_x(x)$.

The maximum ply stress $(a,)$ within the maximum bridging zone and within the minimum bridging zone are plotted from figures 5.22, 5.24-5,26, for different z-fibre densities. All cases showed that in the first 5 mm of delamination growth the maximum stress field due to the external loads was placed at the delamination front, and there wasn't any shielding effect due to z-pinning. When the LSB mechanics started, bridging length I) increased and an un-loaded region behind the crack appeared.

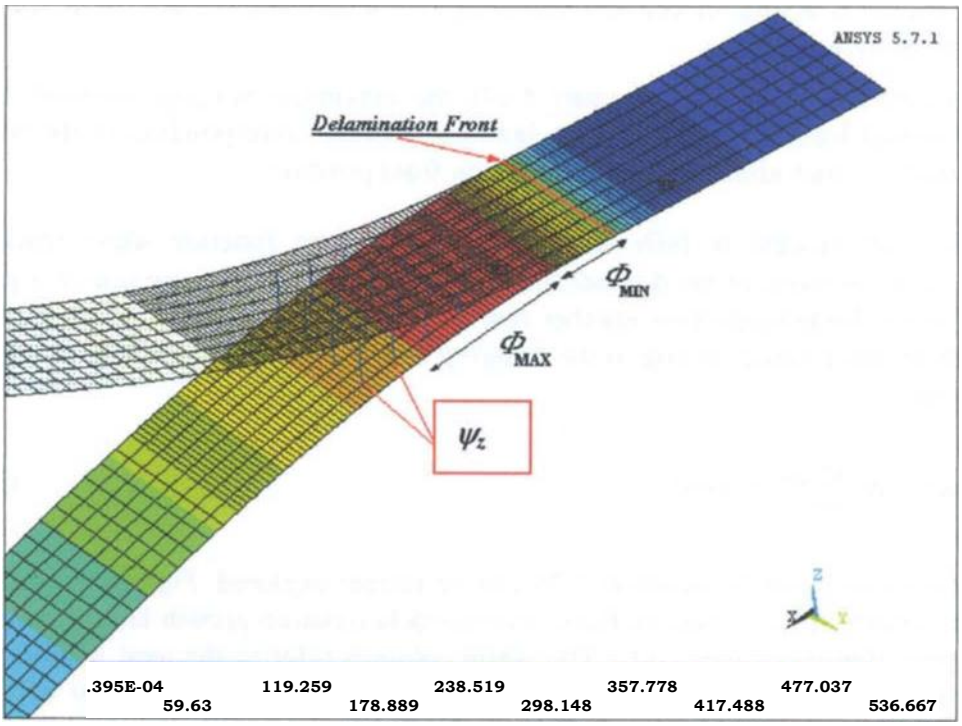

(a)

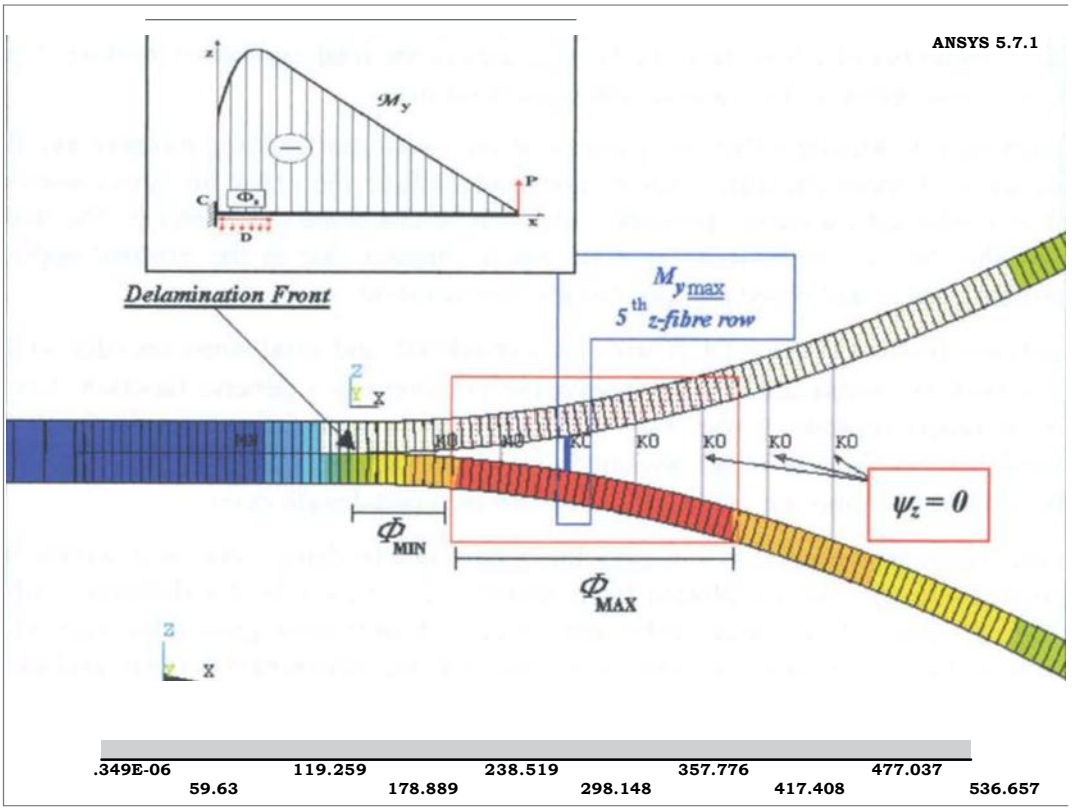

(b)

Figure 5.17 *The 4r4. ,. and the 4ffN LSB areas characterizing the high bending moment (M) and high .ttres ces region off-pin reinforced laminate: (a) 3D view; (6J x: plane view.*

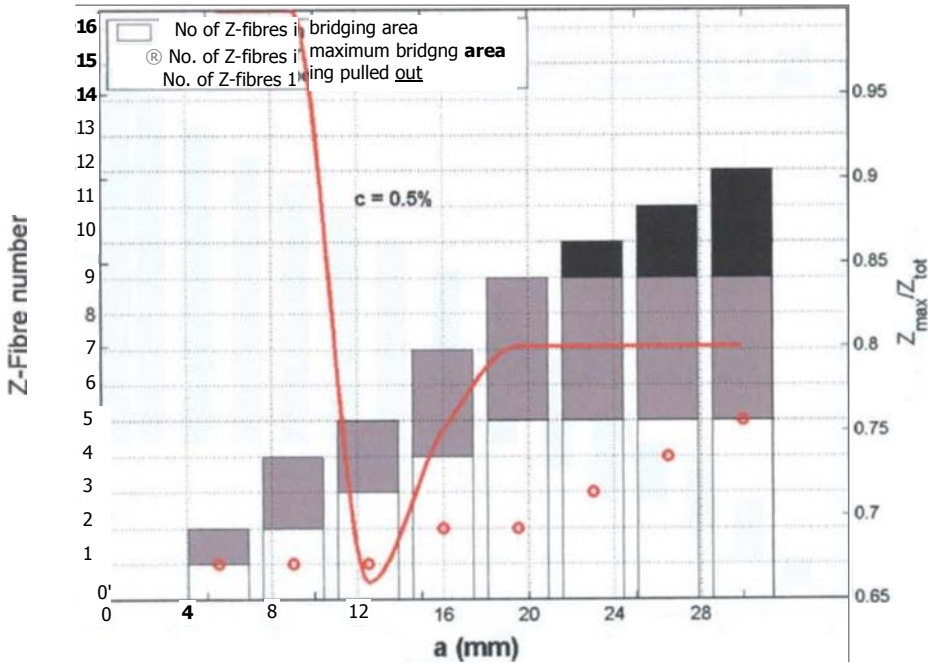

***Figure* 5,18** *Z-fibre bridging process during delamination growth fur a 0.5% :pinned DC I3: :fibre mechanics (bar-chart), MA1:location (o,), -fibre ratio in area (-).*

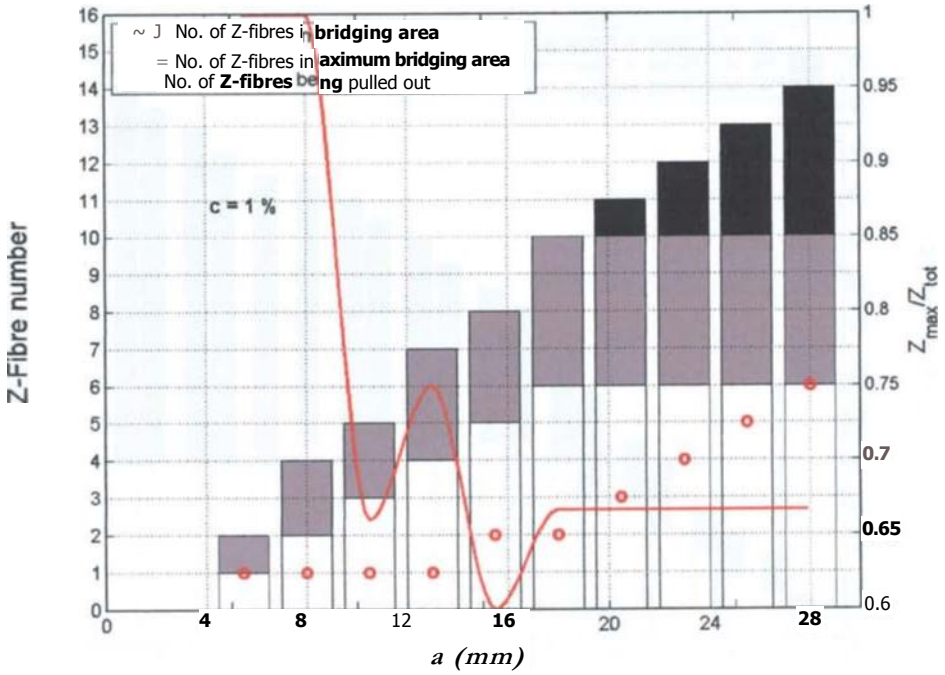

Figure 5.19 *7_ fibre bridging process during delamination growth for a I% :Tinned 13(8. :,-fibre mechanics (bar-chart), $M_{t1\cdot t.ti}$'location (n), z-fibre ratio in 4 , , area (-).*

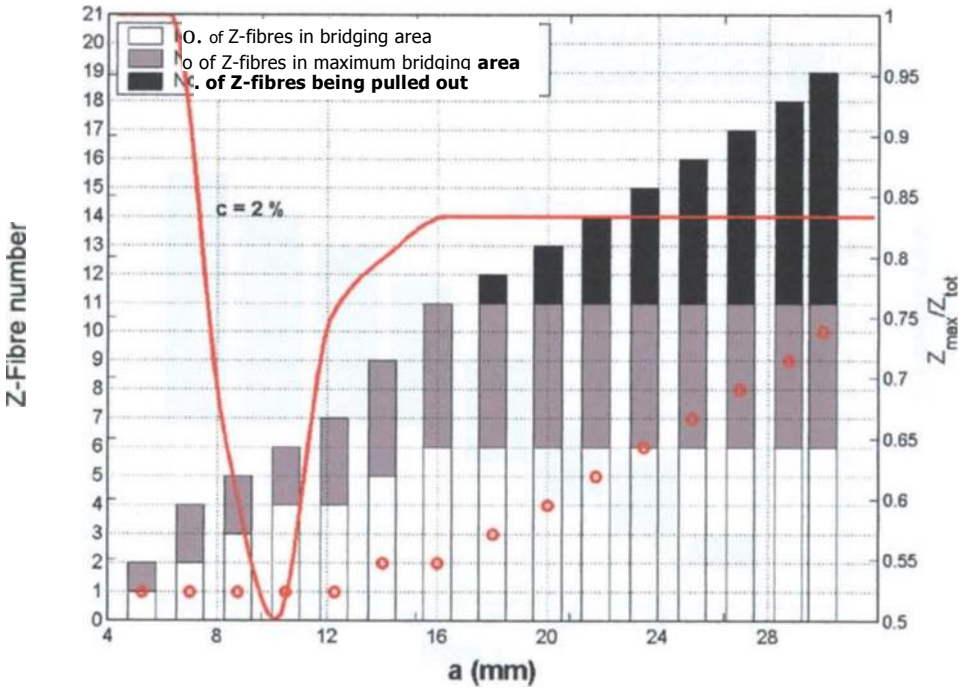

Figure *5.20 Z f fibre bridging process during delamination growth fora 2% :pinned DCB: :-fibre mechanics (bar-chart), atr location (9, fibre ratio in* $4_{,a}$*, area (-).*

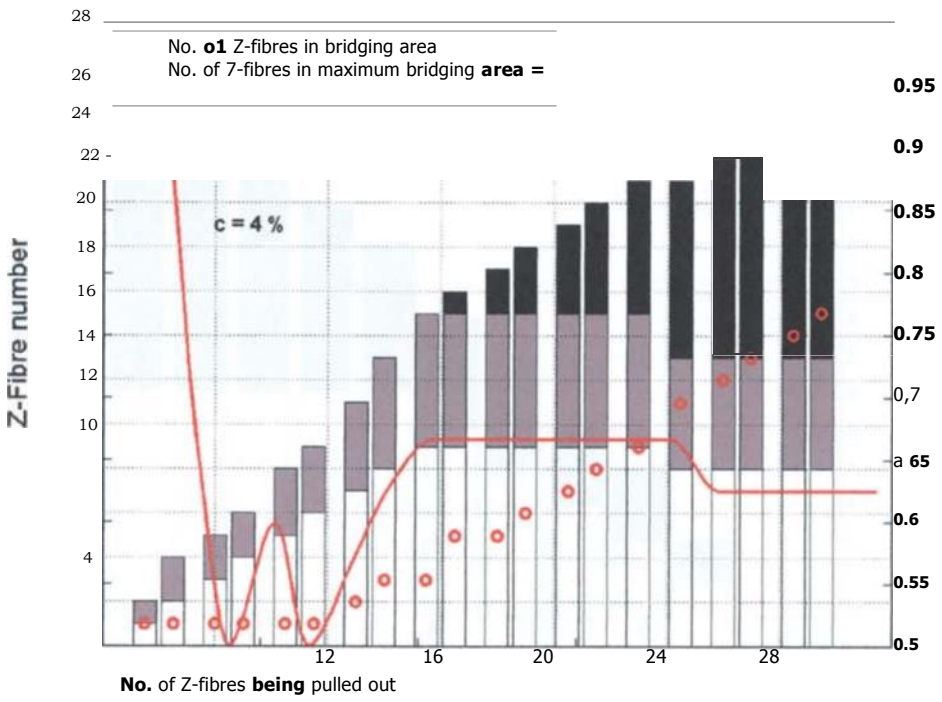

a (mm)

Figure 5.21 *Zfihre bridging process during delamination growth for a 4% .pinned D('B:: fibre mechanics (bar-chart),* $M_{it.t,l}$ *location 69, z-fibre ratio in* $4_{,a}$*, area ( ).*

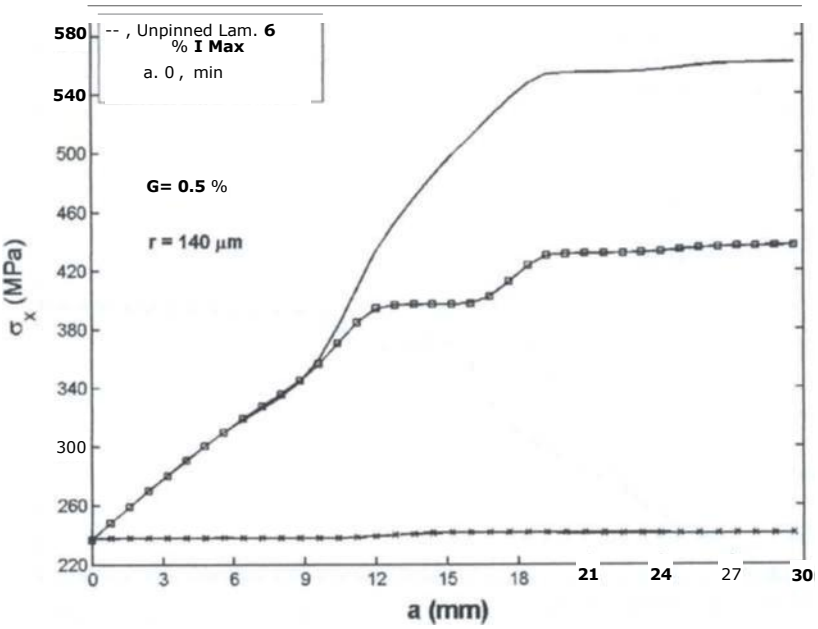

Figure ***5.22*** *Laminate stresses vs. delamination length for 0.5% pinned laminate: Q, at the Om. , at the ax at delamination front section fir unpinned laminate.*

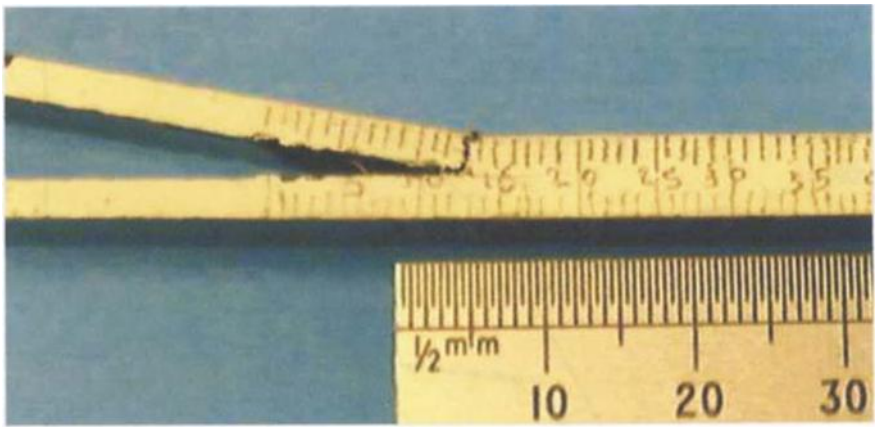

Figure ***5.23*** *Laminate failure mode introduce by LSB mechanics of -fibre reinforcements* *15.*

Courtesy of Carrie DDR. Advanced Materials Department, Cranfield University

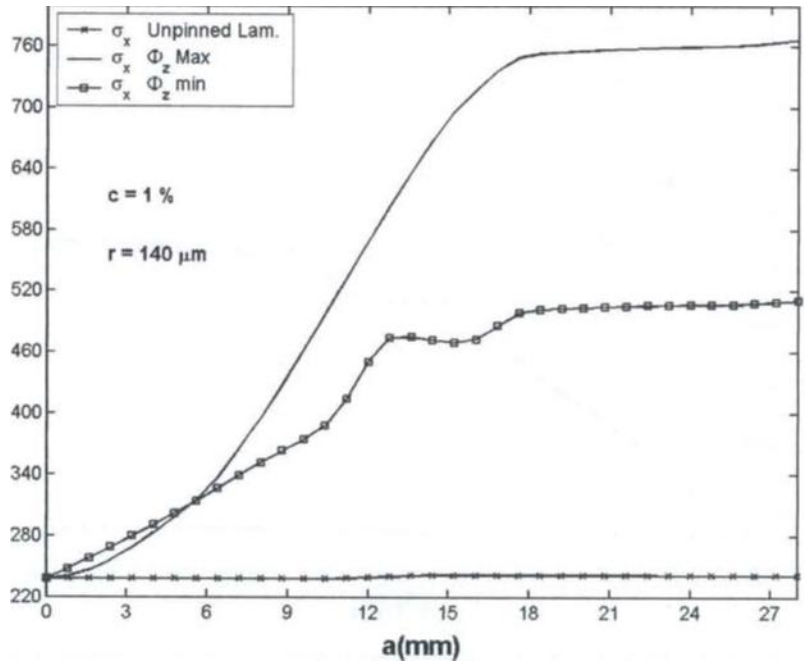

Figure *5.24 Laminate stresses vs. delamination length for 1% pinned laminate: a- at the , a, at the 4n,,. , 6,. at delamination from section fir unpinned laminate.*

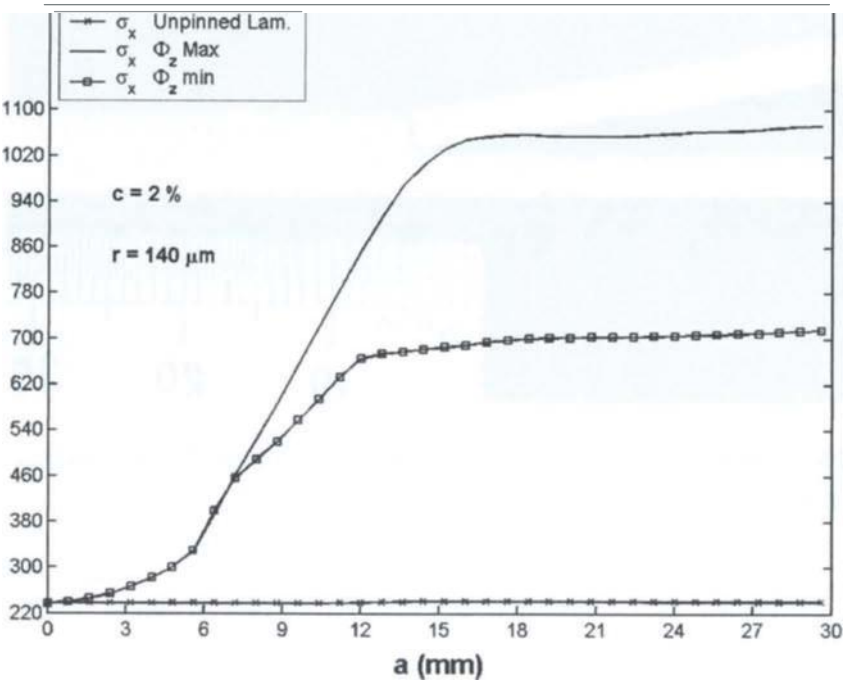

***Figure 5.25** Laminate stresses vs. delamanation length fir 2% =Pinned laminate: a at the rain , ax at the 0,7„• , a at delamination front section, for unpinned laminate.*

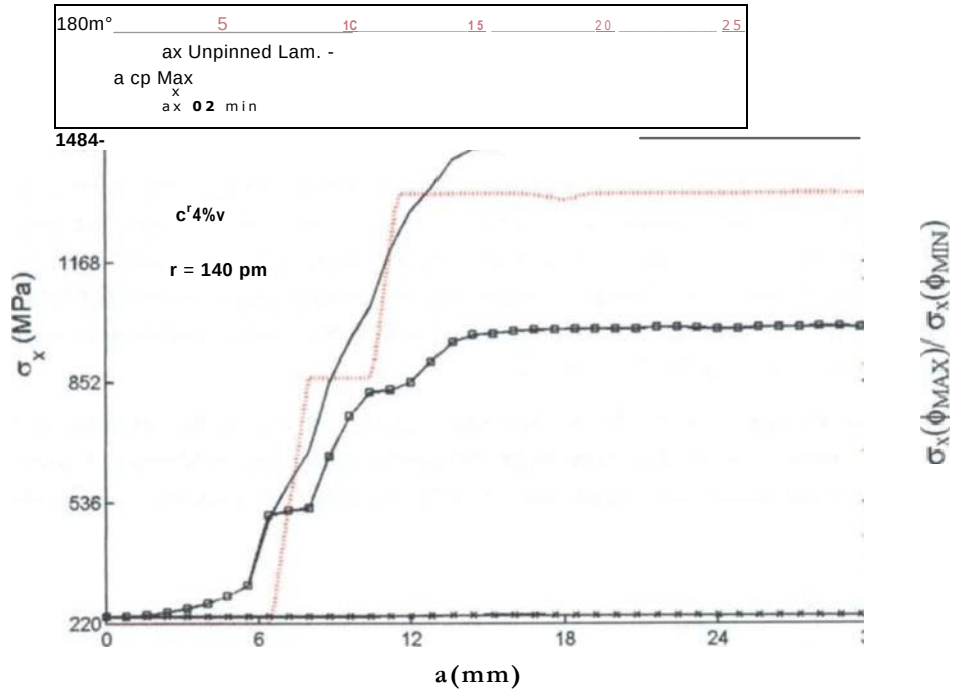

Figure 5.26 *Laminate stresses vs. delamination length for 4% :pinned laminate: at* ***thc~O,,,,,,*** *, o- at the O,,~,* ar, *at delaminalion front section for unpinned laminate.*

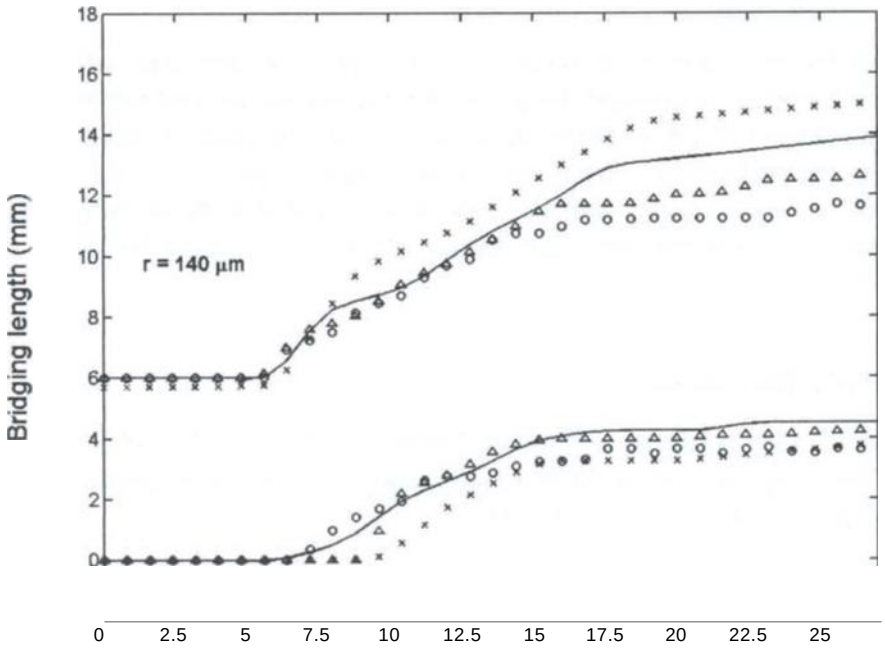

Figure ***5.27*** *Large Scale Bridging length against delaminalion propagation.*

This crack-front shielding effect is associated with a considerable amount of energy absorption, as a drawback new failure modes such as tensile or compressive failure of the external plies could be introduced because of the above described LSB mechanics. During the experimental tests, failure of the DCB arms was reported within the LSB length I) of the sub-laminates (figure 5.23).

Within this un-loaded region the stress field is lower than that in the LSB area (figure 5.22 and 5.24-26) and although several z-fibre rows were just passed by the delamination front, they were not active yet because of the small crack opening displacement field. The stress values within the maximum and minimum bridging areas increased with the increasing crack length, but when the stable conditions (equation 5-24) were satisfied they reached a plateau.

The dotted line in figure 5.26 shows the ratio of the stress in the maximum bridging area over the stress within the minimum bridging area; the reference y-axis for this curve is on the right hand side. Therefore, when the bridging process is fully developed we can write:

$$\frac{\sigma_{x(max)}}{\sigma_{x(min)}} \frac{M_{r(mm)}}{M_{(min}} = \text{cons}/r \qquad \textbf{(5-25)}$$

The location of this maximum bending moment M, was related to the z-fibre row that exerted the highest bridging traction load. A schematic of the bending moment distribution was also presented in figure 5.17 (b).

These numerical findings seemed to be valid for the four z-fibre densities studied in this work, showing that the characteristics of the bridging mechanics could be generalized regardless of the pin density.

Also the LSB length reported in figure 5.27 for the four different z-fibre densities analysed proved to attain a constant length within the maximum and minimum bridging areas. Even though the length of the bridging area seems comparable for the different z-pin densities in the early stage of the LSB, more working z-pin rows with a longer LSB zone seem to characterize lower densities. The lower z-pin density the longer the length of the LSB will be within the maximum bridging zone, when the LSB process is fully developed.

5.5.4 Effect of z-fibre density

Computational P-S curves for both z-pinned (four volume densities of 0.5%, 1%, 2%, and 4% and two typical z-fibre radii of 140 and 250 pm) and un-reinforced DCB specimens are presented in figure 5.28-5.29.

Firstly, these $P\text{-}S$ curves showed that the work done for the onset of delamination extension (at $P(JN\}$ did not change between the pinned and unpinned models, while during the crack growth stage the work done for the reinforced specimens rose to the values that were one order of magnitude higher than that of the unpinned case.

Secondly it was also noticed that as soon as the delamination came across the z-pin bridging field the curve slope changed, which was a function of the z-pin density. A

general trend in the first part of the delamination propagation stage, i.e. before the force P reaches its maximum value, may be expressed mathematically as:

For z-pinned laminate:

$$>0 \qquad \textbf{(5-26)}$$

55

The maximum load in the P-8 curves is related to the pullout of the first z-fibre row defining the starting point of the second part of the delamination process when the so-called LSB is fully developed. It is also noted that the displacement value at which the maximum load occurred increases with the increasing z-pin density.

The above described physical condition occurring in correspondence with the maximum load value may be described mathematically to the value of the first and second derivatives:

$$\frac{a^2}{5}\frac{8_{max}}{\sim 1} - 0 \quad \frac{}{C\,2}\frac{ax}{..} > 0 \qquad \textbf{(5-27)}$$

For a generic z-pinned laminate P-S curve the condition described by equation 5-27, is verified until the delamination process will attain a steady-state which coincides with the full development of the LSB process, described by equation 5-28,

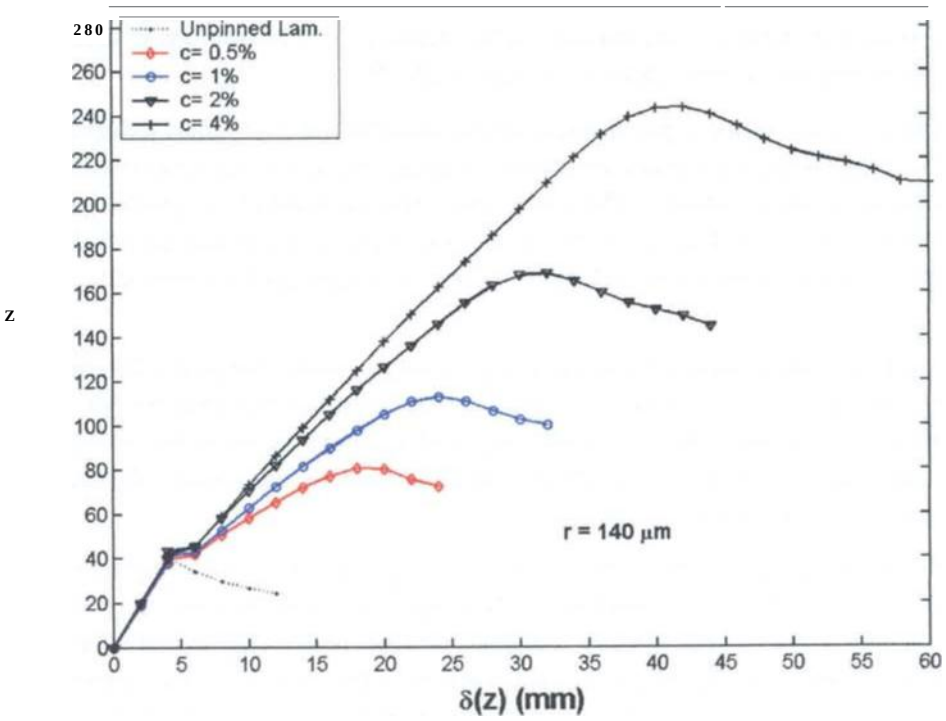

Figure 5.28 *Computational P-S curves J r different :-frhre densities and comparison* ^{n}*with unpinned* case (r == *140 pm).*

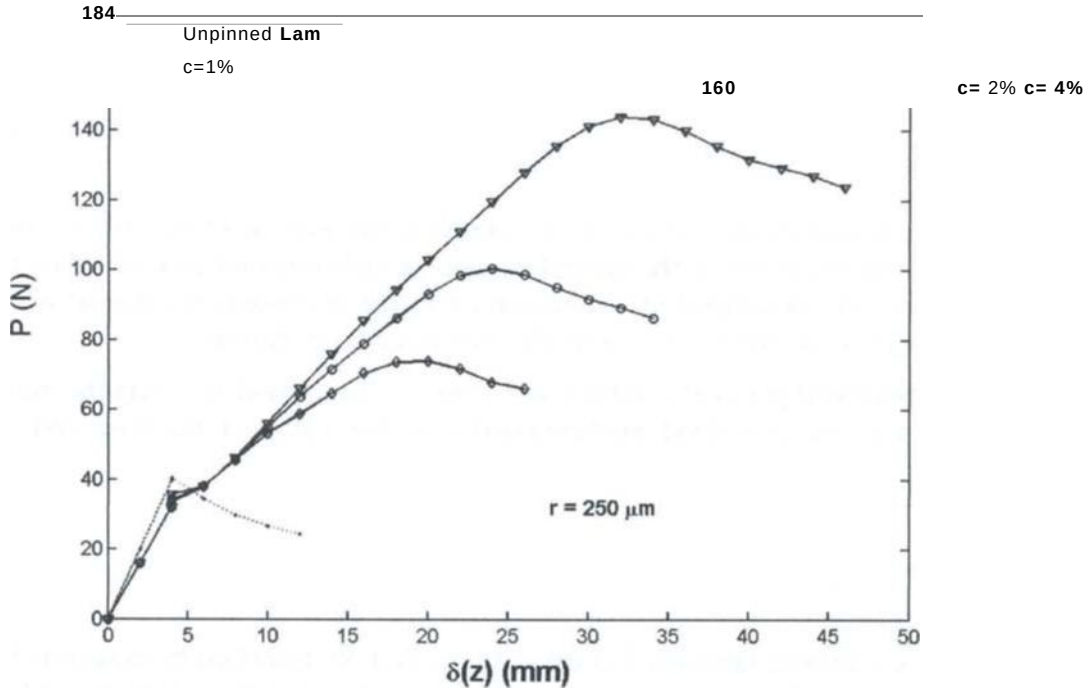

Figure 5.29 *Computational I'-8curves for d *r e n t : fibre densities and comparison with un-pinned case (r - 25() wit).*

The displacement 8(z) at which the maximum total P will occur depends on the z-pin density and increases with the increased z-fibre density. The maximum P value will also increase with increasing z-fibre density (figure 5.28-29).

However, the comparison of z-pin density effect in terms *of P-8* relationship as made in figures 5.28-29 lacks the necessary information about the growing delamination lengths and delamination front positions. Therefore, the external load (I') is plotted against the delamination length (a) in figures 5.30-31, which show computational results (points) and polynomial fitted curves for different z-fibre densities and for two distinct z-fibre radii.

The un-pinned specimen showed a decreasing external load (P) against the propagating delamination damage, i.e. less force was required as the crack became longer. However, for all reinforced laminates the external load had to increase in order to advance the crack until the load reached its maximum value after which a slowly decreasing load value against crack length was predicted.

In terms of structural design the above result is significant. For example, in order to propagate a crack to 15 mm, a load of 37 N would be sufficient for an un-reinforced laminate, whilst the z-fibre reinforced laminate needed much higher external load, e.g. 65, 98, 158, and 240 N, respectively, for the various z-pin densities investigated. ❑n the other hand, if the design load is defined, an upper and lower bound of the required z-fibre density can be determined.

The rising part in the *I'-u* curves is characteristic of z-pinned laminate. This **represents the *stage* when** the first few z-pin rows are engaged in the early bridging process. The

stable LSB process will follow when P reached its summit. Note the sharp rise in the higher z-pin density cases. It is therefore concluded that those models described in the modelling section 2.5.2 that use uniformly distributed z-pin traction forces would have difficulties to capture the sharp rise of the external force shown in figures 5.30-31.

For a higher z-pin density, the number of z-fibre rows involved in the bridging zone is also larger. Therefore, the displacement of the DCB arms would be larger in the LSB zone as shown in figure 5.29, and this will force the first row of z-fibres to stretch, debond, and pullout more quickly comparing to the cases of lower density reinforcement. Therefore, the higher the z-fibre density, the shorter the crack length at the summit of the *P-d* curves and the higher the non-linearity of structural deformation would be.

From the finite element results the number of times when delamination is temporarily arrested can be worked out by counting the consecutive load points where the load is increasing but the delamination length is constant (figure 5.30). It is found that the crack length values at temporary arrestment correspond to the involvement in the bridging process of a new z-fibre row; as soon as the delamination front comes across a new z-fibre row and the displacement vector u of the new bridging row becomes greater than zero (5c=F(u)>0), the crack will be arrested temporarily.

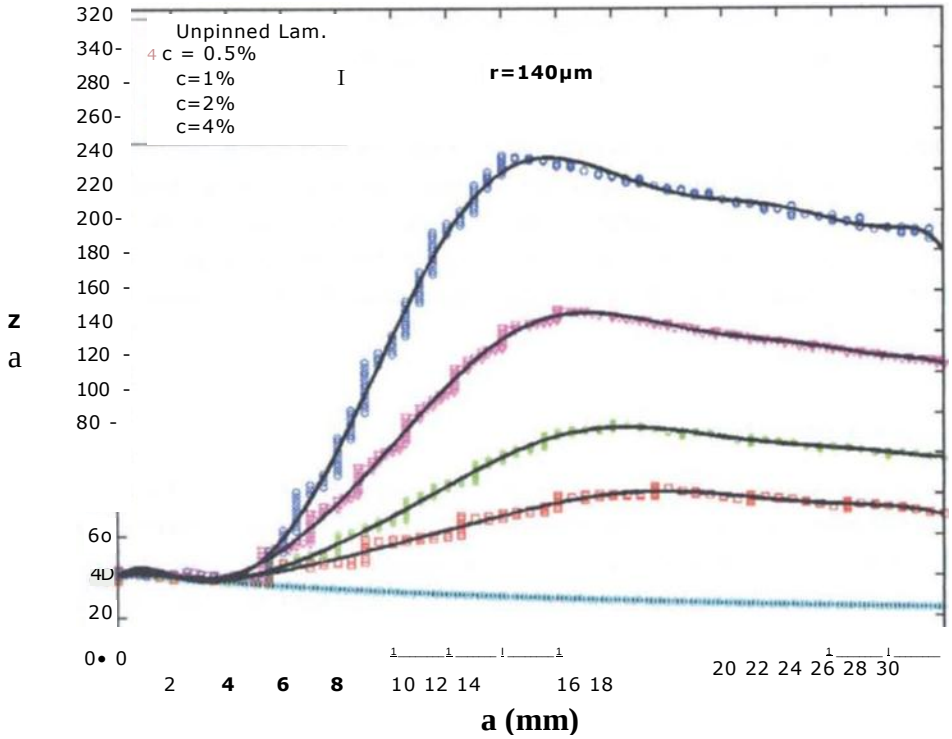

Figure ***5.30*** *Load vs. delamination length Jr idifferent .pin densities (r=140 1.un) and comparison with unpinned case. FE results (symbols): polynomial interpolation (smooth lines).*

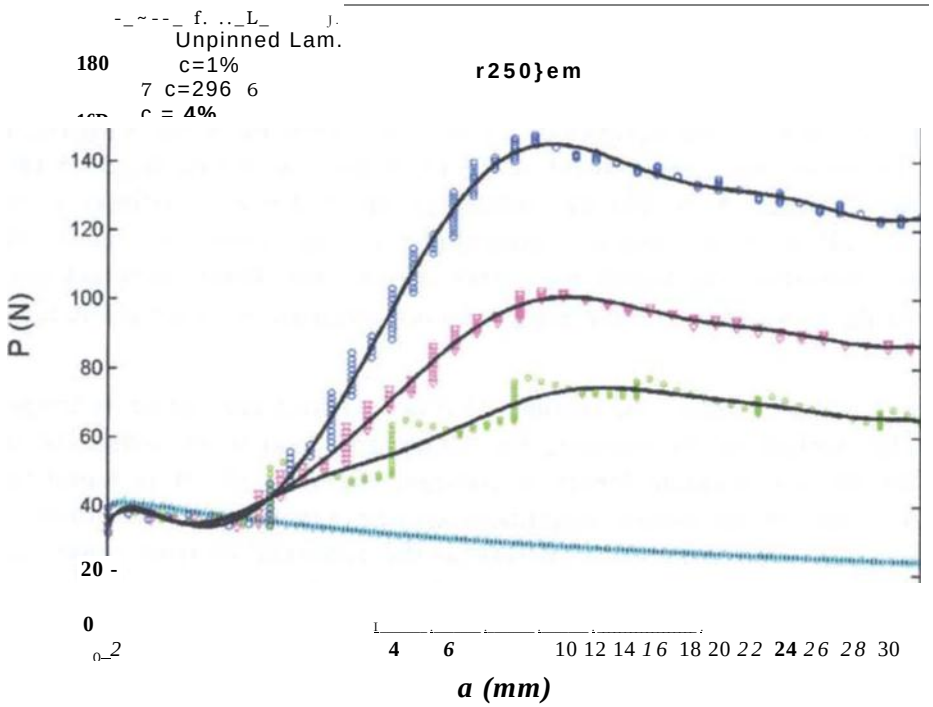

Figure 5.31 *Load vs. delamination length for different Sin densities (r=250 ,wn) and comparison with unpinned case. FE results (symbols); polynomial interpolation (smooth lines).*

This phenomenon is more visible in laminates with low-density z-pins than those with high-density pins in which cases crack arrestment can occur more often due to more pins bridging the crack. For example, after I5 mm crack growth the 0.5% density pinned laminate had 3 rows of z-pin involved in the bridging process, 1% had 4 activated rows, 2% had 6 rows bridging the crack, and 4% had 7 working rows (Fig. 5.30).

5.5.5 Effect of z-fibre diameter

Figures 5.32-33 presents comparison of two typical z-pin radii (r_i=0,14 mm and r_2=0.25 mm) in terms of applied load *(P)* against displacement (6) and delamination length (a), respectively, The z-fibre density was kept constant in the FE models, i.e. 2%, by placing the interface elements (simulating z-pins) at different positions as indicated in Table 2.1. All the other parameters of the finite element and micro-mechanical models were unchanged. The results of unpinned specimen are also reported for comparison.

The better performance of the smaller z-fibre radius (r_t) was demonstrated. When the LSB process was fully developed, the laminate with smaller diameter z-fibres provided more resistance to delamination growth; the external load was almost doubled that by using the thicker z-fibre (r_2) option. The FE results also show that before reaching the stable bridging configuration at the same crack length of 16 mm seven z-fibre rows (for z-fibre radius r1) and four z-fibre rows (for z-fibre radius r2) were passed by the delamination front, respectively (figure 5.33).

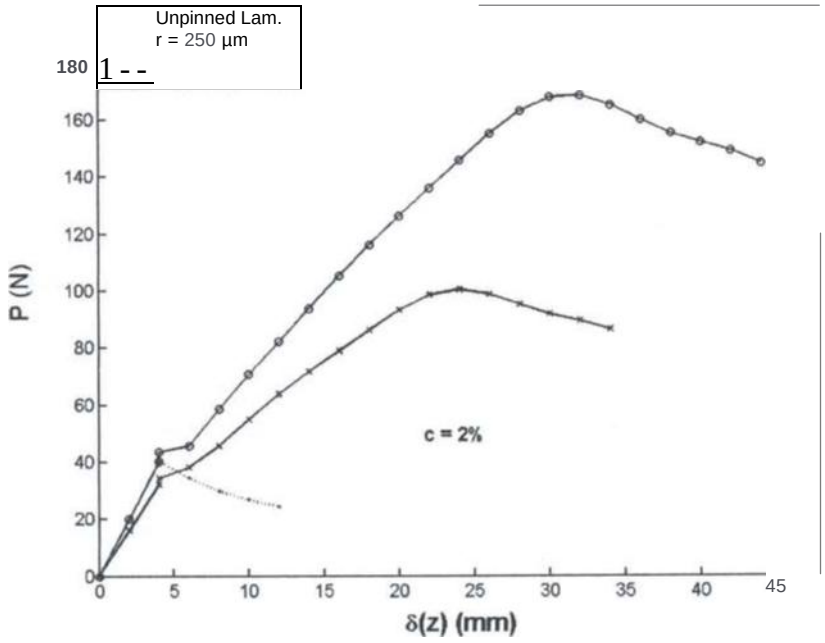

Figure ***5.32*** *Computational P-Scurves for different -fibre radii: r_i=0.14 mm and r_2 0.25 mm.*

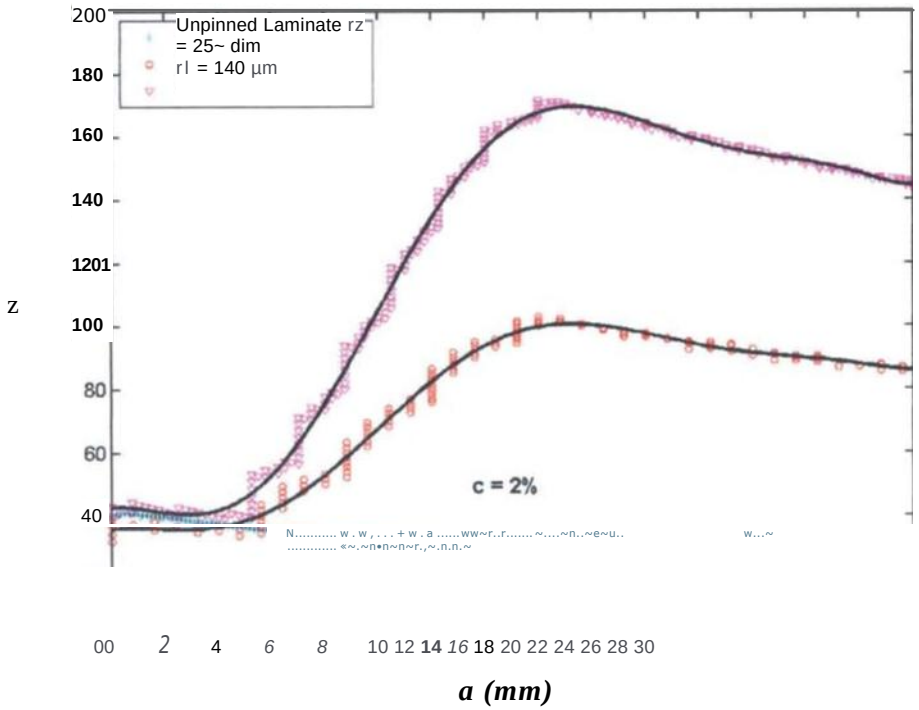

Figure ***5.33*** *Load vs delamination length curves fi)r different _-fibre radii: r_1=0.14 mm and* r_2*-0.25 mm.*

When the dominant energy dissipation mechanism is the z-pin pullout resisted by frictional sliding forces, the micro-mechanical solution presented in Chapter 4 demonstrated that in order to achieve high traction bridging forces at the delamination wake smaller z-fibre diameter was considered a better choice (Dransfield et al., 1994). Moreover, as a generic solution the designer should maximize the ratio of the cross-section perimeter over the cross section area in order to enhance the resistance against the mode I fracture.

5.5.6 Effect of friction energy

The interfacial frictional stress (r) between a z-fibre and the surrounding laminate during frictional sliding will also affect the value of z-fibre bridging traction force. Typical range of the frictional stress was suggested to be between 10 and 80 MPa for the same range of z-fibre diameters, z-fibre material, laminate and resin systems used for this study (Zhang et al., 1999b; Liu and Mai, 2001 a; Cox, 1999),

Figure 5.34 shows the effect of different frictional stresses (10 r, 25 MPa) on delamination growth in terms of external load (P) against propagating delamination length (a)

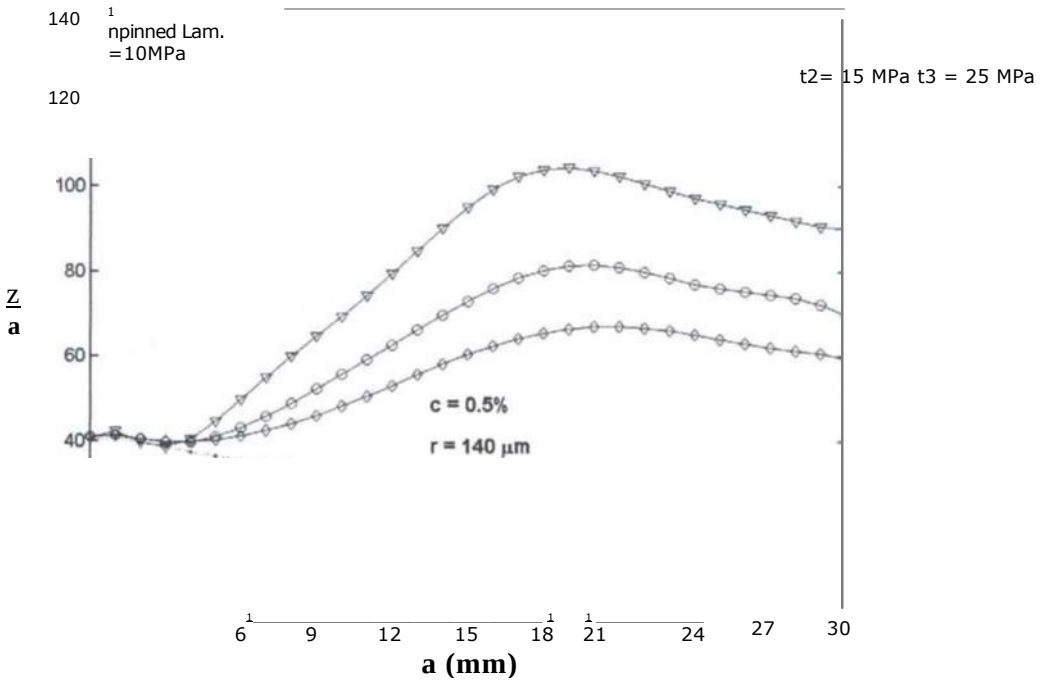

Figure 5.34 *Load* vs *delammatton length curves for different friction stresses (r_j).*

for the case of 0.28 mm diameter carbon pins with 0.5% density. Figure 5.35 presents the effect of different frictional stresses (10 r; 5 25 MPa) on delamination growth in terms of external load *(P)* against propagating delamination length *(a)* for the case of 2% density pinned laminate with 0.5 mm diameter carbon pins.

In both figures an increased friction shear stress (z} corresponds to an increased LSB effect. When z increases, the maximum load position shifts to the left of the graph indicating a smaller bridging domain (I)) but more resistant to further delamination. Therefore, the higher the frictional energy dissipated, the lower the number of z-pin rows actively bridging the crack and the smaller the crack length when stable constant bridging process occurs.

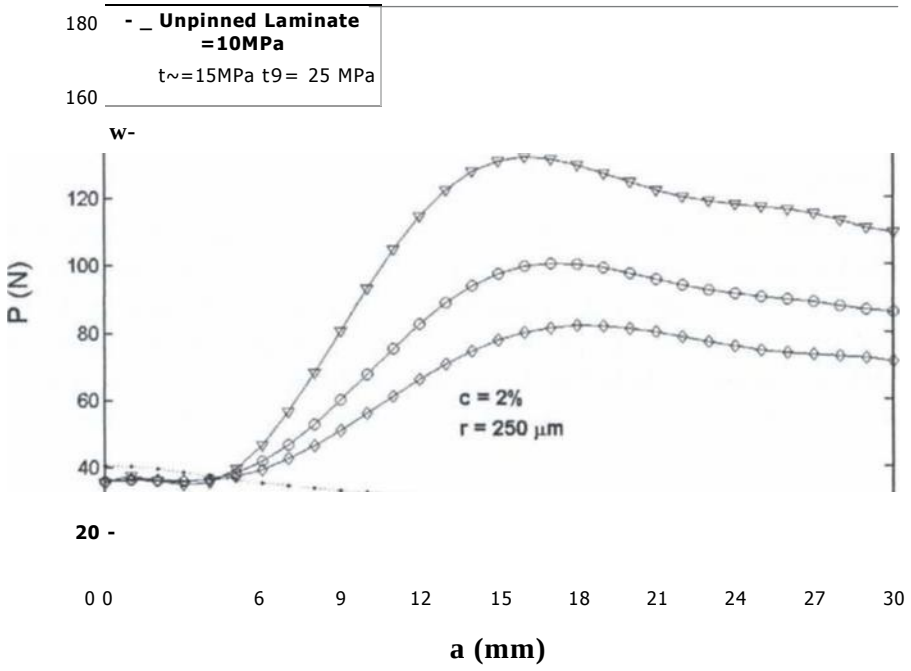

Figure 5.35 *Loud* vs *delamination length curves_for different friction stresses (r_f).*

Comparing the plots in figure 5.31 and 5.35 it is noticed that the 0.5% density pinned laminate with an assigned friction stress of 25 MPa could generate a LSB process (to resist delamination growth) that is equivalent to the one of a 1% density reinforced laminate with a friction shear stress of 15 MPa. Similarly comparing the plots in figure 5.32 and 5.36 a 2% density pinned laminate with an assigned friction stress of 25 MPa could generate a LSB process almost equivalent to the one of a 4% density reinforced laminate with a friction shear stress of 15 MPa.

Therefore from a design point of view, if higher frictional resistance can be achieved, then lower density z-pinning could be applied introducing less in-plane fibre waviness and less stiffness degTradation, saving weight in reinforcing the structure, and ultimately saving costs in the manufacturing process.

To achieve higher frictional *shear* stresses and thereof higher bridging forces different options are available: e.g. enhancing the z-fibre surface roughness, choosing appropriate resin system, optimising the radial stresses arising from the initial thermal mismatch between the z-fibres and surrounding materials.

5.5.7 Effect of laminate flexural rigidity and z-fibre insertion depth

The effect of the laminate flexural rigidity *El* is analysed by dealing at first, with the laminate axial moduli Er and therefore with the laminate thickness, which will obviously change the term I of the laminate flexural rigidity.

Figure 5.36 shows the effect of the laminate elastic moduli on delamination growth of z-pinned laminates. The slopes of the curves either before or after the LSB process being fully developed were almost constant for the different laminate elastic moduli ($^{E}_{r}$). Only the values for the starting delamination load, the maximum load, and relative crack position were affected by the difference in laminate elastic properties.

From the value of the crack Iength where LSB process attained a steady-state, it can be concluded that the more compliant the laminate arms, the fewer z-pin rows involved in the LSB process and the smaller the crack length for stable bridging will he. This conclusion can be further explained in the following figures, where laminate thickness changes are considered.

Figures 5.37-39 show the effects of DCB arm thickness (t) and z-fibre insertion depth (1_r} along with the results for the unpinned specimens. Firstly, the thickness variation affects laminate flexural rigidity and therefore as the previous computation (figure 5.36) a translation of the maximum load position to a longer delamination length for higher Ex. This condition is more evident for the change of thickness compared to the change of Ex, because the flexural rigidity is a cubic function of the laminate thickness.

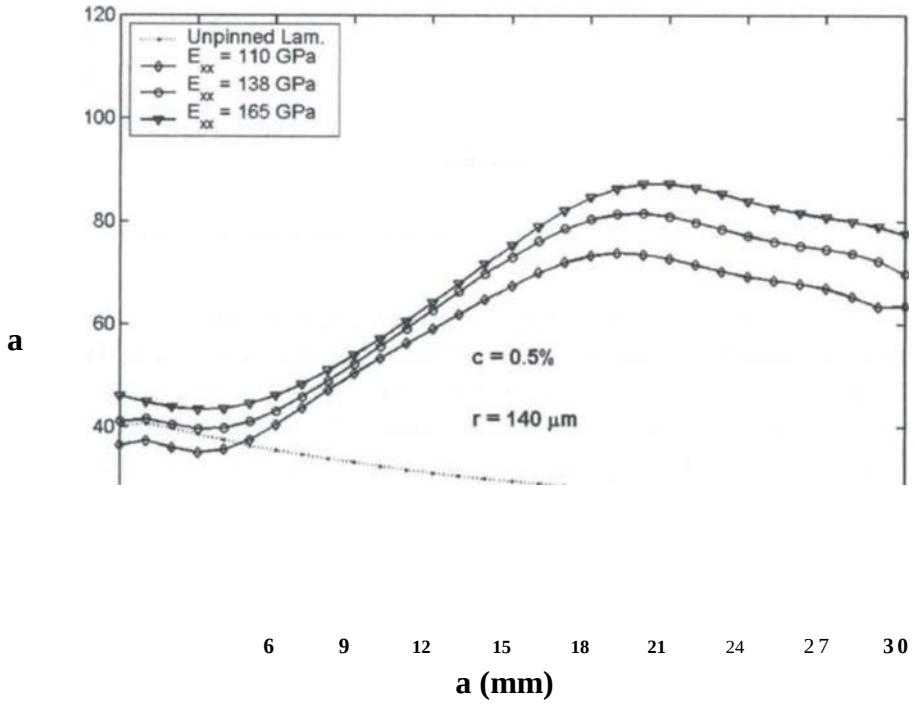

Figure 5.36 *Loud vs. delamination length curves: effect of laminate flexural rigidity (0.5% .pin density and 0.1-1 mm :-fihre radius).*

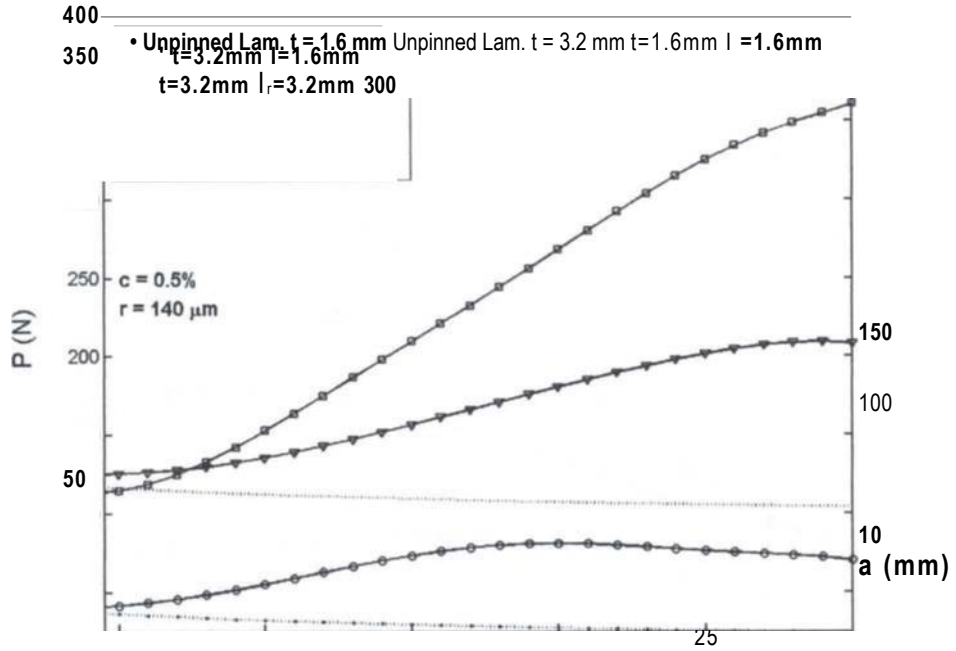

Figure *5.37 Loud* vs. *deluminution length curves: effects of laminate thickness & .pin insertion depth (0.5% :Tin density and 0.14 mm :-frhre radius).*

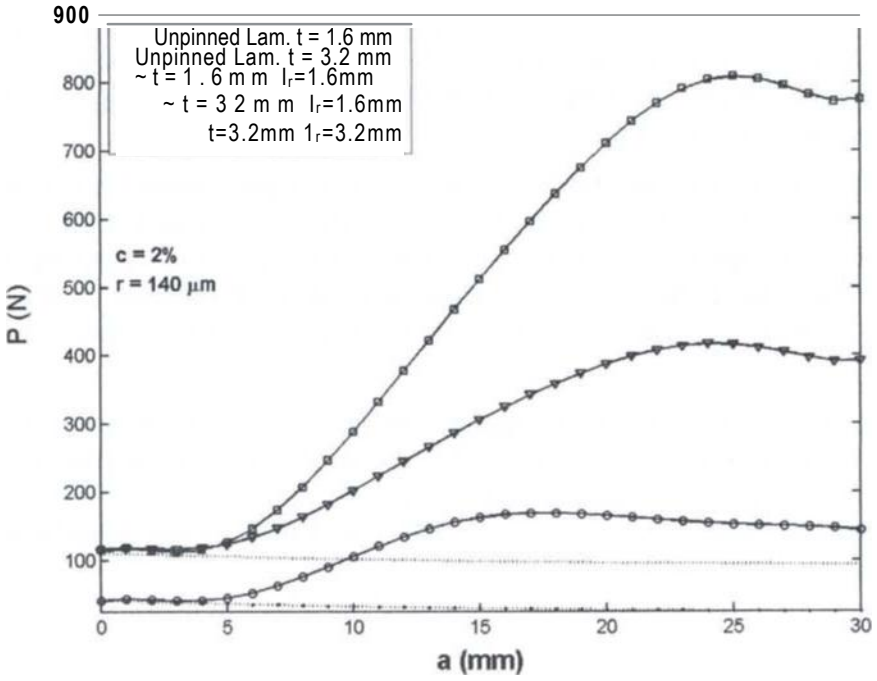

Figure *5.38 Load* vs. *delumination length curves: effects r f luminate thickness & =pin insertion depth (2% =pin density and 0.14* ***mm*** *=fibre radius).*

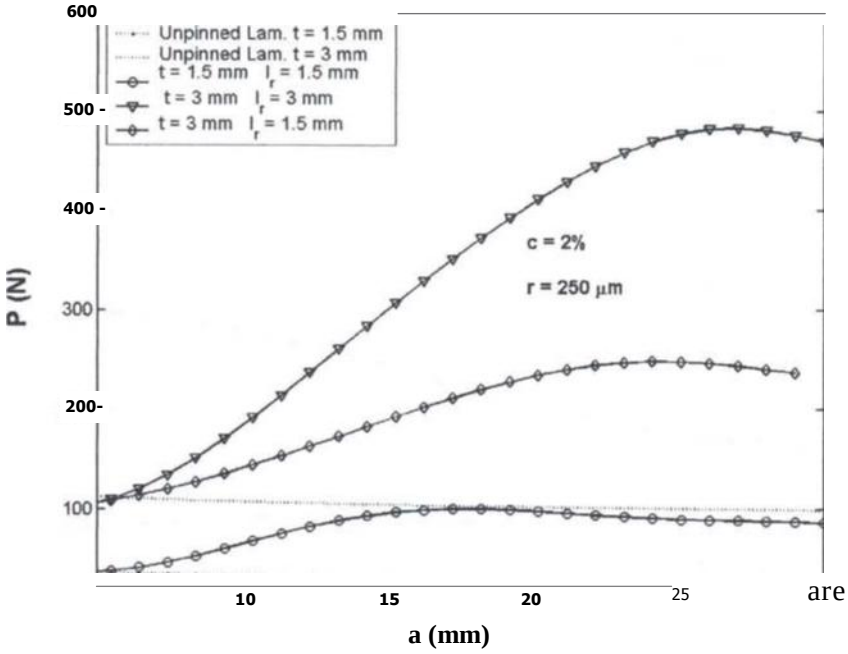

Figure 5.39 *Load* vs. *delamination length curves: effects (illuminate thickness & pin insertion depth (2% :pin density and 0.25 mm :-fibre radius).*

In figure 5.37, for the 3.2 mm thick (2t) laminate after 15 mm of delamination propagation the LSB is fully developed, but for the thicker laminate *(21--6.4 mm)* with the half z-pin embedding depth *(lr -3.2 mm), 30* mm crack is needed for all z-fibres actively bridging the crack wake, the fully pinned laminate has not yet attained the stable LSB process. Similarly in figure 5.38-39 for 2% pinned laminates, thicker laminates exhibited longer LSB zones with an higher number of working rows before z•-fibre stable pullout will commence.

In terms of the z-fibre insertion depth (!r}, for the same z-pin density and diameter, the deeper the z-fibre embedded in the laminate, the higher the required load would be to propagate the delamination. As for the case of the frictional stress, when the dominant mechanism is the z-pin pull-out process a more resistant LSB function can be obtained by a deeper embedding depth ($!_r$), the best embedding depth is the full laminate thickness.

It is also thought that for thicker laminates configuration the z-reinforcement bending stiffness may play a rule in the LSB mechanics definition. The assumptions of the derived micro-mechanical bridging laws may be revised for thicker laminate configurations with the bridging entities providing both closure forces and moments at the crack wake,

5.6 Conclusions

A numerical approach that combines the computational accuracy and versatility of the finite element method with an existing micro-mechanical material model was presented. Satisfactory agreement with experimental data was obtained. The numerical simulation

was executed by including as many parameters as possible to characterise the mode I fracture behaviour of this new reinforced laminate. The following conclusions may be drawn.

The z-fibre technique is very effective in enhancing the resistance to mode I delamination. Crack bridging enhances material resistance by partially shielding the crack tip from the applied delaminating loads. When z-fibre bridging mechanics is activated the order of the magnitudes of the bridging zone length and the total crack length become comparable, therefore the fracture analysis becomes a large scale bridging problem. When the LSB develops the maximum stress field and bending moment are placed away from the crack front but in the area where the large scale bridging is maximum. The bending moment can become severe that even though the delamination is suppressed a new failure mode could be introduced, that is in-plane failure of the delaminated DCB arms.

The load versus delamination length relation is found to be a better indicator of the fracture resistance and the large scale bridging effect. In order to activate the z-fibre bridging mechanism a delamination needs to propagate into the z-fibre field for several millimetres; the LSB can stabilize the crack growth and consequently raises the external load required to propagate the damage or temporarily arrests the crack. Therefore z-pinning is very useful for damage tolerant design. The LSB can become a stable process when z-fibre rows are pulled out from the laminate and new rows enter the LSB; the magnitude of LSB is independent of the crack length and an almost constant bridging area translates forward as the crack grows.

For the DCB configuration, it was found that z-pinning had almost no effect on the initiation of delamination growth from a starter crack, which is consistent with the experimental results and conclusions drawn in Chapter 3.

Delamination resistance can be further enhanced by choosing higher z-fibre density, increasing friction stress at the laminate and z-pin interface, employing finer z-fibre diameters and deeper z-fibre embedding depth. The laminate flexural rigidity defines the number of working z-pin rows and the crack length at which the large scale bridging process wi11 reach a steady state. Finally, the above conclusions should be applicable to mode I fracture analysis at structural levels.

Chapter 6

The energy balance and the fracture toughness of z-pinned laminates

6.1 Introduction

In a number of loading cases, resistance to damage growth, rather than strength, is the key property required by a composite structure, and therefore for design purposes it is very important to know the energy absorbing capabilities of a composite structure.

The proven ability of z-fibres to stabilize delamination growth and to enhance crack resistance can be further analysed from an energy point of view. The large scale bridging processes described in the previous chapter can absorb a significant amount of energy before a crack can extend any further. This absorbed energy would otherwise be used for crack propagation.

Every single z-reinforcement acting in the delamination wake can be seen as an absorber of energy and its micro-mechanics described by the bridging laws represents its energy absorbing capability. From a physical point of view the energy dissipated by a z-fibre is the energy used during pin elastic stretching, debonding and pullout from the laminate; mathematically the bridging law can be integrated numerically to work out the amount of irreversible energy dissipation during the bridging process.

The linear elastic fracture mechanics approach assumes that all the energy dissipations during delamination growth are due to the creation of a new fracture surface and they can therefore be contained in a single term within the energy balance equation. The presence of large scale bridging process away from the crack front, requires that the energy balance for delamination growth analysis has to be reformulated, introducing a term which takes into account the irreversible energy consumed by the z-pins away from the delamination front. Consequently different expressions for energy release rate terms involved in the fracture process can be worked out.

The different terms considered in the energy balance and energy release rate equations can be computed numerically from the finite element model presented in the previous chapter. This can be done by considering specific output results at every single numerical iteration i, and between two consecutive iterations i and i i- 1, respectively.

The use of standard data reduction methods and its validity for z-pinned fracture specimens is also tackled within this chapter, with useful considerations on crack bridging implications for fracture tests. It should be noticed that part of the work reported in this chapter has been formally published (Appendix A).

6.2 Fracture Mechanics with large scale bridging

For standard composite laminates the ability of the material to withstand the formation and propagation of delamination is controlled by a fracture toughness parameter, which is a material property. For z-pinned laminates several z-fibre parameters can determine the toughness of the laminate against delamination growth.

According to the Griffith fracture energy theory, an elastic body subjected to externally applied loads must satisfy the following energy balance:

$$W = [.J_e + [.I_x + \boldsymbol{F} \qquad \textbf{(6-1)}$$

Where, *W* is the external work, UIr the stored elastic energy, Uk the kinetic energy and *1* the total energy dissipation associated with delamination growth.

The total system energy dissipation F can be further expressed as:

$$F = U,_r + \boldsymbol{F} \qquad (6\text{-}2)$$

Where, U,r is the dissipated energy due to some irreversible mechanisms and rthe energy dissipation during the formation of a new crack stuface. This energy is consumed only in a very small cohesive zone at the crack front.

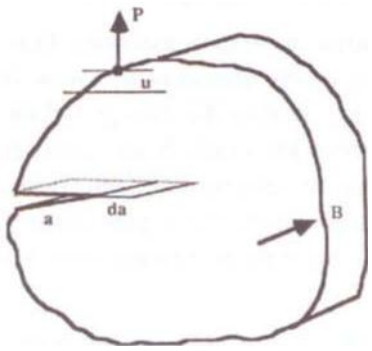

Figure 6.1 *General loading condition for a cracked body undergoing self=.similar crack growth.*

For simplicity if a crack of length a is considered, in a sheet of uniform thickness B, undergoing self-similar propagation (figure 6.1), the change of crack area is given by

$$ctrl = B \bullet da \qquad (6\text{-}3)$$

An increment in the crack area (dA) will require an increment in energy, but the overall energy balance of the system expressed by equation (6-1) remains valid, thus considering equation (6-2) the incremental expression of equation (6-1) becomes:

$$dW = dU, + dU_k + dU_{;r} + df \qquad \textbf{(6-4)}$$

Such kind of incremental energy balance expressions can include all crack growth scenarios including dissipation due to bridging (Urr) and high-load rate processes (Uk). For static fracture tests, the typical experimental loading rates are around 1 mmlmin under a displacement-controlled condition, so the variation of the kinetic energy of the system is negligible. Therefore equation (6-4) simplifies as:

$$dW = WI_{,} + dtl_{,r} + dl\sim \qquad (6\text{-}5)$$

According to the Griffith energy concept the available elastic energy in the system per unit crack area, when the area is assumed to be expressed by equation (6-3), can be written as:

$$G = \frac{dW}{d4d4B} \frac{dUe}{da} \;] \; \frac{(dW - dU,)}{da} \qquad (6\text{-}6)$$

Therefore equation (6-4) can be written as:

$$1\,(dW \; \frac{dUe}{da} - \frac{l \; ff \; dU_{,,}}{B \; da + da} \qquad (6\text{-}7)$$

With reference to mode I delamination of a z-pinned laminate, G1 can be defined as:

$$1 \qquad [\frac{d \quad W}{da} \; \frac{dU,}{da,f} \; 8 \; da \qquad (6\text{-}8)$$

Chapter 6 The energy balance and the fracture toughness of z-pinned laminates

$$G_f = \frac{1}{B}\frac{dF}{da} \qquad (6\text{-}9)$$

$$G_{IC} = \frac{1}{B}\frac{dW_{I,r}}{da} \qquad \textbf{(6-10)}$$

Where, Gf is the strain energy release rate due to applied force, G_{IC} the critical delamination toughness of the composite, and $\Gamma_{i,r}$ the energy dissipation rate due to the irreversible LSB z-pin process, which is the toughening mechanism of z-pinned laminates in terms of the fracture energy theory.

Therefore, the Griffith fracture criterion for z-pinned laminates can be written as:

$$G_I = G_{IC} + \Gamma_i \qquad (6\text{-}11)$$

Here on the left side of equation 6-11, the strain energy release rate G_I plays the role of the crack growth driving force, equals to the right side of equation 6-11, representing the toughness of the z-pinned laminate during crack growth, which is the crack growth resistance.

Fracture criteria for z-pinned laminate would therefore be:

$$G_I \geq G_{I,r} + \qquad \textbf{(6-12)}$$

For fracture, the energy release rate must be equal or greater than the total absorbed energy rates due to the intrinsic toughness of the composite material and the irreversible energy due to LSB mechanisms.

Z-pinned laminates should be designed to achieve a high value of U_{ss} that tinder certain crack conditions may exceed the energy necessary for the creation of a new fracture surface, hence to increase the *fracture* toughness. Thus the magnitude of Γ_{ss} is among the parameters that must be determined for the characterization of the fracture behaviour of z-pinned laminates.

The LEFM theory assumes that all energy dissipations for the creation of a new fracture surface d4 are included in the (term of equation (6-1) and (6-2). It is hence postulated that, during interlatninar delamination in a conventional un-reinforced laminate, the order of magnitude of other energy dissipation occurring away from the damage front zone are negligible, i.e. $U_{ss} = 0$.

The novelty dealing with through-thickness reinforced laminates is the large amount of energy absorption associated with the large scale bridging mechanics; hence the appearance

of the (I;$_r$ and D;r terms in the above derived equations. As a result of this, the material fracture toughness derived using the standard data reduction methods will apparently be improved. This explains the use of the term "apparent fracture toughness" in some recent publications (Cartie, 1999). It means that the structural fracture toughness of a z-pinned laminate has been enhanced.

More precisely it is thought that the material fracture toughness (G_k) relating to the formation of the plastic zone at the crack tip, and to other microscopic damage mechanics occurring during the formation of a new damage zone, can be assumed to be unaffected by the z-fibre presence. The structural toughness to delamination growth has been increased because of the presence of 0,r term in the energy rate equation.

The 0$_{,,}$ can be calculated by taking into account the overall fracture process occurred in the structure. In other words, in a z-pinned stricture, the toughness can become a function of the geometrical and physical parameters of both the laminate and the z-reinforcement. In this sense the toughness appears to be a structural property rather than an independent material property.

6.3 FE computational techniques

6.3.1 Computational energy terms and energy rates

Although the LSB process has a beneficial effect in applications of composites since it increases interlaminar fracture toughness, difficulties can arise in the interpretation of the experimental data. Often during the data analysis it is not possible to separate the different energy terms of equations 6-1 and 6-2, and thus to compute the different *energy rates* during crack propagation (equation 6-11). Using the finite element method, with a modelling methodology that has been explained in the previous chapter, it is possible to compute the different energy terms of the equation 6-1. It is therefore possible to calculate the different energy rates of equation 6-11 under mode I loading condition in the case where LSB exists.

A numerical integration of element stresses and strains over each element volume can be performed. Similarly the nodal forces over the total displacements can be integrated. The displacements refer to those occurring for z-fibre interface elements during crack propagation. Using this method, both the energy release rate corresponding to the formation of new crack area and the energy dissipation, which comes mainly from the bridging effect, can be computed.

From the finite element results the total external work at *i-1h* iteration, can be determined by integrating the reaction load of the master node where the incremental displacement is applied, over the total imposed displacement[16]:

$$w = JP`d5^{z} \qquad dWl = 0 \qquad \textbf{(6-13)}$$

The model total stored elastic energy at the i-th iteration can be computed by integrating over each volume V, of the elements involved and summating each contribution over the total number of elements n:

$$U\sim] = \sum_{J=I} Ja,(x,y,z)\bullet eJ(x,y,z)\bullet dV \qquad \textbf{(6-14)}$$

The strain energy release rate computation in equation (5-3), Chapter 5, is shown below.

$$\frac{1}{B}\frac{d\sim I_{f,}}{da} \qquad \_u. \qquad \textbf{(6-15)}$$

Where the crack increment d coincides with the element size at the crack front, B is the model width, and $-(J$ is the incremental strain energy of the FE model between the two runs. The VCC technique was also introduced in Chapter 5 as a means for computing strain energy release rate.

The total irreversible energy can be obtained from the summation over the total number of working z-fibres, by integration of the interface element nodal forces F3, representative of the single z-fibre bridging law, over each related nodal displacement u3. In figure 6.2 the irreversible energy computation is schematically represented when 3 interface z-fibre elements are assumed to bridge the crack.

When a total of s interface elements are active we can define, in the crack reference system:

$$uir = \sum_{J=i\ 0}^{s\ u3} \int p.,'(x,y,z).du \qquad \textbf{(6-16)}$$

---

16 **Because of die assumption of a displacement controlled analysis during the crack growth, the variation of the tau] external work will be zero.**

Where at the *i-th* iteration F; is the nodal force exerted by the j-th interface element and u is the relative nodal displacement.

The irreversible energy rate is then assumed to be calculated with the following formula:

$$\frac{1}{B}\frac{XI_{rr}}{da} \qquad \frac{\mathbf{U}_{r''} - U_{ir}}{BA} \qquad \textbf{(6-17)}$$

Where ❑ and B have been previously defined, and f1,a^{+} -t1° is the incremental irreversible energy between two FE runs. Some computations relative to the interface nodal forces of a 0.5% reinforced DCB are presented in figure 6.3. The nodal forces are plotted against crack length and the number of working z-pin rows can be easily established for different crack lengths.

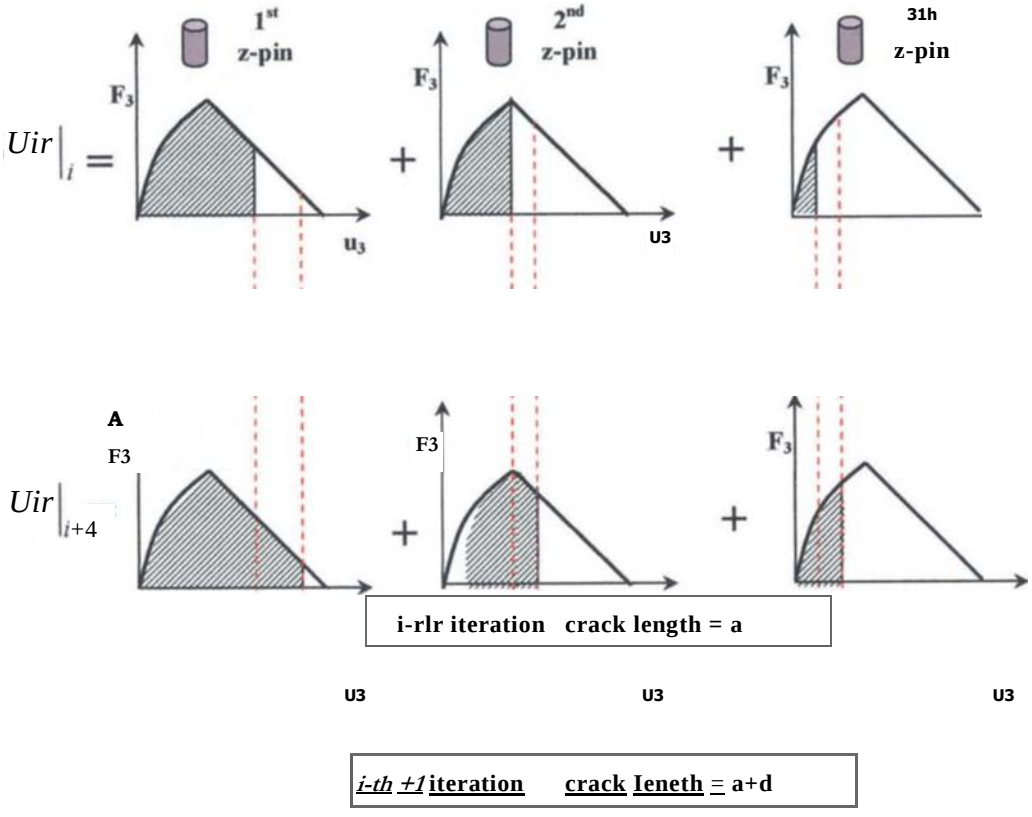

Figure 6.2 *Schematic of irreversible energy (hr computation at iteration i-th and r-th . 1, fit• crack length a, and a . A respectively, when 3 z -pins are active. The incremental variation between the two FE runs is also outlined.*

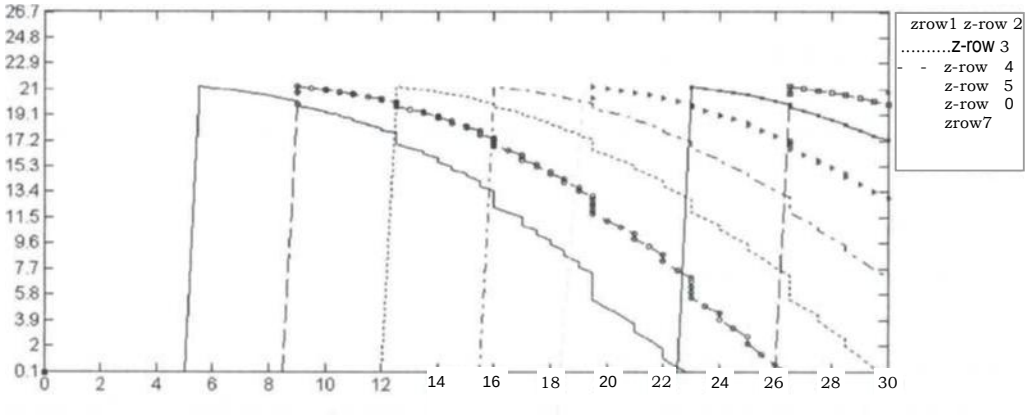

Figure 6.3 *Computational interface element nodal _forces* F3 *for 7 z-fIbre* rows *against crack length a c = 0.5% and r 15 MPa.*

Given the interface element nodal forces such as those of f i r e 6.3 it is possible to apply equation 6-17 for the computation of the irreversible energy rate.

It has to be pointed out that as delamination propagates some interface elements are activated and some others are deactivated as shown in figures 6.3. In the numerical implementation of equations 6-15 and 6-17, relatively scattered data can be found due to relatively large or small variations in the energy terms for any discrete crack advance A. Physically this large or small variation is associated with either a new z-fibre row bridging the crack, or the pullout failure of a z-fibre row. Polynomial interpolation of the FE computational results is therefore used to establish the trend of the energy rates during crack growth.

6.3.2 VCCT for FE models with interface elements

In Chapter 5 it was stated that the direct application of equation 6-15 would give very similar results for strain energy release value as the one calculated by mean of the VCCT, providing the delamination increment (A) was small compared to the overall delamination length (Martin, 1998), In the case of the z-pinned FE model, those strain energy values did not coincide and the difference was due to the irreversible energy rate.

Applying equation 6-15, the total strain energy release rate is computed and therefore both contribution for the creation of a new fracture surface and energy consumed during z-pin failure are included. When applying the VVCT on the other hand, the crack front nodal force values, as well as crack nodal displacements (equation 5-5 to 5-8), are lowered because of the LSB process. The assumed condition for crack growth (equation 5-23 from Chapter 5) stated that the crack driving force computed by means of the VCCT should exceed the material fracture toughness:

$$G_{azcr} = G/\ 1\ j\ G\sim \quad \textbf{(6-18)}$$

The computational G; FN values are found to be comparable in terms of their order of magnitude of (. which refers to the toughness of the unpinned material, this is due to the bridging forces of the interface elements unloading the crack front nodal forces and limiting the opening displacements, in terms of energy rates taking into account equation 6-11 and 6-18 it is possible to write:

$$G,^{E(} = Ci - 0 \quad \textbf{(6-19)}$$

Where G) , is the strain energy computed using the VCCT and G, is the total strain energy release rate computed using equation (6-15). These implications are further explained in figure 6.4, which is divided in three sub-plots: load versus crack length such as those presented in the previous chapter. percentage of load increment required to propagate delamination, 3-D G-plot. Other figures are provided in Appendix E for different z-pin parameters.

The 3-D plot shows the interpolation of the computed data. The G is an out-put array from the FE analysis: the columns represent the different delamination lengths (a) and the rows the number of required sub-steps to propagate delamination (N_s,,h), the data set refers to the G ' (Jim^2) computed values at the delamination front using the VCCT.

From figure 6.4 sub-plot (a), it is possible to work out when delamination reaches a z-fibre row from the condition of the load being incremental and the crack length being constant as explained in detail in Chapter 5. Due to the LSB shielding effect, G; values at crack front drop (delamination arrest) and up to 8-10 load increments *(N4«b)* are necessary to satisfy equation 6-18 and propagate the crack. It is also proved that G ' values are always comparable with the intrinsic fracture toughness G1c of the unpinned material, only the number of load increments required for delamination propagation changes with z-fibre micro-mechanical parameters and laminate flexural rigidity (see Appendix E).

Figure 6.4 *Delamination analysis (c = 0.5%, r = 140μm, τ =15 MPa): (a) Load P against delamination length; (b) percentage of load increment to propagate delamination; (c) G-matrix array interpolation of* G_I^{FEM} *computed using VCCT .*

6.4 Results and discussion

The *energy* balance described by equation 6-1 and 6-2 was calculated from the FE outputs. Figure 6.5 to 6.8 show the individual energy components of the DCB FE model plotted against delamination length for different z-fibre densities c. The plots refer to polynomial interpolation of the FE output results. Other plots are enclosed in Appendix E for different z-pin parameters.

As expected when the delamination propagated within the first 5 mm (no z-pins in this region), the difference between the total external work (W) and the elastic deformation energy (U_P} equalled the fracture energy used at the delamination front for the creation of a new fracture surface (I) (figure 6.5a).

When the delamination propagated into the z-pinned field the irreversible energy term due to the LSB process started rising. The LEFM assumption remained valid until the crack length reaches values between 10 and 15 mm, depending on the z-pin density and radii (figure 6.5b). From this stage the energy absorbed by the LSB mechanism (U;$_r$) became higher than the *energy* dissipated at the delamination front. The term Ufr can no longer be neglected. Moreover, since $_{Ulrr}$ increased significantly with delamination growth, the difference between the external work *(W}* and the stored deformation energy *(U_r)* had to increase in order to provide more driving force for crack growth. Based on these findings, a good design approach for z-fibre reinforced structures should aim at maximizing the energy absorption capability {

The effect of the diffe
the fracture energy
a-composite material,
th radius.

Figure 6.9 presents nc
shows the increasing
have been obtained b
unpinned DCB mode
present in the unpinr
surface energy values

It can be seen that the
much as 12 times the
un-reinforced iaminat
affected by z-fibre der

Since
of the
ty and

arrow
curves
of the
as not
acture
rases.

;orb as
itional
rongly

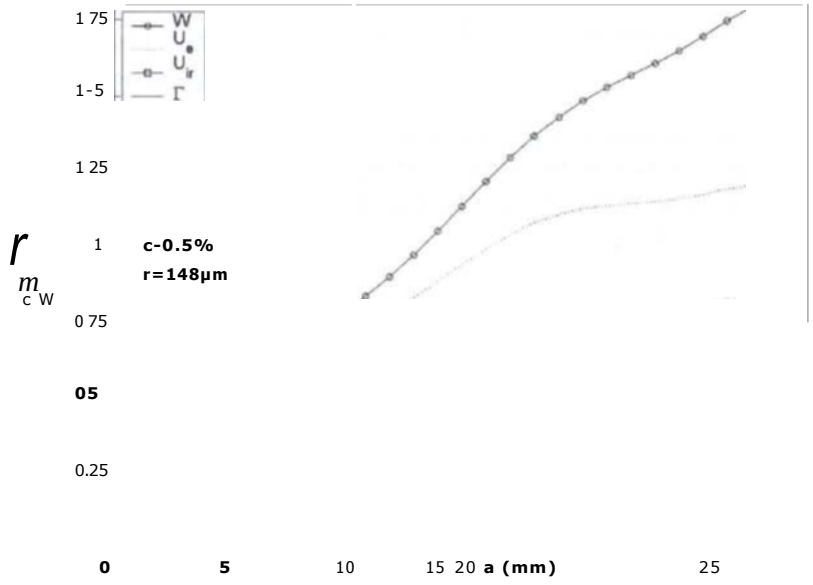

(a)

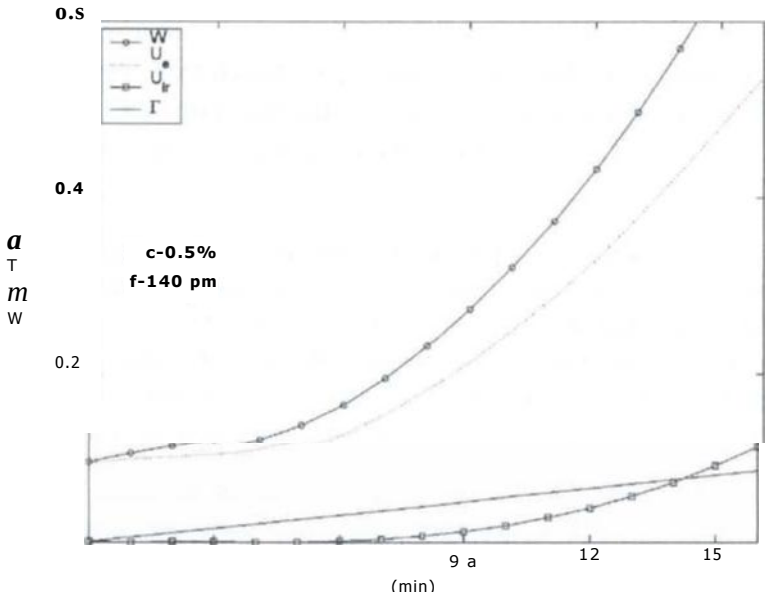

(b)

Figure 6.5 *Computational energy terms, for reinforced 1)C'B /'Is model (c = 0.5%, r = 141) pm): (a) total crack length; (h) end of validity of LEI M assumption.*

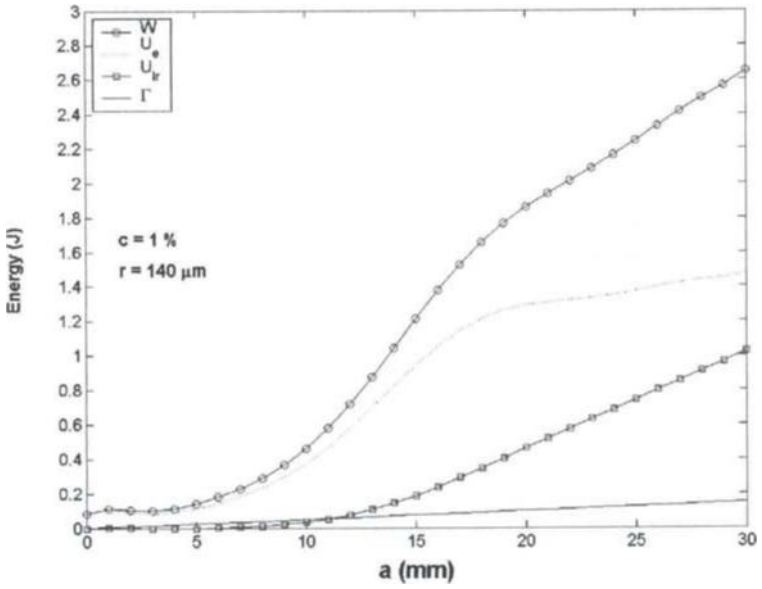

Figure 6.6 *Energy terms Jnrz-reinforced DCB FE model: c - 1%, r = 140 pm.*

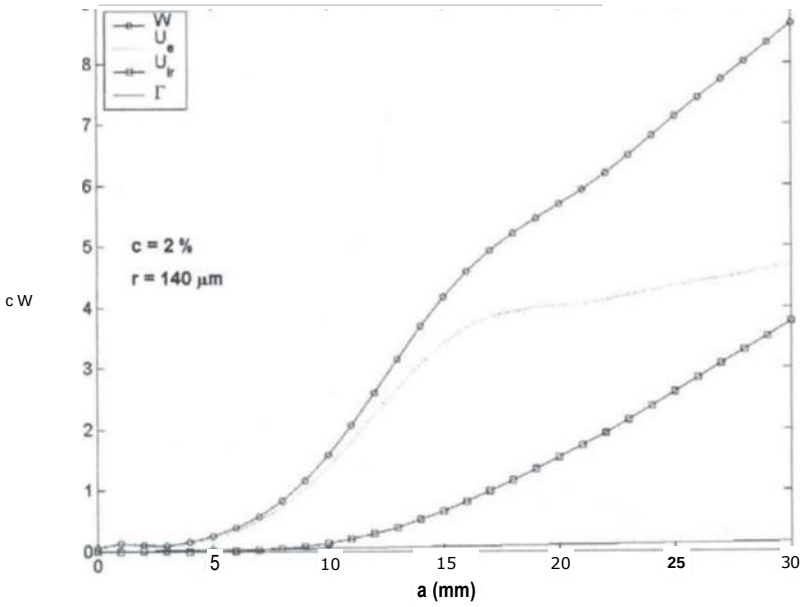

Figure 6.7 *Energy terms for z-reinforced DCB FE model: c = 2%, r 14() /ma.*

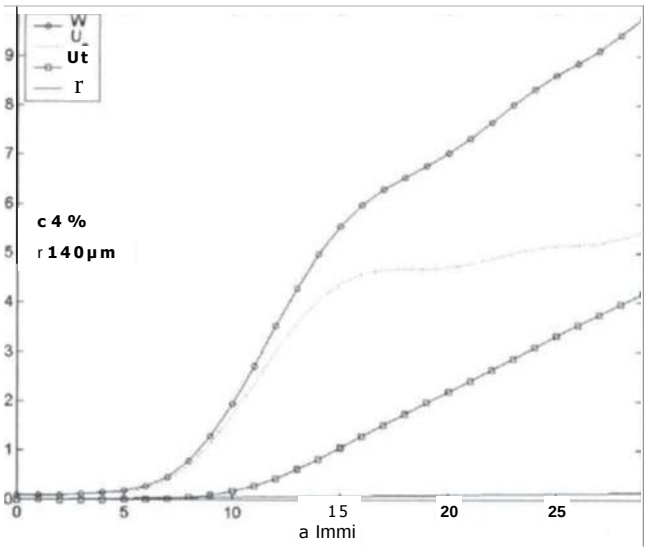

Figure 6.8 *Energy terms for z-reinforced IX 'B I,E model: c = 4%, r - 140 pm.*

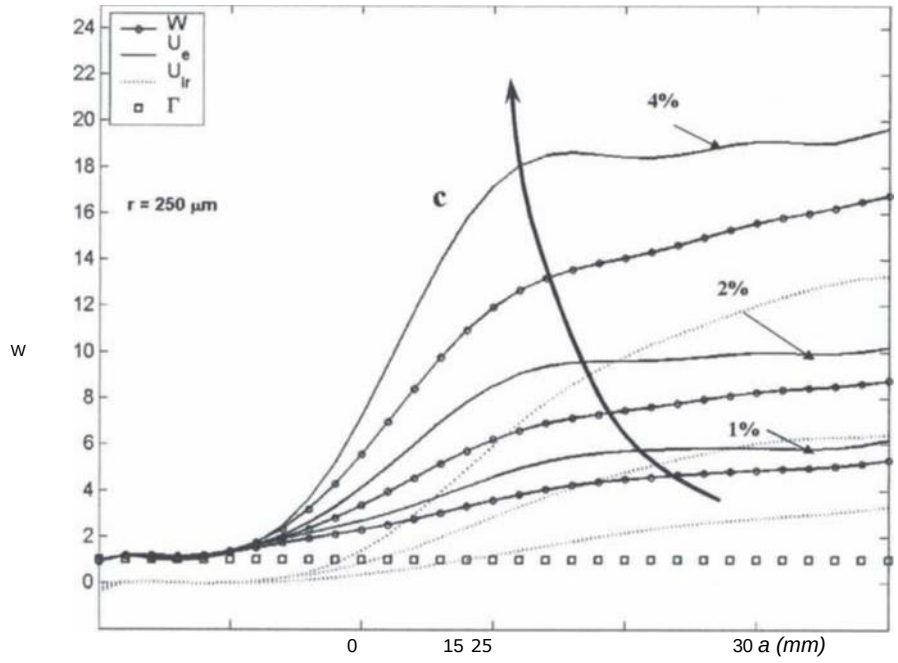

W

Figure 6.9 *Normalised FE energy computations (Ever)for different z-fibre densities.*

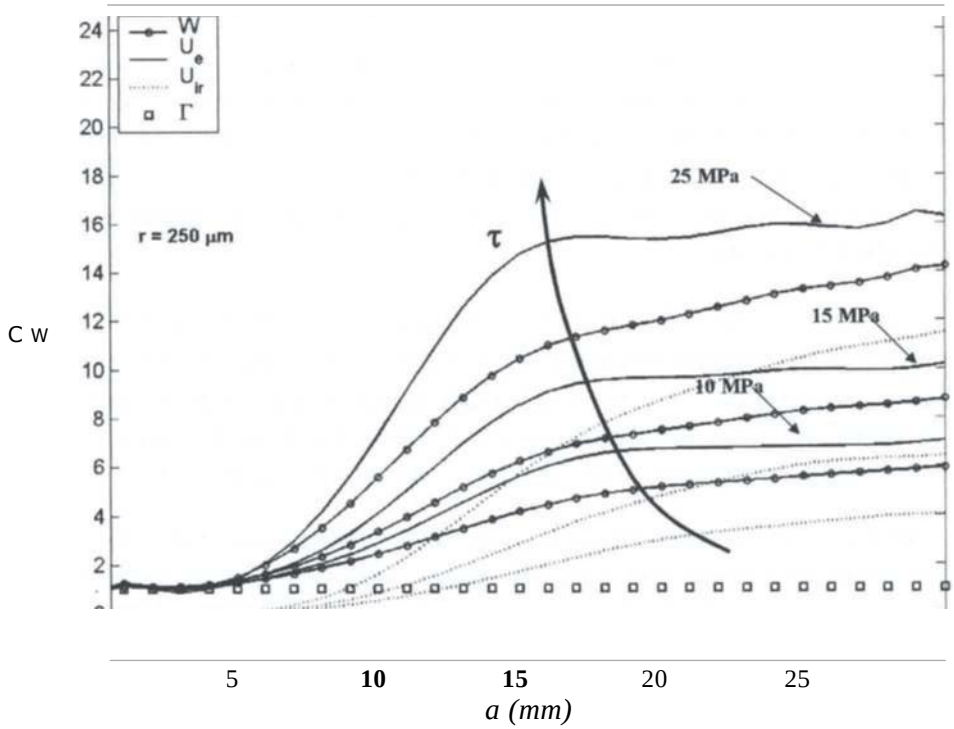

Figure 6.10 *Normalised **FE** ener ry computations (Energy,) Pr deferent z-/ibre ¸friction stresses.*

As a consequence of the LSB shielding of the delamination front, the elastic energy stored in the DCB arms can also attain values *as* much *as* 6, 10 and 20 times larger than the un-reinforced laminate for the case of 1%, 2% and 4% z-fibre densities, respectively. This latest finding is considered to affect considerably the crack growth rate. Thus when the LSB process ends, the enormous amount of stored elastic energy available for crack growth leads to a significant increase in crack propagation rate; in equation 6.1 the kinetic energy term should then be taken into account.

Figure 6.10 shows normalised energy terms for different z-pin friction stresses, for a 2% pin density. Once again the energy consumed at the crack front can be as much as one order of magnitude lower than the energy consumed within the LSB area. The external work required to row the delamination, can be up to 14 times the work required to propagate the crack for 30 mm in an unpinned laminate.

The energy rates per unit crack extension area, G1, 4 , and G1 , as defined by equation 6-11 were also calculated, and are shown from figures 6.1 i to 6.14. The plots present energy

rates against delamination length (a), which are commonly called R-curves in fracture mechanics.

At the small cohesive zone at the crack tip, the fracture surface energy rate G_{K-} has a constant value of 250 J/m^2 for both pinned and unpinned laminates. The "square" and "triangle" symbols represent the computational results of strain energy release rate $(^{G}_{I})$ (computed using eq. 6-15) and energy dissipation rare $_{((D«)}$ (eq. 6-17), respectively. The smooth lines are fitted curves. The results confirm the energy rate balance for z-pinned laminates described by eq. (6-11).

In figures 6.11 and 6.12, within the first 5 mm of crack growth, there is not any LSB. When the crack enters into the z-pinned field the irreversible energy rate (O_i,) is larger then the crack tip fracture toughness (G,), the total strain energy release rate G_I must overcome both terms to propagate delamination. Figures 6.13 and 6.14 show the trend of the energy rates for different z-pin parameters. Other plots are reported in Appendix E.

When the LSB becomes a stable process, with the bridging zone fiilly developed, it is possible to compute an average value for the energy rates of z-pinned laminates. The bar charts in figure 6.15 refer to averaged energy rate values for different z-fibre physical and material parameters. Similar plots for other z-pin parameters are enclosed in Appendix E.

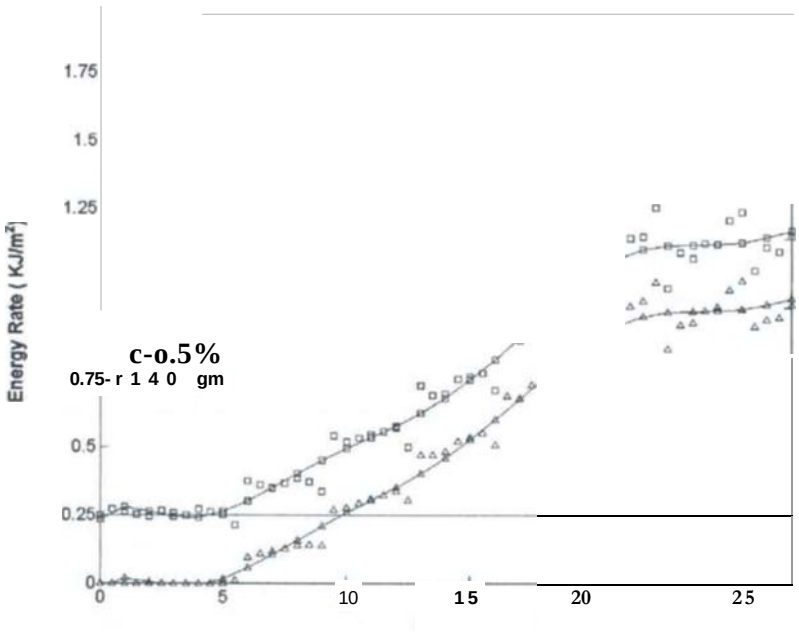

Figure 6.11 *C'amputed energy rates (ICI m') far z-pinned /CB: c - 11,5%, r --* ***1401mi.***

Chapter 6 The energy balance and the fracture toughness of z-pinned laminates

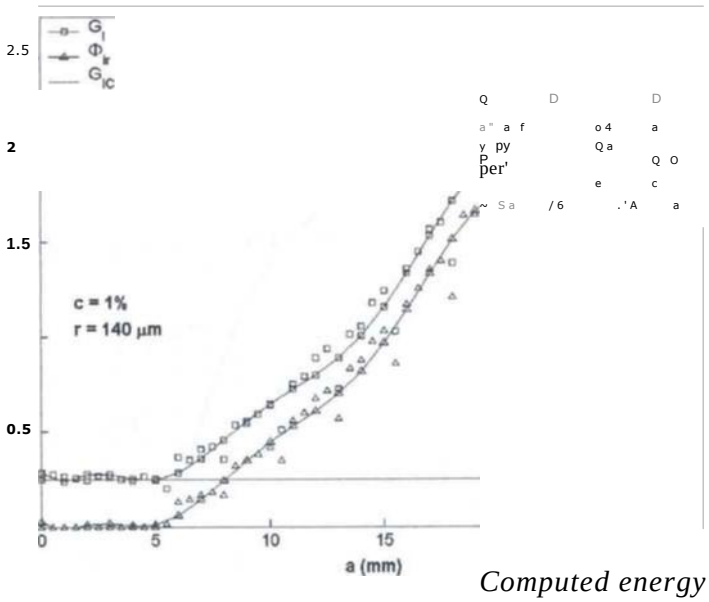

20

Figure 6.12 *Computed energy rates (K.l m) for pinned DCB: c = 1%, r - 140 pm.*

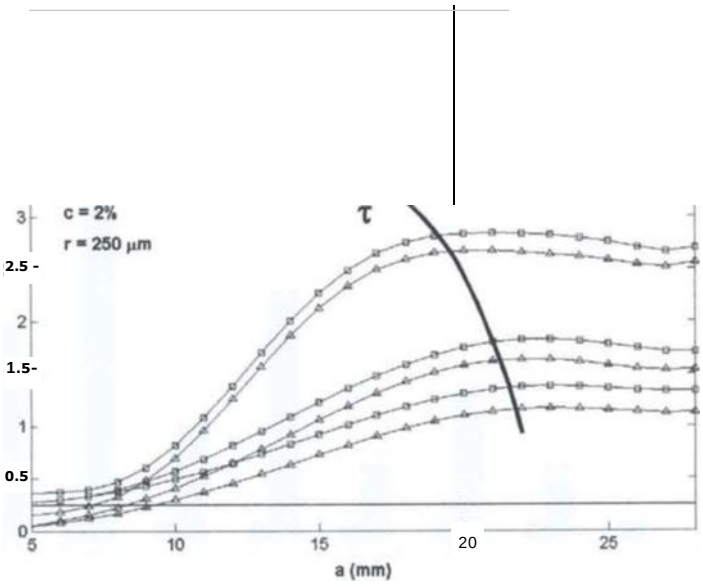

Figure 6.13 *Computed energy rates (m^2) for z -pinned DCB (c = 2%, r = 250 for increasing;* friction stresses *at pin-laminate interface.*

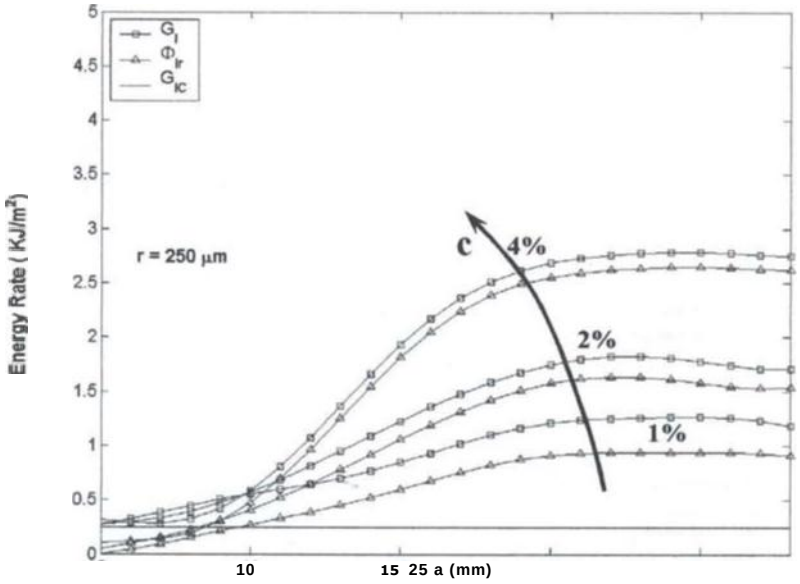

Figure 6.14 *Computed energy rates (Kt:'m') forz-pinned 1X'R (r = 250 arm} for increasing pin densities,*

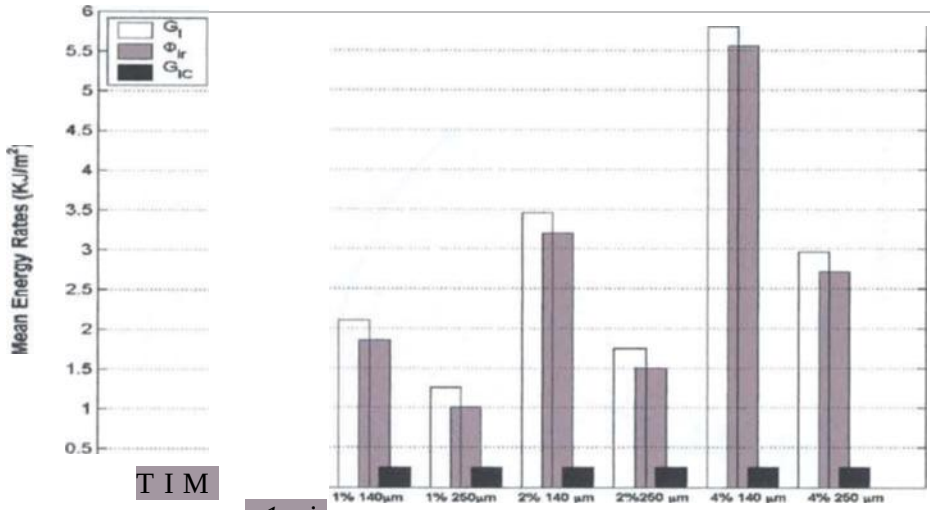

Figure 6.15 *Averaged energy rates during stable LSB process. far different z-pin densities and radii.*

6.5 Conclusions

In terms of energy balance, z-pinned laminates have the capacity to absorb significant quantities of energry. During delamination growth the large scale bridging process consumes considerable amounts of energy that otherwise would be used for delamination growth.

The assumption made by the LEFM that all energy dissipations are included in the fracture energy and confined within the damage front is not valid for z-pinned laminates. The novel and strong benefit dealing with through-thickness reinforced laminates is the large amount of energy absorption associated with the large scale bridging mechanics. Hence the appearance of the irreversible energy dissipation which becomes the dominant term in the energy equations to enhance the delamination resistance.

It is therefore concluded that the material fracture toughness (G_A.) associated with the fracture mechanics occurring at the crack tip can be assumed to be unaffected by the z-fibre presence, whilst the structural toughness to delamination growth has been increased because of the presence of O_{rr} in the energy rate equation. As a result of this, the material

fracture toughness derived using the standard data reduction methods for DCB specimens will be apparently improved, this explains the term used in some recent publications "apparent fracture toughness". Rather than a material parameter the toughness to delamination growth seems to depend on the z-pin micromechanics and its interaction with the laminate geometry and fracture process; in this sense it can be referred to as "structural" fracture toughness.

Computational curves for the energy balance and energy rates were also determined showing that the LSB process absorbed up to 14 times the energy consumed at the crack front. At the same time, the amount of elastic energy stored in the DCB arms was shown to be up to 18 times higher than the unpinned case, with 16 times more work required to propagate the crack,

Structural fracture toughness values of around 2500 Jim` were also achieved. Considering different z-pin micro-mechanical parameters, these values were one order of magnitude higher than typical critical fracture toughness values obtained for unpinned LUD laminates.

Chapter 7
Structural behaviour of through-thickness reinforced composite joints

7.1 Introduction

Analysis and design of strong and durable joints of composite structural parts is now recognized as an engineering problem of prime importance. Adhesively bonded composite joints are the principal alternative to the conventional mechanically fastened joints and have been used in the aerospace and marine industry for more than a decade (Matthews, 1990; Hashim et al., 1998; Knox et al., 2001). Such joints could be even more widely used if inexpensive methods could be demonstrated for enhancing their strength and damage tolerance. One promising approach is the incorporation of TTR such as metallic or fibrous pins.

This method was first motivated by the quest for high damage tolerance in airframe structures (Rugg et al., 1998) but a preliminary study has recently investigated their suitability for joining pipelines (Lees, 2002; 2003), By an attractively inexpensive processing method, in which pins were inserted into holes drilled through bonded joint sections in already-cured specimens, Lees found significant gains in ultimate strength and resistance to debond cracking at the bond line (Lees, 2003).

The optimal design of pin-reinforced joints is a complex problem. The experiments of Lees showed that ultimate strength tends to rise with the density and size of the pins, but the rise can also vary with pin material (carbon or glass fibre composite pins). Furthermore, the effectiveness of the pins in deterring delamination at the bond-line depends on where in the joint area the pins were inserted; pins are more useful if inserted near the ends of the joint. Experiments on pin materials more relevant to airframes, namely pins in carbon/epoxy laminate joints, show that the angle at which the pins are inserted has a strong effect on the mechanics of delamination resistance (Rugg et al., 1998). Optimal angling of the pins is expected to be especially important in cases of mixed mode delamination.

Accurate simulations of debonding and the ultimate failure of pinned joints can streamline the design task, avoiding unnecessary and expensive fabricate-and-test cycles. The simulations must deal with the true geometry of the joint, since geometry determines mode ratio of the debond crack, and include a physically realistic model of the deformation of the pins to simulate the large deformations they experience en route to ultimate failure. This chapter presents an efficient formulation of such a simulation and demonstrates its accuracy by comparison with test data from Lees (2003). The model used for the pins is that developed by Cox and presented in Chapter 4, which is believed valid for pins of arbitrary initial orientation, through large deformations (Cox

and Sridhar, 2002). The model is incorporated here as prescribed bridging tractions, which act on the surfaces of the adherends when a debond crack exists. The model prescribes the bridging tractions as functions of the local mixed-mode crack displacement. Once a joint geometry has been meshed, the simulations allow consideration of arbitrarily varied pin parameters with great ease simply by varying the incorporated bridging tractions. If the pin locations are varied, it is only necessary that a single pair of nodes be available in the adherend meshes at each pin location - a nonlinear spring element between the pair of nodes will fully represent the action of the pin.

The adhesive bonded single-lap joint has been studied extensively with most of the analytical and theoretical work being focussed on predicting the state of the stress within the thin adhesive layer (Goland and Reissner, 1944; Hart-Smith, 1973; Adams, 1986; MIL-Handbook-Chp.5, 1998), but no such kind of study has been reported on pinned or z-pinned joints. The fracture process of the single lap joint debonding is a mixed mode failure (Tong, 1998b), therefore mixed mode failure criteria have to be implemented for the single lap joint failure strength prediction (Ducept et al., 2000).

The FE method has provided a robust and flexible tool to perform analyses involving processes such as non linear joint gross rotation, adhesive failure, mixed mode debonding and TTR bridging mechanics simulation (Glaesgenn et aI., 1999; Bogdanovich and Kizhakkethara, 1999; Grassi and Zhang, 2003)_

The *objective of* this study *is* to quantify the effect of TTR on adhesively bonded composite joints and to provide an envelope of critical behaviour of TTR joints to act as a basis for design guidance. The effect of TTR on the failure of a curved single lap joint (CSL,I) configuration was studied in a combined experimental, analytical and numerical analysis. Failure mechanisms and failure loads of unreinforced and reinforced joints will also be determined. It should be noted that part of the work reported in this chapter has been formally submitted for publication (Appendix A).

7.2 Mechanically fastened or bonded joints vs. through-thickness reinforced joints

Often it is impossible to manufacture a complete component as a unitised structure, and hence separate sections of the component need to be joined together. This is often achieved through the use of bonded or mechanically fastened bolted joints. The analysis of bonded or bolted composite joints has received considerable attention over the past three decades. Standard practice guidelines of bonded and bolted composite joints have been documented in (Hart-Smith, 1973; Matthews, 1990).

Weight efficient stiffened skin panels are often used in aerospace composite structure design. However, the deformation associated with post-buckling response or internal pressure load can produce severe bending and shear loads on the skin panel. These loads may induce large peel and shear stresses at the interface between the stiffener flange and the skin, which are sufficient to cause stiffener debonding and delamination between the co-cured or co-bonded composite parts.

Rather than bolting or bonding parts, the method for joining composite sections by means of z-pinning or simply using small diameter carbon pins inserted into drilled

holes of an already-cured composite part is discussed in this section. The potential benefits of z-pin reinforced joints have been exploited in chapter 2, sections 2.3 and 2.4,1 and include improved manufacturability, increased static strength and increased damage tolerance.

Lightweight carbon fibre composite (CFC) T -joints representative of the skin-stiffener sub-structural components and nodal joint to transmit load along orthogonal stiffeners across a joint attached to a CFC skin are illustrated in figure 7.1. The potential application of z-pinning to enhance the stiffener flange-skin interface of those kinds of structural joints is currently under consideration within the technical partners of the MERCURYM consortium.

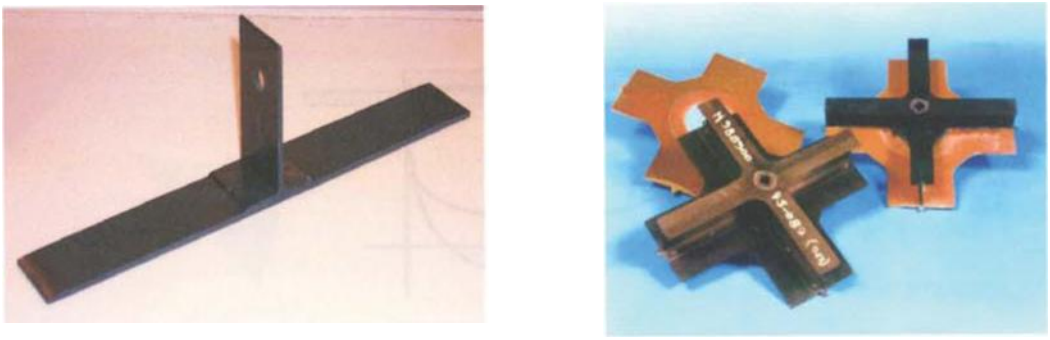

(a) (b)

Figure 7.1 *Lightweight carbon fibre composite joints: (a) T-joint[''](#); (h) nodal join[ts](#).*

Possible T -joint configurations are presented in figure 7.2. The bolts of the T-joint (a) represent a structural redundancy, they can carry load only when the stiffener-skin interface has failed completely. A z-pinned T -joint might stop delamination growing at the stiffener-skin interface, therefore still ensuring a continuous load path between the skin and the stiffeners.

(a) (b)

Figure 7.2 *T -joints structural design: (a) bolted co-bonded T joint;* (b) *1-pinned co-bonded T joint.*

FE models of simple joint configuration along with coupon testing may help to gain insight the z-pinned or pinned joint behaviour and to compare their performances

' Courtesy of QinetiQ Ltd, Farnborough, 2003. '"
Courtesy of Hurel Hispano, Burnley, 2003.

against bolted or bonded joints. Bearing this idea in mind, the structural analysis of a single lap-shear joint will be the subject *of* the remaining parts of this chapter.

7.2.1 Single-lap shear joint

For a single-lap adhesively bonded joint subjected to a tensile load, high shear and transverse normal stresses develop at the ends of the joint, where the stresses increase from zero at the free surface to some maximum value over a very short distance (Adams, 1997) as illustrated in figure 7.3. These stress peaks eventually initiate cracking causing the adhesive bond to break down andlor delamination to occur, leading to failure.

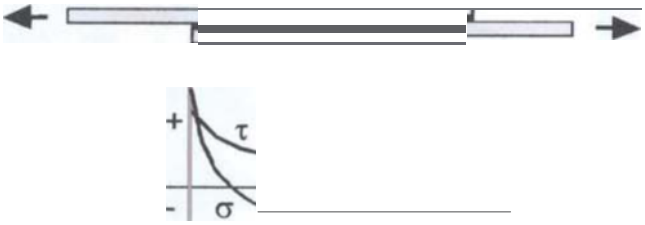

Figure *7.3 Schematic diagram of stresses in a single-lap adhesive joint where the adhesive shear stress is r, and a is the transverse peel stress at the adhesive bond.*

The bonded composite joints are weak in transferring shear and transverse loads and exhibit very low damage tolerance; once the adhesive bond failure has started the debond propagates rapidly leading to catastrophic joint failure.

The insertion of bolts through an adhesive joint is considered as a `fail safe' design to prevent damage from spreading should the adhesive joint fail. In a boltedlbonded joint, the adhesive provides the joint stiffness in the serviceability state but prior to the bond breaking down the influence of the bolts is negligible. With increasing load, the stress peaks at the ends of the joint lead to cracking in the adhesive andlor adherends and much of the load is transferred to the bolts. The system is then almost analogous to a bolted-only joint and the joint is designed for this load case.

To avoid the various failure modes of a bolted (figure 7,4), e.g. net or cleavage tension, shear-out or bearing failures, good detailing practice is followed. For example, the Eurocomp design guidelines (Mottram, 1998) suggest that for a typical bolt diameter of d, a minimum end distance of 3d, a minimum side distance of 1.5d and a minimum distance between holes of > 3d, are required. Although there are advantages to bolted and bonded joints, in particular in terms of robustness, ultimately, there is little enhancement of capacity by combining the two systems. Indeed the Eurocomp guide states that, generally, combining bonding and bolting will not improve the joint strength compared to that of a well designed undamaged bonded joint. Furthermore the bolting process can be expensive and add a weight penalty to the structure.

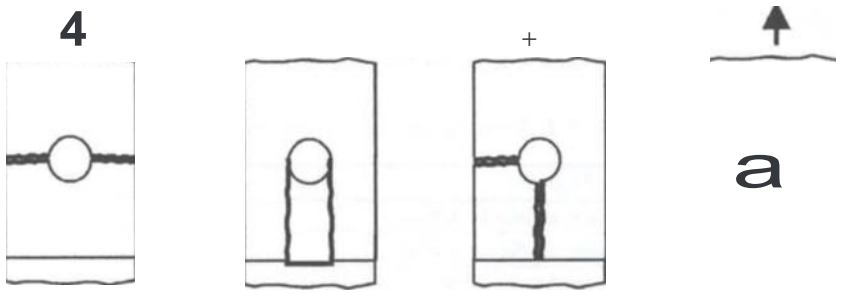

Figure 7.4 *Schematic diagram of failure modes for advanced composite bolted* joints *after Hart-Smith (1987): (a) tension failure: 7) shear-out failure; (c) cleavage-tension failure; (d) bearing failure.*

For boltedlbonded joints (figure 7.5(a)) there are unavoidable limitations imposed through the use of relatively large diameter bolts. In particular, since the bolts are designed for the case where the adhesive has failed, the bolts must be inserted well back from the ends of the joints (in order to mitigate bolt failure modes) and thus do not pick up load until there has been significant bond breakdown,

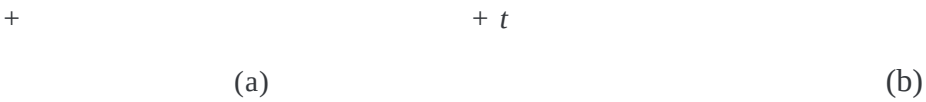

Figure *7.5 Joints design: (a) bolted-bonded single-lap shear joint; (b) pinned-bonded single-lap shear joint.*

Using small rods (of diameter I-2 mm) or z-pins (0.25-0.5 mm diameter) as through-thickness reinforcement, it could be possible to comply with the design constraints of bolted joints while opening up the possibility of inserting the pins in the debonding-prone areas of the joint, ensuring crack bridging between the adherents (figure 7.5 (b)). Therefore, although a crack will still initiate in the joint, with the pins bridging the crack, the debond front would be shielded from the full debonding loads, so the crack growth would be stable and the overall structural damage tolerance greatly enhanced. The result of this concept is a joint with a capacity higher than that of an adhesive-only or a bolt-only joint.

7.3 Problem Statement

7.3.1 Single-lap shear design and experiments

The lap joint studied was a part from a large glass fibre reinforced polymer (GFRP) pipe reinforced by small rods in the thickness direction. The manufacturing process to insert the carbon pins described in the following section will be called "pinning' to distinguish it from the z-pinning process described in chapter 2. Longitudinal sections were readily cut from GFRP pipes and used as coupons. The GFRP pipes were filament wound with

a winding angle of ±55°, an 80 mm internal diameter and a 4 mm wall thickness. Pipe material properties (provided by the manufacturer) are shown in table 7.1.

Table 7.1 *Pipe material properties*[19].

Property	
Axial tensile strength (MWa}	75
Axial tensile modulus (GPa)	l2
Shear modulus (GPa)	l 1.5
Poisson's ratio (hoop)	0.65
Poisson's ratio (axial)	0.38
Glass content (by volume)	52±7%

The typical dimensions of the curved single-lap joint are shown in figure 7.6. In general, the specimen consisted of two 200 mm coupons bonded over a 40 mm length, The 40 mm bonded length was chosen *because* it corresponded to the overlap length of an adhesive joint with a coupler for the 80 mm internal diameter pipe. The adhesive was a two-part cold cure epoxy with a maximum elongation at failure of 21%, an elongation at peak load of 4.7% and a shear modulus of 0.9 GPa at 25 °C.

Aluminium plates, of thickness of either 1.5 mm or 3 mm, were bonded to the top and bottom of each end of the sample to act as a grip during testing.

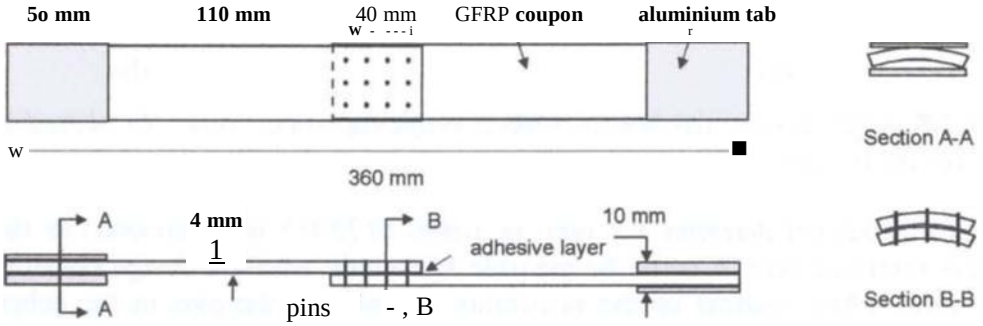

Figure *7.6 Curved single-lap shear specimens*[20].

The reinforcement pins were unidirectional carbon-fibre reinforced polymer (CFRP) rods with 1.0 mm diameter. Mechanical properties of the pins, (supplied by the manufacturers) can be found in table 7.2.

Table 7.2 *Pin material properties.*

Property	CFRP
Tensile strength (GPa)	2.07
Tensile modulus (GPa)	138
Ultimate tensile strain (°/n)	1.5
Ultimate shear strength (MPa)	41.3
Fiber content (by volume) (°/o)	62
Diameters (mm)	l.0

Future Pipe Industries B.V. Hardenberg, Netherlands

z" Courtesy of Dr Lees, Mechanical Engineering Dep., Cambridge University, 2002.

To form a pinnedlbonded joint, a different procedure from z-pinning was followed. Holes were drilled vertically through an already cured bonded joint. The drill bit sizes were typically 0.1 mm larger than the pin diameter. A number of different pin configurations were considered. Adhesive was applied to each pin and the pins were inserted in the drilled holes. Testing was carried under a displacement controlled analysis with a grip that moved at a constant velocity of 1.0 mrr>tmin. Among the configurations tested (figure 7.7), the best performances for the reinforced joint was obtained with pin distribution A6 (Lees, 2002; 2003), i.e. the edge and end distances were fixed at 5mm. This is the configuration that is modeled in this chapter.

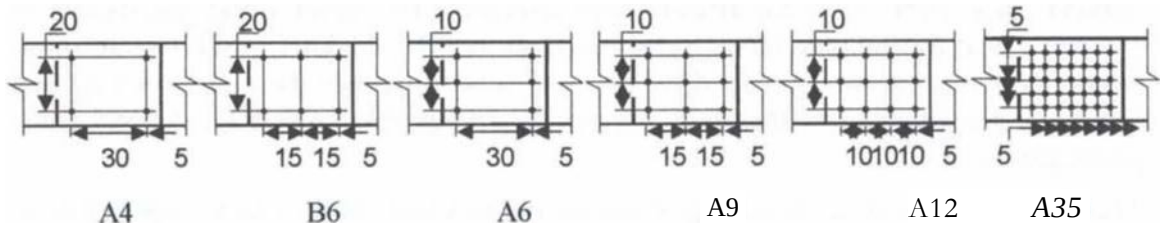

Figure *7.7 Through-thickness reinforced joint: possible pin configurations.*

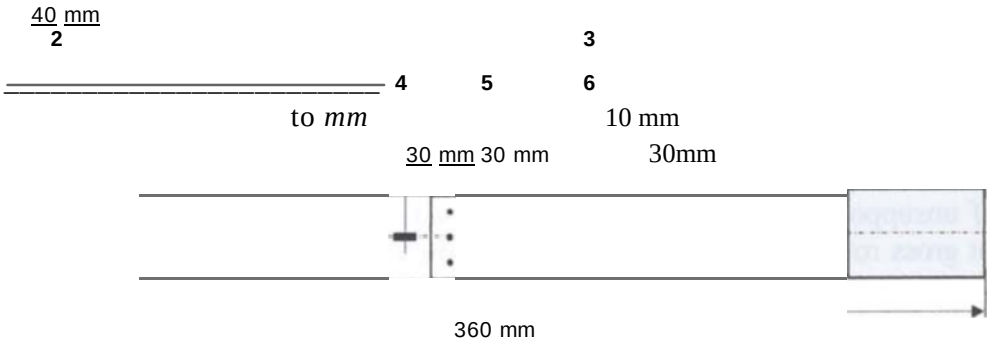

Figure *7.8* *Strain gauge locations on the C'SIJ*[21].

Load-displacement curves and strain gauge readings were taken from the experimental analysis, unfortunately there was no information regarding the crack debond growth in the joint. A total of six strain gauges were attached to each specimen. They were located at the middle of the joint and 10 mm on either side of the joint on top and bottom surfaces of the specimen (see figure 7.8).

7.3.2 Single lap-joint analysis with large scale bridging

The problem of interest is a single-lap shear joint between two composite laminates, bonded with an adhesive and reinforced by pins in the joint region. The failure mechanisms that must be simulated include debond failure of the adhesive and the deformation, pullout and failure of the pins. In the presence of pins, debond failure may be non-catastrophic, but it may still be considered unacceptable if, for example,

z' Courtesy of Dr. Lees, Mechanical Engineering Dep., Cambridge University, 2002.

leakage cannot be tolerated. Pin failure will usually be associated with ultimate (catastrophic) failure of the joint.

Two methods are commonly used to predict the strength of adhesively bonded lap joints, i.e. methods based on the strength of materials and methods based on fracture mechanics. Strength-of'materials approaches such as shear lag theory combined with a critical material strain can be useful as guides for first failure for simple joint geometries, but for pinned joints, the preferred approach is a fracture mechanics approach.

Shear lag approximations cannot capture the shielding effect of reinforcing pins on the debond crack front. As it has already been discussed in Chapter 4 and specifically in Chapter 5 that for the pure mode I loading condition, the shielding is the sum of (non-linear) bridging tractions supplied by the pins, which opposes the crack opening and sliding displacements and therefore reduces the energy release rate for debond crack propagation.

The pin tractions can be increasing or decreasing functions of the crack displacements, depending on the extent of deformation. Since the pins may act over long intervals of a partially debonded joint, the fracture problem is of a class known as "large scale bridging problems" - correct solutions are obtained only by solving the crack displacement profile along the entire debond length and calculating the tractions from each pin given the crack displacement at its location. The pin effect cannot be represented by a constant increment in the fracture toughness.

In a single-lap joint, peel and shear stresses in the adhesive are both expected to be important and therefore mixed mode energy release rates must be considered and mixed mode failure criteria incorporated to describe debond crack propagation. Moreover, analysis of unsupported single-lap joints must include the secondary bending and the consequent gross rotation of the adherends due to the initial eccentricity of the applied loads.

The adherends are loaded along the .r direction of the global coordinate system (Fig. 7.9), while the adhesive layer is subjected to shear stress in the x: plane and peeling stress through the thickness direction If accurate predictions of strength are to be made it is essential to include longitudinal and through-thickness stresses in the adhesive, shear and through-thickness stresses in the adherends, variation of these stresses across the width of a specimen (y-direction), especially for the joint specimens under consideration which are curved, and the elastic-plastic characteristics of the adhesive. Further, since the specimen has a finite width and exhibits gross rotation, the debond front may present mode I, mode II, and mode III components of the strain energy release rate.

Evidently, this is a non-linear problem involving both material non-linearities (pins) and large deformations, further complicated by the curvature and asymmetric behaviour of the two sides of the bonded joint. Simplified representations such as beam or plate theory would not correctly treat such complexity; the finite element method seems the only feasible approach.

7.4 Modelling procedures

7.4.1 Finite element model for curved single-lap joint

A FE model was developed to simulate the Curved Single Lap Joint (CSLJ) reinforced by fibrous or metallic pins that was introduced in the work of Lees (2003), which was briefly described in section 7.3.1. A model was developed as shown in figure 7.9 with typical computational parameters provided in table 7,3. A coarse mesh was adopted in the adherends away from the joint where stress variations are modest and a fine mesh in the area close to and along the joint where the various mentioned failure mechanisms are expected to operate (figure 7.9 (a)).

Table 7.3 *I ypicul parameters of a CSL I FE model.*

Parameters in the FE model	Value
Nodes	2426
Shell 91 (layered elements)	720
Interface springs (adhesive)	210
Interface elements (pins)	12
Initial applied displacement (a,)	1.4 mm
Incremental displacement (8,)	0.025 mm
Sub-steps (N ,b)	50
Newton-Raphson iterations (N,)	99

The adherends were modelled with thick-layered composite shell elements, which have several useful properties such as shape functions with transverse shear deformations, large deformation capability, quadratic element formulation, general definition of laminate stacking sequences, and nodal offsets permitted through the thickness. The layered shell technique is thought to be computationally more effective than 3D hexahedral elements, which have convergence problems due to the high aspect ratios that are required in the joint overlap area for the adhesive layer simulation.

The two ends of the joint overlap are defined as the concave end and convex end, resembling the curvature which the joint develops after deformation. The adherend having strain gauges 1, 4, 5 is defined as lower adherend, whilst the adherend having strain gauges 2, 3, 6 is called upper adherend (figure 7.8)_

The adhesive layer was modelled by shell and spring elements which respectively furnish the rigidity (flexural and membrane stiffness) and elasticity of the adhesive. Between the two adherends two additional layers of shell elements were considered in the joint overlap area, each having half of the total adhesive thickness (figure 7.9(b)). The total adhesive thickness was assumed to have an average constant value of 0.15 mm (Lees, 2002). The nodes were placed with an offset position at the joint interface between the two assumed adhesive layers as reported in the exploded figure 7.9(b).

To account for the adhesive elastic deformation, three linear springs (two shear, one peel) were placed at the adhesive layer interface, between each pair of initially coincident nodes, acting in the x y „ directions of the local coordinate systems, which had the main axes initially parallel to the global Cartesian system (figure 7,9(b)).

linear analysis Guide, 2002), Geometrical parameters (L, L l, L2, t, t.) and material parameters (for the adherends and adhesive) are defined in the list of nomenclature and in figure 7.9a.

• *FE model boundary conditions*

The FE model boundary conditions are reported in table 7.4. To simulate the constraints introduced by the grips on the adherends end, the rotations around the y axis of the global reference system were left free. An imposed constant displacement along the x direction is applied on one adherend end. The model boundary conditions are given in the global cylindrical coordinate system.

Table 7.4 *f :S L I model boundary conditions.*

B x = 0 -- 5 y 5 + 2 ur =u,. =u_ = 0 Br =O_ = 0	x = L - 2 5 y 5 + - $u_x = const$ $u_z = u_y = 0$ $\theta_x = \theta_z = 0$

7.4.2 Model for pin bridging mechanics

The material model presented in Chapter 4 and used in Chapter 5 is assumed to be also valid also for modelling the bridging effect of the carbon pins reinforcing the CSLJ. The bridging function *I (u i,u3)* is the relation between the bridging traction force vector (F) applied to the fracture surfaces by the bridging entities and the crack opening displacement vector (u,w).

7.4.3 Modelling failure modes

The single-lap joint system can fail by several modes. In fact, a failure mode transition occurred in the experiments on GFRP joints reported in (Hashim et al., 1998; Knox et al., 2001) which used similar materials, from adherend delamination (ply delamination within one adherend) to debond failure of the adhesive, with the active mode depending on the system size.

In the experiments by Lees (2003) described in section 7.3.1, three types of failure modes were observed. A joint failure was defined as the failure of the adhesive bond and/or the through-thickness pins. Two types of coupon failure were observed. In the first type, the specimen failed in the free arm away from the joint overlap region. In the second type, it appeared that failure may have initiated in the outer pin hole followed by the propagation of a crack into the free ann. In a given set of three tests, it was possible that one or more specimens failed in the first coupon mode and one or more specimens failed in the second coupon mode. Thus, in the first instance, both types of failure have been grouped into one category.

The complete set of failure modes considered in the FE model are failure of the adherend plies in tension or compression, adhesive bond failure and consequent debonding, and pullout or shear failure of the bridging pins during or after debond growth.

The adhesive bond failure is shown schematically in figure 710, with possible crack growth paths in the overlap lengthwise direction: the first is within the adhesive and is called cohesive bond failure, the second is along the adherents-adhesive interface and the third is a wavy crack path.

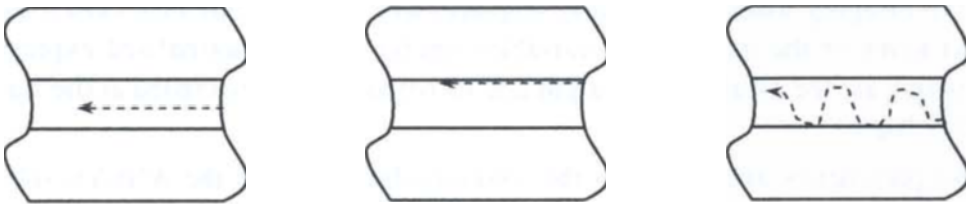

(a) (b) (c)

Figure 7.10 *Schematic of adhesive failure modes: (a) cohesive failure with crack propagation in the adhesive layer; (h) crack propagation* along *or near the adhesive-adherends' interface: (0 wavy crack growth along the two Interfaces.*

For a composite joint due to the laminated nature of the composite members and relative weakness in the through thickness direction, the delamination failure mechanics of the adherends external plies might start before the adhesive bond failure (figure 7.11).

Predicting crack initiation in an adhesive layer remains a problem of current research. In the joints, initiation will be influenced by the spew fillet geometry, which changes the stress concentrations at the adhesive ends (Gang Li et al,, 1999). Furthermore, it is difficult to characterize the adhesive properties, especially when environmental effects are present. In this chapter, adhesive failure was assumed to initiate when a stress component (shear or peel) exceeds its allowable value over a finite zone area that is defined by the element size (da h.).

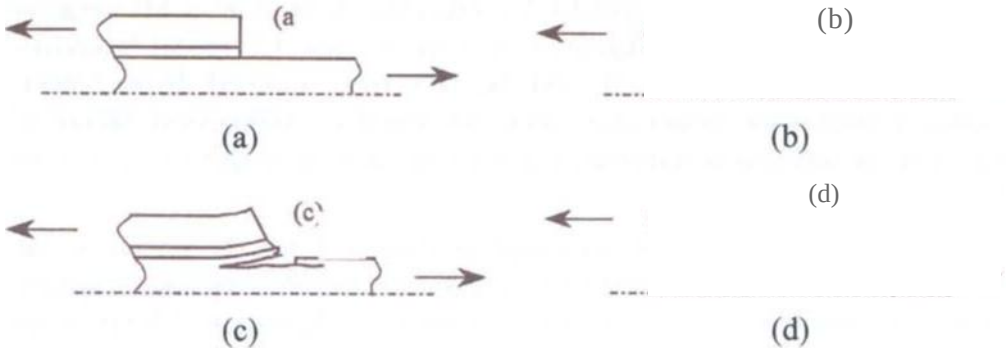

Figure *7.11* *Peel stress induced delamination failure in composite joints.*

As already stated the debond propagation would consist of a mixed mode fracture problem. Strain energy release rate formulas as discussed in Chapter 5 were used to compute the mode ratios at crack front during debond growth, and a simple mixed mode failure criterion introduced in section 5.4.4 was used for the crack growth analysis.

7.4.4 **Computational algorithm**

A solution-algorithm has been developed in MATLAB (version 6.02) and the FE solver used was ANSYS 6.1 (table 7.5), After introducing the parameter definitions for the pin system, the bridging loads *(Ti. T3)* and displacement *(III, U3)* function values can be derived in terms of the independent variables *(c .O ,* or their normalised expressions ($E\sim,,e_0$), which are the axial stress in a pin and its rotation, both evaluated at the fracture plane (see Chapter 4).

The model parameters are input into the solution algorithm and the ANSYS solver is run in batch mode as a MATLAB subroutine. The non-linear analysis iteration is then started, adding iteratively an incremental displacement (0.025 mm). A check of the stress distributions at both sides of the joint overlap is then performed. If the adhesive material strength is exceeded then the stiffness of the interface spring elements simulating the adhesive will be reduced to a very small value (0 le), and debonding will start. The SERR distribution and the fracture mode ratio are computed at the crack front. Three different crack growth scenarios are checked: a crack growing from side 1 ($^{a}+$) named the concave side, or side 2 only (a_2) named the convex side, and cracks growing from both sides (see figure 7.9(a)).

The bridging effect of a particular pin is considered only when the crack front reaches that pin. As it has already been discussed in chapter 5, bridging is the only effect of the pins that is modelled; it is assumed that the pins will not affect the joint's bending and membrane stiffness. This last assumption especially, may be too simple for the larger pin diameters (and larger drilled holes), but such effects are beyond the scope of the present illustrative calculations.

At the i-th iteration the code performs two separate tasks: (1) if the mixed mode failure criterion is not satisfied then the applied displacement is increased by a 4 value and the G, and GPI values at the crack-front are re-computed; (2) if the failure criterion is satisfied then the nodes at the delamination front are uncoupled, the new displacement vectors for the pins are computed and the MATLAB solver then works out the associated bridging forces *(TI, T3)* (Appendix F). Therefore at the *i-th 1* FE iteration the pin stiffness matrices /KJ are updated along with the new FE model boundary conditions due to the new crack length, and the additional imposed displacement. During the solution process the model also checks for tensile or compressive failure of the adherends; and the analysis is terminated at the total debond Iength (al a2) of 40 mm (i.e. the overlap length).

The micro-mechanical material model presented in chapter 4 for the action of the reinforcing pins does not present a closed form solution for the bridging forces against crack displacements when the crack is in a mixed mode configuration. Therefore an additional numerical effort is required to link the implicit material model formulation to an explicit numerical solver for the global problem.

Convergence tests were undertaken with different mesh densities at the crack front and different applied incremental displacements. A stable value of Gi and Gil was achieved with the mesh size of 0.5 mm along the delamination growth direction and the incremental displacement b = 0.025 mm was found suitable for the MATLAB solution search algorithm described in Appendix F. Some of the model outputs are also shown in figure 7.12.

7.4.5 Modelling assumptions and limitations

The assumed causes of non-linearity to be modelled were the eccentric loading path and the consequent large deflections of the adherends (geometric non-linearity), and the pin material non-linear behaviour during large scale bridging (material non-linearity).

The adherends material is assumed to have a linear behaviour and no progressive damage model was implemented at this stage of the analysis. The adherends ply failure is assumed to occur when a stress component exceeds the allowable strength. In these first simulations, the analysis *of* the interlaminar stresses developing among the layers of the composite adherends was not included.

Furthermore the elastic moduli, the membrane and bending rigidity of the adherends shell elements are assumed to be unaffected by the pins presence. Nevertheless, it is thought that the drilling process before pin insertion may cause some damage in the adherends plies and for the bigger pin diameters the holes may cause stress concentrations similar to those encountered in bolted joints.

The assumption for the adhesive layer with an elastic behavior is thought to be over simplistic. A more detailed simulation of the adhesive should consider its elasto-plastic behavior. It is thought that the plasticity occurring at the adhesive crack front might release the stresses and therefore alter the SERB components along the crack front. The total adhesive thickness *to* was split into the thickness *to 2* of the two adhesive layers at the joint overlap interface (figure 7.9(b)). Therefore a cohesive bond failure was assumed, with the crack propagating within the adhesive layer. The spew fillet was not considered in the simulation, and the adhesive material was considered to have linear behaviour before failing. More data about the adhesive would be required in order to implement its non-linear behavior into the spring elements.

Even though the strain energy release rate values varied across the model width, to simplify the analysis the crack front was assumed to be straight during the debond propagation.

One major and important simplification was introduced to the modelling of the pins. According to the pin material model (Chapter 4), these are not represented as solid in-homogeneities penetrating the two adherends. Instead, the adherends are left as unmodified composite material and the effect of the pins is represented entirely as surface tractions acting at points along the debond fracture surfaces. This bridging law representation has been widely exploited in this thesis for the simulation of large scale bridging problems and has been proven able to model delamination accurately in z-pinned laminates under mode I loading conditions (Chapter 5), which are quite similar in mechanics to pinned joints. The line-spring approximation is the key to the ability of the present formulation to examine design options in a rapid and convenient manner.

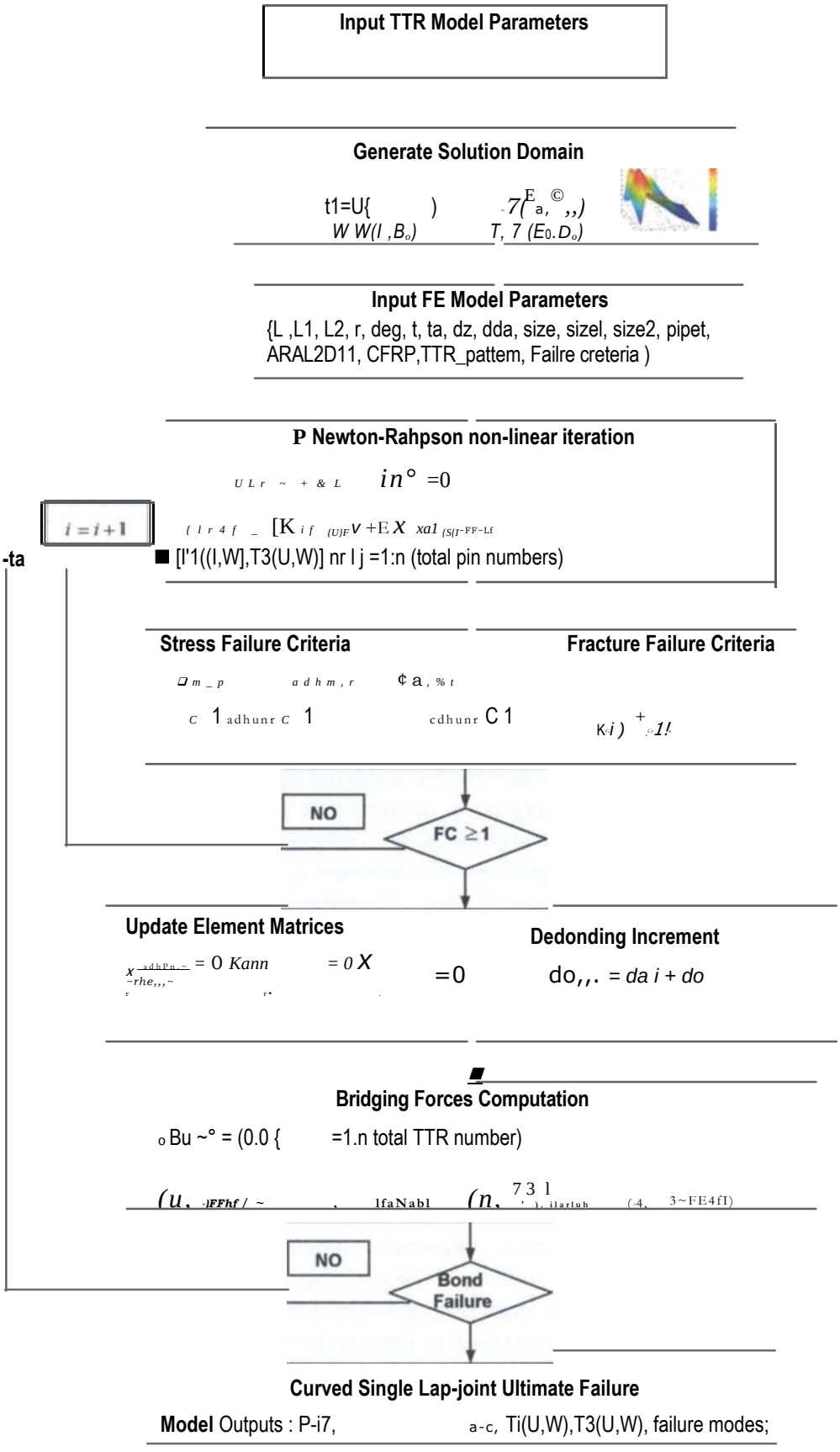

Figure 7.12 *Flow chart of the numerical solution algorithm procedures.*

7.5 Results & Discussion

7.5.1 Numerical examples

The geometrical parameters for the CSLJ specimen modelled in this work (figure 7.9) were taken from the experimental tests in Lees (2003) as briefly described in section 7.3.1. The joint is subjected to monotonic tensile load. The joint length, L, overlap length, L2, and width, B, are 360, 40, and 30 mm respectively, and the Iaminate thickness, t, is 4 mm (figure 7.9a). The distance between the overlap end and the first row of pins is 5 mm and the pin array pattern is the configuration A6 reported in the work of Lees (2003), which has 6 pins of I mm diameter. The adherend material is EST32 glass fibre reinforced epoxy with elastic properties as shown in table 7.1. These properties are inserted in homogeneous orthotropic sheIl elements that represent the adherends. The adhesive fracture toughness values used in the mixed mode failure criteria are G_{IIc}= 800 J/m^2 and Gk= 380 J/rn^2. The assumed parameters for the pin micro-mechanical model studied in Chapter 4 which ensured satisfactory agreement with experimental data were: r = 1 *mm*, **0**= *0,* 4 = *4* mm, $_{zf}$= 30 MPa, ,u = 1,2, P,-300 N/mm, ,r = 3.

The analysis deals first with the bonded joint without pins, defined as Joint P, and then with the pin reinforced joint, defined as Joint Z.

7.5,2 Bonded joint without pin reinforcement: Joint P

Results *are* presented *in figures* 7.13 to 7.19 for Joint P that is adhesively bonded without pin reinforcements. Figure 7.13 shows the external load P against joint displacement along the x axis of the global Cartesian coordinate system (figure 7.9a). The onset of stress-strain non-linearity in the-simulations coincides with the start of debonding failure at the convex end of the joint (figure 7.9a) for an external load P

4645 N.

Encouraging agreement is found between the experimental and predicted curves; and also for experimental and predicted strain readings (figures 7,14 to 7.16).

Figure 7.13 also outlines the debond positions at the external load value *(P' 5200 N)* where the fracture energy failure criterion is met at both ends of the joint and the crack propagates simultaneously from the concave and convex ends. The computed joint strength that corresponds to the total debond failure of the joint is around 5600 N ($P_{c\cdot T}$;,), which shows satisfactory agreement *with* the experimental *value.*

The experimental observations reported in Lees (2003) did not directly associate mechanisms with features on the load-strain data. Measured non-linearity might have corresponded to debond cracking; but it could also be due to tensile failure of the external ply in the adherend, which is suggested by measured strains (figures 7.14 to 7.16) and the predicted crx stress distribution of figure 7.17. The membrane and bending strains have been derived from the nodal strain results on both sides of the same point, using the standard formula:

s, - *(c, y,* $\wedge_{\sim_{e\,r)}}$ **(7-5)**

= i(6,, + s~)

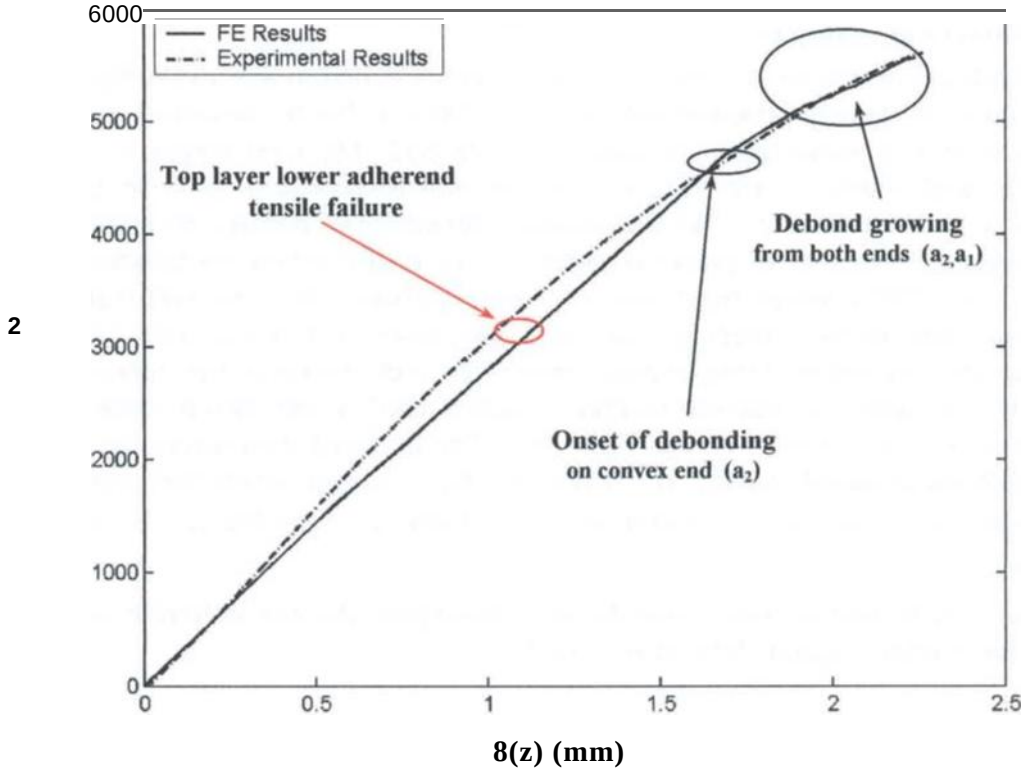

Figure 7.13 *Numerical and experimental results for Joint P: Load (P)-Displacement (d)*

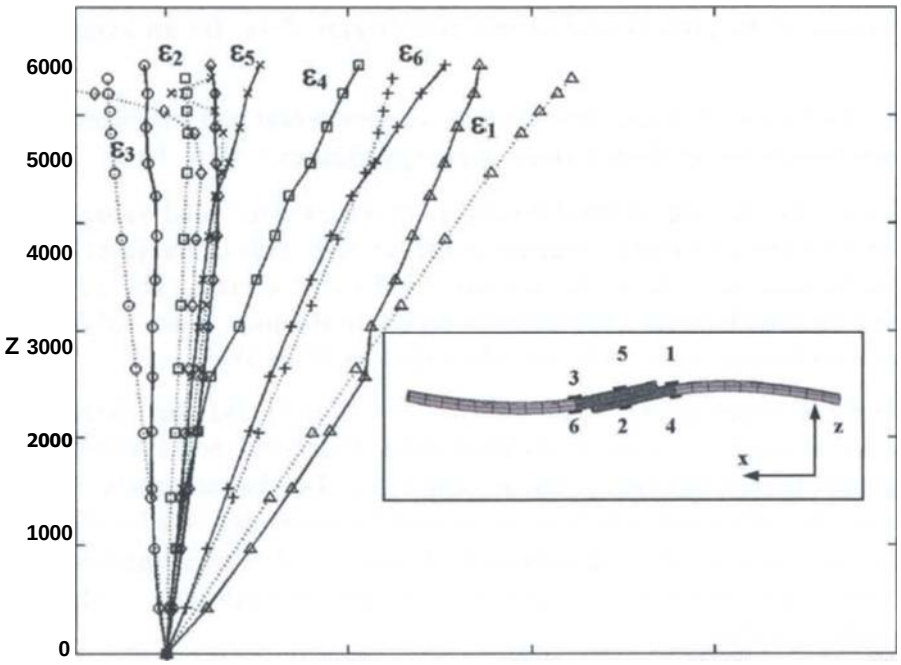

curves. 1.E predicted failure mechanisms are also outlined in the graph.

Figure 7.14 *Strain gauge output (e) fir Joint P: experimental values (thick lines), and*

PE computations (dotted lines).

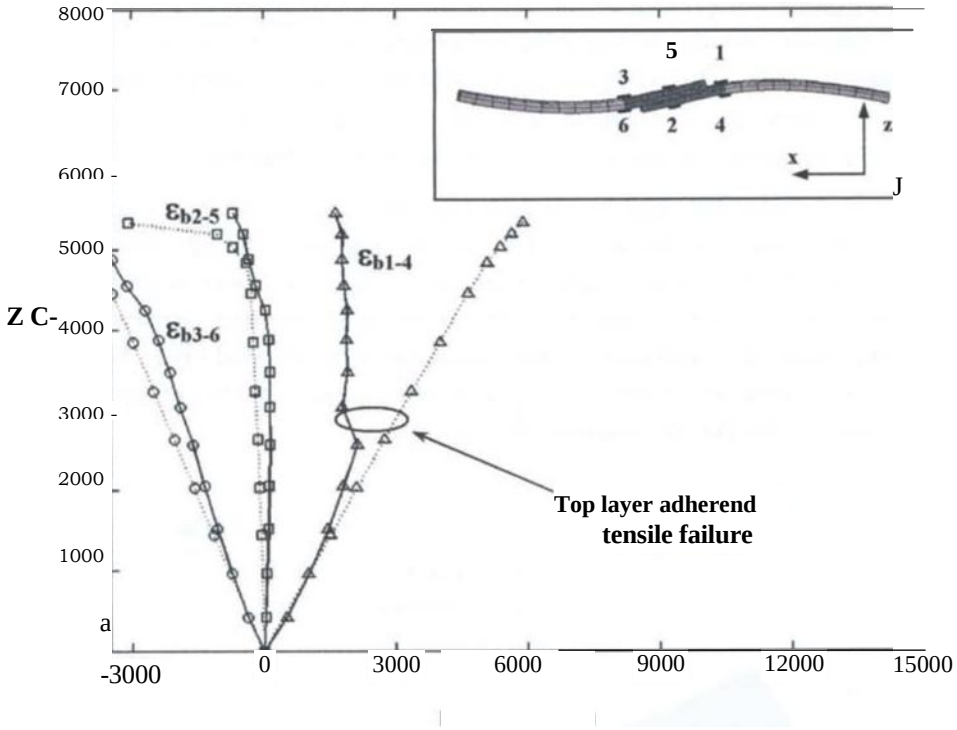

Figure 7.15 Bending strains a *(load direction x) for Joint P: experimental values (thick lines), and FE computations (dotted lines).*

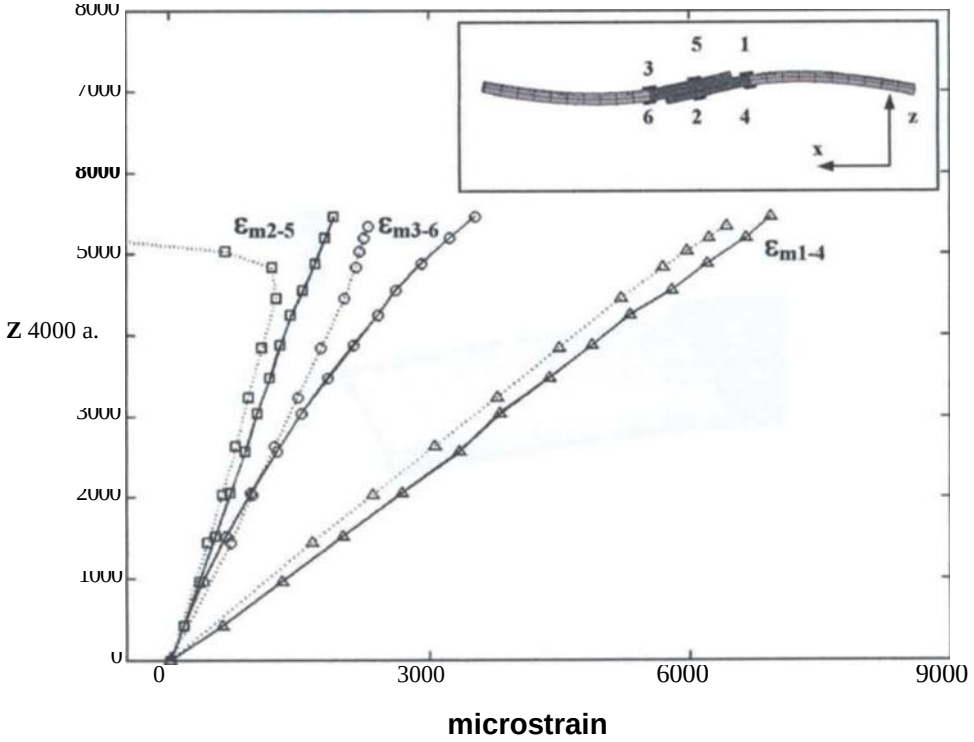

Figure 7.16 *Membrane strains* En, *(load direction x) for Joint P: experimental values (thick lines), and FE computations (dotted lines).*

The simulations show considerable bending and therefore substantial specimen rotation (figures 7.18), so that the top layer of the upper adherend in position 3 is in compression (figure 7.14). Figure 7.18b shows the rotation around they axis in the x-: plane of the global coordinate system. The most stressed joint area occurs where strain gauges 1-4 are placed ($(^{e}_{m1-4}$ = 6000 μc). As shown in figure 7.17, for a load P= 0.55 $_{Pcrir,}$ the FE results predict tensile failure of the top layers of the lower adherend.

The CSLi, having finite width and an asymmetric shape, may exhibit significant modes I, II, and III SERR values (O'Brein, 2001). For the assumed straight debond fronts of the present simulations, *the SERR* values *vary across* the specimen width, as shown in figures 7.19a for mode I, and in figure 7.19b for mode II, for one particular externally applied load. The mode I I component is the larger for both debond ends, but the mode I component is also significant. Quite strong differences exist in the dependences of the SERB components on the position across the specimen,

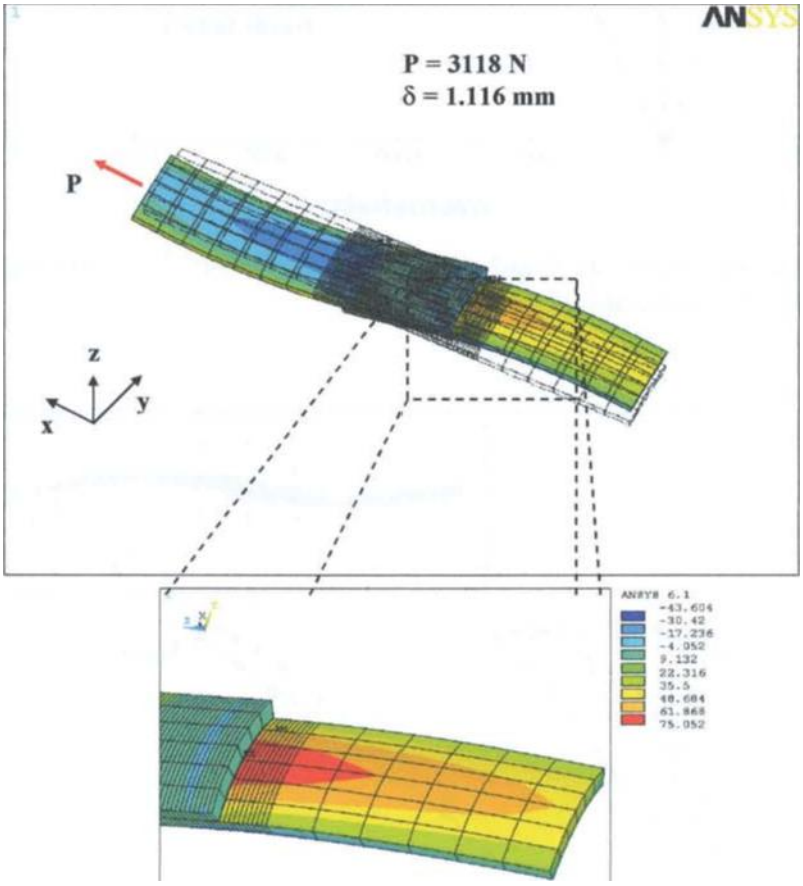

Figure 7.17 *Its results (n; = 15. P = 3118 N): contour plot fur top layer of lower adherend, and deformed shape. The most critical area is outlined in the roomed picture. The tension failure of the top layers in the CIRFC.' lower adherend is predicted to occur before the debonding failure of the joint will start.*

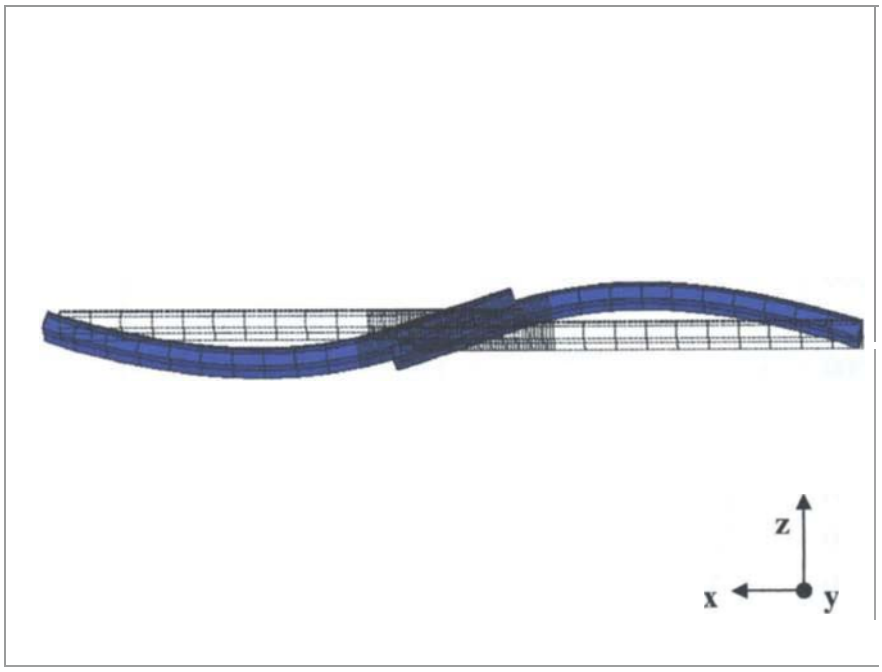

(a)

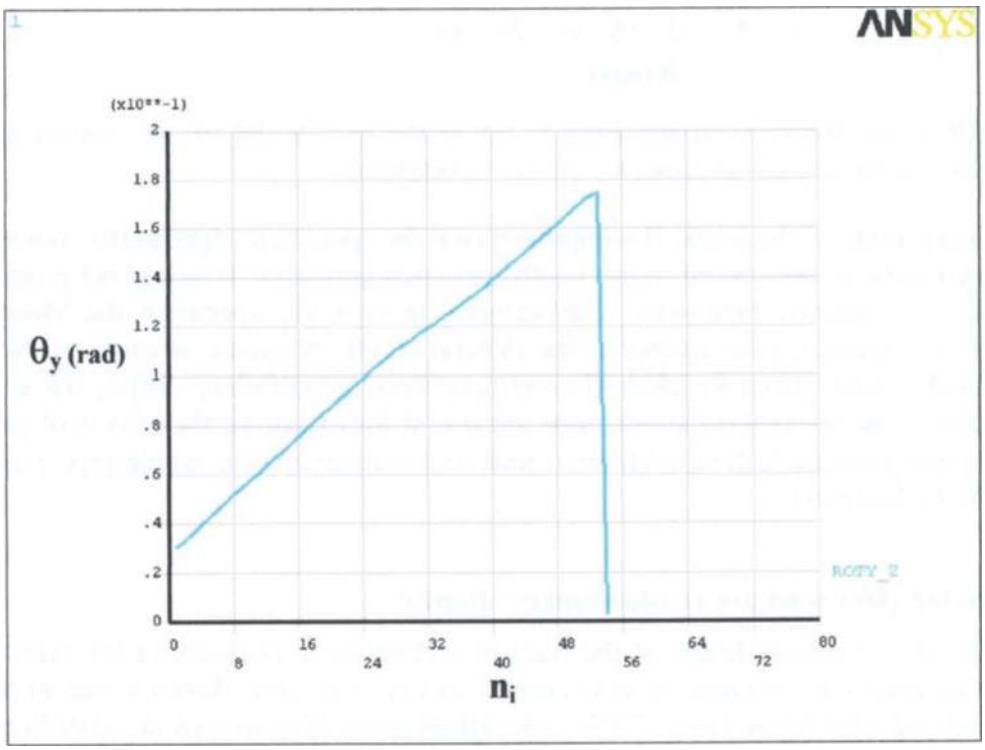

(b)

Figure ***7.18*** *Bending effects due to load path eccentricity: (a) (:S1I deformation showing gross rotation; (b) gross rotation* (in *rad) of the joint overlap vs. non-linear analysis steps (n). The onset oldie dehonding coincides with the 27" iteration W-4645 N).*

If a crack propagation criterion was applied point-wise along the debond fronts, they would develop curvature: at the concave end, the debond front will propagate fastest in the middle of the specimen, while at the convex end, the front will propagate fastest at the specimen edges (figure 7.19). In the present simulations, the propagation criterion was applied as an average over the debond front and the entire front was advanced uniformly. This is not expected to have a large effect on the global response or the bridging **effects of the pins,** which are the main topics of interest.

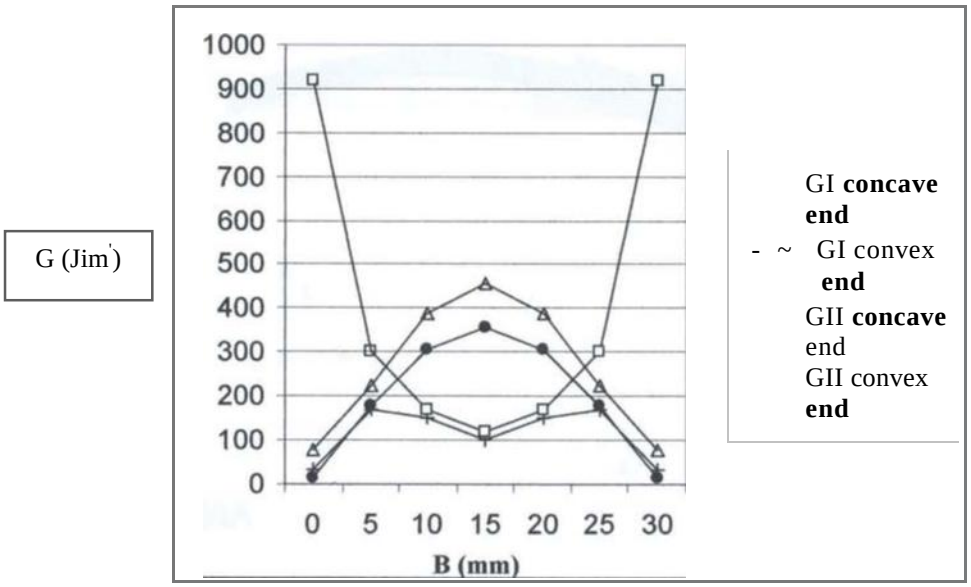

Figure 7.19 SE'RR *distributions for Joint P across the joint width (B) at concave and convex ends: (a) Mode I component;* (b) *Mode II component.*

The large magnitude of the Mode [I component near the specimen edges at the concave end is a peculiarity of the curved, finite width specimen geometry. It would not arise in a complete, axisymmetric pipe joint. Furthermore, in the CSLJ specimen, the Mode I component will increase even further as the debond length increases, whereas a whole pipe joint will exhibit primarily Mode II conditions throughout failure. While the tests in (Lees, 2003) and the present simulations are useful for exploring the effects of pins on fracture and ultimate failure, additional tests and simulations for whole pipe joints would also be of interest.

7.5.3 Bonded joint with pin reinforcement: Joint Z

Figures 7.20 to 7.30 show details of the fracture and bridging phenomena for Joint Z, when debond cracks are bridged by pin reinforcements. The case shown is that of the pin pattern designated A6 in Lees (2003): six carbonlepoxy fibrous pins are distributed in two rows towards the ends of the bonded region of the CSLJ joint specimen.

In approximate agreement with the measurements, the ultimate failure load *(Peru* = 7437.51) for Joint Z is predicted to be 33% above that of Joint P (figure 7.20). The maximum load is associated with the transition to falling loads during pin pullout, following the complete failure of the joint adhesive bond. As in the case without pins, debond is computed to start from the convex end of the joint (figure 7.20), propagate rapidly for the first 6 mm and then slow down due to pin bridging.

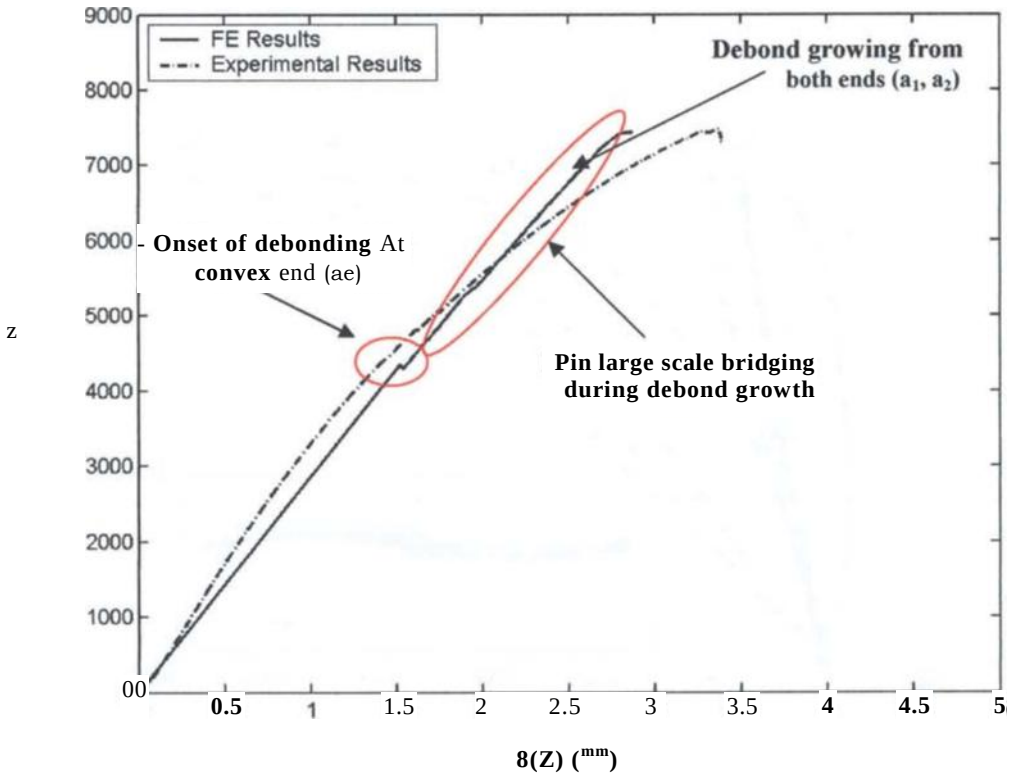

Figure *7.201 Numerical and experimental results ¸for Joint Z: Load (0-DJisplacement (6) curves. FE predicted_ failure mechanisms are also outlined the graph.*

During this propagation, the axial stress, a,, in the adherends in zones 1-4 are computed to be well above the axial tensile strength of the adherend material. Therefore whilst the joint bond is failing, other energy absorbing mechanisms are predicted to take place: tensile failure of the external adherend plies, interlaminar delamination in the adherend layers due to subsequent rising interlaminar stresses. It is thought that the additional non-linear behaviour shown by the experimental *curve in* figure 7.20 was due to the above mentioned non-linearities which were not included in the present model as discussed in section 7.4.5.

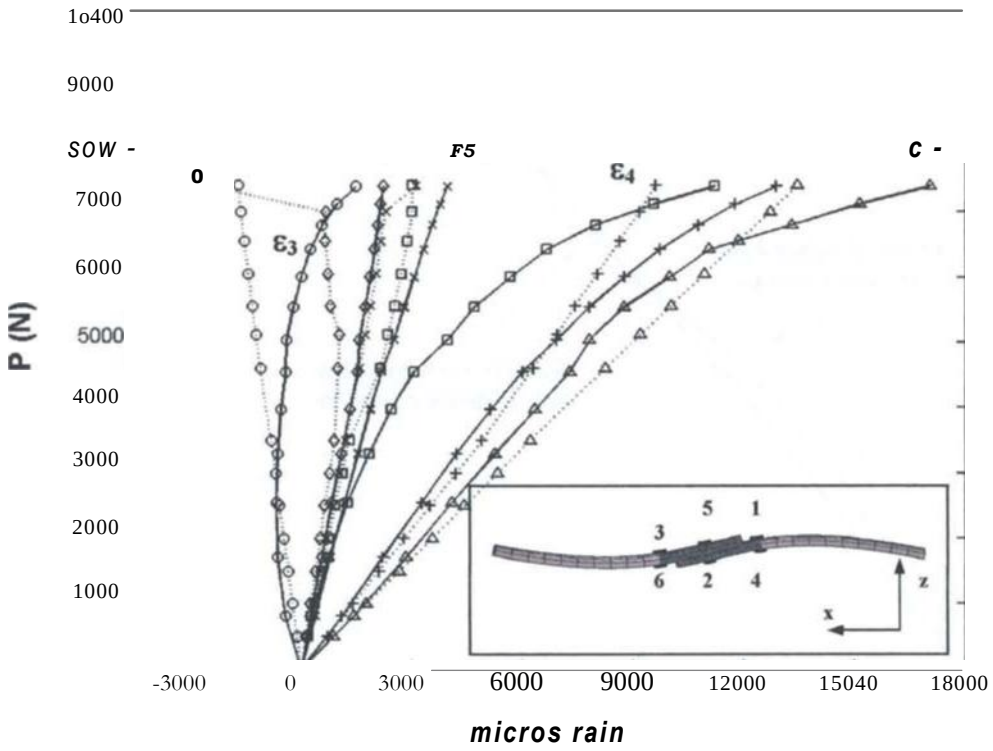

***Figure** 7.21 Strain gauge output (s) fur Joint Z: experimental values (thick lines). and*

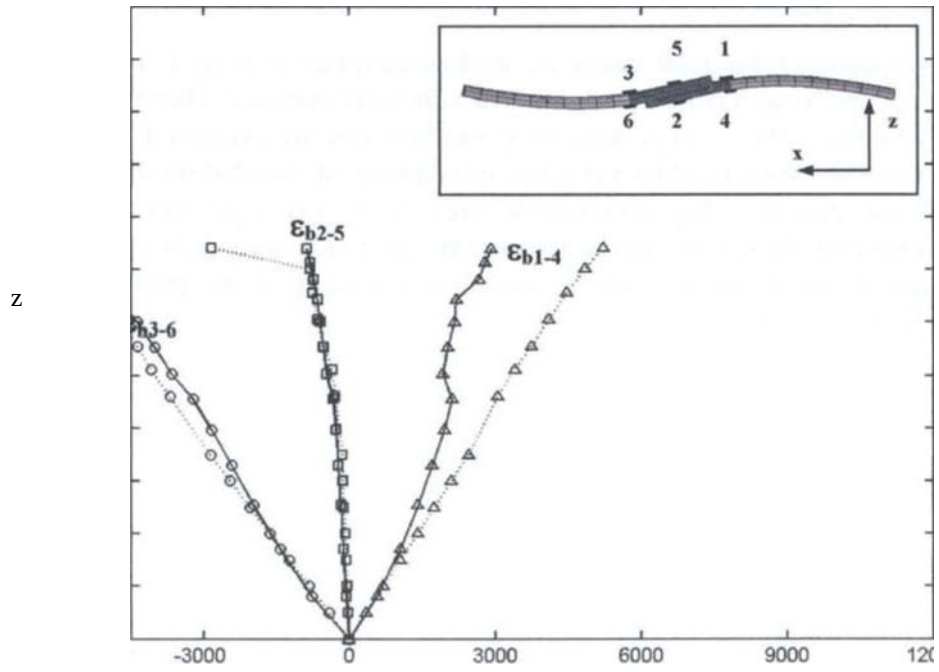

FE computations (dotted lines).

micros rain

Figure 7.22 *Bending strains* 4 *(load direction x). for Joint Z: experimental values (thick lines), and 1·E• computations (dotted lines).*

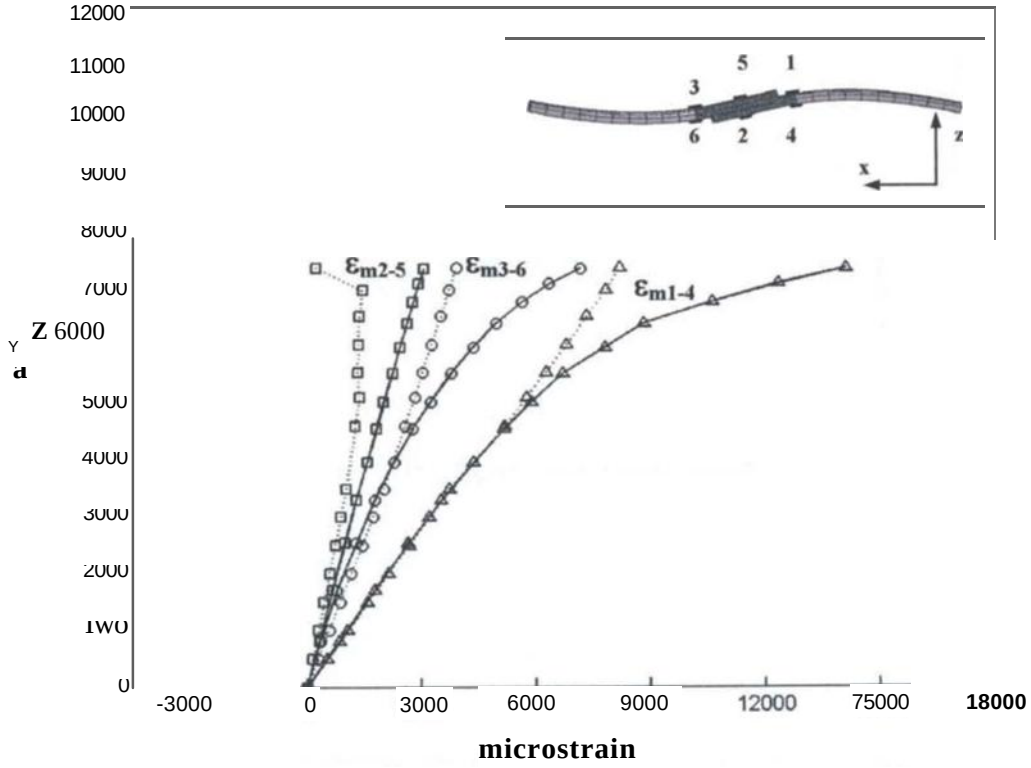

Figure 7.23 *Membrane strains 4, (loud direction x) f rr Joint Z: experimental values (thick lines), and FE computations (dotted lines).*

Figures 7.21 to 7.23 show the strain gauges experimental readings and the FE nodal computations. Due to the bridging of the pins in the debond wake the adherends material experienced higher strain fields up to 11000 ,ue which is a condition reported also in chapter 5 for the laminates of the DCB arms outside the bridging zone. Even though debond failure can be delayed and eventually avoided due to the pin bridging mechanics, the adherend free arms plies could still fail in tension due to the high strain fields to which they are subjected.

Figure 7.24 shows the Mode I and mode II SERR values, averaged across the specimen width as a function of the length a_2, for the debond that originates from the convex end. The Mode II component is by far the larger; the Mode I component is reduced almost to zero as the pins shut down the crack opening displacement. As the debond grows for more then 10 mm into the pin field, the pins tend to align with the shear loads, reducing more effectively the Mode II component (figure 7.24),

The Mode I component rises with debond length, but the mode ratio, $G_I/G_{i,}$, never exceeds approximately l5% for most of the crack growth (figure 7.25). The mode ratio for $a_2 < 6$ mm is thought to be the same as that in the absence of pins (Joint P), because no bridging is yet acting in the crack wake (see figure 7.7 for pin positions *and figure* 7.25 for mode ratio).

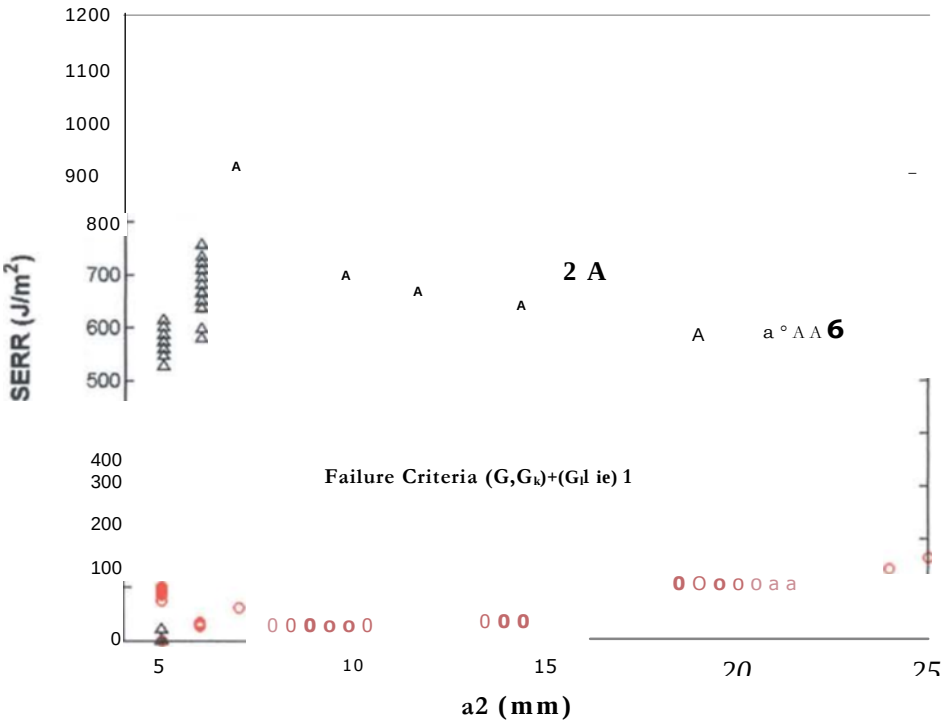

Figure 7.24 *Averaged SERB values* (GI *and* G_{ff}) *at the dehond front vs. dehond length* (a .

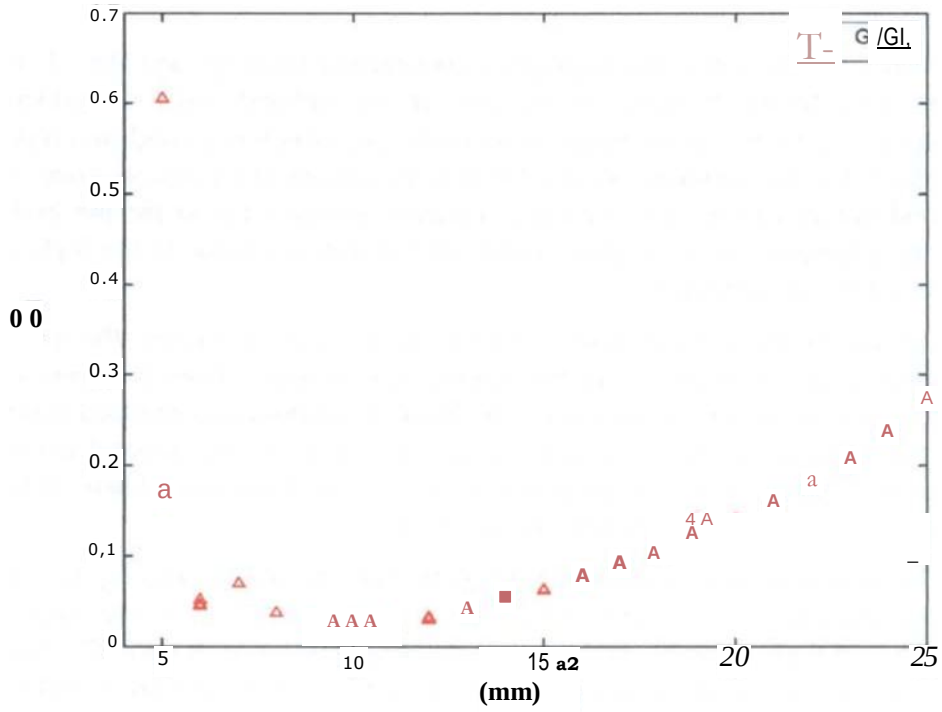

Figure 7.25 *Averaged SERB ratio* G_1,G_{ft} *at the dehond_ front* vs. *dehond length (a2).*

Pins that are initially normal to the debond plane (as in the present specimens) are more effective in shutting down opening crack displacements than sliding displacements because of the micro-mechanics of pin deformation (chapter 4). For initially normal pins, opening displacements act in the direction of the fibres in the pin, which are very stiff Sliding displacements are accommodated by deflection of the pin laterally through the adherends. This deformation occurs by shear deformation of the pins and the adherends, which is controlled by the relatively compliant matrix in these members (Chapter 4).

As the two debond cracks propagate from the two ends of the joint, the magnitude of the bridging tractions are different at different pins, because the opening and sliding displacements are different. The development of the bridging tractions, Fi and E3 , with debond length is shown in figures 7.26 and 7.27 for the pins encountered by the debond that propagates from the convex end (figure 7.26) and from the concave end (figure 7.27) of the joint.

Given the computed tractions at a pin and the corresponding debond crack opening displacement, the various parameters that are embedded in the traction model (Chapter 4) can be evaluated. However, evaluating these parameters is not necessary for executing an FE simulation only the traction law itself needs to be known, i.e. force vs. displacement. In agreement with the SERR distributions shown at the debond fronts, the external pins experience the largest bridging force components at the convex end, whilst the internal pin shows the largest bridging force components at the concave end.

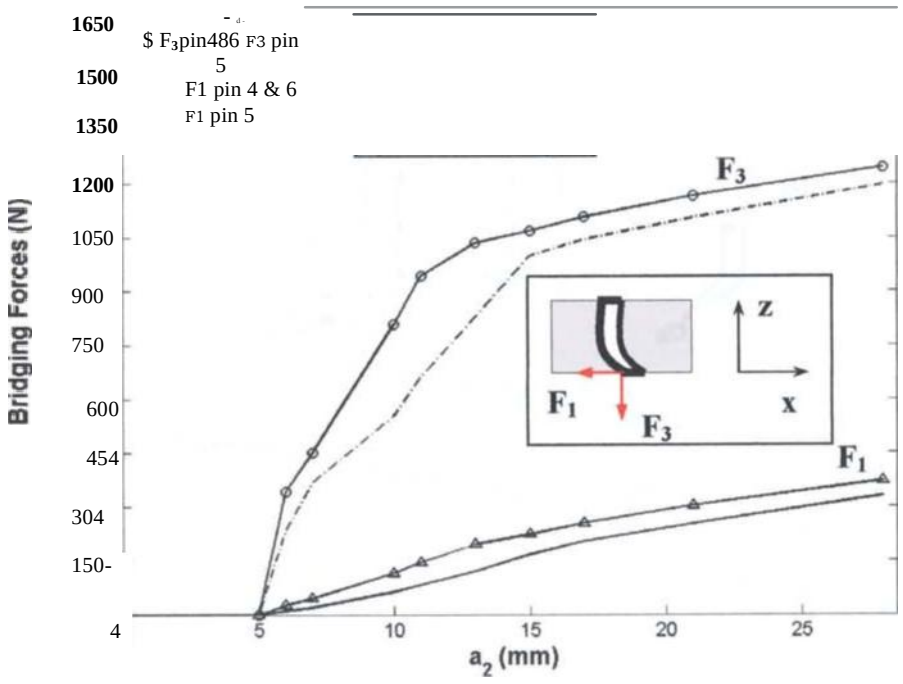

Figure 7.26 *Bridging closure forces Et and F3 opposing sliding and opening displacements, exerted by the pins at the convex end during debond growth.*

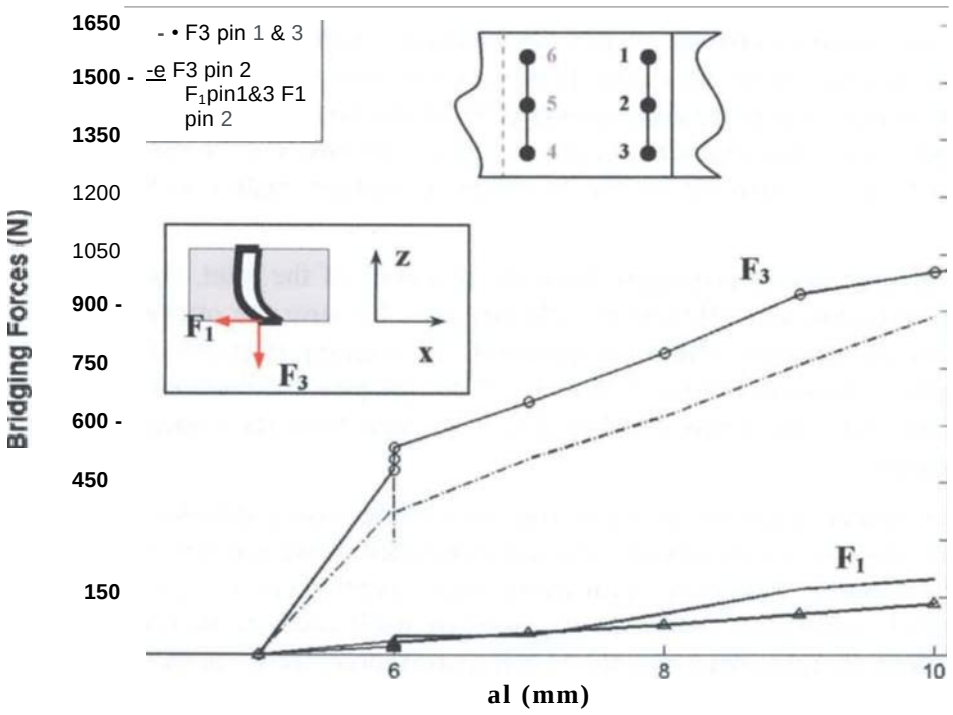

Figure 7.27 *Bridging closure force F1 and F3 opposing sliding and opening displacements, exerted by the pins at the concave end during debond growth.*

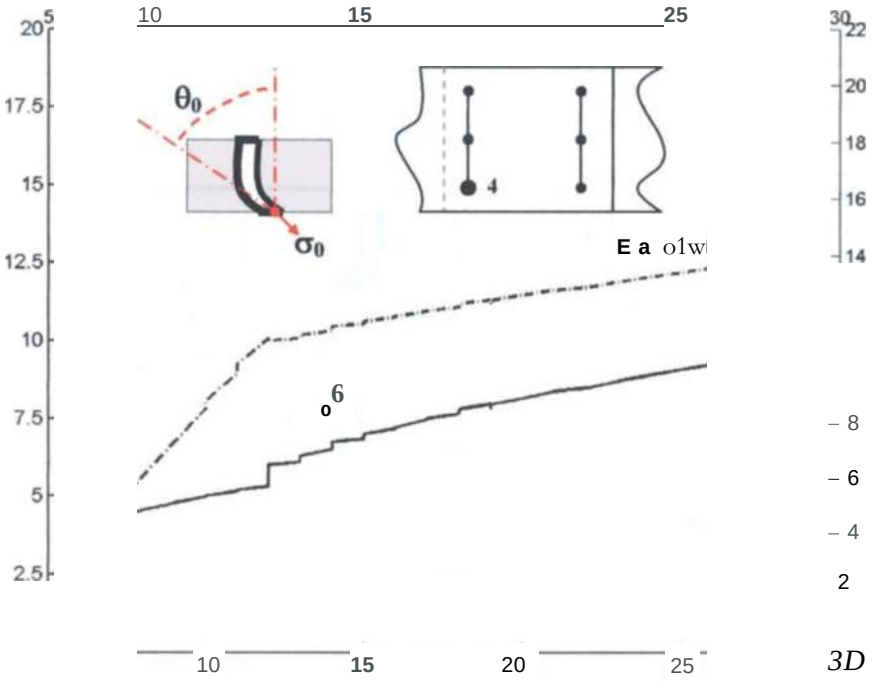

Figure *7.28 Left hand y-axis: angle of deflection at the fracture plane 9a vs. dehond length a2; right hand y-axis: pin axial stress Fr! vs. dehond a2.*

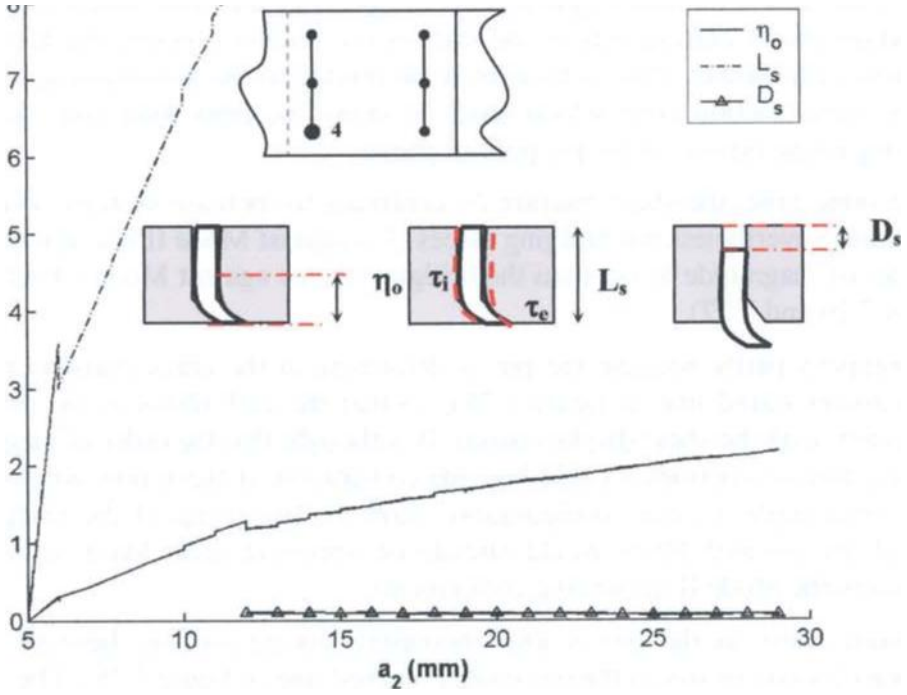

Figure 7.29 *The deflected:one length tlo, the slip length L and the pullout length* D_5 *of pin number 4 vs. dehond length.*

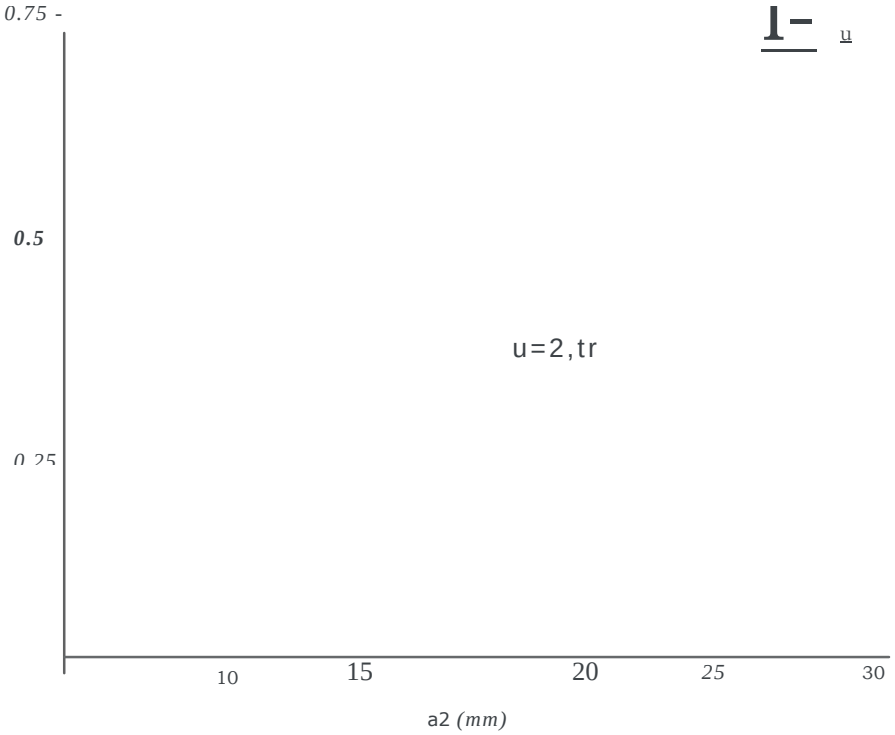

Figure 7.30 *The crack sliding displacement at the pin 4 location* vs. *debond length.*

In general the normal traction F3 increases initially very rapidly during the pre-pullout phase, then after a debond length a_2=12 mm has been attained, which model parameter evaluation shows corresponds to the start of the pullout process, the *force* magnitude increases very slowly. This is thought to be related to the simultaneous growth of the enhancement friction zone which tends to delay the peak load and successive load declining phase typical of the pin pullout phase.

At the same time, the shear traction F continues to increase steadily, even as pullout continues. Nevertheless the bridging forces (F_1) against Mode II fracture are as much as an order of magnitude lower than the bridging forces against Mode I fracture (F3) (see figures 7.26 and 7.27).

This happens partly because the pin is deforming at the crack plane to progressively larger angles (solid line in figure 7.28), so that the stiff fibres in the pin align more completely with the shear displacements. It is thought that the order of magnitude of the bridging force components could become comparable if these pins were inserted with an inclined angle. In this configuration, from the beginning of the bridging process, most of the pin stiff fibres would already be opposing shear loads, contrasting more effectively the Mode II debonding components.

The axial stress in the pin is also increasing during pullout, because the zone of enhanced friction grows as the pin rotates (dashed line in figure 7.28). The development of the deflected zone rb_0, the slip zone growth L, and the progression of pullout length of the pin Ds are illustrated in figure 7.29. As the zone of enhanced friction and pin deformation grows, the pullout length tends to remain very small, therefore delaying the pin pullout failure mode. Concluding the analysis of the micro-mechanical parameters for the pins in the Joint Z, the sliding displacements for pin number 4 are also reported in figure 7.30.

7.6 Conclusions

An alternative design method was presented to enhance the structural performances of composite joints. Through-thickness reinforcement of composite joints using small diameter carbon pins via the z-pinning or a simple pinning procedure was discussed.

A simple curved single-lap shear joint was studied to prove the effectiveness of through thickness reinforcements against joint debond failure. Large scale bridging calculations rather than shear lag approximations were used to capture the shielding effect of reinforcing pins on the debond crack front.

An FE model of the CSLJ was developed. The analytical micro-mechanical model discussed in Chapter 4, and implemented under Mode I loading conditions **in** Chapter 5, was extended to analyse a debond crack under mixed-mode crack loading conditions for simulating a group of carbon pins in a composite single-lap joint. Other important energy absorbing mechanisms were not included, but were indicated and should be considered for future improvements of the model.

The FE model successfully predicted the stiffness and strength (failure loads) of both unpinned and pinned joints. Agreement with experiments was acceptable. The failure strength was increased by 33% in the pinned joint. The strain analysis was close enough to the experimental readings showing that during debond propagation. The pinned joint

experienced as much as twice the strain fields of the unpinned joint, reaching the adherend material tensile strength.

These findings were attributed to the pin mechanics which delayed the debond growth, enhancing the load bearing capacity of the joint. The bridging mechanisms of the carbon pins, provided a shielding effect *for the* debond front against the full debonding loads. The shielding was shown to be the sum of (non-linear) bridging tractions supplied by the pins, which opposed crack opening and sliding displacements and therefore reduced the strain energy release rate for debond crack propagation.

The opening displacements were more effectively opposed by the bridging pins, having therefore more impact on mode I strain energy release components. Nevertheless, with a sufficient debond growth the pins' deformation at the fracture plane allowed the alignment of the stiff fibres in the pin with the shear loads, ensuring more resistance against the mode I I loads.

Among all the different micro-mechanical parameters the zone of enhanced friction coefficient, which never exceeded 25% of the total pin length, was found to play a crucial rule in delaying the pin pullout failure and increasing the amount of axial stress carried by the deformed pins. It was therefore concluded that pin insertion at an inclined angle, would imply that a larger number of the pin stiff fibres would oppose shear loads at the beginning of the bridging action, ensuring higher resistance against Mode II loading conditions.

Through-thickness reinforcement is proved to improve the joint damage tolerance, stabilizing and delaying the debond growth and ultimately raising the joint failure load. TTR proved to be more effective in reducing the Mode 1 than the Mode II debonding component.

Chapter 8

Conclusions and future studies

8.1 Conclusions (b)

After an exhaustive review of the z-fiber[m1]
pinning technique and the state of the art research efforts, this thesis has concentrated on developing numerical models to study the effect of through-thickness reinforcement on the stiffness, strength, and fracture toughness of pinned laminates and structural joints. Specific conclusions have been drawn at the end of each chapter. The main conclusions are summarised as follows.

8.1.1 Engineering elastic constants and interlaminar *stresses*

Three-dimensional micro-mechanical finite element models were presented to examine the mechanical behaviour of z-pinned laminates. It was found that by adding two percent volume fraction of z-fibres, the through-thickness Young's modulus (E2) was increased significantly, i.e. by 22-35%, for the four different laminates studied. The reductions in the in-plane moduli were limited to 7-10%.

The interlaminar stress distributions near the free edge of a z-pinned laminate were significantly affected only when *z-fibres were* placed within a characteristic distance of one z-fibre diameter from the free-edge.

8.1.2 Z-pin bridging mechanics

The micro-mechanical analysis of a z-fibre bridging a delamination crack under mixed-mode loading condition was performed. Z-pin bridging laws were computed for mode I and mode II loads.

Z-pin bridging traction forces against the mode I loads were shown to increase by employing smaller pill diameters, maximum pin insertion depth and by enhancing the pin surface roughness. The pin pullout rather than tensile axial failure was shown to limit the load carrying capability of the z-pins.

In the case of mode II loads, bridging forces were shown to increase due to the z-fibre alignment with the shear loads, with the axial stiffness of the rotated pins supporting those loads. It was therefore concluded that inclined z-pins would provide a better bridging force against shear loads having part of the axial stiffness already oriented towards the load direction.

8.1.3 Interface elements for z-pin bridging laws

The implementation of the analytical bridging laws into specifically defined interface elements for the FE analysis was considered a crucial step to achieve efficient modelling capabilities. This hybrid approach using analytical micro-mechanical models and numerical FE methods was thought to provide a robust design tool to assess z-fibre effect on composite structural components, without the necessity to simulate the z-pin micro-mechanics with a very complex FE model.

(b)

8.1.4 Effect on mode 1 delamination

The numerical simulation was aimed to characterise the mode I fracture behaviour of z-pinned laminates. Satisfactory agreement with experimental data was obtained for a DCB example.

The z-fibre technique was found very effective in enhancing the resistance to inode I delamination. Crack bridging enhanced material resistance by partially shielding the crack tip from the applied delaminating loads. When z-fibre bridging mechanics was activated the order of the magnitudes of the bridging zone length and the total crack length became comparable, therefore the fracture analysis became a large scale bridging problem.

For the DCB configuration, it was found that z-pinning had almost no effect on the initiation of delamination growth from a starter crack. In order to activate the z-fibre bridging mechanism a delamination needed to propagate into the z-fibre field for several millimetres; the LSB then stabilized the crack growth and consequently raised the external load required to propagate the damage or temporally arrested the crack. Therefore z-pinning was considered to be useful for a damage tolerant design. The LSB was shown to become a stable process with the magnitude of LSB being independent of the crack length.

8.1.5 Fracture toughness and energy balance

The assumption made by the LEFM that all energy dissipations were included in the fracture energy and confined within the damage front were shown not to be valid for z-pinned laminates. The novelty dealing with through-thickness reinforced laminates was found to be related to the large amount of irreversible energy consumed due to large scale bridging.

The material fracture toughness (0_k) was considered to be unaffected by the z-fibre presence, whilst the structural toughness to delamination growth was seen to be increased because of the presence of 0,r in the energy rate equation. Rather than a material

parameter the toughness to delamination growth seemed to depend on the z-pin micromechanics and its interaction with the laminate geometry during the fracture process, in that sense it was defined as structural fracture toughness.

8.1.6 Reinforced structural joints

A simple curved single-lap shear joint was studied to prove the effectiveness of through thickness reinforcements against joint debond failure. Large scale bridging calculations were used to capture the shielding *effect* of reinforcing pins on the debond crack front tinder mixed-mode loads.

(b)

Through thickness reinforcements proved to improve the joint damage tolerance, stabilizing and delaying the debond growth and ultimately rising the joint failure load. The TTR presence showed to delay the propagation of the debonding and generally to enhance the load carrying capability of the joint. TTR proved to be more effective in reducing mode I than the mode II debonding component. The strain analysis showed that during debond propagation pinned joint experienced as much as twice the strain fields of the unpinned joint, reaching the adherend material tensile strength.

8.2 Future studies

8.2.1 3D FE micro-mechanical model of a single z-pin failure

A detailed 3-D FE model to simulate a single TTR bridging a delamination crack under quasi-static loads and in the presence of frictional contact between the z-fibre/matrix interface could be used to assess the validity of assumptions made by the analytical micro-mnechanical model.

Within the limited amount of time of this research study, some preliminary modeling was done. The pull-out simulation was considered assuming a constant friction coefficient at the interface along the TTR axial direction and using contact-elements to solve the frictional contact problem. Loadldisplacement bridging curves of the fibre pull-out process, which includes elastic deformation with a fullylpartially bonded interface plus frictional sliding, were calculated. Moreover, the effect of friction forces was also investigated. Numerical results were validated by experimental observations of debonding and frictional sliding of a fiber in steady-state pull-out tests (figure 8.1).

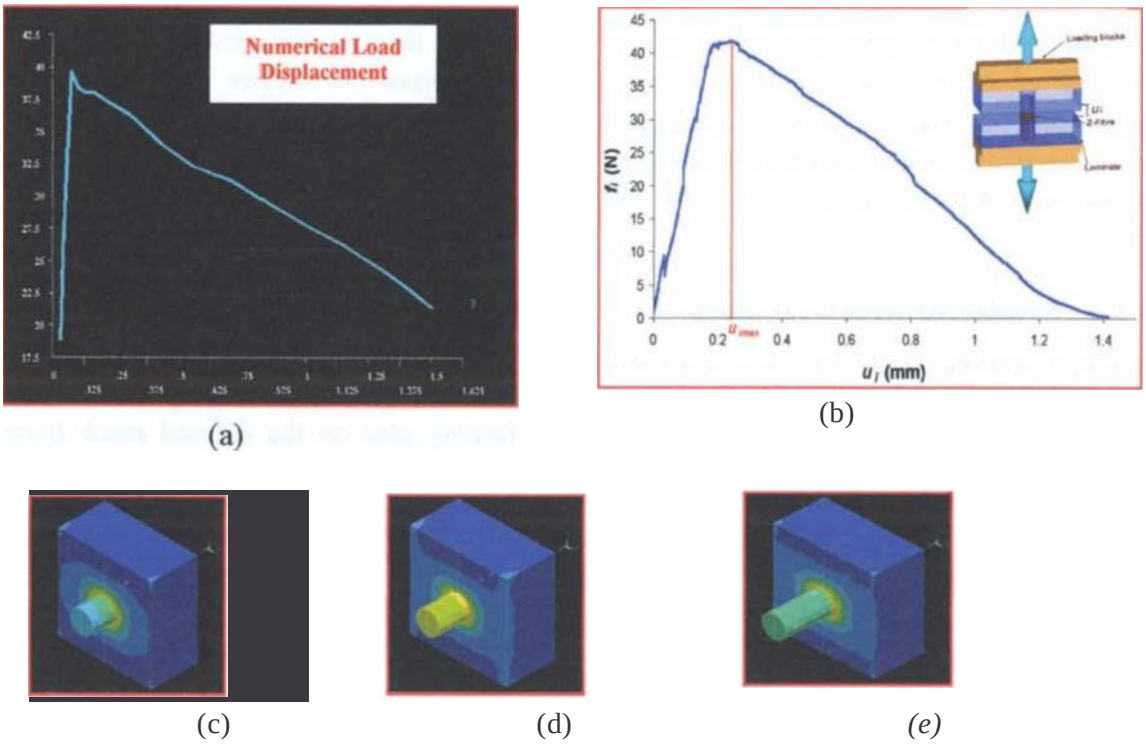

Figure 8.1 *Pull-out failure process of a single z-pin: (a) Load displacement curve-numerical simulation: (h) Load Displacement curve- experimental results--; (c) z -pin elastic stretching: (d) z-pin debonding; (e) z-pin frictional sliding.*

A more detailed FE model should take into account different load modes for the z-pin. A damage mechanics formulation may be applied for the solid elements to simulate the damage occurring within the z-pin during the bending in the fracture plane (matrix cracking, fibre splitting), then apply a fracture criteria for the propagation of the debonding at the pin-laminate interface (in our simulation a simple shear stress-based criteria was used), and define a non-homogeneous distribution of the friction coefficient in order to account for the variability of the surface roughness.

An extended study of the previous model could also tackle the interaction of an array of pins during crack bridging. If crack bridging should also be investigated for different delamination rates, inertial effects related to the pin pullout should also be taken into account.

"Courtesy of D.D.R Cartie, Cranfield University, Advanced Material Department.

8.2.2 Implementation of the z-pin interface elements into a Global-Local FE analysis

It is unlikely that the simulation of every single z-pin with an interface element would be applicable to large FE models of composite structural elements. The mesh refinements required to incorporate the through-thickness-reinforcement elements into the FE model would imply an excessive number of degrees of freedom, resulting in a very expensive computational model. What has become common practice in the FE modelling is the use of the global-local approach to analyse specific areas of interests where a more detailed model might be required (figure 8.2),

Figure 8.2 *Global FE model of a composite stiffened panel, with a local model to simulate local damage growth.*

This approach might prove to be valid also for FE models with TTR. The global FE model can give general information about the stress-strain field of the component, identifying possible areas prone to delamination-debonding failure. At this stage the TTR presence into the global FE model can be taken into account by modifying the elastic constants of the shell or solid elements in the areas where TTR are placed.

Once the kind of failure has been established, whether a delamination or debonding might grow, a design choice can be made on TTR implementation.

This study can be done numerically by developing a refined FE local model with the boundary conditions and displacements derived from the global FE model. This model will simulate a crack growth and implement the TTR interface elements into the crack we. The effect of the TTR on the strain energy release rates along the crack front will therefore be studied investigating the mode ratio changes due to TTR bridging mechanics and whether or not LSB mechanics would stop delamination.

For large FE global models it is thought that the local refined models simulating delamination growth will have to incorporate several hundreds of TTR interface elements, due to the typical distances between reinforcements in a laminate. In order to reduce the computational effort, the stiffness matrices [KJ; of those elements could be assembled into a z-pin macro-element /K/) (figure 8.3). The size of the interface element array to be embedded into the macro-element could match the size of the composite shell or solid elements. Multi Point Constraints (MPC) could relate the displacements of the shell or solid

nodes to the ones of the macro element. It should be therefore assumed that a square array of pins will exert a uniform LSB process.

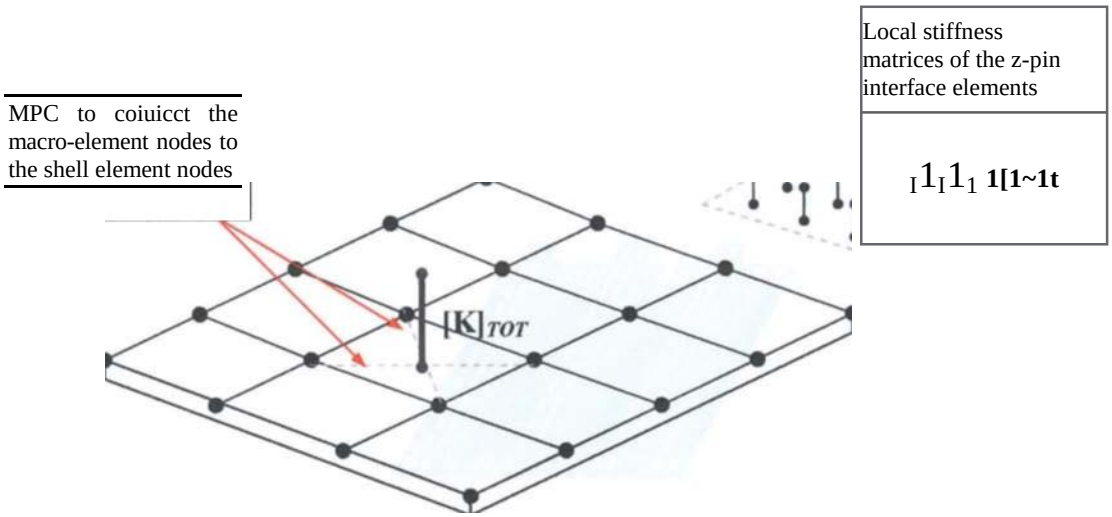

Figure 8.3 *Implementation of the z-pin macro-element into a shell FE model,*

Another consideration could simplify the FE modelling effort. Considering the typical scale lengths where the LBS is acting, if the FE model has typical element sizes comparable with the LSB length (10mm < D < 20mm), the experimentally derived "apparent fracture toughness" could be used as critical parameter for fracture propagation. Even though this simplification is very crude comparing to an accurate analysis of the crack growth and LSB, it could provide enough information about the delamination path and how z-pinned areas might stop delamination growth.

References

Adams, R.D., Theoretical stress analysis of adhesively bonded joints. In: *Joining Fibre-Rein/nrced Plastics,* edited by Elsevier Applied Science, Chapter 5, 1986, 185-226,

Allix, O., and Ladeveze, P., Interlaminar interface modelling for the prediction of delamination. *Composite Structures, 22,* 1992. *235-242.*

Altergott, W., The Z-Fiber process, through-thickness reinforcement for composite structures. In: *Proceedings of the 10`h DOD NASA FAA Conference of Fibrous Composites in Structural Design,* NAWCADWAR-94096-60, 1994. 71-93,

ANSYS, Non-linear structural analysis, In: *ANSYS Structural and analysis guide,* edited by SAS 1P Inc., Chapter 8, 2001_

Baillie, C., Kim, P.J., and Mai, Y.W., Fracture toughness of CFRP with modified epoxy resin matrices. *Composite Science & Technology,* 43, 1992. *283-297.*

Bao, G., and Suo, Z., Remarks on crack bridging concepts. *Applied Mechanics Review,* 45, 1992. 355-366.

Barret, D,J,, The analysis of z-fiber reinforced plate. *Aircraft Division Report,* NAWCADWAR-95-12-TR, 1995,

Barret, D.J., The mechanics of z-fiber reinforcement. *Composite Structures, 36,* 1996, 23-32.

Bersuch, L., Benson, R., and Owens, S., Affordable Composite Structures for next generation **fighters.** In: ***43'd*** *International SAMPE Symposium,* 1998.

Bitsianis, N., The influence of z-pinning on toughness and impact performance of carbon fibre polymer composite materials. *MSc Thesis,* Cranfield University, edited by Cranfield University, 1999.

Bogdanovich, A.E., Kiihakkethara, I., Three-dimensional finite element analysis of double-lap composite adhesive joint using sub-modeling approach. Composites: Purl B, 30, 1999. 537-551.

Borg, R., Nilsson, L., Simonsson, K., Simulation of delamination in fibre composites with a discrete cohesive failure model. *Composite Science & 7eclznolo€;y,* 61, 200I_ 667-677.

Carlsson, L.A., Gillespie, J.W., and Pipes, R.B., On the analysis and design of the end notched flexure (ENF) specimen for mode II testing. *Journal of Composite Materials,* 20, 1986. 594-604.

Cartie, D.D.R., and Partridge, I.K,, Z-pinned composite laminates: improvements in delamination resistance. In: *Proceedings of the 5'h International C'onfirence on Deformation and Fracture of Composites DN:5,* London, UK, April 1999.

Cartie, D.D.R., Effect of Z-Fibres on delamination behavior of carbon fibre epoxy laminates. *PhD Thesis,* Cranfield University, edited by Cranfield University; 2000.

Cartie, D.D.R., and Partridge, I.K., A Finite Element tool for parametric studies of delamination in z-pinned laminates. In: *Proceedings of'the 6t International Conference on Deformation and Fracture of('omposites D R* '6, Manchester, UK, April 2001,

Cartie, D.D.R., Cox, B.N., and Fleck, N., Mechanisms of damage in laminates reinforced through the thickness by metallic and fibrous pins. 2003, (unpublished).

Childress, J.J., and Freitas, G., Z-direction pinning of composite laminates for increased survivability. In: *Proceedings of the AIAA Aerospace Design Conference,* 1992. 1092-1099.

Chou, T.W., and Ko, F.K., Textile Structural Composites, In: *Composite Materials* Series, edited by Elsevier, 1989.

Cox, B.N., Massabo, R., Mumm, D., Turrettini, A., and Kedward, K., Delamination fracture in the presence of through-thickness reinforcement. In: *International Conference of Composite Materials,* ICCM 1 1, Naples, 1997.

Cox, B.N., Constitutive model for a fiber tow bridging a delamination crack. *Mechanics of Composite Materials and Structures, 6,* 1999a. 117-138.

Cox, B.N., A constitutive model for through-thickness reinforcement bridging a delamination crack. *Advanced Composites Letters, 8,* 1999b. *249-256.*

Cox, B.N., Massabo R., and Rugg, K., The science and engineering of delamination suppression. In: *Proceedings of the 6rh International Conference on Deformation and Fracture of Composites DEC'6,* Manchester UK, April 2001.

Cox B.N., and Sridhar N.A., A traction law for inclined fibre tows bridging a mixed mode cracks. *Mechanics of Composite Materials and Structures, 9, 2002.* 299-331.

Cox, B.N., Private communications, 2003.

Crews, J.H., and Reeder, JR., A mixed mode bending apparatus for delamination testing. NASA technical memorandum, 1000662, 1988.

Davidson, B.D., Krueger, R., and Konig, M., Three-dimensional analysis of center-delaminated unidirectional and multidirectional single-leg bending specimens. *Composite Science and l echnologry, 54,* 1995, *385-394.*

Dasgupta, A,, Agarwal, L.K., and Bhandarkar, S.M., Three-Dimensional modeling of woven-fabric-composites for effective thereto-mechanical and thermal properties. *Composite Science & 1 echnology, 56,* 1996. 209-223.

De Roeck, G., and Wahab, A.M., Strain Energy Release Rate formulae for 3D finite element. *Engineering Fracture mechanics, 50 (4), 1995. 569-580.*

Dickinson, L.C., Prediction of effective three-dimensional elastic constants of translaminar reinforced composites. *Journal of Composite Materials, 33 (11), 1999.* 1003-1028.

Dow, M.B., and Smith, D.L., Improving the delamination resistance of CFRP by stitching carbon fabrics. In: *21 s International SAMPE Technical Conference,* 21, 1989. 595-605.

Dransfield, K.A., Baillie, C., and Mai, Y.W., Improving the delamination resistance of CFRP by stitching a review. *Composite Science & Technology, 50,* 1994. *305-317.*

Dransfield, K.A., Jain, L.K,, and Mai, Y.W., On the effects of stitching in CFRPs-I. Mode I delamination toughness. *Composite Science & Technology, 58,* 1998, 815-827.

Ducept, F., Davies, P., and Gamby, D., Mixed mode failure for a glass/epoxy composite and an adhesively bonded composite/composite joint. *International Journal of Adhesion and Adhesives, 20,* 2000. 233-244.

Falzon, B.G., Hitchings, D., and Besant, T., Fracture mechanics using a 3D composite element. *Composite Structures, 45,* 1999. *29-39.*

Fortsch, W., Franz, H.E., and Friedrich, K., Investigation into damage mechanisms in advanced composite materials for the purpose of material improvement and damage prediction. In: *l European Conference for Composite Materials,* ECCM-10, *Bruges,* June 2002. Paper 359.

Freitas, G., Fusco, T., Magee, C., and Dardzinski, P., Fibre insertion process for improved damage tolerance in aircraft structures. *Journal of Advanced Materials, 25,* 1994. 36-44.

Freitas, G., Fusco, T., Campbell, T., Harris J., and Rosenberg, S., Z-Fiber technology and products for enhancing composite design. 1n: *Proceedings of 83"t Meeting of the AGARD SMP,* 1996. CP-590.

Friedrich, *Fracture Mechanics,* Edited by Elsevier Science; Netherlands, 1989.

Gangi, Li, Pearl, Lee-Sullivan, Ronald W., Nonlinear finite element analysis of stress and strain distributions across the adhesive thickness in composite single-lap joints. *Composite Structures,* 46, 1999. 395-403.

Gdoutos, E.E., Pilakoutas, K., and Rodopoulos, C.A., *Failure Analysis of Industrial Composite Materials.* edited by McGraw Hill, 2000.

Glassgen, E.H., and Raju, I. S., Three-dimensional effects in the plate element analysis of stitched textile composites. *AJAR Paper-1416.* 1999a.

Glaessgen, E.H., Raju, I,S., and Poe, C.C., Delamination and Stitch failure in stitched composite joints. *AIAA paper /247,* 1999b.

Goland, M., and Reissner, E., The stresses in cemented joints. *Journal of Applied Mechanics,* 1 l , 1944. 17-27,

Graftieaux, B,P.H,, Investigation of delamination of Z-pinned composite laminates under Mode 1 and Mode II cyclic loading. *MSc Thesis,* SIMS Department Cranfield University, edited by Cranfield University, 1999.

Graftieaux, B., Rezai, A., and Partridge, I.K., Effects of z-pin reinforcements on the delamination toughness and fatigue performance of unidirectional AS4/8552 composite. In: *9 i' European Conference for Composite Materials, ECCM9,* Brighton, April 2000.

Grassi, M., and Nicastro, G., Structural design of a carbon fiber reinforced UAV. *Thesis in Aerospace Engineering,* Aerospace Design Department, edited by University of Naples, 1999. (in Italian).

Hart-Smith, L.J., Adhesive-bonded single-lap joints. *Langley Research Center, NASA CR112236,* 1973.

Hart-Smith, L.J., Design and Empirical Analysis of Bolted or Riveted Joints, In: *Joining Fibre-Reinforced Plastics,* edited by F.L. Matthews, Elsevier Applied Science, London and New York, Chapter 6, 1987. 227-271.

Hashim, S. A., Cowling, M. J., and Lafferty, S., The integrity of bonded joints in large composite pipes. *InternationalJournal of Adhesion & Adhesives,* 18, 1998.421-429.

He, M., and Cox, B.N., Crack Bridging by through-thickness reinforcement in delaminating curved structures. *Composites Part A,* 29A,1998. 337-344.

Houslow, L.E., The influence of z-pinning on low velocity impact performance of laminated carbon composites. *ll~Sc Thesis,* Cranfield College of Aeronautics, edited by Cranfield University, 2000.

Hu, F.Z., Soutis, C., and Edge, E.C., Interlaminar stresses in composite laminates with a circular hole. *Composite Structures, 37,* 1997, 223-232.

Jain, L.K., and Mai, Y.W., On the effect of stitching on Mode I delamination toughness of laminated composites. *Composite Science & T echnology,* 51, 1994. 331-345.

Jain, L.K., and Mai, Y.W., Determination of Mode II delamination toughness of stitched laminated composites. *Composite Science & T'echnoloy, 55,* 1995. 241-253,

Jain, L.K., Dransfield, K.A., and Mai, Y.W., On the effects of stitching in CFRPs-I1. Mode II delamination toughness. *Composite Science & Technology, 58,* 1998. *829-837.*

Jegley, D., Effect of low speed impact damage and damage location on the behaviour of composite panels. In: *DoD NASA FAA on Fibrous Composites in Structural Design,* 1991.

Johnson, A.F., and Pickett, A.K., Impact and crash modelling of composite structures: a challenge for damage mechanics. In: *Proceedings of European Conference on Computational Mechanics, EC'CM99,* Munchen, 1999.

Johnson, A.F., and Pickett, A.K., Numerical modelling of composite structures under impact loads, *DYMAT,* Krakow, *25-29* September, 2000.

Kant, T,, and Swaminathan, K., Estimation of translaminariinterlaminar stresses in laminated composites - a selective review and survey of current developments. *C'ompo.site Structures, 49,* 2000. 65-75.

Kehlenhach, M., and Betz, D., Fibre-optic Bragg grating sensors for strain measurement inside composite materials. In: *1V11 European Conference fbr Composite Materials,* ECCM-10, Bruges, June 2002.

Ker, J.C., Numerical representative volume element modelling of the elastic response of through-thickness reinforced fibre-composite laminates. *MSc Thesis,* Cranfield College of Aeronautics, edited by Cranfield University, 2001.

Koo, J.H., and Schoeppner, G.A., Structures, Design and Test. *Aerospace America,* December 2002. A1AA 12: 82-83.

Kim, J.K., and Mai, Y.W., High strength, high fracture toughness fibre composites with interfacial control: *a review. Composite Science & Technology,* 41, 1991. *333-378.*

Knox, E.M., Lafferty, S., Cowling, M.J., and 1-lashim, S.A., Design guidance and structural integrity of bonded connections in GRE pipes. *Composites: Part A,* 32, 2001. 231-241,

Kruger, R., Minguet, P., and O'Brien, T.K., A method for calculating Strain Energy Release Rates in preliminary Design of composites SkinlStringer Debonding under Multi-axial Loading. *NASA Langley Research Center,* NASA TM-209365. 1999.

Krueger, R., and O'Brien, T.K., A Shell/3D Modeling technique for the Analysis of De laminated Composite Laminates. *NASA Langley Research (.'enter,* NASA TM-210287, 2000.

Larsson, F. Damage Tolerance of a stitched and unstitched composite plates subject to impact loading. *Journal of Reinforced Plastics and Composites, 9,* 1990. *56-69.*

Lagace, P., Towards design methodologies for more effective use of composite structures. Invited lecture at *European Conference for Composite Materials,* ECCM-10, Bruges, June 2002.

Lees, J., "Pin Reinforced GFRP Single Lap Joints: Test Summary", Internal Report, Cambridge University, 2002 (Unpublished).

Lees, J., Mechanicallbonded joints for advanced composite structures. to appear in *Journal of ('ivil* Engineering, 2003.

Lessard, L., Schmidt, B., and Shokrieh, M., Three-dimensional stress analysis *of free*-edge effects in a simple composite cross-ply laminate. *International Journal Solid Structures,* 33 (15), 1996. 2243-2259.

Li, V.C., Postcrack scaling relations for fiber reinforced cementitious composites. *Journal of Materials and Civil Engineering,* 4 (1), 1992. 41-57.

Lindhagen, J.E., and Berglund, L.A., Application of bridging-law concepts to short-fibre composites. Part 1: DCB test procedures for bridging law and fracture energy. *Composite Science & Technology, 60, 2000.* 871-883.

Lin, C.Y., and Chan, W.S., Stiffness of composite laminates with z-fiber reinforcement. *AIAA AWE' ASCE AHS. ASC Structures, Structural Dynamics, and Materials Conf* , St. Louis, April, 1999. Paper No. AIAA-99-1294.

Liu, D., Delamination resistance in stitched and unstitched composites plates subjected to impact *loads. Journal of Reinforced Plastics and Composites, 9,* 1990. *56-69.*

Liu, H.Y., and Mai, Y. W,, Effects of z-pin reinforcement on interlaminar mode I delamination. *International Conference of Composite Materials,* ICCM 13, Beijing 2001.

Mabson, G.E., and Deobald, L.R., Design curves for 3D reinforced composite laminated double cantilever beams. In: *Proceedings of ASME Int. Mechanical Engineering Congress and Exposition, 2000. 89-99.*

Marasco, A., Low velocity impact on K-Cor^{r}'', X-Cor^{r}' sandwich constructions. PhD annual review report, Cranfield University, 2003 (unpublished).

Martin, R.H., Local facture mechanics analysis of stringer pull-off and delamination in a post-buckled compression panel. *Applied Composite Materials, 3,* 1996. 249-264.

Martin, R.H., Mode II fracture toughness evaluation using a four point bend end notched flexure test. In: *Proceedings of the 4th International Conference on Deformation and Fracture ofC:omposites DFC4,* Manchester, UK, March 1997.

Martin, R.H., incorporating interlaminar fracture mechanics into design. In: *International Conference on designing cost-effective composites,* IMechl Conference Transactions, London, UK, 1998. 83-92,

MassabO, R., Mumm, D., and Cox, B.N., Characterizing mode II delamination cracks in stitched composites. *International Journal of Praclure,* 92, 1998. 1-38.

Massabe, R., and Cox, B.N., Unusual characteristics of mixed mode delamination fracture in the presence of large scale bridging. *Mechanics of Composite Materials and Structures,* 8 (1), 2001. 61-80.

Matthews, F.L., Load-Carrying Joints. In: *Composite Materials in Aircraft Structures,* edited by Middleton, 1990. 142-154.

Mi Y., Crisfield M.A., Davies, G.A.O., Hellweg, H.B., Progressive delamination using interface elements. *Journal of Composite Materials, 32 (14),* 1998. 1247-1272.

MIL-HDBK-17-3E, Structural Behaviour of Joints, *In: MM.-HD3K-17-3E,* Chapter *5,* 1998.

Mottram, J.T., Bonded Connections, 1n: *State-of-the-art Review on Design, Testing, Analysis and Applications of Polymeric Composite Connections,* Chapter 5, edited by European Commission European Cooperation in the Field of Scientific and Technical Research, Luxemburg., 1998. 56-70.

Mouritz, A.P., Leong, K.H., and Herszberg, I., A review of the effect of stitching on the in-plane mechanical properties of the fibre reinforced polymer composites. *Composites Part A,* 28, 1997. 979-971.

Mouritz, A.F., and Cox, B.N., A mechanistic approach to the properties of stitched laminates. *C'omposiles Part A,* 31, 2000, 1-27.

0' Brien, T.K., Characterization of delamination onset and growth in a composite laminate. *ASTM STP,* 1982. *775.*

0' Brien, T.K., Iterlaminar fracture toughness: the long and winding road to standardization. *Composites Part B,* 29, 1998. 57-62.

0' Brien, T.K., and Martin, R.H., Round robin testing for mode I interlaminar fracture toughness of composite materials. *Journal of Composites' Technology and Research,* 15 (4), 1993. 269-281.

0' Brien, T.K., A shell/3D modelling technique for the analysis of delaminated composite laminates. *Composites Part A.* 32 (1), 2001. 25-44.

Offringa, A., Composite wing increases mileage. *Reinforced Plastics,* December 2002.

Palazotto, A.N., Gummadi, L.N.S., Vaidya, U.K., and Herup, E.J., Low velocity damage characteristics of z-fiber reinforced sandwich panels- an experimental study. *Composite Structures,* 43, 1999, 275-288.

Pochiraiuju, K.V., Tandon, G.P., Pagano, N.J., Analyses of single fiber push out considering interfacial friction and adhesion. *Journal of Mechanics and Physics of Solids,* 49, 2001. 2307-2338.

Poe, C.C., Dexter, H.B., and Raju, I., A review of the NASA textile composites research. *AIAA Journal,* 1321, 1997. 1-13.

Raju, I.S., Calculation of strain-energy release rates with higher order and singular finite elements. *Engineering Fracture mechanics, 28 (3),* 1987. 251-274.

Raju, I.S., Wang, J.T., Strain-Energy Release Rates formulae for skin-stiffener debond modeled with plate elements. *Engineering Fracture mechanics, 54 (2),* I996a. 211-228.

Raju, I.S., Sistla, R., and Krishnamutry, T., Fracture mechanics analyses for skin-stiffener debonding. *Engineering Fracture mechanics, 54 (3),* 1996b. 371-385.

Raju, I.S., Glassgen, E.H., and Poe, C., Fracture mechanics analysis of stitched skin-stiffener debonding. A/AA *Paper 98-2022-CP,* 1998a.

Raju I.S., Glassgen E.H., and Riddel T. Effect of shear deformation and continuity on delamination Strain Energy Release Rate. *AIAA Paper 98-2023-CP* , 1998b.

Rybicki, E.F., and Kanninen, M.F., A Finite Element calculation of stress intensity factors by a modified crack closure integral, *Engineering Fracture mechanics, 9,* 1977. 931-938.

Rouchon, J., Certification of large airplane composite structures. In: *Recent progress and new trends and compliance philosophy, /CAS,* Vol.2, 1990, 1439-1447.

Roudolff, F., and Gadke, M., Damage tolerance of composite structures for large transport aircraft. *Aerospace Science Technology, 4,* 2000, *23-32.*

Rugg, K.L., Cox, B.N., Ward, K.E., and Sherrick, G.G., Damage mechanics for angled through-thickness rod reinforcement in carbon-epoxy laminates. *Composites Part A,* 29, 1998. 1603-1613.

Rugg, K.L., and Cox, B.N., Mixed mode delamination of polymer composite laminates reinforced through the thickness by z-fibers. *Composites Part A,* 33, 2002. 177-190_

Russel, A.J., Micro-mechanics of interlaminar fracture and fatigue. *Polymer Composites,* 1987. 342-350.

Shen, F., Lee, K.H., and Tay, T.E., Modelling delamination growth in laminated composites. *Composite Science & Technology,* 61, 2001. 1239-1251.

Sheahen, P., Schmidt, R., and Holcombe, T., Primary sandwich structure: a unitised approach. In: *4I'z AIAA'ASMEASCEAHS:ASC Structures, Structural Dynamics, and Materials Conference, 2000. 700-707.*

Singh, S., and Partridge, I.K., Mixed-Mode fracture in an interleaved carbonfibre/epoxy composite. *Composite Science & Technology, 55,* 1995. 319-327.

Sohn, M.S., and Hu, X.Z., Mode II delamination toughness of carbon fibre epoxy composites with chopped Key tar fibre reinforcement. *Composite Science & Technologry,* 52, 1994. 439-448.

Sorensen, B.F., and Jacobsen, T.K., Large scale bridging in composites: R-Curves and bridging laws. *Composites Part A,* 29, 1998. 1443-1451.

Steeves, C.A., and Fleck, N.A., In-plane properties of CFRP laminates containing trough-thickness reinforcing rods (Z-Pins). In: *International Conference of Composite Materials,* ICCMI2, Paris 1999a.

Steeves, C.A., and Fleck, N.A., Z-pinned composite laminates: knockdown in compressive strength. In: *Proceedings 5`h International Conference on Deformation and Fracture of Composites* DFC5, London UK, 1999h. 60-68.

Sun, C.T., and Li., S., Three-dimensional effective elastic constants for thick laminates. *Journal o_f Composite Materials, 22,* 1988. *629-639.*

Sun, C.T., and Vaidya, R.S., Prediction of composites properties from a representative volume element. *(.'omposite Science & Technology, 56,* 1996. 17I-179.

Sun, W., Lin, F., and Hu, X., Computer-aided design and modelling of composite unit cells. *C.'omposite Science & lechnologry,* 61, *2000. 289-299.*

Tahmasebi, F., Software tools for Analysis of Bonded Joints, FEMCI Workshop, NASAIGSFG (2001), code 542.

Tanzawa, Y., Watanabe, N., and Ishikawa, T., Interlaminar fracture toughness of 3-D orthogonal interlocked fabric composites. *Composite Science & T echnoIog', 59,* 1999. 1261-1270.

Tong, L., Jain, L.K., and Leong, K.H., Failure of a transversely stitched RTM lap joint. *Composite Science & Technology, 58,* 1998a. 221-227.

Tong, L., Strength of adhesively bonded single-lap and lap-shear joints, *International Journal Solids and Structures,* 35 (20), 1998b. 2601-2616.

Tropis A., Thomas, M., Bounie, J.L., and Lafon, P., Certification *of* the composite outer wing of the ATR72. *Journal of Aerospace Engineering, 209,* 1994. *327-339.*

Troulis, M., Cartie, D.D.R., and Partridge, I.K., Z-pinned woven laminates: interlaminar *fracture* results *and* pinning quality considerations. In: *Proceedings of the 6th International C'onference on Deformation and Fracture of Composites DFC6,* Manchester, UK, April 2001,

Troulis, M., Delamination test data on z-pinned composite specimens, *MERCURYM Report,* Advanced Materials Department, Cranfield University: 2002a (unpublished).

Troulis, M., Open hole tension test on z-pinned laminates. *MERCURYM Report,* Advanced Materials Department, Cranfield University, 2002b. (unpublished)

Troulis, M., Effects of Z-Fiber pinning on the mechanical properties of carbon fibre/epoxy composites. *PhD Thesis,* Cranfield University, edited by Cranfield University; 2003.

Turrettini, A., An investigation of the Mode I and Mode II stitch bridging laws in stitched polymer composites. *lvISc Thesis,* Department of Mechanical and Environmental Engineering, Edited by University of California, Santa Barbara; 1996.

Turton, T.J., MERCURYM: interim report on crack stopping methods. DERA, 2000 (unpublished).

Vlot, A., Glare: history of the development of a new aircraft material. Edited by *Kluwer Academic Publisher*, 2001.

Wang, J.T., and Raju, I.S., Strain-Energy Release Rates formulae for skin-stiffener debond modeled with plate elements. *Engineering Fracture mechanics, 54 (2), 1996.* 21 1-228.

Weinecke, Brockenbrough, J.R., and Romanko, A.D., Three-Dimensional Unit Cell model with application toward particulate composites. *Journal of Applied Mechanics, 62 (1),* 1995. 136-140.

Wie, J., and Zhao, J.H., Three-dimensional finite element analysis of interlaminar stresses of symmetric laminate. *Computers & Structures,* 41 (4), 1991. *561-567.*

Whitcomb, J. D., Chapman, C. L., and Tang, X., Derivation of boundary conditions for micro-mechanics analyses of plain and satin weave composites. *Journal of ('omposite Materials, 34,* 2000. 734-747,

Wilkins, D.J., Eisenmann, J.R,, Camin, R.A., Margolis, W.S., and Benson, R.A., Charachterizing delamination growth in graphite-epoxy, *ASTMSTP,* 360, 129-134.

Woods, D.W., Hine, P.J., and Ward, I.M., The impact properties of Hybrid Composites Reinforced with high modulus Polyethylene Fibres and Glass Fibres." *Composite Science & Technolo, 52,* 1994. *397-405.*

Yang, T.J., and He, C.C., Three-dimensional finite element analysis of free edge stresses and delamination of composite laminate. 28 (15), 1994. 1395-1412.

Zhang, X., Liu, H.Y., Mai, Y.W., and Diao, X.X., On steady-state fibre pull-out I the stress field. *('omposite Science & I echnolo , 59,* 1999a. 2179-2189.

Zhang, X., Liu, H.Y., Mai, Y.W., and Diao, X.X., On steady-state fibre pull-out II computer simulation. *Composite Science & Technolo, 59,* 1999b. 2191-2I99.

Zhang, X., Hounslow, L., and Grassi M. Improvement of low-velocity impact and compression-after-impact performance by z-fibre pinning. Proceedings of the 14`h International Conference on Composite Materials (ICCM14), San Diego, 2003.

Appendix A

List of published papers from this research study

1 Grassi, M., Zhang, X., and Meo, M., "Numerical prediction of stiffness and stresses in Z-Fibre reinforced laminates." 6'h *International Conference on Defthrmation and Fracture of Composites DEC'6,* Manchester, April, 2001.

2 Grassi, M., Zhang, X., Meo, M., "Prediction of stiffness and stresses in z-fibre reinforced composite laminates", *(."omposites: Part A,* 33, 1653-1664, 2002.

3 Grassi, M., and Zhang, X., "Numerical modelling of Z-Fibres effects on Mode I interlaminar delamination" *10h European Conference on Composite Materials* Is CCMI 0, Bnigge 3 -7 June, 2002.

4 Grassi, M., and Zhang, X., "Finite Element Analyses of Mode-I interlaminar delamination in Z-fibre reinforced Composite Laminates" Composites *Science & T echno1o, 63,* 1815-1832, *2003.*

5 Zhang H., Hounslow, L., and Grassi, M., "Improvement of low-velocity impact and compression-after-impact performance by z-fibre pinning" */4 i International Conference on Composite Materials ICY:MI4,* 11-14 *July,* San Diego, CA, 2003.

6 Partridge, I.K., C i e , D.D,R., Troulis, M., Grassi M., and Zhang, M., "Evaluating the mechanical effectiveness of z-pinning" *SAMPF. International conference,* September 2003.

? Grassi, M., Cox, B.N,, and Zhang, X., "Structural behaviour of z-pinned composite joints under mixed-mode failure." (to be published), 2004.

Appendix B

Micro-mechanical model equations

Micro-mechanical model equations for pre-pullout and pullout regime (Cox, private communications, 2003). The notation used in this appendix confonrs to that of Cox and Sridhar (2002, 2003). The constitutive equations for the z-pin axial stress and angle of deflection in the fracture plane (equations 4-6, 4-7 and 4-8) are reported here for clarity sake:

$$\frac{\partial \sigma}{\partial z} = -4\tau_i \frac{r_e}{r} \cos\theta \qquad (0 \le z \le z_0) \qquad \text{(B.1a)}$$

$$\frac{\partial \theta}{\partial z} = -\frac{2\tau_i}{E_f r \sigma} \cos\theta \qquad (z_0 \le z \le L) \qquad \text{(B.1b)}$$

$$\frac{\partial \delta}{\partial z} = -\frac{\varepsilon_m}{\varepsilon_f} \cos\theta \qquad \text{(B.2)}$$

Two cases are distinguished: if the frictional slip zone has not reached the end of the z-pin ("pre-pullout" regime), then σ vanishes at z =1, given by

$$\sigma = \sigma_0 + s_2 z_0 \frac{1}{s_i} \qquad (B.3)$$

Where σ_0 is the boundary value at the fracture plane, z = 0; while if the slip zone has reached the end of the z-pin ("pullout" regime), then $\sigma = \sigma_0$ where 1r is the half-length of the z-pin and ds is the distance the end of the z-pin has pulled away from its original location in the laminate. The following dimensionless variables are introduced:

$$\Sigma = \frac{\sigma}{\sigma_0} \qquad Z = \frac{z}{R} \qquad W = \frac{2\delta}{R} \qquad Y = \frac{2A}{rR} \qquad (B.4)$$

$$\Sigma_0 = \frac{\sigma_0}{\tau_i} \qquad E = \frac{E_t}{\tau_i} \qquad \Gamma = \frac{n}{s_{ri}} \bar{p} e^{re} \qquad T_i$$

Deflection Zone

The solution to Eq. (B,2) that satisfies the boundary conditions on Bis, in normalized form,

$$B\text{-}Bo = -\frac{1}{Pe}\,n\,\frac{E_o^{ycos}O\text{-}Pe^{1}z}{EoycosE} \qquad \textbf{(B.5)}$$

and the end of the deflection zone (0= 0) therefore resides at $q = i$ given by $\underline{Egf'cosO}$

$$[l\_e^{-9014e^{:1'}}]$$

$Ro \qquad Pe$

In the following, solutions will be completed for the pre-pullout and pullout regimes (before and after the slip zone reaches the end of the z-pin). Quantities associated with the pre-pullout and pullout regimes will be distinguished by the superscripts "<" and ">" respectively. In the pullout regime, ds will denote the distance over which the end of the z-pin has slipped from its original position. The boundary stress, *a),* and the boundary deflection, 0„ can be regarded as independent variables. The end displacements of the z-pin, and the slip length, is (pre-pullout *regime), the* pullout distance, ds (pullout regime), and the deflection zone length, zp, are sought.

The Pre-Pullout Regime

The axial stress in the pre-pullout regime can be written as:

$$Ed\_ \;\; y \;\; sO\sim lo+ycoso \;\; s \;\; q0) \;\;]\;\; r\;\; \_ \qquad \textbf{(B.7a)}$$

and hence

$$Ls = 'To(1-p_e)+Eoycoso \qquad \textbf{(B.7b)}$$

With Eq. (B.6) this can be rearranged as

$$Ls = q\,o + Eoycos\phi e^{Pe\,f'}{}^{eo} \qquad \textbf{(B.7c)}$$

so that Ls > 17(always (tensile En). The mode I displacement is defined as:

$$W\sim = W_{def} + W_{el} \qquad \textbf{(B.8a)}$$

$$W_{def} \approx \int \frac{\cos(\theta + \beta)}{\cos\theta} \, d \qquad (B.8b)$$

$$W_{el} \approx \frac{\cos(\theta + \beta)}{\cos\theta} \frac{P}{E_f A_f} z \qquad (B.8c)$$

Where $\theta = 0$ if $z > z_0$. Here W_{def} is the contribution to W from the change in path length of the locus of the z-pin in the zone of deflection, which is identical in the pre-pullout and pullout regimes and therefore carries no distinguishing superscript, while W_{el} is the contribution from the elastic stretch of the z-pin. Equation (B.8b) leads to

$$W_{def} = \frac{P}{2} g(P/P_e, \theta_0, \beta) \qquad (B.9a)$$

$$g(P/P_e = 0, \beta) = \frac{P}{P_e} \cos(\theta + \theta_0) - \cos\theta_0 + \frac{P}{P_e} \sin(\theta + \beta) - \sin\theta_0 \qquad (B.9b)$$

of g is small (e.g., ≈ 0.01 for $\theta_0 = \pi/8$ in the case shown). The consequent maximum magnitude of W is also small (e.g., -- few tim for a 0.5 mm diameter z-pin when = rn$}. *With the bilinear distribution expected for the axial stress, Eq. (B.8c) yields*

$$W_{el} \approx \frac{\cos\theta}{2 E_f A_f} \left(P_e^2 - P^2 \right) L_s \qquad (B.10a)$$

Which reduces using Eqs. (B.6) and (B.7c) to

$$W_{el} = \frac{\cos\theta}{2 E_f A_f} \left(P_e^2 - P^2 \right) \frac{\delta_0}{P_e} \qquad (B.10b)$$

In the approximation of linear B(z), which probably remains reasonable for the pre-pullout regime, Eqs. (B.7a) and (R 10) give

$$w^{<} = -r \frac{1}{0}\,0e0\cos O + \sin O - \sin(+\ 6rq)\}$$

$$+y \_\_ \ 2F, \qquad \cos r\ 1-2 \quad 1- \ 1 \quad \underline{dye}\ Pe \qquad \textbf{(B.11)}$$

The mode II displacement follows from Eqs. (4.16 in Chapter 4):

$$U< = zldef + \tan(O+a_o)W` \qquad \textbf{(B.12a)}$$

$$t\,I_{det}{}^{\cdot} = \frac{[\sin(O+\underline{0})}{} - \tan \quad dz = Y\ 19\ ,^{B}\mathbf{o,Al} \qquad \textbf{(B.12b)}$$

$$g_u[P/\mu_e,\theta_0,\phi] = \frac{P/\mu_e}{1+P^2/\mu_e^2}\left\{\sin(\phi+\theta_0)-\sin\phi\right.$$

$$\textbf{(B.12c)}$$

$$-P\,i\,p_e\ [\cos(\sim^{+Oo)}\_\cos\ -90Pe \qquad +\ P/p_e\ \sin 0(1 -- e\ B_0\sim_e Y)\ ]\ \}$$

Here $II_{\sim\sim 1}$ is the contribution to II from *the* change in path length of the locus of the z-pin **in** the zone of deflection, which, like $W_d a$, is identical in the pre-pullout and pullout regimes; while the second term in Eq, (B.12a) represents the additional mode II displacement that is created by that part of the z-pin that lies between the fracture surfaces (having slid out of the laminate). For given 2 and q,, Eqs. (B.6) - (B.8), (B.12), solve it for the function qz) that is exact within the definition of the model.

The Pullout Regime

The solution to Eq. (B.l) subject to *is = I , - d s* is

(B.13)

$$E \qquad 1\ \_\_\ \underline{'lo}\ \_\_\ \underline{+I_r}\ \_\_\_\_\ - D\,s$$
$$e \ - \ y\cos \qquad\qquad \text{icoso}$$

The mode I displacement is given by

(B.14a)

$$W'W_{def}{}^{+}Wl^{+W}{}_{pull}$$

(B.14b)

$$W, \ - \ !r\text{-}ds\ \underline{coS(o + 0)\ at\ dz}\ \text{el}\ \text{-}\sim ft \quad cos0\ Et$$

$$w_{punos} \quad \frac{\cos(O + 0_0)}{\cos O} \qquad \textbf{(B.14c)}$$

In Eq. (B. 14a), W,r is the displacement due to the path length change in the deflection zone (identical to the corresponding term in the pre-pullout regime), W i is due to the elastic stretch of the z-pin inside the laminate, and Wp,, 1 is the displacement contribution of the part of the z-pin that has already pulled out of the laminate. The protruding part of the z-pin is assumed to be straight and lie at an angle $0_{4-}a$ to the normal to the fracture plane, i.e., to be smoothly connected to the segment of the z-pin that is still embedded in the laminate.

$$W' = 2E\ 7]_0 E_0 + E_0 - \_\__e \frac{7O}{l\ y\cos O,}\ (jr - Ds \qquad \textbf{(B.15a)}$$

Eliminating Ds and iio through Eqs. (B.6) and (B,13) yields

$$Wei \sim [le\ y\ 2E \cos 4 + \frac{E}{Lyle} - 1 \qquad -20oP_e Pi \qquad \textbf{(B.19b)}$$

which is the same as the expression, Eq. (B,1 0b), for W l , Thus when expressed in terms of Eo and a,, 1 W~ and k V> are not distinct. Iii the approximation of linear fez) to

$$w' = -y - \{6o\cos O + \sin O - \sin(0+0o)\{ - 12$$

$$+ -y\cos 1 - \frac{i_e - I\}^{oo}}{P2} + (P_{e^-} \ldots 2fs \quad P \qquad \textbf{(B.20)}$$

$$Lr\_ \ oi\cos O\ 1 - (p_e - 1)6p \frac{\cos(O+0)}{\cos O} L\ P$$

+ In the second and third lines, the terms containing the factor A - 1 show the effect of the enhanced friction zone. The mode [I displacement is given by

$$U' - [I\ def + \tan(0+0o\}W^{>} \qquad \text{(B.21a)}$$

The tenns in Eq. (B.21a) have the same significance as the corresponding terms in Eq. (B.14a). In the approximation of linear FJ(z)

$$(I> = -y\ 4\ \{\cos(O+Bo) - \cos 0 + Bo\sin 0\{ + \tan(O+Bo)W' \qquad \text{(B.21b)}$$

For given $^{s}_{ue,}$ and O, Eqs. (B.17), (B.20), and (B.21b) solve the pullout regime in the approximation of linear 0z); while Eqs. (B.17), (B.18), (B.19), and (B.21a) solve it for the function *biz)* that is exact within the definition of the model.

Appendix C

Matlab sub-routine for z-pin interface finite element

Example of MATLAB program to calculate the z-piu bridging laws and to generate the input file for the **FE interface element deck.**

Bridging-I.m

```
----------Define generic variables
% % % % % % % % % % % % % % %
%Thickness of the total laminate (mm)
h=2;
%
%%%%%%%%%%% ----------Define z-pin paremeters ----------
%%%%%%%%%%%%%%a
%
%Z-Fibre Tensile Modulus (MPa)
Ex=144*10^3;
%Z-fibre radius
r=0.25;
n'Constrained mismatch due to curing
r=r-r*0.5/100;
%Z-Fibre   area
A=3.14r^2;
'Z-Fibre embedded depth
L=2;
%Shear strength z-fibre/matrix
tau=17;
%Tensile allowable
sigma=3000;
%
%%%`k%%%%%%% ----------Bridging Laws ----------
%%%%%%%%%%%%%%%

delta=((pi*r*L^2*tau)1(A*Ex))114:((pi*r*L^2*tau)1(A*Ex)-.
   ((pi*r*L^2*tau)/(A*Ex))/14)110:(pi*r*L^2*tau)/(A*Ex);
F=(sgrt(4*pi*r*tau*A*Ex*delta));
deltal=(pi*r*L^2*tau)/(A*Ex)+((pi*r*L^2*tau)1(A*Ex))/14:(LH
pi*r*L^2*tau)/(A*Ex)+((pi*r*L^2*tau)1(AEx))/14))/7:L;
F1
((2pi*r*tau*L-A*Ex)+(A*Ex)*sgrt(1+((2*pi*r*tau*L)/(A*Ex))^2-((2*
deltal)IL)*(2*pi*r*tau*L)/(A*Ex)));
grid on
figure(4)
  plot(delta,F,'-bs','LineWidth',1,...
                     'MarkerEdgeColor','b',...
                     'MarkerFaceColor','r',...
                     'MarkerSize',4)

grid on
```

```
%hold on
%figure(5)
%plot(delta,F);
%Define the array for the material real constants definition (Combin
39)ANSYS Data set
D=[delta deltal L+0.01;F Fl 0];
%Define the Bridging force vector
A[F  Fl];
`Define the Equivalent Displacement vector
U=[delta deltal];
R=fA;U);
%
%Save L-D points for the E curve interpolation
                    save 'delta.dat' U -ascii; save 'force.dat' A -ascii;

x=0:0.00001:L;
E=energy(x);
figure(8)
plot(x.E,'b');
%Integrate the pullout curve in a defifined range
int = quad('energy',0.00016,1.6)

 Define the ANSYS macro to implement the Load-Displacement Curve in the
C0MBIN39
%
%Real Constant Number(ANSYS)for the NON-Linear Spring

real numb=4;
%Define real parameters in the COMBIN real constant Data block
fid_2=fopen('C:1My Documents\PhD\Analyses\Ansyslinsert.mac','W');
dim_vect=['r,',num2str(real_numb),',',num2str(D(1,1),'14.8e')
, ',',num2str(D(2,1),'%14.8e'),',',num2str(D(1,2),'%14.8e')
, ',',num2str(D(2,2),'%14.8e'),',',num2str(D(1,3),'%14.8e')
, ',',num2str(D(2,3),'%14.8e')];
fprintf(fid 2,'%50s1n',dim_vect)
for i=1:6
   if i<6
   dim_vest=['rmore,',num2str(D(1,3+(i-1)*3+1),'%14.8e')
, 'r'rnum2str(D(2,3+(i--1)*3+1),'%14.8e'),',',num2str(D(1,4+(i
-1)3+1),'%14.8e')
,',',num2str(D(2,4+(i-1)*3+1),'%14.8e'),',',num2str(D(l,5+(i--
1)*3+1),'%14.Be')
, 'r',num2str(D(2, 5+(i-1) *3+1),' %14.8e') ] ;
   fprintf(fid 2,'%50s\n',dim vest)
   else
   dim_vest=['rmore,',num2str(D(1,3+(i-1)*3+1),'%14.8e1)
, ',',num2str[D(2,3+(i---1)*3+1) , 1114.Be'
),',',num2str(D(1,4+(i--1)*3+1),'%14.Be')
,',',num2str(D(2,4+(i-1)'3+1),'.14.8e')];
   fprintf(fid_2,'%50s\n',dim_vect)
   end
end

fclose(fid 2)
```

input file for ANSYS Combin39 element

```
r, 4,
6.73349256e-005,9.39856302e+000,1.54870329e--004,1.42
536266e+001,2.42405732e--004, 1.78325195e+001 rmore,
3.29941135e--004,2.08046061e+001,4.17476539e-004,2.34
022332e+001,5.05011942e-004,2.57390249e+001 rmore,
5.92547345e-004,2.78806436e+001,6.80082749e-004,2.986
91006e+001,7.67618152e-004, 3.17332011e+001
rmore,8.55153555e-004,3.34937148e+001,9.42688958e-004
,3.51662Q28e+001,1.01002388e-003,3.51646242e+001
rmore,2.15151449e--001,3.Q1438129e+001,4.29292874e--0
01,2.51221002e+001, 6.43434299e-001,2.00994858e+001
rmore, 8. 57575725e-
001,1.50759690e+001,1.07171715e+000,1.00515494e+001,1.28585857e+000,5.026
22660e+000
rmore,1.50000000e+000,3.63797881e-012,1.51000000e+000,0.00000Q40e+0Q0
```

Appendix D

FE model for delamination growth analysis

ANSYS **subroutines** for z-pinned DCB simulating delamination growth.

< Dcb.mac

```
  ------------------------------------------------------------------------

!***************--DOUBLECANTILEVER-BEAM MACRO--*************++



! ----------------------------WARNING ----------------------------------------
 ----------------
!
The parameters values are : N,mm

 ------------------------------------------------------------------------------
- - - - - - - - - - - - - - - - -
!*****************************--DEFINE INITIAL
PARAMETERS--*****.t******+************

/GRA,POWER
/REPLOT,     RESIZE
     *set,L,110
     *set,A,50
     *set,t,1.5
     *set,B,6.4
     *set,dz,2
     *set,size,0.4
     *set,size2,3.2
     *set,ratio,1 *set, L1, 4 5
     *set, L2, 10
     *set,material,'IMS-924'
 +**+***+**+*++*++************+**************+*********************
**********


---------------

 !*+*****+*********************--DEFINE MATERIAL-LIBRARY AND MATERIAL
MODEL USED--********
IPREP7
IMPLIB, READ,Y:lunixlmat\Material-Library
IMPLIB, WRITE, Y:lunixlmatlMaterial-Library

MAT,1,
MPREAD,IMS-924,user MPL,Y:lunixlmat\Material-Library ,LIB /COM,ANSYS
RELEASE Y5.6.1 UP20000209                    12:03:44    05/31/2001
INOP
```

```
ICOM,Internal UNITS set at file creation time = USER
                                        TBDEL,ALL, MATL MPDEL,ALL,-_MATL
MPTEMP,R5.0, 1,  1,    0.00000000
MPDATA,R5.0, 1,EX   , MATL   ,   1,    138000.000
MPTEMP,R5.0, 1,  1,    0.00000000
MPDATA,R5.0, 1,EY   , MATL   ,   1,    11000.0000
MPTEMP,R5.0, 1,  1,    0.00000000
MPDATA,R5.0, 1,EZ   , MAIL   ,   1,    11000.0000
MPTEMP,R5.0, 1,  1,    0.00000000
MPDATA,R5.0, 1,GXY ,_MATL   ,   1,    4400.00000
MPTEMP,R5.0, 1,  1,    0.00000000    .
MPDATA,R5.0, 1,GYZ , MATL   ,   1,    2700.00000
MPTEMP,R5.0, 1,  1,    0.00000000
MPDATA,R5.0, 1,GX2 ,_MAIL   ,   1,    4400.00000
MPTEMP,R5.0, 1,  1,    0.00000000
MPDATA,R5.0, 1,PRXY, MATL ,   1,    0.340000000
MPTEMP,R5.0, 1,  1,    0.00000000
MPDATA,R5.0, 1,PRYZ,_MATL ,   1,    0.390000000
MPTEMP,R5.0, 1,  1,    0.00000000
MPDATA,R5.0, 1,PRXZ,_MATL ,   1,    0.340000000
/GO

'.Get the bending stiffness Dxx for the analytical calculation
MPLIST,1,,,EX
*GET,EX,EX,1,TEMP,
!Define only half DCB model
/Expand
!
!**********************+*********************************+  *+**+*******
**
!*****'****+*+****''*****'****__j7EFINE ELEMENT TYPE--******************
!Define nodal off-set position for intact laminate,and delaminated sub-!laminate
!
!  ----------------------------Key option for Shell9l non-linear layered element
!Special Features
!                          Plasticity, Stress stiffening, Large deflection,
!Large strain, Adaptive descent.
!KEYOPT(1)
                          The maximum number of layers used by this element !type
for storage in the .ESAV and .OSAV files; default =
!                          16. The first real constant (NL) must be no greater !than
the value you specify. The maximum number of layers
!                          may be no greater than 100.
!KEYOPT(2)
                           1 - Must be set before supplying real constant !values in
the input format described above (no default; you !          must specify
KEYOPT(2) = 1)
!KEYOPT(4)
'                          0 - No user subroutines to define element
!coordinate system
```

```
                    4 - Element x-axis located by user subroutine
!USERAN
                    5 - Element x-axis located by user subroutine
!USERAN and layer x-axes located by user subroutine
! KEYOPT (5 )
                    0 - Print average results at layer face farthest !from
element nodal plane
                    1  - Print average results at layer middle
                    2  - Print average results at layer top and bottom ı
                      3 - Print results, including failure criterion, at
!layer top and bottom 4 integration points and averages
!                    4 - Print results at layer top and bottom 4 corner !points
and averages
!KEYOPT(6)
                    0 - Do not print interlaminar shear stresses 1 -
!                   Print interlaminar shear stresses
!KEYOPT(8)
                    ❑ - Store data for bottom of bottom layer and top of I
!top layer.
                        - Store data for all layers.Warning:Volume of data

may be excessive_
1.KEYOPT(9)
                    0 - Do not use sandwich option 1 -
                    Use sandwich option
UKEYOPT(lO)
!                   0 - Print summary of the maximum of all failure
!criteria
ı                   1 - Print summary of all the failure criteria
!KEYOPT(11)
!                   0 - Nodes located at middle surface
!                   1 - Nodes located at bottom surface
!                   2 - Nodes located at top surface I
!!! ! ! ! ! ! ! ! ! ! !
!*
 ------------------- intact part of the laminate(node at mid-surface) ET,
1, SHELL91„ 1


!KEYOPT,1,1,16,
KEYOPT, 1, 2, 1
KEYOPT,1,4,0
KEYOPT,1,5,0
KEYOPT, 1, 6, 0
KEYOPT,1,8,1
KEYOPT, 1, 9, 0
KEYOPT, 1, 10, 0
KEYOPT,1,11,0 !*
!*
1 ----------------- upper part of the sub-laminate(node at bottom-surface) ET,
2, SHELL91, , 1
I*
I*
!KEYOPT,2,1,16,
KEYOPT,2,2,1
```

```
KEYOPT,2,4,0
KEYOPT,2,5,0
KEYOPT,2,6,1
KEYOPT,2,8,1
KEYOPT,2,9,0
KEYOPT,2,10,0
KEYOPT,2,11,1
!*
! -----------------lower part of the sub-laminate(node at Top-surface) ET,
3,5HELL91,,1
f*
?KEYOPT,3,1,16,
KEYOPT,3,2,1
KEYOPT,3,4,0
KEYOPT,3,5,0
KEYOPT,3,6,1
KEYOPT,3,6,1
KEYOPT,3,9,0
KEYOPT,3,10,0
KEYOPT,3,11,2


!*
 !**********************--Assign thickness-************************

.l  ---------- Define constants for the undamaged laminate !*
R,1
i*
RMODIF,1,1,1,0, ,,0 }
RMODIF,1,13,1,0,2*T,0,0,0,
f
! -------------Define constants upper sub-laminate
1k
R, 2
!*
RMODIF,2,1,1,0, , , ,0 ! *
RMODIF, 2, 13, 1, 0, T, 0, 0, 0,
! ------------------ Define constants lower sub-laminate
R, 3
RMODIF, 3, 1, 1, 0, , , ,0
RMODIF,3, 13, 1,O,T,0,0,0,
!*
t
}*
!**************************,F-- DOD ENF GEOMETRY--********************
!!.Intact Laminate-Beam part
```

```
RECTNG,O,L-A-L1,O,B

!**----------Semi-DCB upper part----**!

RECTNG,L-A-LI,L-A,O,B
RECTNG,L-A,L-A+L2,0,B
RECTNG,L-A+L2,L,O,B

!**----------Semi DBC lower part---


RECTNG,L-A-L1,L-A,O,B
RECTNG,L-A,L-A+L2,0,B
RECTNG,L-A+L2,L,0,B

APLOT

LSEL,S,  ,  ,       2
LSEL,A,  ,  ,       8
KSLL,S
NUMMRG,KP,,  ,  ,LOW
KSEL,ALL
LSEL,ALL
LSEL,S,  ,  ,       6
LSEL,A,  ,  ,       12
KSLL,S
NUMMRG,KP,,  ,  ,LOW
KSEL,ALL
LSEL,ALL
LSEL,S,  ,  ,       10
LSEL,A,  ,  ,       16
KSLL,S
NUMMRG,KP,,  ,  ,LOW
KSEL,ALL
LSEL,ALL
LSEL,S,  ,  ,       2
LSEL,A,  ,  ,       20
KSLL, S
NUMMRG,KP,,  ,  ,LOW
KSEL,ALL
LSEL, ALL
LSEL,S,  ,  ,       24
LSEL,A,  ,          18
KSLL,S
NUMMRG,KP,,  ,  ,LOW
KSEL,ALL
LSEL,ALL
LSEL,S,  ,  ,       28
LSEL,A,  ,  ,       22
KSLL,S
NUMMRG,KP,,  ,  ,LOW
KSEL,ALL
LSEL,ALL

!**++.+++**+++++++++++++++-- DEFINE MESH PA.RAMETERS--**********'`***+*
```

```
ASEL,S, , ,          1
AATT,       1,          1,   1,
 LSLA, S
 1*
 IF A RATIO BETWEEN THE CENTER OF THE SPECIMEN AND THE FREE EDGE HAS TO BE
DEFINED AFTER
 THE NUMBER OF ELEMENTS B/SIZE2 DEE -x x>1)
LESIZE,4, , ,B/SIZE2,ratio, , ,
LESIZE,2, , ,B/SIZE2,ratio, , ,
LESIZE,1,SIZE2, „ , , ,
LESIZE,3,SIZE2, „ , , , ,1
AMESH, 1
allsel

!** ----- Semi-DCB upper part----**!

ASEL,A, , ,        4
AATT,        1,       2,   2,
LSLA,S
LESIZE,10, , ,BISIZE2,ratio, , ,
LESIZE,14,     ,BISIZE2,ratio, , ,
LESIZE,15,SIZE2, „ , , ,
LESIZE,13,SIZE2, ,, , , , ,1 AMESH,4
ALLse1
LESIZE,2, , ,BISIZE2,ratio, , ,
LESIZE,6, , ,BISIZE2,ratio, , , ■1
!LESIZE,10, , ,B/SIZE2, , , , LESIZE,5,
, ,L1/SIZE, , , , ,1 LESIZE,7, ,
,L1/SIZE, , , , ,1 LESIZE,9, ,
,L2/SIZE, , , , LESIZE,11, , ,L2/SIZE,
, , , TYPE, 2
MAT,        I
REAL,        2
ESYS,        0
                                                          AMESH,2 AMESH, 3

!** ----- Semi-DCB lower part----**'

ASEL,A, , ,        7
AATT,        1,       3,   3,
LSLA, S
LESIZE,26,  ,  ,BISIZE2,ratio,
LESIZE,22,  ,  ,BISIZE2,ratio,
LESIZE,25,SIZE2, ,, , , , rl
LESIZE,27,SIZE2, ,, , , , ,1
AMESH,7
allsel
LESIZE,18, , ,B/SIZE2,ratio,    , , 1
LESIZE,19, , ,L1/SIZE, , , , , 1
```

```
LESIZE,17,   ,   ,L1/SIZE, , , , ,1
LESIZE,23,   ,   ,L2/SIZE, , , , rl
LESIZE,21,   ,   ,L2/SIZE, , , , ,1
TYPE,    3
MAT,       1
REAL,       3
ESYS,       0
AMESH,S
AMESH, 6



 !******+******************--DEFINE BOUNDARY CONDITIONS--*************+**+**

!** ------Define coordinate system along the crack front ------ **!
LSEL,S, , ,        6
NSLL,S,1
*GET,ar24,NODE,,NUM,MIN,
NSEL,S, , ,       ar24
ESLN,S
*GET,ar24,ELEM,,NUM,MAX, , ,
ESEL,S, , ,       ar24
NSLE,S
*GET,AR32,ELEM,AR24,NODE,1
*GET,AR26,ELEM,AR24,NCDE,2
*GET,AR27,ELEM,AR24,NODE,3
CS,  11,  0,AR32,AR26,AR27,1,1,
WPCSYS,-1,11,

!** -------------- Clamped constraint at beam end ------------------ **!
CSYS,O

DL, 4, 1, ALL, 0

!** ---- Cylindrical Bending----**!
!

!** ------Semi-DCB upper part - **!

DL,3,1,UY,0
DL,3,1,ROTX,0
DL,7,2,UY,0
DL,7,2,ROTX,O
DL, 11, 3,UY, 0 DL,
11, 3, RDTX, O


DL, 1, 1, UY, 0
DL,1,1,ROTX,0
DL, 5, 2, UY, 0 DL,
5, 2, RCTX, 0
DL,9,3,UY,0 DL,
9, 3, RDTX, 0

r**-------Semi-DCB lower part----**'.
```

```
DL,19,5,UY,0
DL,19,5,ROTX,O
DL,23,6,UY,0
DL,23,6,ROTX,0
!
DL, 17, 5, UY, 0
DL, 17, 5, ROTX, 0
DL,21,6,UY,0
DL,21,6,ROTX,0
1
!!11I!!!!!Last 2 areas where the load is applied
!To AVOID BOUNDARY CONDITION PROBLEMS WITH COUPLED SETS AT THE DCB
LOADING POINTS
LSEL,S,    ,    ,13
LSEL,A,    ,    ,15
LSEL,A,    ,    ,25
LSEL,A,    ,    ,27
NSLL,S
D,all, ,0, , , ,UY,ROTX, , , ,
Allsel

 ------------------------------------------------------------------------
1

1***+****+****__DEFINE COUPLING FOR CRACK-TIP ELEMENTS--****+**********

ASEL,S, , ,             2
ASEL,A, , ,             5
ESLA,S
NSLE,S
!Coupling the only degree of freedom required for the MODE
!CPINTF,UX
!CPINTF,UY
CPINTF,   UZ
allsel
!
 ------------------------------------------------------------------------

   { ***##*#*********************************+*#***#*#****f*******+***

FINISH


1***********+**__APPLING LOAD ON THE DCB ARMS--**********

sub, 14, dz
sub,26,-dz

SAVE
```

```
z-pinning, 0.5,0.5, 30
```

SUB.mac

```
IPREP7
CSYS,O
LSEL,R, , ,       argl
NSLL,R, 1
NSEL,R,LOC,X.L-size2l3,L+size2/3
NSEL,R,LOC,Y,B12-size13,B12+sizel3
*GET,ar20,NODE „ NUM,MAX, , ■ ,
allsell
LSEL,S, , ,       argl
NSLL, R, i
NSEL,U, , ,      ar20
*GET,ar21,NODE „COUNT, , , ,
*DIM,block,ARRAY,ar21,1,1,
*DO,1,1,ar2l
             *GET,orgi,NODE,,NUM,MIN, , , ,
             *VFILL,block(i,1),DATA,orgi,,,,r„ , ,
             NSEL,U, , ,      orgi
*ENDDO
allsell
*DO,i,l,ar2l
             NSEL,S, , ,black(i,ly
             DDELE, ALL, ALL

*ENDDO
allsell
CP, ,ALL,ar2O,block(1,I)¦block(2,1),block(3,1)¦block(4,1)
D,ar20,  .arg2,  ,  ,  ,UZ
D,ar20,  ,arg2,  ,  ,  ,U2
block=
```

F1N1SH

< z-pinning.mac a

```
!****************2-PINNING SOUBROUTINE(MACROS) ***********.*!

This macros allow the user,once defined the model and '. mesh
to z-pin it

!*************************************************************!
```

IPMACRO

```
IPREP7

 !Define z-fibre diameter
 *SET, d,argl
 !Define z-fibre density
 *SET, density, arg2
 !length of z-pinned area
 *SET,zpath,arg3
 }****************+*******Z-PINNING ARRAY PARAMETERS ASSIGN************!
```

```
* IF, density, EQ, 0 .5, THEN
                          *IF,d,EQ,0.28,THEN
                          *SET,dex,3.51
                          *ELSE
                          *SET,dex,6.39
                          *ENDIF
 *ELSEIF,density,EQ,1,THEN
                           *IF,d,EQ,0.28,THEN
                           *SET,dex,2.48
                           *ELSE
                           *SET,dex,4.52
                           *ENDIF
 *ELSEIF,density,EQ,2,THEN
                          *IF,d,EQ,0.28,THEN
                          *SET,dex,1.75
                          *ELSE
                          *SET,dex,3.2
                          *ENDIF
 *ELSE
                          *IF,d,EQ,0.28,THEN
                          *SET, dex, 1.24
                          *ELSE
                          *SET,dex,2.26
                          *ENDIF
 *ENDIF
! ---------------------------------- Define bridging law element


ET,4,COMBIN39

                                       KEYOPT,4,1,0 KEYOPT,4,2,0
!Key option 3,stiffness along x-y-z axis(z=3)
KEYOPT,4,3,3
KEYOPT,4,4,0
KEYOPT,4,6,0


!Bridging curve vector(run MACRO}{MATLAB OUTPUT)
insert
!*
TYPE,    4
MAT,        1
READ,        4
ESYS,        11
! SECNUM,


!*************** Difine z-pinning AREA ******************!
CSYS,1i,
!NSEL,S,LOC,X,-zpath,0
!NPLOT
 *****************+********************* ********* + *******
```

```
'.Define numbers ❑f pins along the axis }
z pins x=HINT(zpath/dex)
z pins y=NINT(B/dex)

!List parameters

NSEL,S,LOC,X,-(5.2)-0.1,-(5.2)+0.1
*DO,AR29,1,z pins x NSEL,A,LDC,X,-(5.2+AR29*6.4)-0.1,-(5.2+AR29*6.4,45+0.1
         *ENDDO
NSEL,R,LOC,Y,b/2-0.001,b/2+0,001

EINTF,0.0001,
FINISH
!/FILNAME,arg4,0
! *
ALLSEL
SAVE
  IRE PLOT
```

grawth.mac

```
!Define the displacement increment

/SOLU
ANTYPE,0
NLGEOM,1
!OUTPR,ALL,BASIC,
OUTRES,ALL,LAST,
TIME, l
AUTOTS, 0
NSUBST,1,1,1,0
KBC,O
RESCONTROL,DEFINE,NONE
ISTAT,SOLO
SOLVE       FINISH
vcct3
*VA.BS,0,1,0,0
*VSCFUN,GI,MAX,G_VCCT(1)
'"VABS, 0, 1, 0■ 0
*VSCFUN,G_av,MEAN,G_VCCT(l)
*VSCFUN,G_stdv,STDV,G_VCCT(1)
crack=0
j=1
k=1
*GET,AR20,'EARM',G_VCCT,DIM,X
*DIM,SERR,ARRAY,IOOO,L1/SIZE,1, , ,
*DIM,G_AVE,ARRAY,1000,L1/SIZE,
*DIM,G_STDEV,ARRAY,1000,L1/SIZE,

*DO,AR22,1,AR20 *VFILL,SERR(AR22,k),DATA,G
VCCT(AR22,1)
```

```
*ENDDO
*VFILL,G_AVE(j,k),DATA,G_av
* VFILL, G_STDEV (j , k) , DATA, G_stdv
G_VCCT=
save

*DO,i,1,10000                LE,250,THEN
1                              j=j+1
                               q=1
*IF, crack, LT, 30, THEN       /SOLD
                 *IF,G_av,     ANTYPE„REST
                               DOFSEL,5,UZ
                               DCUM,ADD,1, ,0, DOFSEL,ALL
                               CSYS0
                                    O
                               NSEL,R,LOC,X,L-size2/3,L+si
                               NSEL,R,LOC,Y,B/2-size/3,B12
                               *GET,ar24,NODE,,NUM,MIN,
                               D,ar24, ,0.15, , , ,UZ *GET,
                               ar24, NODE„ NUM, X, D,ar24,
                               ,-0.15, , , ,UZ allsell
                                                              ze2/3
                                                              +size/3
                                                              , ,

                                                              , ,

                               SOLVE
                               FINISH
                               G_VCCT=
                               vcct3
                               *VABS,0,1,0,0
                               *VSCFUN,GI,MAX,G VCCT(1)
                               *VABS,0,1,0,0
                               *VSCFUN,G_av,MEAN,
                               G_VCCT(1) *VSCFUN,G,DATA,G_av
                               stdv,STDV,G VCCT(1)k) , DATA, G_s tdv
                               *VFILL,G_AVE(j,k)  1)+1,AR20*j
                               *VFILL,G_ STDEV(j,k) ,DATA, G VCCT (q, l )
                               *D0,AR22,AR20*(j-V
                               FILL,SERR(AR22,   q
                               q+ 1
                               ENDDO
                               *VFILL,G_AVE(j,k),DATA,G_av
                               *VFILL,G-_STDEV(j,k),DATA,G_stdv
                               allsell
                               save
                  *ELSE
                               j=1
                               k=k+l
                               /PREP7
                               crack=crack+size
                               add
                               NSEL,R,LOC,X,sizel2,size
                               CPDELE,all,,,ANY allsell
                               FINISH
```

```
                        CSYS,O
                        SAVE
                        1 SOLO
                        ANTYPE„REST
                        SOLVE   FINISH
                        G_VCCT=  vcct3
                        *VABS,0,1,0,0
                        *VSCFUN, GI,MAX.G_VCCT(1)
                        *VABS,0,1,0,0
                        *VSCFUN,G av,MEAN,G_VCCT(1)
                        *VSCFUN,G_stdv,STDV,G_VCCT(1)
                        *VFILL,G AVE(j,k),DATA,G_av
                        *VFILL,G STDEV(j,k),DATA,G_stdv
                        *DO,AR22,1,AR20
                        *VFILL,SERB(AR22,k),DATA,G_VCCT(AR2^2,^1)
                        *ENDDO
                        *VFILL,G_AVE(j,k),DATA,G_av
                        *VFILL,G STDEV(j,k),DATA,G_stdv
                        allsell
                        save
               *ENDIF
*ELSE
   *EXIT
*ENDIF
save
*ENDDO
!write out-put SERB matrix for MATLAB
save
/INPUT,ansuitmp
*CREATE,ansuitmp
*CFOPEN,GI,dat,
*VWRITE,SERR(1,1),SERR(1,2),SERR(1,3),SERR(1,4),S^ERR(^1,^5),^SERR(^1,^6),^SERR(
1,7),SERR(1,8),SERR(1,9),SERR(1,10)
(F20.10,Flo.10,F20.10,F20.10,F20.10,F20.10,F20.10,F20.10,^F20.^10,^F20.10)
*CFCLOS
*END
*CREATE,ansuitmp
*CFOPEN,GI,dat „append
*VWRITE,SERR(1,11),SERR(1,12),SERR(1,13),SERR(1,14),SE^RR(^1,^15),^SERR(^1,^16)
,SERR(1,17),SERR(1,18),SERR(I,19),SERR(1,20)
(F20.10,F20.10,F20.10,F20.10,F20.10,F20.10,F20.10,F20.^10,^F20.10,^F20.10)
*CFCLOS
*END
*CREATE,ansuitmp
*CFQPEN,GI,dat„append
*VWRITE,SERR(1,21),SERR(1,22),SERR(1,23),SERR(1,24),SERR(1,25), SERR(1,26)
,SERR(1,27),SERR(1,28),SERR(1,29),SERR(1,30)
(F20.10,F20.10,F20.10,F20.10,F20.10,F20.10,F20.10,F2^0.^10,^F20.10,^F20.10) *CFCLOS
*END
```

```
*CREATE,ansuitmp
*CFOPEN,GI,dat „append
*VWRITE,SERR(1,31),SERR(1,32),SERR(1,33),SERR(1,34),SERR(1,35),SERR(1,36)
,SERR(1,37),SERR(1,38),SERR(1,39),SERR(1,40)
(F20.10,F20.10,F20.10,F20.10,F20.10,F20.10,F20.10,F20.10,F20.10,F20.10)
*CFCLOS
*END
*CREATE,ansuitmp
*CFOPEN, GI, dat„append
*VWRITE,SERR(1,41),SERR(1,42), SERR(1,43),SERR(1,44),SERR(1,45),SERR(1,46)
,SERR(1,47),SERR(1,48),SERR(1,49),SERR(1,50)
(F20.10,F20.10,F20.10,F20.10,F20.10,F20.10,F20.10,F20.10,F20.10,F20.10)
*CFCLOS
*END
*CREATE,ansuitmp
*CFOPEN,GI,dat „append
*VWRITE,SERR(1,51),SERR(1,52),SERR(1,53),SERR(1,54),SERR(1,55),SERR(1,56)
,SERR(1,57),SERR(1,58),SERR(1,59),SERR(1,60)
(F20.10,F20.10,F20.10,F20.10,F20.10,F20.10,F20.10,F20.10,F20.10,F20.10)
*CFCLOS
*END
*CREATE,ansuitmp
*CFOPEN, GI, dat„append
*VWRITE,SERR(1,61),SERR(1,62),SERR(1,63),SERR(1,64),SERR(1,65),SERR(1,66)
,SERR(1,67),SERR(1,68),SERR(1,69),SERR(1,70)
(F20.10,F20.10,F20.10,F20.10,F20.10,F20.10,F20.10,F20.10,F20.10,F20.10)
*CFCLOS
*END
/INPUT,ansuitmp
*CREATE,ansuitmp
*CFOPEN,GI_av,dat,
*VWRITE,G_AVE(l,1),G_AVE(1,2),G AVE(1,3),G AVE(1,4),G AVE(1,5),G AVE(1,6)
,G_AVE(1,7),G_AVE(1,8),G_AVE(1,9),G_AVE(1,10)
(F20.10,F20.10,F20.10,F20.10,F20.10,F20.10,F20.10,F20. 10,F20.10,F20.10)
*CFCLOS
*END
/INPUT,an.suitmp
!
C=YS,0
LSEL,R, , ,      14
NSLL, R, 1
NSEL,R,LOC,X,L-size2/3,L+size2/3
NSEL,R,LOC,Y,B/2-size/3,B/2+size/3
*GET,ar20,NODE,,NUM,M X, , , ,
allsell
/POST26
NSOL,2,ar20,U,Z,
RFORCE,3,ar20,F,Z,
To compare with experimental data: (force/$)*20(width of the test
specimen)
!displ=2*d(total displacement ❑f the DCS arms
QUOT,3,3, , , , , ,1, ,
```

```
PROD,3,3, , , , , ,1,20,1,
PROD ,2,2, , , , , ,1,2,1,
*GET,AR20,ACTIVE, ,SOLU,NCMLS
*DIM,load(1),ARRAY,AR20+1,1,1,
*DIM,diSpl(l),ARRAY,AR20+1,1,1,
VGET,displ(1),2, , VGET,load{1},3,

*CREATE,ansuitmp
*CFOPEN,'Load','dat','    '
*VWRITE,LOAD(1,1), , ,    , , , , ,
(F20.10)
*CFCLOS
*END
/INPOT,ansuitmp
t
*CREATE,ansuitmp
*CFOPEN,'Displ','dat','
*VWRITE,DISPL(1,1) ,,,
{F20.10)
*CFCLOS
*END
/INPUT,ansuitmp
t*
!Plotting the specimen
Eplot
/VIEW, 1, 1, 1, 1
/VUP, 1, Z
/SHRINK,0
/ESHAPE,1.0
IEFACET,1
/RATIO,1,1,1
IPBC,ALL, ,1
IREP
IREPLOT
/EXPANDS 2,RECT,HALF „ 0.00001
IREPLOT
SAVE
```

E add.mac

```
WPCSYS,-1▪11,
CSYS,11,
NSEL,S,LOC,X,-Size/3, size/3
ESLN,S
NSLE,S
*get,AR24,ELEM,O,NUM,MIN
*GET,AR32,ELEM,AR24,NODE,1
*GET,AR26,ELEM,AR24,NODE,2
*GET,AR27,ELEM,AR24,NODE,3
CS,11,0,AR32,AR26,AR27,1,1,
WPCSYS,-1,11,
```

ailsell /REPLOT

VCCT.mac

```
!***************--VIRTUAL CRACK CLOSURE TECHNIQUE MACRO--********s*****

  ----------------------------------------------------------------------


!The SERR values in the out-put arrays are given in J/m2 !The
input values in the parameters are given in : !Force:Newton
!Length:mm

!Enter in to the postprocessing enviroment

/POST1
!
'



!*********--Select ELEMENTS and NODES along the crack front--'***''**

!

CSYS,11
RSYS,11
ASEL,S, , ,2
NSLA,S,1
NSEL,R,LOC,X,-size/3, size/3

!Calculate number of nodes along the crack-line
*get,ARZO,NODE,O,COUNT
ESLN,S
NSLE,S
IREPLOT
r
!Calculate element number along the crack-tip front *get,

AR21, ELEM, 0, COUNT

      !ar22 is the result number from the esummation of !the elements behind and
                                                        infront of the crack-tip

*SET,AR22,AR21/2
```

```
!ar23 is the number of columns of the array for the VCCT calculation the
mid-side nodes along the crack are not considered

*SET,AR23,AR20-AR22

!arrays with node numbers inside

*DIM,line,ARRAY,AR23,1,1, , ,
*DIM,behind,ARRAY,AR23 , 1 , 1 ,,,
*DIM,frontup,ARRAY,AR23,1,1, , ,
*DIM,mfrontup,ARRAY,AR23,1,1, , ,
*DINT, frontlow,ARRAY,AR23, 1, 1, , ,
*DIM,mfronlow,ARRAY,AR23,1,1, , ,
!select the first element on the crack-tip front from wich
!start extract first four nodes

*get,AR24,ELEM,O,NUM,MIN
*
!Initialize the first places in the two arrays on the crack-tip and behind
the crack-tip
!nodes for the extraction of the nodal-forces
!
GET, AR25, ELEM, AR2 4 ,NODE, 2
GET,AR26,ELEM,AR24,NODE,5
*GET,AR27,ELEM,AR24,NODE,3
*GET,AR28,ELEM,AR24,NODE,7
*VFILL, line (1, 1) , DATA,AR25,,
*VFILL,behind(1, 1),DATA,AR26
*VFILL,line(2,1),DATA,AR27,,
*VFI LL, behind (2, 1) , DATA, AR28
1
!fill in the other places in the
arrays

 *DO,AR29,3,AR23
   ESEL,U, , ,                    AR24
              *GET, ar24,ELEM,ar24,ADJ,3
              *GET,AR25,ELEM,AR24,NODE,3
              *GET,AR26,ELEM,AR24,NODE,7
              *VFILL,line(AR29,1),DATA,AR25,
              *VFILL,behind(AR29,1),DATA,AR2
 *ENDDO

 !Initialize the first places in the two arrays close and to the crack-tip
 in-front of the crack-tip
 !nodes for the extraction of the nodal-displacement

 ESEL,U, , ,      AR24
 *get,AR24,ELEM,O,NUM,MIN
 *GET,AR25,ELEM,AR24,NODE,2
 *GET,AR26,ELEM,AR24,NODE,5
 *GET,AR27,ELEM,AR24,NODE,3
 *GET,AR28,ELEM,AR24,NODE,7
 *VFILL,frontup(1,1),DATA,AR25,,,,,,
```

```
*VFILL,mfrontup(1,1),DATA,AR26,,,,,,, , ,
*VFILL,frontup(2,1),DATA,AR27,■,,,,, r,,
*VFILL,mfrontup(2,1),DATA,AR28,,,,,,, r,

!fill in the other places in the arrays of the upper semi-laminate
displacement

*DO,AR29, 3,AR23
             ESEL,U, , ,       AR24
             *GET, ar24,ELEM,ar24,ADJ,3
             *GET,AR25,ELEM,AR24,NODE,3
             *GET,AR26,ELEM,AR24,NODE,7
             *VFILL,frontup(AR29,l),DATA,AR25,,,,,,,
             *VFILL,mfrontup(AR29,l),DATA,AR26,,,,,,, , , ,
*ENDDO
!Reselect all the entities of the system

a11sell

r
ASEL,S, , ,5
NSLA,S,1
NSEL,R,LOC■X,-size/3,size/3
                                                    ESLN, S NSLE,S

*get,AR24,ELEM,O,NUM,MIN
!exclude elements behind the crack-front to consider elements !only
associated with displacement in front of the crack tip

*DO,AR29,1,AR23-1
             ESEL,U, , ,       AR24
             *GET,ar24,ELEM,ar24,ADJ,3
*ENDDO
!Calculate the first element in front of the crack-tip

*get,AR24,ELEM,O,NUM,MIN

 *
!Initialise the first places in the two arrays of
the lower semi laminate displacement

*GET,AR25,ELEM,AR24,NODE,2
*GET,AR26,ELEM,AR24,NODE,5
*GET,AR27,ELEM,AR24,NODE,3
*GET,AR28,ELEM,AR24,NODE,7
*VFILL,frontlow(l,1),DATA,AR25,,,,,,, , , ,
"VFILL,mfronlow(l,1),DATA,AR26,,,,,,, , ,
*VFILL, frontlow(2,1),DATA,AR27,,,,,,, , , ,
*VFILL,mfronlow(2,1),DATA,AR28,,,,,,, , ,

!fill in the other places in the arrays of the lower semi-laminate
displacement
```

```
*DQ,AR29,3,AR23
           ESEL,U, , ,       AR24
          *GET,ar24,ELEM,ar24,ADJ,3
          *GET,AR25,ELEM,AR24,NODE,3
          *GET,AR25,ELEM,AR24,NODE,7
          *VFILL,frontlow(AR29,1),DATA,AR25,,,,,,, , , ,
          *VFILL,mfronlow(AR29,I),DATA,AR26,,,,,,, , , ,
*ENDDQ

allsell

 ------------------------------------------------------------------------

!********--DEF ARRAYS : TOTAL NODAL FORCES AND DISPLACEMENTS--*********

!  ------------------------------------------------------------------------

+.Define an array for the total nodal forces

*DIM, FORCE ,,AR23
*DIM,FORCEB,,AR23
```

!Select *the* nodes along the crack-tip front and behind the crack-tip

```
*DO,AR29, 1,AR23
           NSEL,S, , ,       line(AR29,1)
           ".Calculate the total nodal forces Fx,Fy,Fz

           FSUM

           !Define a local var Fz-component front crack-tip

           *GET,AR30, FSUM,,ITEM, FZ
                  *VFILL,FORCE(AR29,1),DATA,AR30 NSEL,S, , ,  behind(AR29,1)

           !Calculate the total nodal forces Fx,Fy,Fz

           FSUM

             !Define a local var with Fz-comp. behind crack-tip

           'GET,AR30, FSUM, , ITEM, FZ
           *VFILL,FORCEB(AR29,1),DATA,AR30
*ENDDO
!
!Define an array of the nodal displacement
!where DISPLEI and DISPLEB1 are for the upper semi-laminate and DISPLE2
  and DISPLEB2 for the lower part

*DIM,DISPLEI,,AR23
*DIM, DISPLEBI,,AR23
*DIM, DISPLE2 ,,AR23
* DIN DISPLEB2 , , AR23
```

```
!Select the nodes along this line and fill in the displacement arrays
!Displacement vectors
*DO,AR29, 1,AR23
            NSEL,S, , ,         frontup(AR29,l)
            *GET,AR31,NODE,frontup(AR29,1),U,Z
            *VFILL,displel(AR29,1),DATA,AR31
            NSEL,S, , ,       mfrontup(AR29,1)
            *GET,AR3I,NODE,mfrontup(AR29,1),U,Z
            *VFILL,displebl(AR29,1),DATA,AR31
            NSEL,S, , ,       frontlow(AR29,1)
            *GET,AR3I,NODE,frontlow(AR29,1),U,Z
            *VFILL,disple2(AR29,1),DATA,AR31
            NSEL,S, , ,       mfronlow(AR29,1)
            *GET,AR3I,NODE,mfronlow(AR29,1),U,Z
            *VFILL,displeb2(AR29,1),DATA,AR31
*ENDDQ



!
 !**********--DEFINE ARRAYS FOR THE FINAL SERR CALCULATIONS--************
  ------------------------------------------------------------------------

!Define Arrays for the SERR calculations

*DIM , DELTA„ AR23
*DIM,DELTAB „AR23
*DIM, BJ„AR23+1
*DIM,COEFF „AR23 *
DIM, PRODO„AR2 3
*DIM,PRODOB „AR23
*DIM,SUMCOMP„AR23
*DIM, GvVCCT„AR23

!formula : Bi = 1/6[(Bj)+F(Bj+1)]

*VFILL,Bj(1,1),DATA,❑
*D0,AR29, 2,AR23
*GET,AR32,NODE,Iine(AR29-1,1),LOC,Y
*GET,AR33,NODE,1ine(AR29,I),LOC,Y
*SET,AR34,AR33-AR32
*VFILL,Bj(AR29,1),DATA,AR34
*ENDDQ
*VFILL, Bj (AR23+1, 1) ,DATA, O

*DO,AR29, 1,AR23
*SET,AR34,BJ(AR29,1)+BJ(AR29+l,1)
*SET,AR34,(1/6)*AR34
*SET,AR34,--(1*10**3)1(2*SIZE*AR34)
*VFILL,COEFF(AR29,1),DATA,AR34
*ENDDQ
```

!formula : (DELTA crackfront UPPER - DELTA crackfront LOWER)

*VOPER,delta(1,.1), displel(1,1),SUB,disple2(1,1), ,

!formula : (DELTA behindcrack UPPER - DELTA behindcrack LOWER)

*VOPER,deltab(1,1) ,displebl(1,1),SUB,displeb2(1,1),

```
!formula : FZ_crackfront*(DELTA crackfrant_UPPER -
DELTA crackfront LOWER)

*VOPER,prodo(1,1),delta(1,1),MULT,FORCE(1,1),

!formula   FZbehindcrack*(DELTA_behindcrack_ UPPER -
DELTA behindcrack LOWER)

*VOPER,prodob(1,1),deltab(1,1),MULT,FORCEB(1,1),

!formula    [FZ1*(DELTA1)+FZ2*(DELTA2)]

*VOPER,sumcomp(1,1),prodo(1,1),ADD,prodob(1,1), , ,

?formula : [FZ1*(DELTA1)+FZ2*(DELTA2)]
}
!formula    (1/(2DELTA crack*Bi))*[FZ1*(DELTAI)+FZ2*(DELTA2)]

!formula for the total SERR coefficient : (1/(2*DELTA crack*Bi)) !N.B.
10**3 is the convertion factor to have SERR calc in JIm2

?COEFF=

*VOPER,G VCCT(1,1),COEFF(1,1),MULT,SUMCOMP(1,1), , ,
line=
behind=
frontup=
mfrontup=
front1ow=
mfron1ow=
DISPLE1=
DISPLEB1=
DISPLE2=
DISPLEB2=
FORCE=
FORCEB=
DELTA=
DELTAB=
PRODO=
PRODOB=
SUMCOMP=
COEFF=
BJ=
FINISH
```

Appendix E

Energy plots

Energy balance and energy rates graphs for different z-pin parameters.

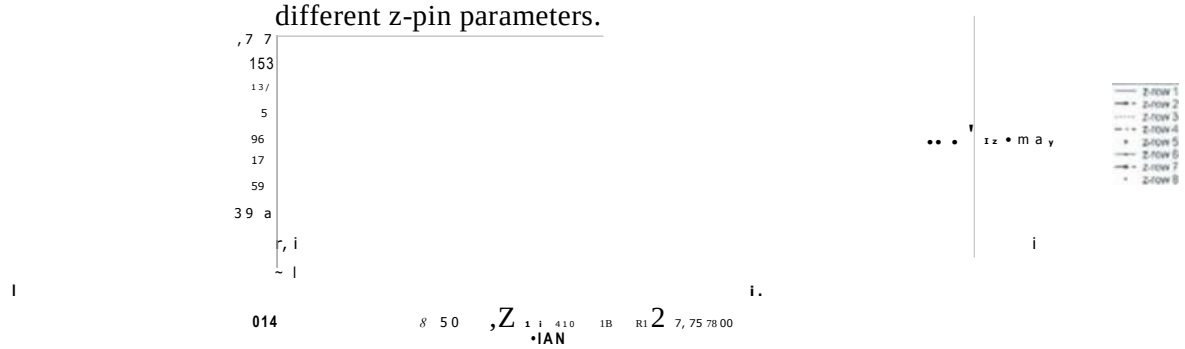

Figure E-1 *Computational interface element nodal forces for 8 z-fibre rows against crack length a: (a) c = 0.5% and r = 15 MPa; (b) c - 0.5% and r = 10 MPa.*

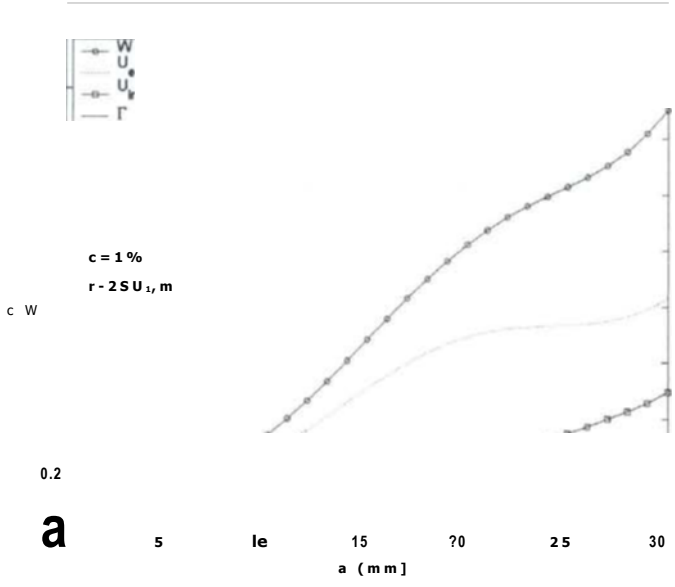

Figure E-2 ***Computational*** *energy terms for z-reinforced* ***OCR FE model: c = 0.5%, r = 250 Wn.***

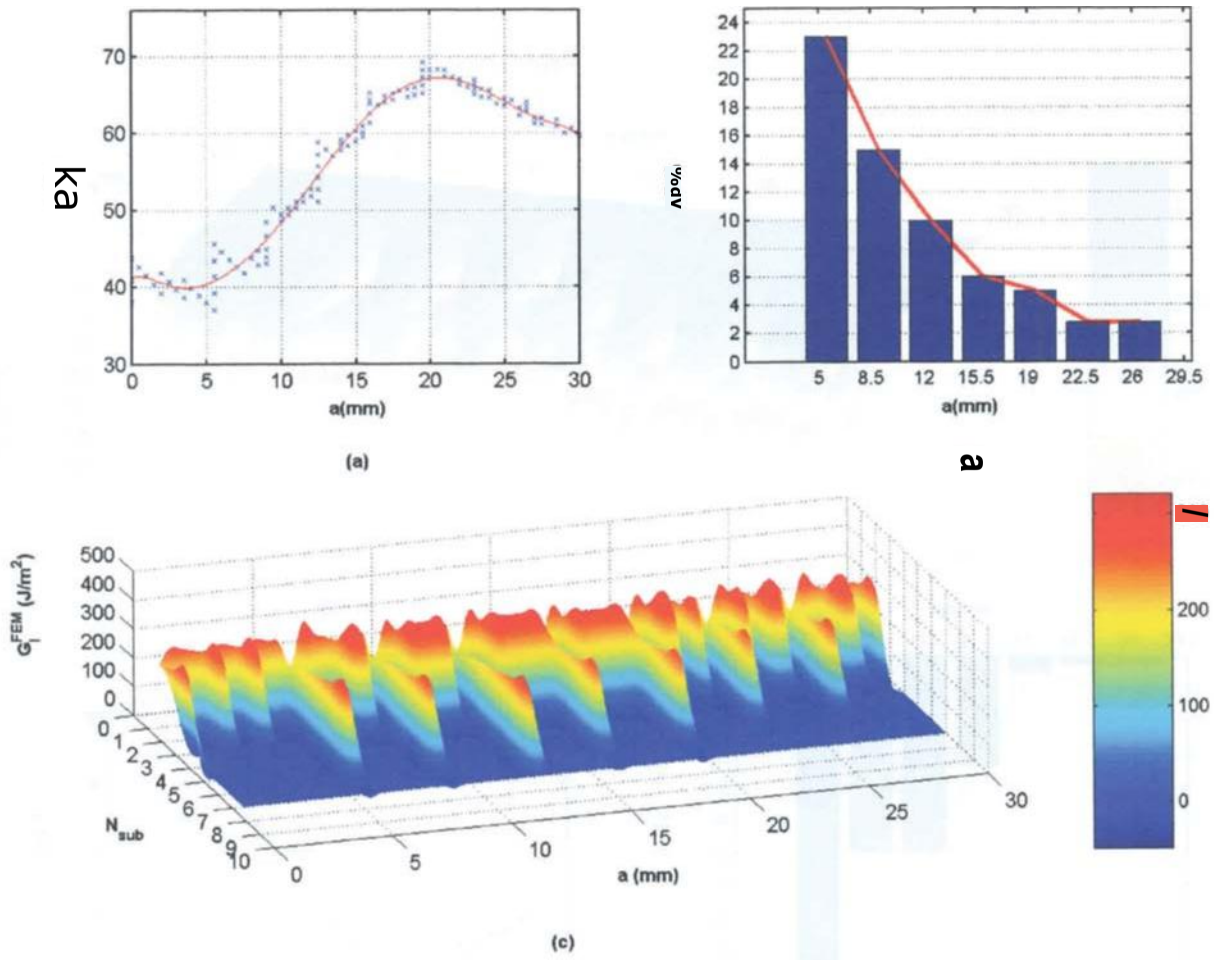

Figure E-3 *The delamination arrest analysis (c = 0.5%, r = 140μm, τ =10 MPa): (a) Load P against delamination length; (b) percentage of load increment to propagate delamination; (c) G-matrix array interpolation of* G_I^{FEM} *computed using VCCT .*

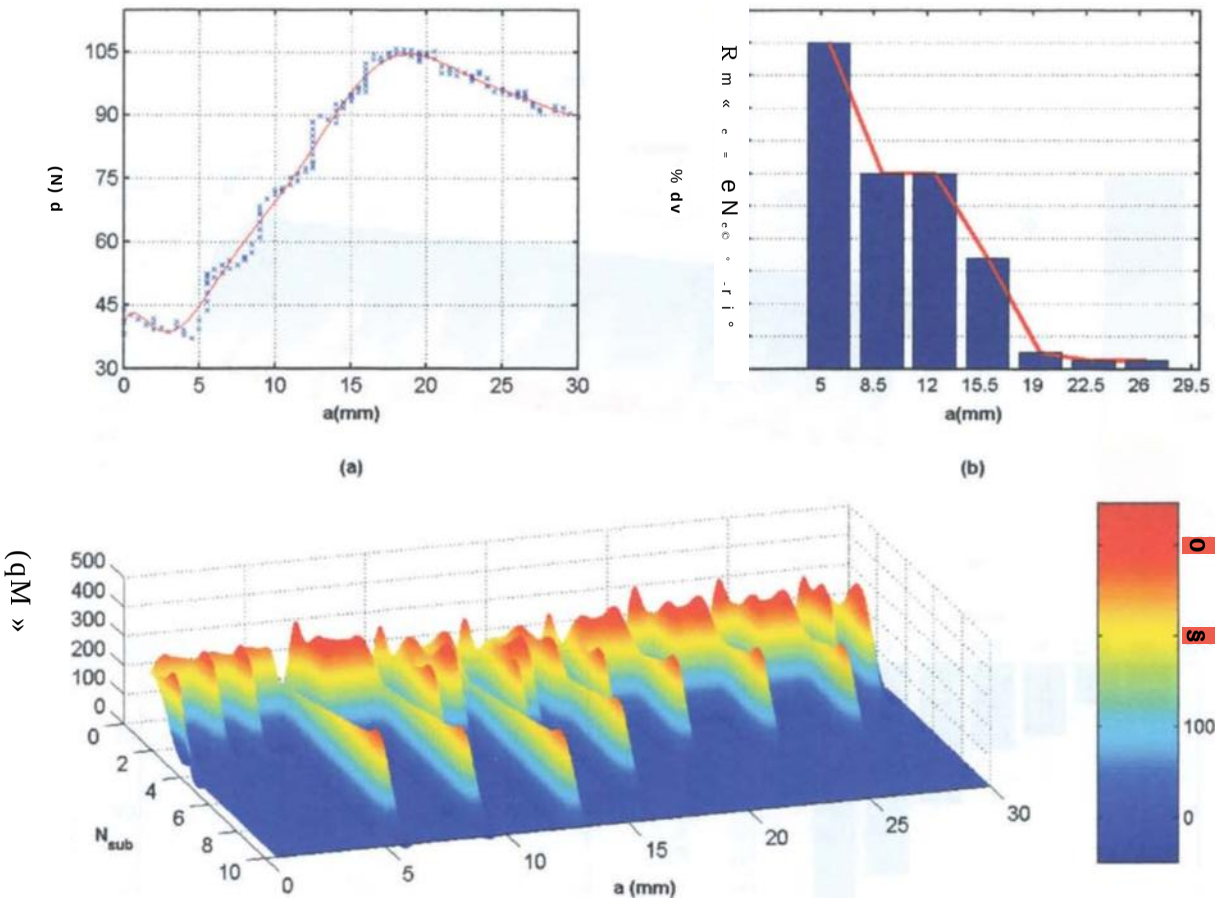

Figure E-4 *The delamination arrest analysis (c = 0.5%, r = 140μm, τ =25 MPa): (a) Load P against delamination length; (b) percentage of load increment to propagate delamination; (c) G-matrix array interpolation of* G_I^{FEM} *computed using VCCT .*

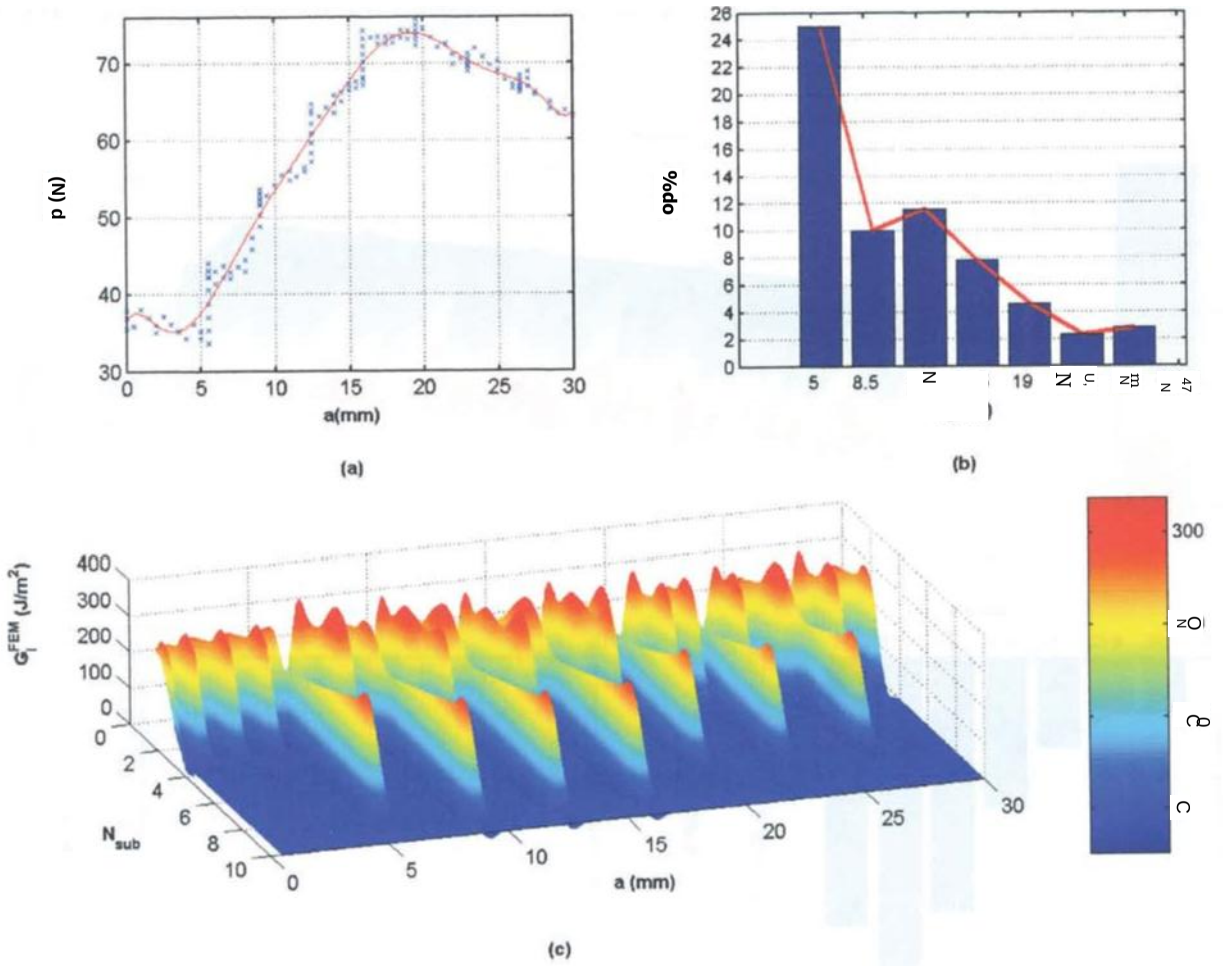

Figure E-5 *The delamination arrest analysis (c = 0.5%, r = 140μm, E_{xx}=110 GPa): (a) Load P against delamination length; (b) percentage of load increment to propagate delamination; (c) G-matrix array interpolation of G_I^{FEM} computed using VCCT .*

Figure E-6 *The de*
delamination leng
interpolation of G

140μm, E_{xx}=165 GPa): (a) Load P aga
'opagate delamination; (c) G-matrix ar

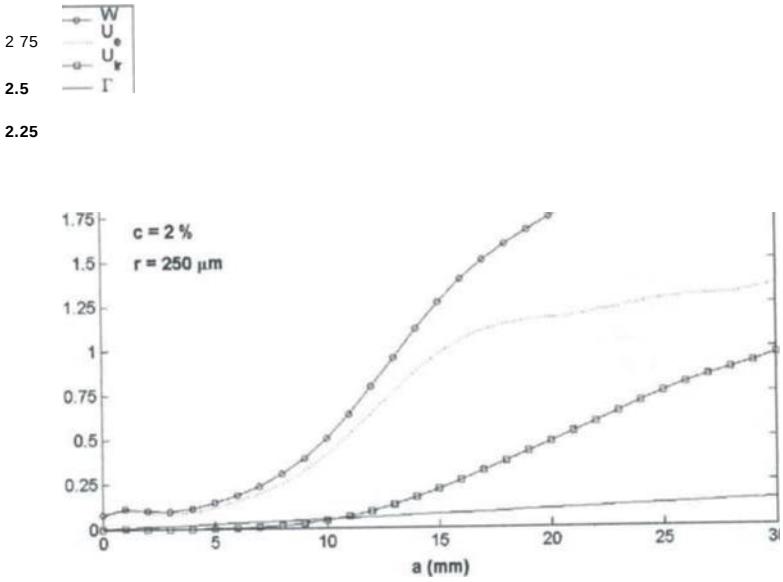

Figure *E-7* *Computational energy terms for z-reinforced DCB FE model: c = 2%, r = 250* pn.

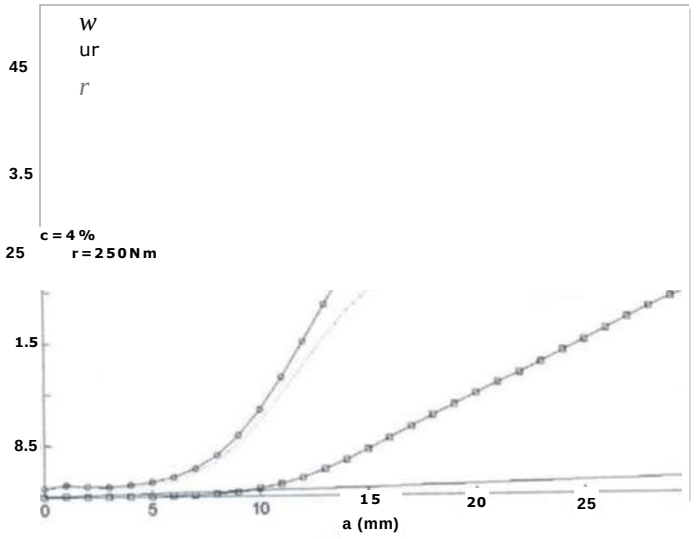

Figure E-8 *Computational energy terms for z-reinforced DC'B FE model: c = 4%, r = 25() pot.*

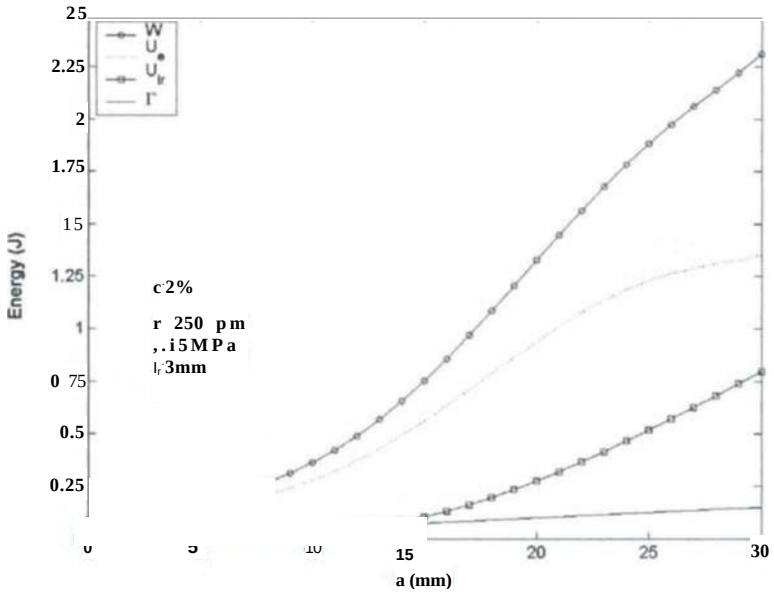

Figure E-9 *Computational energy terms for reinforced DC'B FE model: c = 2%, r - 250 /tm, l,. -- 3mm (partially pinned).*

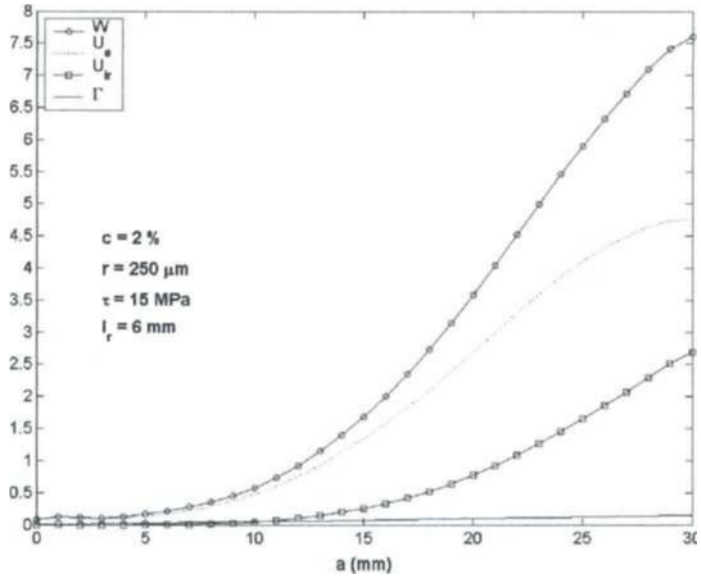

***Figure* E-10** *Computational energy te/ Ls for z-reirafiirced IXB FE model: c = 2%, r = 250 gm, 1r = 6mm (fiully pinned)*

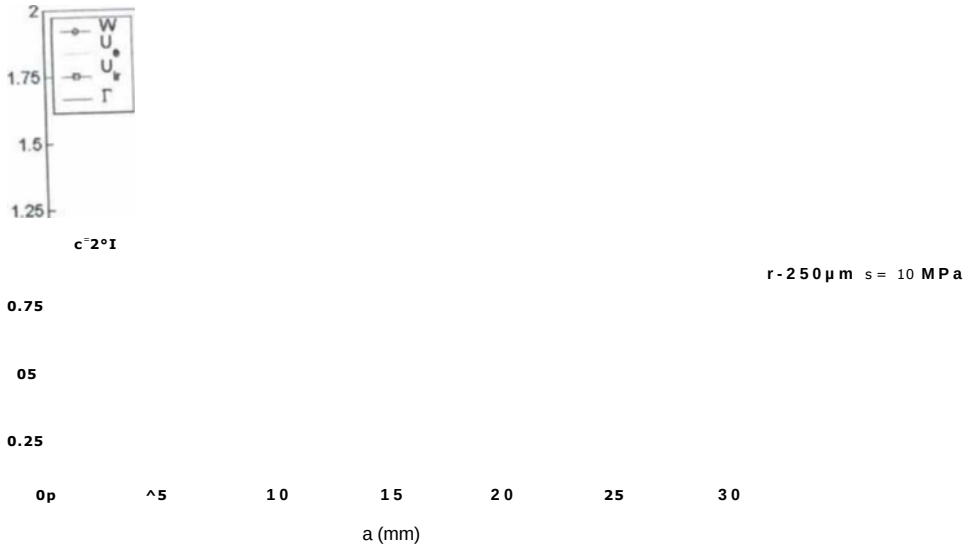

***Figure* E-11** *Computational energy term, for z-reinforced DCB FE model: c 2%, r = 250 pm r = 10 MPa.*

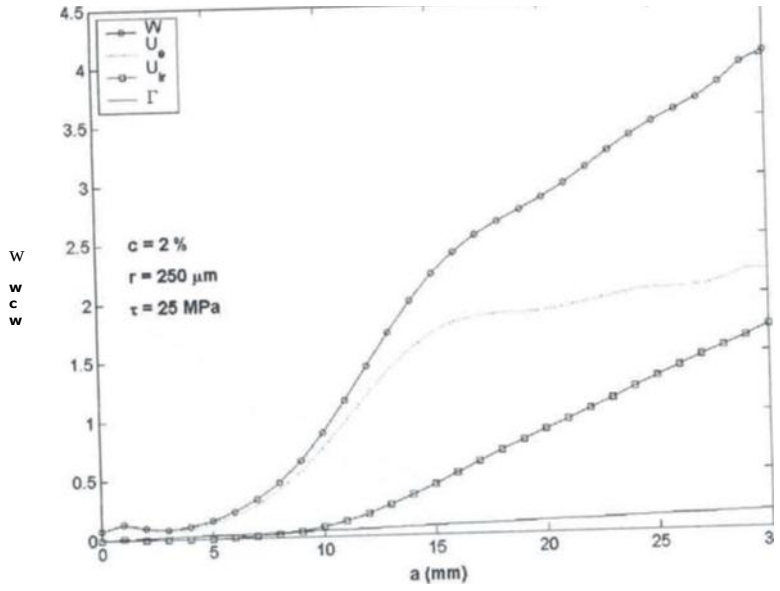

Figure E-12 ***Computational energy terms for z-reinforced DCB FE model: c = 2%, r 250pm, r=25MPa.***

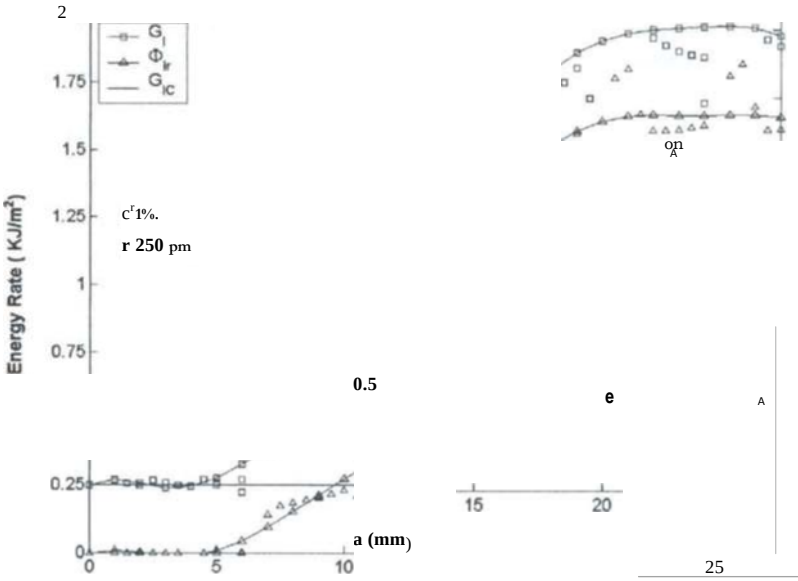

Figure E-13 *Computed energy rates (KI m2) /br pinned 1_)t'R: c - 1%, r - 250 gym.*

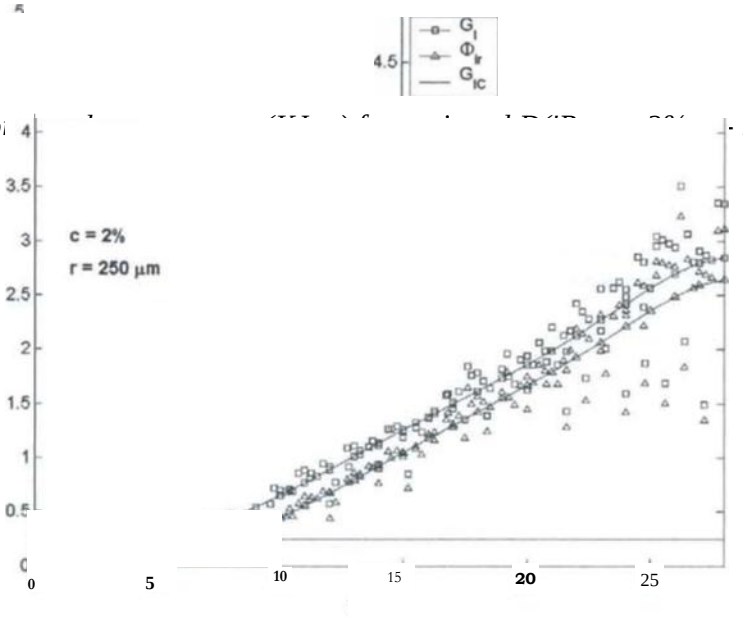

Figure E-14 *Co 250* m t.

Figure E-15 Computed *energy rates (KJ m') fnrzTinned DCB: c = 2%, r - 1401.un.*

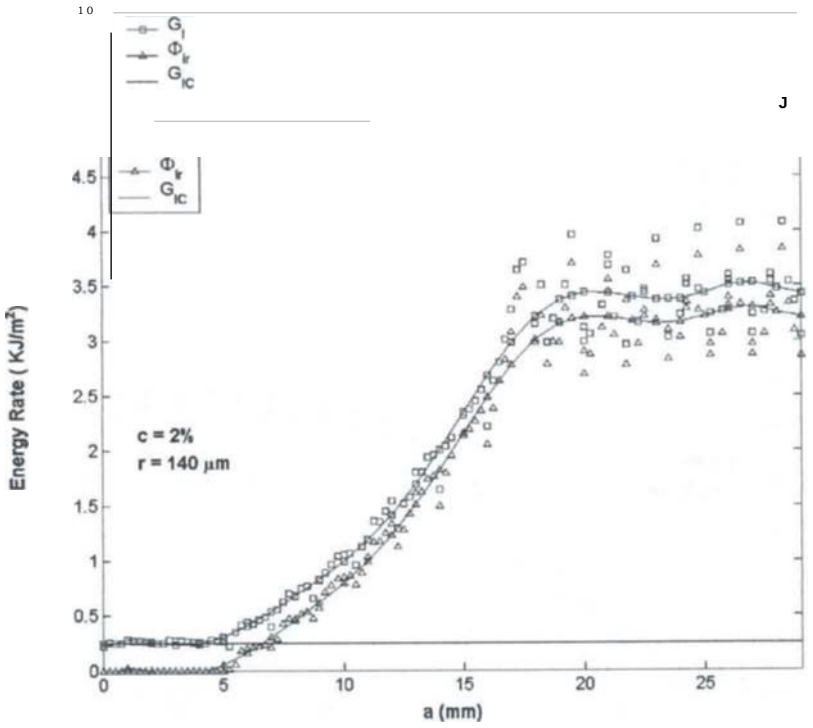

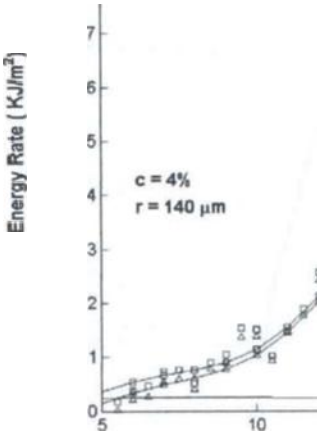

Figure *E-16*

Computed energy rates (KJ m 2), for z-pinned DCB: c = 4%, r = 140 pm.

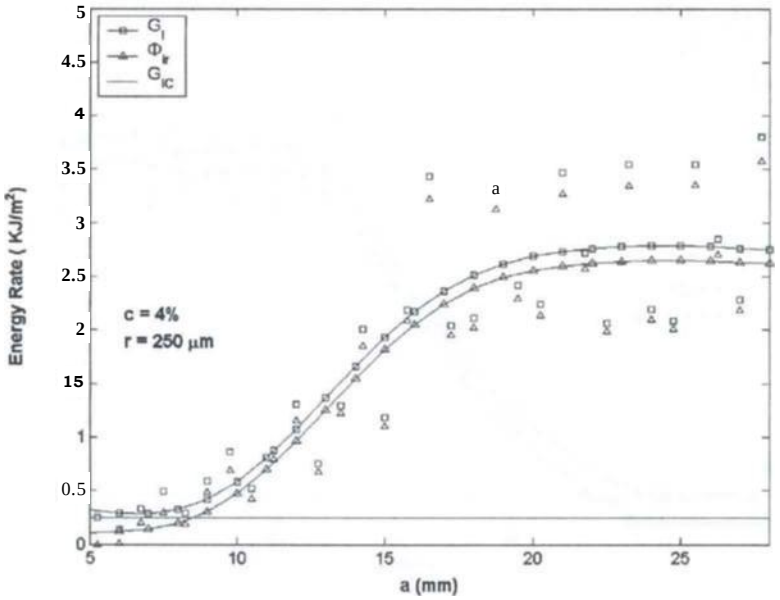

Figure E-17 *Computed energy rates (ICJ "m) fnr z -pinned DC:B: c = 4%, r - 250* m *a.*

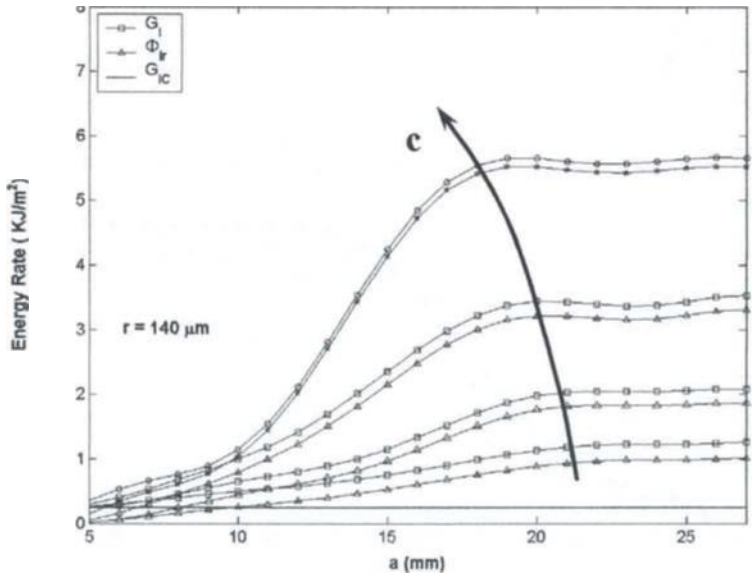

Figure E-18 *Computed energy rates (ICJ n) for z-pinned DCB with an increased z-pin density.*

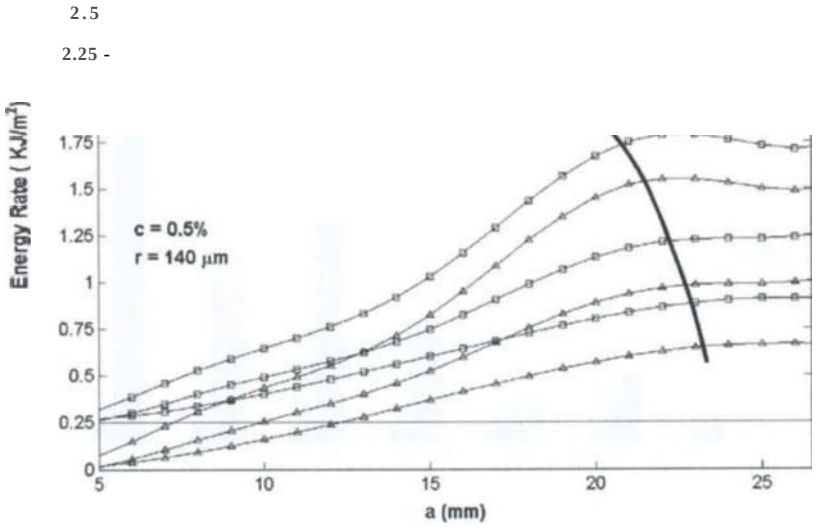

Figure E-19 *Computed energy rates (KJ in') for z -pinned DCB with increasing friction* stress.

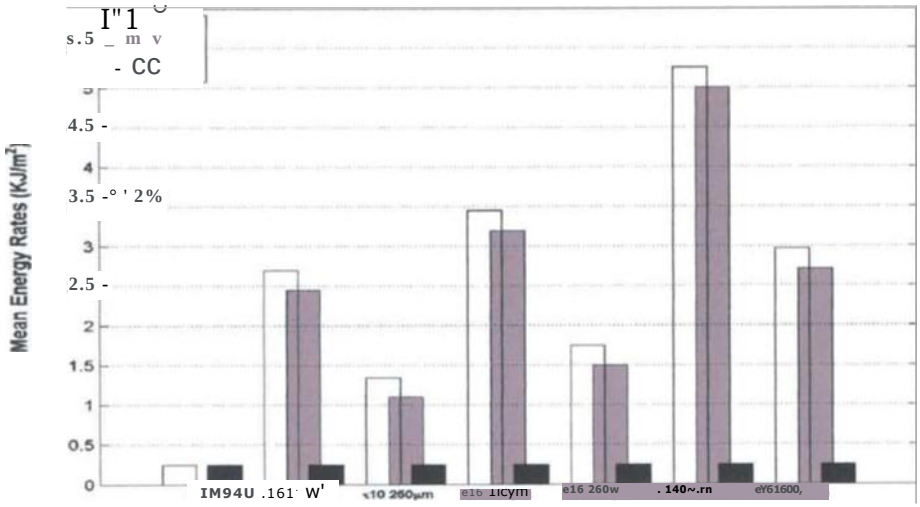

Figure E-20 *Averaged energy rates during stable I, B process P r different z-pin friction* stresses.

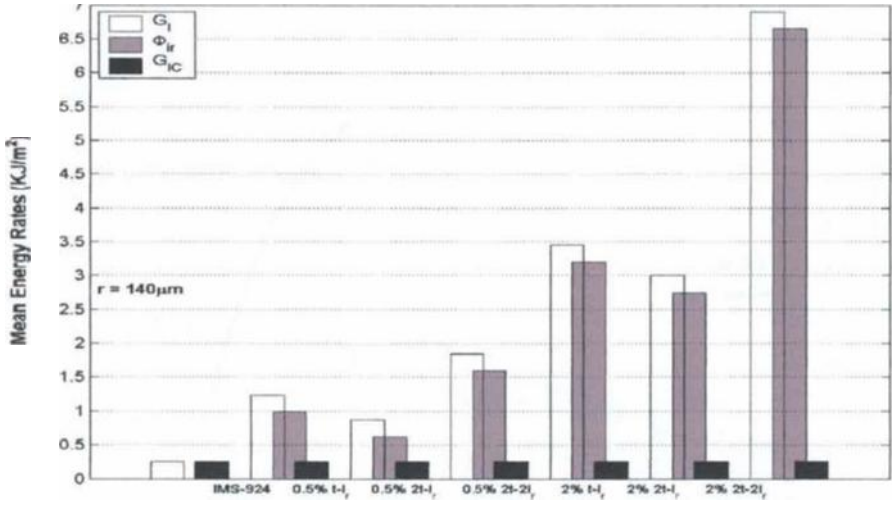

Figure E-2 *i Averaged energy rates during stable LSB process fnr different* z-pin *friction stresses.*

Appendix F

The domain of the possible solutions from the model presented in Appendix B, is firstly computed for the displacements vectors (U`,W) and (U',W'), for all the possible (O,E_o). Some constraint equations are defined to restrict the functions domain:

D S E o 5 $_{max}$ z-pin axial failure

- maximum deformation angle 2

Furthermore for the pre-pullout regime:

Ls Lr

Ls-- *rj,*

the pullout equations are computed until

I)s 5Lr

Considering (O,,E) as indipendent variables a discrete array of data U(£r$_j$, *ad* and W(), 6,) can be computed and then with MATLAB interpolation a continuous solution surface can be generated for U and W (figure F- l a).

Zl = griddata(x,y,z,XI,YI) fits a surface of the form z = f(x,y) to the data in the (usually) non-uniformly spaced vectors (x,y,z), interpolating this surface at the points specified by (XI,YI) to produce ZI. The surface always passes through the solution data points. Xl and YI usually form a uniform grid (as produced by mesligrid) (figure F-la).

The interpolation function can be linear, cubic, based on the nearest point, the different methods define the type of surface fit to the data. The 'cubic' method produce smooth surfaces while 'linear' and 'nearest' have discontinuities in the first and second derivatives, respectively. All these methods are based on a Delaunay triangulation of the data.

Form the FE $_{1th}$ run the TTR displacement vectors are sought *(U, W),* the initial condition for the single z-pin is assumed to be

(Bih E) = (0,0) *(initial condition)*

The FE computed displacement vectors are then inputted in a specifically written MATLAB solution search algorithm that finds the closest point to the previous couple (t_{om}, L) that satisfies the computed displacement vectors (U, W)$_{PEM}$ (figure F- l b). From the new computed couple (8,,.I;), a new set of traction component is sought *(fi,T3)* and then a new set of TTR element stiffness matrix is computed for the successive FE run.

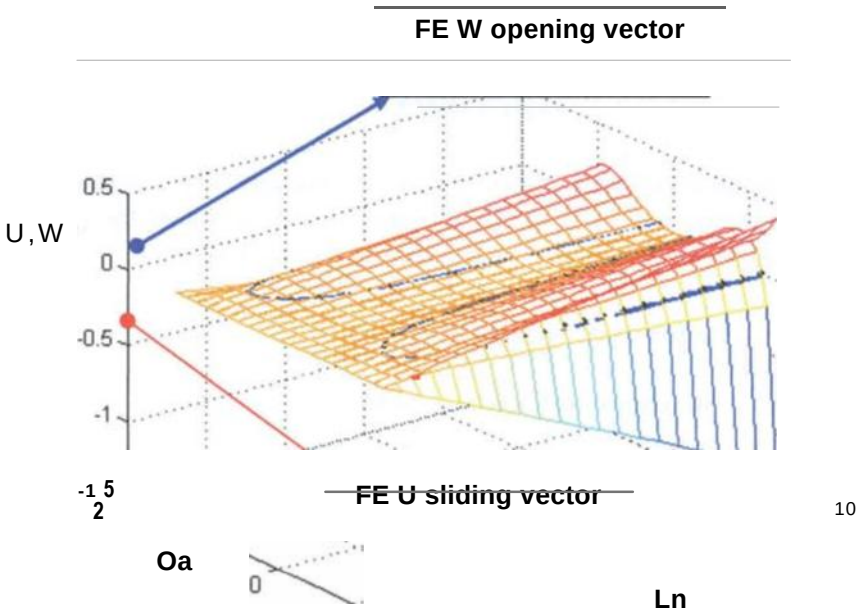

(a)

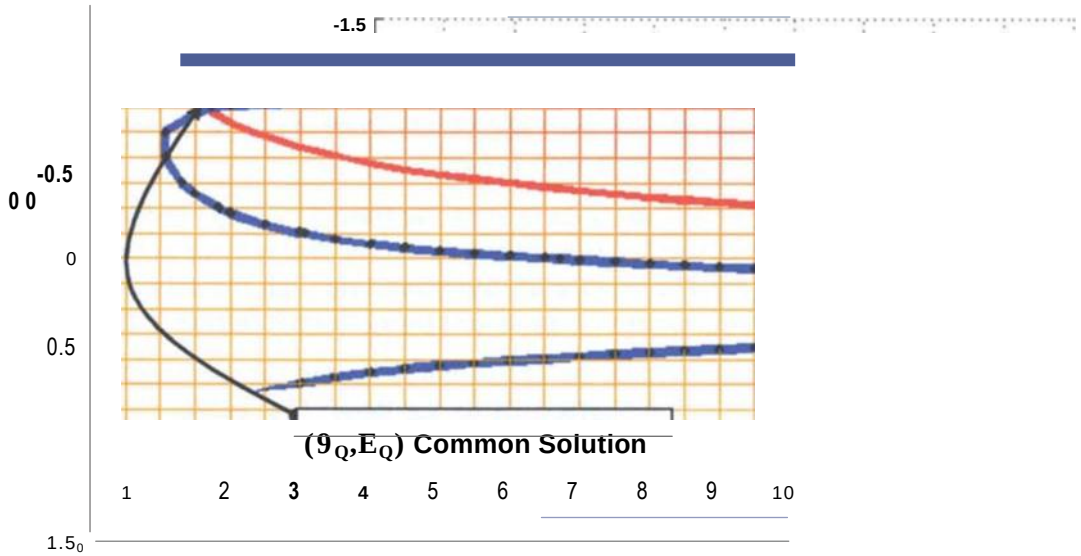

(b) Figure F-1 *(a)The U(Z, 6 and W (, 6) solution domain, a common solution is .sought for a* given *displacement vector generated by the FE* analysis. (h) *The intersection of the curves gives the only possible* (Z, *6) for such displacement vector 01,W).*